

# Vectorial properties and laser control of molecular dynamics



## Dissertation

zur Erlangung des naturwissenschaftlichen Doktorgrades  
der Julius-Maximilians-Universität Würzburg

vorgelegt von

**Philipp Marquetand**

aus

Heidelberg

Würzburg, 2007



Eingereicht am: .....

bei der Fakultät für Chemie und Pharmazie

1. Gutachter: .....

2. Gutachter: .....

der Dissertation

1. Prüfer: .....

2. Prüfer: .....

3. Prüfer: .....

des öffentlichen Promotionskolloquiums

Tag des öffentlichen Promotionskolloquiums: .....

Doktorurkunde ausgehändigt am: .....



# Contents

<b>1</b>	<b>Introduction</b>	<b>1</b>
<b>2</b>	<b>Basic principles</b>	<b>5</b>
2.1	Classical dynamics . . . . .	5
2.2	Quantum dynamics . . . . .	7
2.3	Properties of electro-magnetic fields . . . . .	11
2.3.1	Chirp and Fourier transform . . . . .	13
2.4	Interaction of electro-magnetic fields with matter . . . . .	18
2.4.1	Time-dependent perturbation theory . . . . .	19
2.4.2	Fermi's golden rule . . . . .	20
2.4.3	Rotating wave approximation . . . . .	22
2.4.4	Rabi oscillations . . . . .	23
2.5	Adiabatic vs. diabatic potentials and Born-Oppenheimer approximation . . . . .	25
2.5.1	Adiabatic expansion . . . . .	26
2.5.2	Diabatic expansion . . . . .	27
2.5.3	Example . . . . .	28
2.6	Landau-Zener theory . . . . .	29
<b>3</b>	<b>Numerical Methods</b>	<b>31</b>
3.1	Runge-Kutta algorithm for classical trajectories . . . . .	31
3.2	Short-time propagator . . . . .	32
3.3	Split-operator technique . . . . .	32
3.4	Relaxation method . . . . .	34
3.5	The rotational degree of freedom . . . . .	36
3.6	Simpson integral . . . . .	38

---

<b>4</b>	<b>Control theories - A short overview</b>	<b>39</b>
4.1	Brumer-Shapiro quantum interference . . . . .	39
4.2	STIRAP . . . . .	40
4.3	Tannor-Kosloff-Rice pump-dump . . . . .	41
4.4	Chirping . . . . .	42
4.5	Genetic algorithms and feedback control . . . . .	42
4.6	Optimal control theory . . . . .	44
4.7	Local control theory (LCT) . . . . .	46
<b>5</b>	<b>Local control theory revisited</b>	<b>47</b>
5.1	Energy objective . . . . .	48
5.2	Vibrational eigenstate objective . . . . .	49
5.3	Electronic state objective . . . . .	50
5.4	Energy objective including rotation . . . . .	50
5.5	Orientation objective . . . . .	51
<b>6</b>	<b>Laser control of the NaI molecule</b>	<b>53</b>
6.1	Heating and cooling within an electronic state . . . . .	56
6.1.1	Heating . . . . .	57
6.1.2	Cooling . . . . .	61
6.2	Dissociation and Predissociation . . . . .	63
6.2.1	Na + I vs. Na <sup>+</sup> + I <sup>-</sup> . . . . .	65
6.2.2	Suppressing predissociation . . . . .	69
6.3	Complete control of NaI . . . . .	72
<b>7</b>	<b>Vectorial properties: ro-vibrational dynamics in external fields</b>	<b>81</b>
7.1	Predissociation in a static electric field . . . . .	81
7.1.1	The model system . . . . .	82
7.1.2	Pendular states . . . . .	88
7.1.3	Quantum dynamics . . . . .	90
7.1.4	Pump-probe spectroscopy . . . . .	96
7.2	LCT - the rotational degree of freedom . . . . .	98
7.2.1	Fixed orientation . . . . .	100
7.2.2	Rotational-vibrational dynamics . . . . .	100
7.2.3	Rotational-vibrational dynamics in a static field . . . . .	107
7.3	Molecular polarizability and orientation . . . . .	111

---

<b>8</b>	<b>Laser control of a molecular motor</b>	<b>117</b>
8.1	Model and control scheme . . . . .	118
8.2	Ground state as initial state . . . . .	120
8.3	Arbitrary initial state . . . . .	123
8.4	Dressed initial state in a static field . . . . .	125
<b>9</b>	<b>Photoassociation</b>	<b>131</b>
9.1	Model and control schemes . . . . .	131
9.2	Fixed orientation: s-wave scattering . . . . .	135
9.3	The role of orientation . . . . .	143
<b>10</b>	<b>Molecular dump processes induced by chirped laser pulses</b>	<b>147</b>
10.1	Model . . . . .	149
10.2	Linear chirp . . . . .	150
10.3	Triangular phase . . . . .	158
<b>11</b>	<b>Summary</b>	<b>171</b>
<b>12</b>	<b>Zusammenfassung</b>	<b>177</b>
<b>A</b>	<b>Appendix</b>	<b>183</b>
A.1	Change between adiabatic and diabatic picture . . . . .	183
	<b>Bibliography</b>	<b>185</b>
	<b>List of publications</b>	<b>205</b>
	<b>Danksagung</b>	<b>209</b>
	Curriculum Vitae	





*Intelligence is the ability of the intellect that allows us to comprehend that everything is incomprehensible.*

Charles Émile Picard



# 1 Introduction

One of the central problems in chemistry is to control the outcome of reactions. This is usually realized by adjusting temperature, concentration or pressure, i.e. on the macroscopic level. In this way, the yield of kinetically favored products can be maximized, while the formation of unwanted ones is suppressed. Another means is the use of catalysts or enzymes, which influence the reaction on a microscopic scale. Even products, which are not dynamically favored, can be synthesized in this manner. Nevertheless, no general solution is provided to the primary goal.

A different way to control chemical reactions is the application of electro-magnetic radiation to molecular species. In general, every molecular system can be modified by a molecule-field interaction to yield a desired product. This universality arises from the large variety of parameters, which can be adapted to yield electro-magnetic fields of the most different shapes and colors. In this way, chemical bonds can be broken and formed selectively.

To effectively apply light to a given chemical system, usually lasers are used. The latter provide high intensities of coherent radiation, which is desirable to exert control on the molecules. Of course, the employed light has to be distinctly shaped in order to achieve a predefined objective. But how have phase and amplitude of the electro-magnetic field to look like? This problem is addressed by several theories, and also experimental techniques are available, see e.g. the monographs [1–3] and review articles [4–11]. These methods are also shortly summarized in chapter 4. One of the theoretical approaches is called “local control theory” and will be the main subject in this thesis.

As laser light is polarized, also directional aspects have to be considered. The treatment of vectorial properties, especially the orientation of a molecule with respect to the polarization vector of the electric field, is often difficult and/or time-

consuming. This extension goes beyond existing work, where the rotational degree of freedom nearly always is neglected. In this work, vectorial properties are explicitly addressed in many of the studied examples. Hence, the existing gap is narrowed.

The temporal structure of the regarded laser fields is associated with the timescale of quantum-mechanical motion. As rotations and vibrations occur within picoseconds ( $1 \text{ ps} = 10^{-12} \text{ s}$ ) or even femtoseconds ( $1 \text{ fs} = 10^{-15} \text{ s}$ ), the duration of the pulses have to be comparable or even shorter. Such ultra-short laser pulses are nowadays experimentally available. They made possible the real-time observation of the nuclear motion within molecules, which exhibits velocities of approximately  $1 \frac{\text{km}}{\text{s}}$  and covers distances of a few Ångström ( $1 \text{ Å} = 10^{-10} \text{ m}$ ). The corresponding research field is often termed “femtochemistry” [12] and Ahmed Zewail was awarded the Nobel Prize in 1999 for his outstanding achievements in this area [13]. Soon after the availability of femtosecond pulses, different shaping techniques were applied, which had already been established in the picosecond range [14]. In this way, phase, amplitude and polarization of the electro-magnetic fields can be formed and adapted in almost any arbitrary design.

The shaping of laser fields is not only useful for chemical reaction control. By this manner, also the properties of the underlying system can be investigated in more detail than it would be possible with other means. Albeit not treated here, the feasibility of shaping laser pulses opens up a wealth of applications in quantum optics, quantum computing, telecommunications, etc. [15].

Today, we are still at the beginning of this interesting field of research. The systems investigated are usually two- or three-atomic molecules or simplified models of larger systems. A very well known vision of how far the development in this domain could proceed in the future, occurs in the science fiction movies of “Star Trek”. Here, machines – called replicators – synthesize e.g. a cup of coffee by shining light on a beam of atoms. Beforehand, a source for the atoms is needed. In this context, the global waste problem could be solved. So the first step would be to split up waste into atoms, which afterwards could be reassembled in a desired way. In other words, we are far away from what can be dreamed of, but the foundation is layed. This work aims at a deeper understanding of the relation between laser control fields, molecular dynamics and the selectivity of a control process.

It is organized as follows: The theoretical background of the performed numerical calculations is presented in chapter 2. Here, classical and quantum-mechanical dynamics are discussed, as well as properties of electro-magnetic fields. Numerical methods are summarized in chapter 3, where e.g. a fast algorithm for wavefunction propagation including the rotational degree of freedom is described. The state of the art in control strategies is reviewed in chapter 4. From the various approaches, local control theory, which is employed in this thesis, is analyzed in more detail in chapter 5.

Numerical examples are presented in the subsequent chapters. Energy transfer induced by a control field is studied within a restricted model in chapter 6. There, the goal is to deposit enough energy in a molecule so that fragmentation is effective. In this case, sodium iodide is taken as model. The limitations of the model system are successively abolished and processes like predissociation due to a non-adiabatic coupling are included.

In chapter 7, the rotational degree of freedom is fully taken into account. As a first example, the influence of a static electric field on the NaI rotational-vibrational dynamics is discussed. Afterwards, the effects of control fields are investigated.

Directed quantities are also considered in chapter 8, where the rotation of a functional group around a bond axis in a molecule is controlled. As in the preceding chapters, it is shown, that local control theory yields pulse shapes, which are easily understood.

The counterpart to fragmentation is association, which is examined in chapter 9. This topic has attracted many scientists recently due to the availability of methods to trap molecules. Here, local control theory is applied for the first time to the process of photoassociation.

In chapter 10, an approach different from local control is chosen to systematically analyze the properties of control fields. After an electronic excitation (pumping) with an unshaped pulse, the effectivity of a selective de-excitation (dumping) with tailored pulses is investigated. Thus, the new concept of a pump/shaped-dump

scheme is applied [16, 17], while in common control experiments the first pulse is shaped and eventually following pulses remain unchanged. In this work, only one or two pulse parameters are scanned systematically, while the other parameters are fixed. The efficiency of the different resulting pulse shapes is compared and connections to the physics of the underlying system are established with the help of control landscapes.

Finally, the results are summarized in chapters 11 and 12.

# 2 Basic principles

## 2.1 Classical dynamics

In 1687, Sir Isaac Newton published his work “*Philosophiae Naturalis Principia Mathematica*” [18]. It contains Newton’s equations of motion, which form the foundation of classical mechanics. Joseph Louis Lagrange introduced a re-formulation in 1788 [19].

In Lagrangian mechanics, especially the motion of bodies restricted by certain constraint conditions is considered [20]. The constraints can take different forms, e.g. a mass point bound to a surface.

Generalized coordinates  $\{q_i\}$  are employed, because the equations show the same form for different representations. For the ease of writing, in what follows only one coordinate  $q$  and its time derivative, i.e. velocity  $v = \frac{dq}{dt} = \dot{q}$  is used. The Lagrangian equation of motion then reads [20, 21]

$$\frac{d}{dt} \left( \frac{\partial \mathcal{L}}{\partial \dot{q}} \right) = \frac{\partial \mathcal{L}}{\partial q}, \quad (2.1)$$

where  $\mathcal{L}$  is the so-called Lagrangian, defined as the difference between kinetic energy  $T$  and potential energy  $V$ . For a particle of mass  $m$ , this results in

$$\mathcal{L} = \frac{1}{2}m\dot{q}^2 - V(q). \quad (2.2)$$

Due to fact that  $V$  is independent of the generalized velocity

$$\frac{\partial V}{\partial \dot{q}} = 0 \quad (2.3)$$

and  $T$  is independent of the generalized coordinate

$$\frac{\partial T}{\partial q} = 0, \quad (2.4)$$

the connection between the Newtonian and the Lagrangian mechanics can be easily seen:

$$\frac{\partial \mathcal{L}}{\partial q} = \frac{d}{dt} \left( \frac{\partial \mathcal{L}}{\partial \dot{q}} \right) \quad (2.5)$$

$$\Rightarrow -\frac{\partial V}{\partial q} = \frac{d}{dt} \left( \frac{\partial \frac{1}{2} m \dot{q}^2}{\partial \dot{q}} \right) \quad (2.6)$$

$$\Rightarrow F = m\ddot{q} \quad (2.7)$$

Here,  $F$  is the force, connected to the potential energy via

$$-F = \frac{\partial V}{\partial q}. \quad (2.8)$$

This is the basic equation used for molecular dynamics simulations and the classical calculations in this work. Here, a trajectory, i.e. the route of a particle's position in space is evaluated via

$$q(t + dt) = q(t) + \dot{q}(t) \cdot dt \quad (2.9)$$

$$\dot{q}(t + dt) = \dot{q}(t) + \ddot{q}(t) \cdot dt = \dot{q}(t) + \frac{F}{m} \cdot dt = \dot{q}(t) - \frac{\partial V}{\partial q} \cdot dt \quad (2.10)$$

These equations are exact within first order, but can be easily extended to second-order correctness, see section 3.1.

A re-formulation of the Lagrangian mechanics was pointed out in 1833 by William Rowan Hamilton [22]. One advantage among others of the Hamiltonian formalism is that it allows for an extension to quantum mechanics (see section 2.2). It involves rather the generalized momenta  $p = m\dot{q}$  than the generalized velocities  $\dot{q}$ . From eqns. (2.3-2.7), the relation to the Lagrangian already is uncovered:

$$\frac{\partial \mathcal{L}}{\partial \dot{q}} = m\dot{q} = p \quad (2.11)$$

Additionally, the Lagrangian is replaced by the Hamiltonian  $\mathcal{H}$ , which is the sum of kinetic and potential energy:

$$\mathcal{H} = \frac{p^2}{2m} + V(q) \quad (2.12)$$

The two functions  $\mathcal{H}$  and  $\mathcal{L}$  are connected via a Legendre transformation:

$$\mathcal{H} = \mathcal{H}(q, p, t) = p\dot{q} - \mathcal{L}(q, \dot{q}, t) \quad (2.13)$$



The equations of motion in the Hamiltonian representation are:

$$\frac{\partial \mathcal{H}}{\partial p} = \dot{q} \quad (2.14)$$

$$\frac{\partial \mathcal{H}}{\partial q} = -\dot{p}. \quad (2.15)$$

Regarding more than one particle (e.g. in the case of different starting conditions), an ensemble of trajectories  $q_i$  can be investigated. Statistical weights are introduced by a probability  $P_i$  to construct a classical density

$$\rho(q, t) = \sum_i^{\infty} q_i P_i. \quad (2.16)$$

The classical density's motion is expressed by the classical Liouville equation

$$\begin{aligned} \frac{d\rho}{dt} &= \frac{\partial \rho}{\partial t} + \left[ \frac{\partial \rho}{\partial q_i} \dot{q}_i + \frac{\partial \rho}{\partial p_i} \dot{p}_i \right] \\ &= \frac{\partial \rho}{\partial t} + \left[ \frac{\partial \rho}{\partial q_i} \frac{\partial \mathcal{H}}{\partial p_i} - \frac{\partial \rho}{\partial p_i} \frac{\partial \mathcal{H}}{\partial q_i} \right] = 0. \end{aligned} \quad (2.17)$$

The total time derivative of the classical density vanishes because the density along a trajectory is constant (Imagine a drop of water moving on an uneven surface: The drop gets narrower and wider but the amount of water stays the same). The Liouville theorem is often restated using Poisson brackets (the quantum mechanical analogue is the commutator, see section 2.2):

$$\frac{\partial}{\partial t} \rho = - \{ \rho, \mathcal{H} \}. \quad (2.18)$$

The above expression is reduced to Hamiltonian equations of motion for a density represented by a  $\delta$ -function [23].

## 2.2 Quantum dynamics

The publication of Louis de Broglie's thesis on matter waves in 1924 [24], together with works from 1905 by Albert Einstein, lay the foundation for the concept of wave-particle duality [25]. The idea of particles as waves (and vice versa) was developed into the theory of quantum mechanics by Erwin Schrödinger and many others. Here, the Hamiltonian formulation of classical mechanics is adopted with some modifications. Classical variables are assigned to quantum mechanical operators

(principle of correspondence) and the vectors  $q(t)$  are replaced by state vectors  $|\psi(q, t)\rangle$  in Hilbert space. The resulting equation of motion is the time-dependent Schrödinger equation

$$i\hbar \frac{\partial}{\partial t} |\psi(q, t)\rangle = \hat{H} |\psi(q, t)\rangle. \quad (2.19)$$

The Hamilton operator  $\hat{H}$ , similar to the classical Hamiltonian, consists of the sum of kinetic and potential energy operators ( $\hat{T} + \hat{V}$ ).

Originally, Schrödinger derived his wave equation as an eigenvalue problem in time-independent form [26]

$$(\hat{H} - E) |\psi(q)\rangle = 0, \quad (2.20)$$

where  $E$  is the system's eigenenergy.

As Briggs and Rost pointed out, this equation is a real quantum mechanical one, while the time-dependent form is a mixed quantum-classical equation [27, 28]. The time enters only by introducing classical approximations. To show this, the universe is divided into the quantum system of interest (index  $S$ ) and an environment (index  $E$ ):

$$[\hat{H}_S(q) + \hat{H}_E(Q) + \hat{H}_I(q, Q)] \Psi = E \Psi. \quad (2.21)$$

Here,  $\hat{H}_I$  is the interaction between the system with coordinates  $q$  and the environment with coordinates  $Q$ . Accordingly, the total wavefunction can be expanded

$$\Psi(q, Q) = \sum_m \chi_m(Q) \phi_m(q, Q). \quad (2.22)$$

As a consequence of the environment being much “larger” than the quantum system, the coupling  $\hat{H}_I$  is asymmetric. In other words, a state  $\chi$  of the environment hardly depends on the system's variables  $q$ , while a state  $\phi$  of the system depends on the environment's variables  $Q$ . The first approximation is to neglect the coupling of the system to the environment and to ease the expansion of the total wavefunction

$$\Psi(q, Q) = \chi(Q) \phi(q, Q). \quad (2.23)$$

The second approximation is to make the ansatz of a semi-classical wavefunction [29] for a state  $\chi$  of the environment:

$$\chi(Q) = A(Q) \cdot e^{\frac{i}{\hbar} W(Q)}, \quad (2.24)$$

where  $W(Q) = \int dq p = \int dq \sqrt{2m[E - V(q)]}$  is the classical action. This is justified by the environment being large and quasi-classical. Nevertheless, its exact eigenvalue equation

$$(\hat{H}_E + \hat{U}_S)\chi = E\chi, \quad (2.25)$$

with  $\hat{U}_S$  representing the small influence of the system on the environment, is used to obtain the precursor to the time-dependent Schrödinger equation:

$$\chi(\hat{U}_S - \hat{H}_E - \hat{H}_I)\phi = \frac{\hbar}{i}\chi \frac{1}{m} \frac{\partial W}{\partial Q} \frac{\partial \phi}{\partial Q}. \quad (2.26)$$

Here, the classical approximation of  $\hbar \rightarrow 0$  is applied. Now employing that the spatial derivative of the action is the classical momentum

$$\frac{\partial W}{\partial Q} = p = m \frac{\partial Q}{\partial t}, \quad (2.27)$$

leads to the form

$$(\hat{H}_E + \hat{H}_I - \hat{U}_S)\phi = i\hbar \frac{\partial \phi}{\partial t}. \quad (2.28)$$

A phase or gauge transformation with

$$\phi = e^{\frac{i}{\hbar} \int_{-\infty}^t dt' \hat{U}_S(t')} \psi \quad (2.29)$$

and consequently,

$$\begin{aligned} i\hbar \frac{\partial \phi}{\partial t} &= i\hbar \frac{\partial}{\partial t} e^{\frac{i}{\hbar} \int_{-\infty}^t dt' \hat{U}_S(t')} \psi \\ &= -\hat{U}_S(t) e^{\frac{i}{\hbar} \int_{-\infty}^t dt' \hat{U}_S(t')} \psi + i\hbar e^{\frac{i}{\hbar} \int_{-\infty}^t dt' \hat{U}_S(t')} \frac{\partial \psi}{\partial t} \end{aligned} \quad (2.30)$$

leads to the well-known time-dependent Schrödinger equation for the system only:

$$(\hat{H}_E + \hat{H}_I)\psi = i\hbar \frac{\partial \psi}{\partial t}. \quad (2.31)$$

The interaction term  $\hat{H}_I$  can be e.g. classical electro-magnetic fields. In other words,  $\hat{H}_I$  depends on classical variables.

To summarize, the key approximation is to treat the environment classically in order to introduce the time-dependence.

The solution of the time-dependent Schrödinger equation for a given initial wavefunction  $|\psi(t_0)\rangle$  is obtained by separation of variables and subsequent integration, leading to (for a time-independent Hamiltonian only)

$$|\psi(t)\rangle = e^{-\frac{i}{\hbar}\hat{H}\cdot(t-t_0)}|\psi(t_0)\rangle, \quad (2.32)$$

where  $e^{-\frac{i}{\hbar}\hat{H}\cdot(t-t_0)} = \hat{U}(t, t_0)$  is the so-called propagator. For a time-dependent Hamiltonian, a propagator of the form

$$\hat{U}(t, t_0) = e^{-\frac{i}{\hbar}\int_{t_0}^t \hat{H}(t')dt'} \quad (2.33)$$

could be presumed. This however, holds only for operators, where the following commutator vanishes:

$$[\hat{H}(t), \frac{\partial \hat{H}}{\partial t}] = \hat{H}(t) \frac{\partial \hat{H}}{\partial t} - \frac{\partial \hat{H}}{\partial t} \hat{H}(t) = 0. \quad (2.34)$$

Otherwise, the evaluation of  $\frac{\partial}{\partial t} e^{\hat{H}(t)}$  according to the chain rule to  $\frac{\partial \hat{H}}{\partial t} e^{\hat{H}(t)}$  is not valid [30]. The general form is obtained, when assuming that a propagator exists, which achieves the time evolution

$$|\psi(t)\rangle = \hat{U}(t, t_0)|\psi(t_0)\rangle. \quad (2.35)$$

Because this must hold for any wavefunction and any time, the result for  $t_0$  is:

$$\hat{U}(t_0, t_0) = \mathbb{1}. \quad (2.36)$$

Furthermore, if the time evolution is inserted into the time-dependent Schrödinger equation

$$\frac{\partial}{\partial t} \hat{U}(t, t_0) |\psi(t_0)\rangle = -\frac{i}{\hbar} \hat{H}(t) \hat{U}(t, t_0) |\psi(t_0)\rangle, \quad (2.37)$$

then this expression must also be fulfilled for any initial wavefunction. Consequently, the following expression is also valid:

$$\frac{\partial}{\partial t} \hat{U}(t, t_0) = -\frac{i}{\hbar} \hat{H}(t) \hat{U}(t, t_0). \quad (2.38)$$

Integration yields the general form

$$\hat{U}(t, t_0) = \mathbb{1} - \frac{i}{\hbar} \int_{t_0}^t dt' \hat{H}(t') \hat{U}(t', t_0). \quad (2.39)$$

An approximate solution to this equation can be obtained by iteration

$$\begin{aligned}\hat{U}(t, t_0) &= \mathbb{1} - \frac{i}{\hbar} \int_{t_0}^t dt' \hat{H}(t') \left[ \mathbb{1} - \frac{i}{\hbar} \int_{t_0}^{t'} dt'' \hat{H}(t'') \left[ \dots \right] \right] \\ &= \mathbb{1} - \frac{i}{\hbar} \int_{t_0}^t dt' \hat{H}(t') + \left( \frac{i}{\hbar} \right)^2 \int_{t_0}^t dt' \int_{t_0}^{t'} dt'' \mathcal{T} \hat{H}(t') \hat{H}(t'') + \dots,\end{aligned}\tag{2.40}$$

where  $\mathcal{T}$  is a time-ordering operator, since the equation is only satisfied if  $t \geq t' \geq t'' \geq \dots \geq t_0$ . Now, the expansion can be rewritten as

$$\hat{U}(t, t_0) = \mathcal{T} e^{-\frac{i}{\hbar} \int_{t_0}^t \hat{H}(t') dt'}.\tag{2.41}$$

The time-ordering problem is usually circumvented in numerical applications by using very short time intervals (see section 3.2).

## 2.3 Properties of electro-magnetic fields

The time dependency of a Hamiltonian usually arises from scattering processes or the interaction of the system with electro-magnetic radiation. Such a problem would be treated exactly within quantum electrodynamics. The latter was developed to a large extent by Richard Feynmann, Julian Schwinger and Sin-Itiro Tomonaga, who were awarded the Nobel Prize in physics 1965 for their work. But since in the limit of large photon numbers the fields can be treated classically, which is the case throughout this work, only classical aspects are addressed, here.

The basis for classical electrodynamics are Maxwell's equations, published in 1865 by James Clerk Maxwell [31]. Together with the Lorentz force equation and Newton's second law of motion, they provide a complete description of the classical dynamics of interacting charged particles and electromagnetic fields [32].

Due to the fact that the magnetic interaction of the field with a particle usually is much weaker than the electric one, the discussion is restricted to electric fields. From the Maxwell's equations, the wave equation for electric fields  $\vec{E}$  in the vacuum can be derived [33]

$$\frac{1}{c^2} \frac{\partial^2}{\partial t^2} \vec{E} = \nabla^2 \vec{E},\tag{2.42}$$

with  $c$  being the speed of light. A solution to this equation is

$$\vec{E}(\vec{q}, t) = \vec{\epsilon} \cos(\omega_0 t - \vec{k}\vec{q}), \quad (2.43)$$

where  $\vec{k}$  is the wave vector and  $\vec{\epsilon}$  is the polarisation vector. Under the assumption that an envelope function  $A(t)$  varies little within one optical cycle, the following equation is also valid (compare “slowly-varying envelope approximation”) [33, 34]:

$$\vec{E}(\vec{q}, t) = \vec{\epsilon} A(t) \cos(\omega_0 t - \vec{k}\vec{q}), \quad (2.44)$$

The polarisation vector  $\vec{\epsilon}$  will be dropped in what follows, because only the absolute value of the field will be regarded.

Additionally, the dipole approximation is used, i.e. the position dependency  $\vec{k}\vec{q}$  is neglected due to the wavelength of the field being much larger than the system’s dimension. Now, the above equation can be rewritten as

$$\begin{aligned} E(t) &= \frac{A(t)}{2} (e^{i\omega_0 t} + e^{-i\omega_0 t}) \\ &= A(t) \Re(e^{i\omega_0 t}). \end{aligned} \quad (2.45)$$

Here, the argument  $\omega_0 t$  is called the temporal phase. The envelope function resembles a Gaussian for usual laser pulses

$$A(t) = E_0 e^{-\beta t^2}. \quad (2.46)$$

The pulse duration  $\tau_E$  is given as the full width at half maximum (FWHM) of this function, which is connected to the exponential factor  $\beta$  via:

$$\beta = \frac{4 \ln 2}{\tau_E^2}. \quad (2.47)$$

It is important, not to confuse this  $\tau_E$  with the pulse duration  $\tau_I$  (often used in experimental publications) according to the temporal intensity function  $I(t)$ . The latter is defined proportional to the temporal average of  $E(t)^2$  over one oscillation period  $T = \frac{2\pi}{\omega}$ ,

$$\begin{aligned} I(t) &= \varepsilon_0 c n \frac{1}{T} \int_{t-\frac{T}{2}}^{t+\frac{T}{2}} dt' E(t')^2 \\ &= \frac{1}{2} \varepsilon_0 c n A(t)^2, \end{aligned} \quad (2.48)$$

with the vacuum dielectric constant  $\varepsilon_0$ , the speed of light  $c$  and the refractive index  $n$ . The intensity  $I(t)$  is usually given in  $W/cm^2$ , while  $V/cm$  is used for the temporal amplitude  $A(t)$ .

### 2.3.1 Chirp and Fourier transform

The momentary light frequency of a laser puls is defined as the time derivative of the temporal phase  $\Phi(t)$ :

$$\omega(t) = \frac{d\Phi(t)}{dt}. \quad (2.49)$$

In the electric fields mentioned above, the phase was  $\Phi(t) = \omega_0 t$  and thus, the momentary frequency was constant ( $\omega(t) = \omega_0$ ). This is not necessarily the case and for a general form, the phase term may be expanded as Taylor series around  $t_0$

$$\Phi(t) = a_0 + a_1(t - t_0) + \frac{a_2}{2}(t - t_0)^2 + \dots = \sum_{j=0}^{\infty} \frac{a_j}{j!}(t - t_0)^j, \quad (2.50)$$

where the former  $\omega_0$  was renamed  $a_1$ , consistently.

Regarding the temporal derivative of the instantaneous frequency  $\frac{d\omega(t)}{dt} = \frac{d^2\Phi(t)}{dt^2}$ , three cases can be distinguished

- $\frac{d\omega(t)}{dt} > 0$  (up-chirp),
- $\frac{d\omega(t)}{dt} = 0$  (unchirped),
- $\frac{d\omega(t)}{dt} < 0$  (down-chirp).

The special case, when  $a_2$  is not equal to zero, but all higher  $a_j$  are, is called linear chirp, because then the momentary frequency  $\omega(t)$  changes linearly in time.

An equivalent description of the temporal field  $E(t)$  is obtained by its frequency domain representation  $E(\omega)$ . The latter can be evaluated by a complex-valued Fourier transform

$$E(\omega) = \frac{1}{\sqrt{2\pi}} \int_{-\infty}^{\infty} dt E(t) e^{-i\omega t}. \quad (2.51)$$

The field in time domain is recovered by the inverse Fourier transform

$$E(t) = \frac{1}{\sqrt{2\pi}} \int_{-\infty}^{\infty} d\omega E(\omega) e^{i\omega t}. \quad (2.52)$$

As  $E(t)$  is real valued,  $E(\omega)$  is hermitian, i.e. it obeys the condition ( $*$   $\hat{=}$  complex conjugation)

$$E(\omega) = E^*(-\omega). \quad (2.53)$$

Hence, the knowledge of the positive frequency part

$$E^+(\omega) = \begin{cases} E(\omega) & \text{if } \omega \geq 0, \\ 0 & \text{if } \omega < 0 \end{cases} \quad (2.54)$$

is sufficient for a full characterization of the field. The use of complex-valued functions for the real electric field  $E(t)$  simplifies the Fourier analysis. Therefore,  $E^+(t)$  is defined as the part which contains only the positive frequency segment of spectrum. The former is also known as analytic signal. Its complex conjugate  $E^-(t)$  contains the negative frequencies. Accordingly,  $E^+(t)$  is defined with a positive exponential

$$E^+(t) = A(t) e^{i\Phi(t)}, \quad (2.55)$$

while  $E^+(\omega)$  consequently must be defined with negative exponential

$$E^+(\omega) = A(\omega) e^{-i\Phi(\omega)}. \quad (2.56)$$

Just as the temporal phase  $\Phi(t)$ , the spectral phase  $\Phi(\omega)$  can be expanded as Taylor series around  $\omega_0$  ( $= a_1$  from temporal phase expansion)

$$\Phi(\omega) = b_0 + b_1(\omega - \omega_0) + \frac{b_2}{2}(\omega - \omega_0)^2 + \dots = \sum_{j=0}^{\infty} \frac{b_j}{j!} (\omega - \omega_0)^j. \quad (2.57)$$

Analogous to introducing a chirp by  $a_{j \geq 2} \neq 0$ , a chirp can also be achieved by  $b_{j \geq 2} \neq 0$ . The difference between these two ways of chirping is the pulse duration and intensity for conserved pulse energy. The energy  $\tilde{I}$  of the pulse is proportional to the time integral of the squared electric field

$$\tilde{I} \sim \int_0^{\infty} dt E(t)^2. \quad (2.58)$$

While the envelope of a temporal-chirped pulse stays the same as for an unchirped one, the pulse duration gets longer and the intensity in time domain becomes smaller for a frequency-chirped pulse. The latter is the experimental accessible way.

This is now illustrated with some examples regarding a linear chirp. A Gaussian is employed as envelope function and therefore, the general formula [35]

$$\int_{-\infty}^{\infty} dx e^{-ax^2+bx} = \sqrt{\frac{\pi}{a}} e^{\frac{b^2}{4a}} \quad (2.59)$$



is helpful for the Fourier transform below. The starting point is an electric field of the form

$$E(t) = A_0 e^{-\beta(t-t_0)^2} e^{i[a_0+a_1(t-t_0)+\frac{a_2}{2}(t-t_0)^2]}, \quad (2.60)$$

with

$$\begin{aligned} A_0 &= \frac{1}{\sqrt{2\pi}} \sqrt{\frac{\pi}{\gamma + i\frac{b_2}{2}}} e^{ib_1\omega_0} B_0, & \beta &= \frac{\gamma}{4\gamma^2 + b_2^2}, & t_0 &= b_1, \\ a_0 &= -b_0, & a_1 &= \omega_0, & a_2 &= \frac{b_2}{4\gamma^2 + b_2^2}. \end{aligned}$$

The Fourier transform yields

$$E(\omega) = B_0 e^{-\gamma(\omega-\omega_0)^2} e^{-i[b_0+b_1(\omega-\omega_0)+\frac{b_2}{2}(\omega-\omega_0)^2]}, \quad (2.61)$$

with

$$\begin{aligned} B_0 &= \frac{1}{\sqrt{2\pi}} \sqrt{\frac{\pi}{\beta - i\frac{a_2}{2}}} e^{-ia_1t_0} A_0, & \gamma &= \frac{\beta}{4\beta^2 + a_2^2}, & \omega_0 &= a_1, \\ b_0 &= -a_0, & b_1 &= t_0, & b_2 &= \frac{a_2}{4\beta^2 + a_2^2}. \end{aligned}$$

It can be readily seen, that a pulse not centered around time zero, simply means a non-zero first-order spectral phase coefficient  $b_1$ . If the FWHM of the Gaussian field envelope in frequency domain  $\varpi_E$  is compared with its counterpart in time domain  $\tau_E$  via a Fourier transform, the following relation is found:

$$\varpi_E \tau_E = 8 \ln 2. \quad (2.62)$$

The corresponding expression for the respective FWHM of the intensity functions is termed time-bandwidth product and is evaluated as

$$\varpi_I \tau_I = 4 \ln 2, \quad (2.63)$$

where

$$\beta = \frac{2 \ln 2}{\tau_I^2} \quad (2.64)$$

and

$$\gamma = \frac{2 \ln 2}{\varpi_I^2} \quad (2.65)$$

were used. Note however, that the temporal intensity and the spectral intensity are not directly connected via a Fourier transform.

Fig. 2.1 shows firstly a transform limited (i.e. unchirped) pulse with parameters  $A_0 = 1$  a.u.,  $\tau_E = 10$  fs,  $t_0 = 0$  fs,  $a_0 = 0$  and  $a_1 = 800$  nm is adopted. Then, a temporal chirp of  $a_2 = \pm 0.14/\text{fs}^2$  is added.

In Fig. 2.2, a phase factor  $a_0 = -\frac{\pi}{2}$ ,  $t_0 = 15$  fs and a frequency chirp of  $b_2 = 50$  fs<sup>2</sup> are applied to the original pulse. Here, the analytic form of the frequency-chirped pulse in time domain, with respect to the parameters of the unchirped pulse (indicated by a prime), is obtained via (since  $a'_2 = 0$  and thus,  $\gamma = \frac{1}{4\beta'}$ )

$$\begin{aligned} A_0 &= \sqrt{\frac{1}{1 + i2\beta'b_2}} A'_0, & \beta &= \frac{1}{\frac{1}{\beta'} + 4\beta'b_2^2}, & t_0 &= t'_0, \\ a_0 &= a'_0, & a_1 &= a'_1, & a_2 &= \frac{b_2}{\frac{1}{4\beta'^2} + b_2^2}. \end{aligned}$$

Another interesting pulse form is achieved, if applying a “triangular” phase in frequency domain, according to

$$E(\omega) = B_0 e^{-\gamma(\omega-\omega_0)^2} e^{-i[b_0+b_1|\omega-\omega_0|]}. \quad (2.66)$$

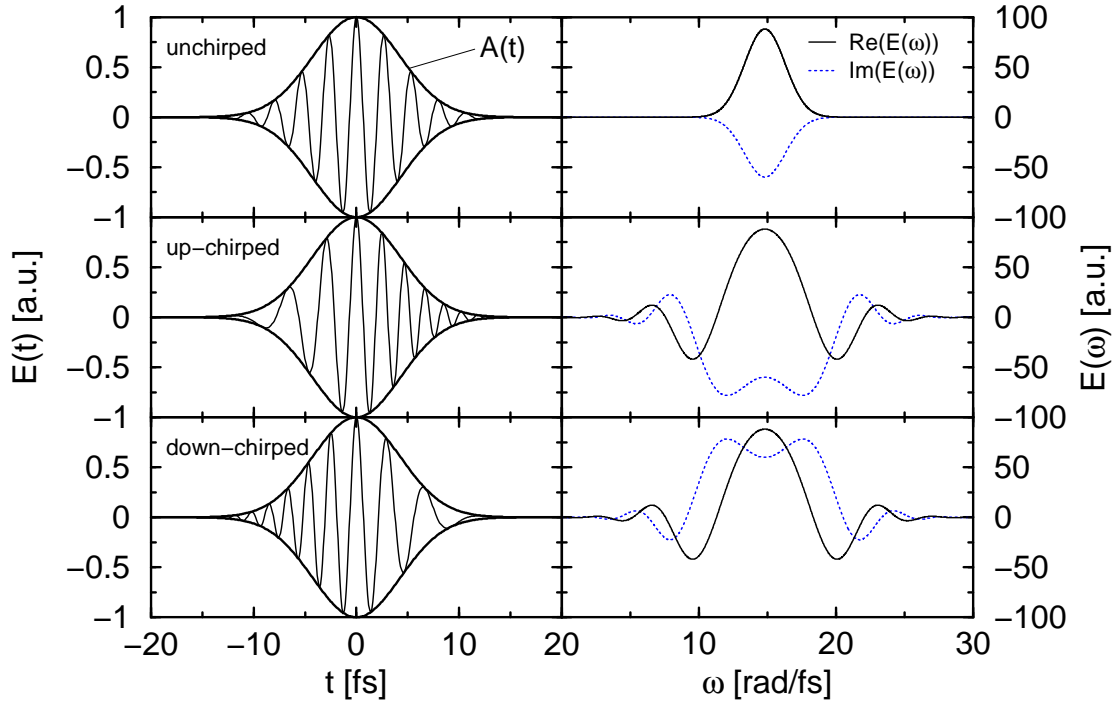


Figure 2.1: Left panels: field in time domain; right panels: field in frequency domain. Upper panels: unchirped; middle panels: up-chirped with  $a_2 = 0.14/\text{fs}^2$ ; lower panels: down-chirped with  $a_2 = -0.14/\text{fs}^2$ .

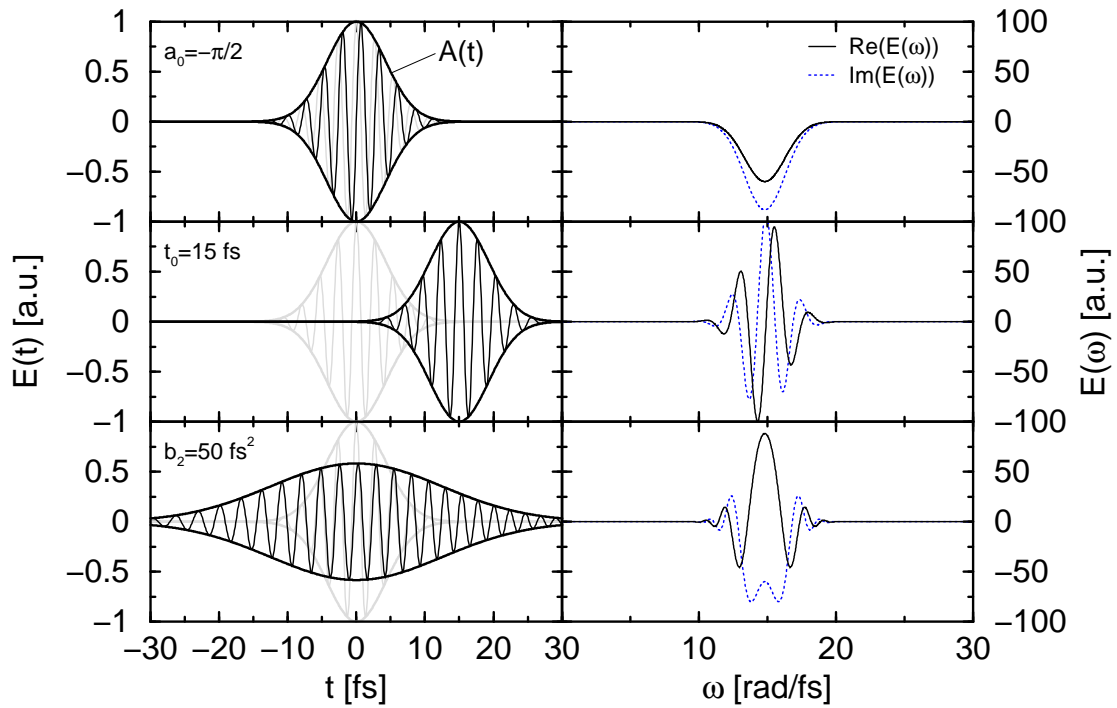


Figure 2.2: Left panels: field in time domain, the original pulse is depicted in gray for comparison; right panels: field in frequency domain. Upper panels: sine pulse with  $a_0 = -\frac{\pi}{2}$ ; middle panels: pulse centered around  $t_0 = 15$  fs; lower panels: up-chirped with  $b_2 = 50$  fs<sup>2</sup>.

The resulting temporal field exhibits a double peak structure (see Fig. 2.3). The reason is, that parts with higher energy than the carrier frequency are shifted to

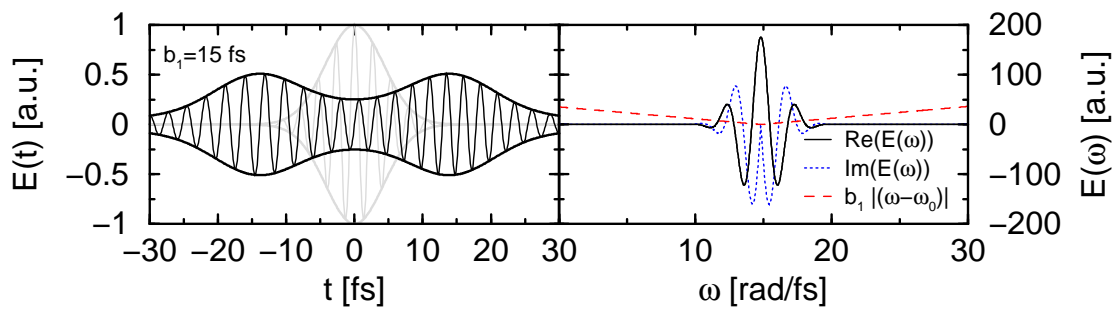


Figure 2.3: Field shaped with a triangular spectral phase  $b_1 = 15$  fs. Left panel: field in time domain, the original pulse is depicted in gray for comparison, right panel: field in frequency domain and triangular spectral phase  $b_1 |(\omega - \omega_0)|$ .

earlier times, while parts with lower energy are shifted to later times. This is only valid for positive  $b_1$ , whereas for negative  $b_1$  the shifting is reversed. Hence, one also speaks of a “blue pulse” followed by a “red pulse” in the case of positive  $b_1$ .

An example is shown in Fig. 2.3. Starting from the same unchirped pulse as in Fig. 2.1, a triangular phase with  $b_1 = 15$  fs is applied in frequency domain. The field in time domain is then evaluated via Fourier transform.

## 2.4 Interaction of electro-magnetic fields with matter

The interaction of a molecule with a time-dependent electric field leads to a time-dependent Hamiltonian of the general form

$$\hat{H}(t) = \hat{H}_0 + \hat{W}(t), \quad (2.67)$$

where  $\hat{H}_0$  is the Hamiltonian of the unperturbed system and  $\hat{W}(t)$  the time-dependent interaction. For a purely vibrational excitation, the molecule has to exhibit a permanent dipole moment  $\mu$ . Then the interaction term  $\hat{W}(t)$  is of the form

$$\hat{W}(t) = -\vec{\mu} \vec{E}(t). \quad (2.68)$$

With the angle  $\theta$  between the field vector on the dipole moment vector, the absolute value is obtained as

$$\hat{W}(t) = -\mu E(t) \cos \theta. \quad (2.69)$$

In the case of a transition between two electronic states  $|1\rangle$  and  $|2\rangle$ , the Hamiltonian is usually written as

$$\hat{H}(t) = \begin{pmatrix} \hat{T} + V_1 & -\vec{\mu}_{12} \vec{E}(t) \\ -\vec{\mu}_{12} \vec{E}(t) & \hat{T} + V_2 \end{pmatrix} \quad (2.70)$$

or

$$\hat{H}(t) = |1\rangle(\hat{T} + V_1)\langle 1| + |1\rangle(-\vec{\mu}_{12} \vec{E}(t))\langle 2| + |2\rangle(-\vec{\mu}_{12} \vec{E}(t))\langle 1| + |2\rangle(\hat{T} + V_2)\langle 2| \quad (2.71)$$

with the kinetic energy operator  $\hat{T}$ , the potential energy  $V_n$  in state  $|n\rangle$  ( $n = 1, 2$ ) and the transition dipole moment  $\vec{\mu}_{12}$ . Here, the projection of the field vector on the transition dipole moment vector leads to

$$-\vec{\mu}_{12} \vec{E}(t) = \begin{cases} \mu_{12} E(t) \cos \theta & \text{for a parallel transition} \\ \mu_{12} E(t) \sin \theta & \text{for a perpendicular transition.} \end{cases} \quad (2.72)$$

The type of transition (parallel or perpendicular) is determined by the symmetry of the involved states.

Regarding the special case of a static electric field, the Hamiltonian is not time-dependent and the corresponding Schrödinger equation yields field-dressed eigenstates [36, 37]. The latter are also termed pendular states [38], because the corresponding molecule is oriented to some extent and librating like a pendulum around the preferred direction.

### 2.4.1 Time-dependent perturbation theory

The interaction of a weak laser field with a molecule can be described within time-dependent perturbation theory [39]. The system obeys for  $t \leq 0$ , when no perturbation is present

$$i\hbar \frac{\partial}{\partial t} \Psi_0(t) = \hat{H}_0 \Psi_0(t). \quad (2.73)$$

For larger times, due to the perturbation, this changes to

$$i\hbar \frac{\partial}{\partial t} \Psi(t) = \left\{ \hat{H}_0 + \hat{W}(t) \right\} \Psi(t). \quad (2.74)$$

It is convenient for such problems to change to the interaction representation (index  $I$ ) [40], where

$$\Psi(t) = e^{-\frac{i}{\hbar} \hat{H}_0 t} \Psi_I(t) \quad (2.75)$$

and

$$\hat{W}_I(t) = e^{\frac{i}{\hbar} \hat{H}_0 t} \hat{W}(t) e^{-\frac{i}{\hbar} \hat{H}_0 t}. \quad (2.76)$$

The Schrödinger equation for the perturbed system now reads

$$i\hbar \frac{\partial}{\partial t} \Psi_I(t) = \hat{W}_I(t) \Psi_I(t). \quad (2.77)$$

Time integration leads to (analogue to Eq. (2.39) for the propagator)

$$\Psi_I(t) = \Psi_I(0) - \frac{i}{\hbar} \int_0^t dt' \hat{W}_I(t') \Psi_I(t'), \quad (2.78)$$

where at time  $t = 0$ , the wave function  $\Psi_I(0) = \Psi(0)$ . An approximate solution can be obtained by iteration

$$\begin{aligned}\Psi_I(t) &= \Psi_I(0) - \frac{i}{\hbar} \int_{t_0}^t dt' \hat{W}_I(t') \left[ \Psi_I(0) - \frac{i}{\hbar} \int_{t_0}^{t'} dt'' \hat{W}_I(t'') \left[ \dots \right] \right] \\ &= \Psi_I(0) - \frac{i}{\hbar} \int_{t_0}^t dt' \hat{W}_I(t') \Psi_I(0) \\ &\quad + \left( \frac{i}{\hbar} \right)^2 \int_{t_0}^t dt' \int_{t_0}^{t'} dt'' \hat{W}_I(t') \hat{W}_I(t'') \Psi_I(0) + \dots\end{aligned}\tag{2.79}$$

If the expansion is truncated after the first integral, the wave function is termed  $\Psi_I^{(1)}$ , because a first order correction is applied. The notation for higher orders proceeds analogously.

The first-order wave function in the Schrödinger picture can be evaluated by using Eq. (2.75):

$$\begin{aligned}\Psi^{(1)}(t) &= e^{-\frac{i}{\hbar} \hat{H}_0 t} \Psi_I^{(1)}(t) \\ &= e^{-\frac{i}{\hbar} \hat{H}_0 t} \left[ \Psi_I(0) - \frac{i}{\hbar} \int_0^t dt' \hat{W}_I(t') \Psi(0) \right] \\ &= e^{-\frac{i}{\hbar} \hat{H}_0 t} \Psi(0) - \frac{i}{\hbar} \int_0^t dt' e^{-\frac{i}{\hbar} \hat{H}_0 (t-t')} \hat{W}(t') e^{-\frac{i}{\hbar} \hat{H}_0 t'} \Psi(0).\end{aligned}\tag{2.80}$$

Accordingly, higher-order wave functions can be obtained.

### 2.4.2 Fermi's golden rule

An application of time-dependent perturbation theory is to describe transitions between two eigenstates of a quantum system. The eigenstates  $|n\rangle$  build an orthonormal basis and obey the time-independent Schrödinger equation

$$\hat{H}_0 |n\rangle = E_n |n\rangle\tag{2.81}$$

Assume, that the system, described by the total wave function  $\Psi(t)$ , is in state  $|1\rangle$  initially, which needs not be the groundstate necessarily. The probability  $P_{12}$  of a transition to an eigenstate  $|2\rangle$  (which can be any other eigenstate) at time  $t$  is given by [41]

$$P_{12}(t) = |\langle 2 | \Psi_I(t) \rangle|^2 = |\langle 2 | \Psi(t) \rangle|^2.\tag{2.82}$$

To evaluate this equation, the transition amplitude  $\langle 2|\Psi(t)\rangle$  is examined within first-order perturbation theory (compare Eq. (2.80)):

$$\begin{aligned}\langle 2|\Psi^{(1)}(t)\rangle &= \overbrace{\langle 2|e^{-\frac{i}{\hbar}\hat{H}_0 t}|1\rangle}^{=0} - \frac{i}{\hbar} \int_0^t dt' \langle 2|e^{-\frac{i}{\hbar}\hat{H}_0(t-t')} \hat{W}(t') e^{-\frac{i}{\hbar}\hat{H}_0 t'}|1\rangle \\ &= -\frac{i}{\hbar} e^{-\frac{i}{\hbar}E_2 t} \int_0^t dt' e^{\frac{i}{\hbar}(E_2-E_1)t'} \langle 2|\hat{W}(t')|1\rangle\end{aligned}\quad (2.83)$$

Therefore, the transition probability can be written as

$$P_{12}(t) = \left| \frac{i}{\hbar} \int_0^t dt' e^{\frac{i}{\hbar}(E_2-E_1)t'} \langle 2|\hat{W}(t')|1\rangle \right|^2. \quad (2.84)$$

Now, suppose  $\hat{W}$  is independent of time, i.e. a small constant term  $W$  is added to the Hamiltonian at  $t = 0$ , then

$$\begin{aligned}P_{12}(t) &= \left| \frac{i}{\hbar} \frac{e^{\frac{i}{\hbar}(E_2-E_1)t} - 1}{\frac{i}{\hbar}(E_2-E_1)} \langle 2|W|1\rangle \right|^2 \\ &= \left| \frac{e^{-\frac{i}{\hbar}E_1 t} - e^{-\frac{i}{\hbar}E_2 t}}{(E_2-E_1)} \langle 2|W|1\rangle \right|^2 \\ &= \left| \frac{2 \sin(\frac{1}{2} \frac{E_2-E_1}{\hbar} t)}{(E_2-E_1)} \langle 2|W|1\rangle \right|^2,\end{aligned}\quad (2.85)$$

where  $e^{ia} - e^{ib} = 2 \sin \frac{1}{2}(a-b)$  was used and the transition frequency is  $\omega_{12} = \frac{E_2-E_1}{\hbar}$ . Usually, several states  $|k\rangle$  are lying energetically around  $|2\rangle$  and are accessible through  $W$  due to its spectral width. To calculate the total transition probability, one has to sum over these states. The sum is approximated by an integral over the energies  $E_k$  times the density of states  $\rho$  (number of states per unit energy). Thus, the transition probability is

$$\sum_k P_{1k}(t) \approx |\langle k|W|1\rangle|^2 \int dE_k \rho(E_k) \left| \frac{2 \sin(\frac{1}{2} \frac{E_k-E_1}{\hbar} t)}{(E_k-E_1)} \right|^2. \quad (2.86)$$

In the limit of long times, the density of states factor goes against the one at  $E_1$  ( $\rho(E_k) \rightarrow \rho(E_1)$ ) and can be taken outside the integral. The latter can be evaluated as

$$\int dE_k \left| \frac{2 \sin(\frac{1}{2} \frac{E_k-E_1}{\hbar} t)}{(E_k-E_1)} \right|^2 = \frac{2\pi}{\hbar} t. \quad (2.87)$$

This leads to the transition rate  $\Gamma = \frac{d}{dt} \sum_k P_{1k}(t)$ , which is now approximately

$$\Gamma = \frac{2\pi}{\hbar} |\langle k | W | 1 \rangle|^2 \rho(E_1). \quad (2.88)$$

This equation is known as *Fermi's golden rule*.

### 2.4.3 Rotating wave approximation

In the model of a two-level system, the eigenstates  $|n\rangle$  with  $n = 1, 2$  obey

$$\hat{H}_0 |n\rangle = E_n |n\rangle. \quad (2.89)$$

Their time evolution

$$|n(t)\rangle = e^{-\frac{i}{\hbar} E_n t} |n\rangle. \quad (2.90)$$

can be obtained from the time-dependent Schrödinger equation. The wave function of the complete system is then a superposition of these states:

$$|\Psi(t)\rangle = c_1(t) e^{-\frac{i}{\hbar} E_1 t} |1\rangle + c_2(t) e^{-\frac{i}{\hbar} E_2 t} |2\rangle. \quad (2.91)$$

The time dependency of the coefficients  $c_n$  stems from an external interaction  $\hat{W}(t)$  (e.g. a laser field), which causes transitions between state  $|1\rangle$  and  $|2\rangle$ . The time-dependent Schrödinger equation for the total system now reads

$$\begin{aligned} i\hbar \frac{d}{dt} \left( c_1(t) e^{-\frac{i}{\hbar} E_1 t} |1\rangle + c_2(t) e^{-\frac{i}{\hbar} E_2 t} |2\rangle \right) \\ = \left[ \hat{H}_0 + \hat{W}(t) \right] \left( c_1(t) e^{-\frac{i}{\hbar} E_1 t} |1\rangle + c_2(t) e^{-\frac{i}{\hbar} E_2 t} |2\rangle \right), \end{aligned} \quad (2.92)$$

which simplifies with Eq. (2.89) to

$$\begin{aligned} i\hbar \left( e^{-\frac{i}{\hbar} E_1 t} |1\rangle \frac{d c_1(t)}{dt} + e^{-\frac{i}{\hbar} E_2 t} |2\rangle \frac{d c_2(t)}{dt} \right) \\ = \hat{W}(t) \left( c_1(t) e^{-\frac{i}{\hbar} E_1 t} |1\rangle + c_2(t) e^{-\frac{i}{\hbar} E_2 t} |2\rangle \right). \end{aligned} \quad (2.93)$$

Projection onto  $\langle 1(t) |$  reduces the Schrödinger equation to

$$i\hbar \frac{d c_1(t)}{dt} = c_1(t) \langle 1 | \hat{W}(t) | 1 \rangle + c_2(t) e^{-\frac{i}{\hbar} (E_2 - E_1) t} \langle 1 | \hat{W}(t) | 2 \rangle, \quad (2.94)$$

while projection onto  $\langle 2(t) |$  results in

$$i\hbar \frac{d c_2(t)}{dt} = c_1(t) e^{\frac{i}{\hbar} (E_2 - E_1) t} \langle 1 | \hat{W}(t) | 2 \rangle + c_2(t) \langle 2 | \hat{W}(t) | 2 \rangle. \quad (2.95)$$



Assuming an interaction of the form  $\hat{W}(t) = -\mu_{12}E_0 \cos(\omega t)$ , the elements  $\langle n|\hat{W}(t)|n\rangle$  vanish. This is due to the odd parity of the interaction, i.e. the integrands are odd functions of position.

Despite the simplicity of the resulting equations, they are difficult to solve in general [42]. An approximate solution is obtained by adopting the initial occupation of the states for  $c_n(t)$ . More explicitly,  $c_1(t) = c_1(0) = 1$  and  $c_2(t) = c_2(0) = 0$  and time integration yields (compare first-order perturbation theory)

$$c_1(t) = 1 \quad (2.96)$$

$$c_2(t) = -\frac{i}{\hbar} \int_0^t dt' e^{i\omega_{12}t'} \langle 1| -\mu_{12}E_0 \cos(\omega t')|2\rangle \quad (2.97)$$

with the transition frequency  $\omega_{12} = \frac{E_2 - E_1}{\hbar}$ . This expression for  $c_2(t)$  can now be inserted in Eq. (2.94) and an improved solution for  $c_1(t)$  is then obtained by time integration. This iterative procedure can be repeated until the result is precise enough.

Usually, Eq. (2.97) meets this requirement and can be rewritten as

$$\begin{aligned} c_2(t) &= -\frac{i}{\hbar} \int_0^t dt' e^{i\omega_{12}t'} \frac{E_0}{2} \left( e^{-i\omega t'} + e^{i\omega t'} \right) \langle 2| -\mu_{12}|1\rangle \\ &= -\frac{i}{\hbar} \int_0^t dt' \frac{E_0}{2} \left( e^{i(\omega_{12}-\omega)t'} + e^{i(\omega_{12}+\omega)t'} \right) \langle 2| -\mu_{12}|1\rangle. \end{aligned} \quad (2.98)$$

For  $\omega_{12} > 0$  (absorption), the second exponential term is usually much smaller than the first one and therefore it is neglected. The reverse holds for  $\omega_{12} < 0$  (stimulated emission), i.e. the first exponential term is dropped. The neglect is called *rotating wave approximation (RWA)*.

#### 2.4.4 Rabi oscillations

The interaction of light with a two-level system (e.g. an atom or ion with a ground state and an excited state) can lead to a periodic exchange of energy between the electro-magnetic field and the two-level system. This exchange can be interpreted as alternating absorption and stimulated emission of photons. Such oscillations are called Rabi oscillations (in reference to the Nobel laureate Isidor Isaac Rabi). They are associated with oscillations of the level populations and quantum-mechanical

probability amplitudes.

A mathematical description is obtained, if eqns. (2.94) and (2.95) are written down for an interaction of the form  $\hat{W}(t) = -\mu_{12}E_0 \cos(\omega t)$

$$i\hbar \frac{d c_1(t)}{dt} = c_2(t) \frac{E_0}{2} (e^{-i(\omega_{12}-\omega)t} + e^{-i(\omega_{12}+\omega)t}) \langle 1 | -\mu_{12} | 2 \rangle \quad (2.99)$$

$$i\hbar \frac{d c_2(t)}{dt} = c_1(t) \frac{E_0}{2} (e^{i(\omega_{12}-\omega)t} + e^{i(\omega_{12}+\omega)t}) \langle 2 | -\mu_{12} | 1 \rangle, \quad (2.100)$$

where  $\langle 2 | -\mu_{12} | 1 \rangle = \langle 1 | -\mu_{12} | 2 \rangle$  are taken to be real [43]. Within the *RWA*, this results in

$$\frac{d c_1(t)}{dt} = -\frac{i}{\hbar} \frac{E_0}{2} e^{-i(\omega_{12}-\omega)t} \langle 2 | -\mu_{12} | 1 \rangle c_2(t) \quad (2.101)$$

$$\frac{d c_2(t)}{dt} = -\frac{i}{\hbar} \frac{E_0}{2} e^{i(\omega_{12}-\omega)t} \langle 2 | -\mu_{12} | 1 \rangle c_1(t). \quad (2.102)$$

In this set of coupled equations,  $c_1(t)$  can be eliminated. Therefore, the time derivative of Eq. (2.102) is built

$$\begin{aligned} \frac{d}{dt} c_1(t) &= \frac{d}{dt} i\hbar \frac{2}{E_0 \langle 2 | -\mu_{12} | 1 \rangle} e^{-i(\omega_{12}-\omega)t} \frac{d c_2(t)}{dt} \\ &= i\hbar \frac{2}{E_0 \langle 2 | -\mu_{12} | 1 \rangle} e^{-i(\omega_{12}-\omega)t} \left( -i(\omega_{12} - \omega) \frac{d c_2(t)}{dt} + \frac{d^2 c_2(t)}{dt^2} \right) \end{aligned} \quad (2.103)$$

and employed in Eq. (2.101), which then gives

$$\frac{d^2 c_2(t)}{dt^2} - i(\omega_{12} - \omega) \frac{d c_2(t)}{dt} + \frac{E_0^2}{4\hbar^2} \langle 2 | -\mu_{12} | 1 \rangle^2 c_2(t) = 0. \quad (2.104)$$

A trial solution to this differential equation is

$$c_2(t) = e^{i\lambda t}, \quad (2.105)$$

which leads to

$$\lambda_{1,2} = -\frac{1}{2} \left( \Delta\omega \pm \sqrt{\Delta\omega^2 + \frac{E_0^2}{\hbar^2} \langle 2 | -\mu_{12} | 1 \rangle^2} \right), \quad (2.106)$$

where  $\Delta\omega = \omega_{12} - \omega$  is the detuning of the transition frequency and the field frequency. Furthermore, the Rabi frequency  $\Omega_R$  is defined as [34]

$$\Omega_R = \frac{E_0}{\hbar} \langle 2 | -\mu_{12} | 1 \rangle \quad (2.107)$$

and

$$\Omega = \sqrt{\Delta\omega^2 + \Omega_R^2}. \quad (2.108)$$

Hence, the general solution is

$$c_2(t) = A_1 e^{i\lambda_1 t} + A_2 e^{i\lambda_2 t}, \quad (2.109)$$

where  $A_{1,2}$  can be determined from the initial conditions

$$A_{1,2} = \pm \frac{1}{2} \frac{\Omega_R}{\Omega}. \quad (2.110)$$

The coefficients then are

$$c_2(t) = i \frac{\Omega_R}{\Omega} e^{-\frac{i}{2}\Delta\omega t} \sin\left(\frac{\Omega}{2}t\right) \quad (2.111)$$

and analogous

$$c_1(t) = e^{-\frac{i}{2}\Delta\omega t} \left[ \cos\left(\frac{\Omega}{2}t\right) + i \frac{\Delta\omega}{\Omega} \sin\left(\frac{\Omega}{2}t\right) \right]. \quad (2.112)$$

The probability to find the system in state  $|2\rangle$  is now

$$\begin{aligned} P_2(t) &= |c_2(t)|^2 \\ &= \frac{\Omega_R^2}{\Omega^2} \sin^2\left(\frac{\Omega}{2}t\right), \end{aligned} \quad (2.113)$$

which in the case of resonance ( $\Delta\omega = 0$ ) simplifies to

$$P_2(t) = \sin^2\left(\frac{\Omega_R}{2}t\right). \quad (2.114)$$

The population oscillates between the two states of the system. This process is called Rabi oscillation. At time  $t = \pi \frac{1}{\Omega_R}$ , all population has been transferred to state  $|2\rangle$ . Thus, a pulse which achieves population inversion is referred to as  $\pi$ -pulse.

## 2.5 Adiabatic vs. diabatic potentials and Born-Oppenheimer approximation

The total Hamiltonian of a molecule consists of parts, which depend on electron coordinates  $r$  and nuclear coordinates  $R$ . It reads

$$\hat{H}(R, r) = \hat{T}(R) + \hat{T}(r) + \hat{V}(R, r), \quad (2.115)$$

where  $\hat{T}(R)$  is the kinetic energy operator of the nuclei,  $\hat{T}(r)$  is the kinetic energy operator of the electrons and  $\hat{V}(R, r)$  is the (coulombic) potential. Consequently, the system's wave function also depends on  $R$  and  $r$ . The corresponding Schrödinger equation is

$$\hat{H}(R, r)\Psi(R, r) = E\Psi(R, r). \quad (2.116)$$

Usually, one tries to separate nuclear dynamics from the electron motion, which yields the electronic Schrödinger equation at fixed nuclear coordinates:

$$\underbrace{\left[\hat{T}(r) + \hat{V}(r, R)\right]}_{\hat{H}_{el}} \phi_n(r, R) = V_n(R)\phi_n(r, R). \quad (2.117)$$

Here,  $\phi_n(r, R)$  are the electronic eigenfunctions, which form a complete orthonormal system. Hence, the total wave function can be expanded in this basis:

$$\Psi(R, r) = \sum_n \chi_n(R)\phi_n(r, R). \quad (2.118)$$

### 2.5.1 Adiabatic expansion

The normal case is to solve the electronic Schrödinger equation at different fixed nuclear coordinates, yielding the so-called adiabatic potentials  $V_n(R)$  of electronic state  $n$ . The latter are coupled kinetically. To get the type of the coupling elements, the basis-set expansion is inserted into the complete Schrödinger equation, which is then projected onto an electronic eigenfunction  $\phi_m(r, R)$ :

$$\left\langle \phi_m(r, R) \left| \hat{H}(R, r) \right| \sum_n \chi_n(R)\phi_n(r, R) \right\rangle_r = E \left\langle \phi_m(r, R) \left| \sum_n \chi_n(R)\phi_n(r, R) \right\rangle_r, \quad (2.119)$$

where the index  $r$  denotes integration over electron coordinates only. The kinetic energy operator of the nuclei is of the form  $\hat{T}(R) = -\frac{\hbar^2}{2M} \frac{\partial}{\partial R}$  with the masses of the nuclei  $M$ . Hence, the above equation can be evaluated as

$$\begin{aligned} \sum_n \left\langle \phi_m(r, R) \left| \hat{T}(R) \right| \chi_n(R)\phi_n(r, R) \right\rangle_r + \underbrace{\sum_n \left\langle \phi_m(r, R) \left| \hat{H}_{el} \right| \chi_n(R)\phi_n(r, R) \right\rangle_r}_{V_m(R) \chi_m(R)} \\ = E \underbrace{\left\langle \phi_m(r, R) \left| \sum_n \chi_n(R)\phi_n(r, R) \right\rangle_r}_{E \chi_m(R)} \end{aligned} \quad (2.120)$$

$$\Rightarrow \sum_n -\frac{\hbar^2}{2M} \left[ 2 \left\langle \phi_m(r, R) \left| \frac{\partial \phi_n(r, R)}{\partial R} \right\rangle_r \frac{\partial \chi_n(R)}{\partial R} + \left\langle \phi_m(r, R) \left| \frac{\partial^2 \phi_n(r, R)}{\partial R^2} \right\rangle_r \chi_n(R) \right] + \left[ \hat{T}(R) + V_m(R) \right] \chi_m(R) = E \chi_m(R), \quad (2.121)$$

where often the following abbreviations are used

$$T_{mn}^{(1)}(R) := -\frac{\hbar^2}{M} \left\langle \phi_m(r, R) \left| \frac{\partial \phi_n(r, R)}{\partial R} \right\rangle_r \frac{\partial}{\partial R} \quad (2.122)$$

$$T_{mn}^{(2)}(R) := -\frac{\hbar^2}{2M} \left\langle \phi_m(r, R) \left| \frac{\partial^2 \phi_n(r, R)}{\partial R^2} \right\rangle_r \quad (2.123)$$

As stated above, the  $V_m(R)$  are the adiabatic potentials. The kinetic couplings  $T_{mn}(R)$  are neglected within the *Born-Oppenheimer approximation* ( $T_{mn}^{(1)}(R) = T_{mn}^{(2)}(R) = 0$ ) and the resulting nuclear Schrödinger equation for a fixed electronic state  $m$  reads:

$$\left[ \hat{T}(R) + V_m(R) \right] \chi_m(R) = E \chi_m(R). \quad (2.124)$$

## 2.5.2 Diabatic expansion

Another description of the system stems from an expansion, where only one fixed nuclear geometry  $R_0$  is adopted for the electronic wave functions.

$$\Psi(R, r) = \sum_n \chi_n(R) \phi_n(r, R_0). \quad (2.125)$$

The corresponding electronic Schrödinger equation reads

$$\hat{H}_{el}(r, R_0) \phi_n(r, R_0) = V_n(R_0) \phi_n(r, R_0). \quad (2.126)$$

Now, the basis functions  $\phi_n$  not even parametrically depend on the nuclear coordinate and the convergence for this expansion is questionable. Nevertheless, the total system can be described within this picture and projection onto  $\phi_m(r, R_0)$  of the complete Schrödinger equation yields

$$\underbrace{\left\langle \phi_m(r, R_0) \left| \hat{T}(R) \right| \sum_n \chi_n(R) \phi_n(r, R_0) \right\rangle_r}_{\hat{T}(R) \chi_m(R)} + \left\langle \phi_m(r, R_0) \left| \underbrace{\hat{T}(r) + \hat{V}(r, R_0)}_{\hat{H}_{el}(r, R_0)} - \hat{V}(r, R_0) + \hat{V}(r, R) \right| \sum_n \chi_n(R) \phi_n(r, R_0) \right\rangle_r = E \left\langle \phi_m(r, R_0) \left| \sum_n \chi_n(R) \phi_n(r, R_0) \right\rangle_r. \quad (2.127)$$

With the definition

$$U_{mn}(R) := \left\langle \phi_m(r, R_0) \left| \hat{V}(r, R) - \hat{V}(r, R_0) \right| \phi_n(r, R_0) \right\rangle_r, \quad (2.128)$$

the above equation is simplified to

$$\sum_n U_{mn}(R) \chi_n(R) + \left[ \hat{T}(R) + V_m(R_0) \right] \chi_m(R) = E \chi_m(R). \quad (2.129)$$

Here, it can be readily seen, that the electronic states are connected by a potential coupling.

### 2.5.3 Example

The above is now illustrated with an example. In Fig. 2.4 the groundstate and first-excited-state potentials of sodium iodide (NaI) are shown in both the adiabatic and the diabatic picture. In the adiabatic picture, the point, where the curves come close to each other, is referred to as avoided crossing. Because the two states are coupled, which is not included in the adiabatic potentials, one also speaks of a non-adiabatic coupling. This interaction is only possible for states of the same symmetry.

The Hamiltonian can be written in matrix representation, which is two-dimensional for this model system. The adiabatic form (index  $a$ ) shows kinetic coupling and

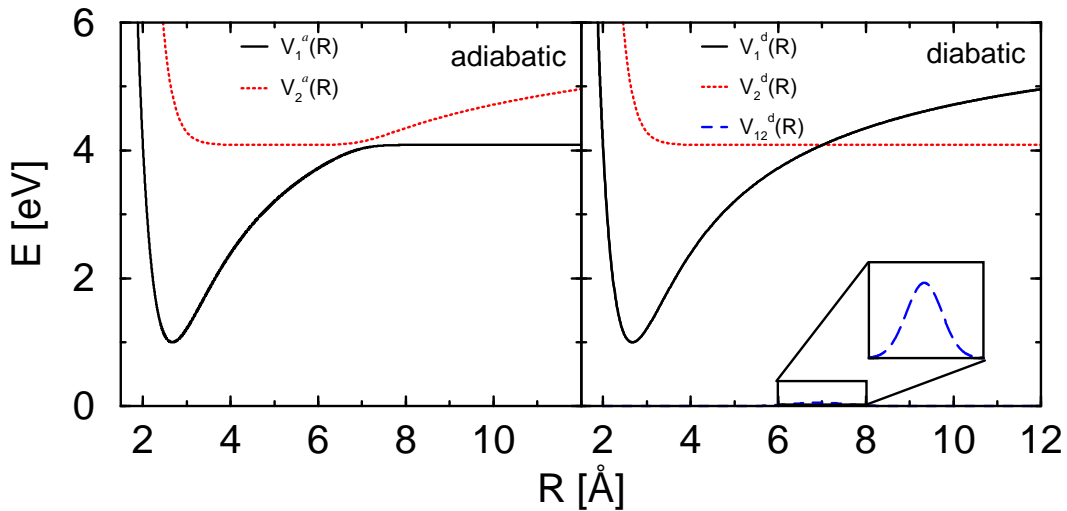


Figure 2.4: Adiabatic (left panel) and diabatic (right panel) potentials of sodium iodide.

thus, off-diagonal elements in the kinetic operator matrix

$$\begin{aligned}\hat{H} &= \begin{pmatrix} T(R) + T_{11}^{(1)} + T_{11}^{(2)} & T_{12}^{(1)} + T_{12}^{(2)} \\ T_{21}^{(1)} + T_{21}^{(2)} & T(R) + T_{22}^{(1)} + T_{22}^{(2)} \end{pmatrix} + \begin{pmatrix} V_1(R) & 0 \\ 0 & V_2(R) \end{pmatrix} \\ &= \begin{pmatrix} T_1^a(R) & T_{12}^a(R) \\ T_{12}^a(R) & T_2^a(R) \end{pmatrix} + \begin{pmatrix} V_1^a(R) & 0 \\ 0 & V_2^a(R) \end{pmatrix}.\end{aligned}\quad (2.130)$$

In contrast, the diabatic form (index  $d$ ) exposes potential couplings

$$\begin{aligned}\hat{H} &= \begin{pmatrix} T(R) & 0 \\ 0 & T(R) \end{pmatrix} + \begin{pmatrix} V_1(R_0) + U_{11}(R) & U_{12}(R) \\ U_{21}(R) & V_2(R) + U_{22}(R) \end{pmatrix} \\ &= \begin{pmatrix} T_1^d(R) & 0 \\ 0 & T_2^d(R) \end{pmatrix} + \begin{pmatrix} V_1^d(R) & V_{12}^d(R) \\ V_{21}^d(R) & V_2^d(R) \end{pmatrix},\end{aligned}\quad (2.131)$$

where  $U_{12}(R) = U_{21}(R)$  and  $V_{12}^d(R) = V_{21}^d(R)$ , respectively. Changing from the adiabatic to the diabatic picture is called ‘‘diabatisation’’. Several procedures have been proposed (see Ref. [44] and references therein). An example for a  $2 \times 2$ -matrix is given in the appendix A.1.

## 2.6 Landau-Zener theory

In 1932, both L. D. Landau and C. Zener published their work on curve crossings [45–47]. They described the probability of a transition from one adiabatic state to another via a non-adiabatic crossing. Within this so-called Landau-Zener theory, the probability  $P^{LZ}$  that such a transition occurs is [48]

$$P^{LZ} = e^{-\pi^2 \frac{\Delta E_c^2}{v\hbar\Delta F_c}}, \quad (2.132)$$

where  $\Delta E_c$  is the potential energy difference at the crossing point  $R_c$ . The expression furthermore contains the relative velocity  $v$  of the system along the nuclear coordinate  $R$  when passing the crossing point, and the force term:

$$\Delta F_c = \left| \frac{d\Delta E_c}{dR} \right|_{R_c}. \quad (2.133)$$

From the LZ-expression, Eq. (2.132), the following conclusions can be taken. On the one hand, with increasing velocity  $v$ , the probability for a non-adiabatic transition gets higher. On the other hand, with a smaller energy gap between the potentials, the same effect is associated.





# 3 Numerical Methods

## 3.1 Runge-Kutta algorithm for classical trajectories

A particle's position  $q(t)$  at a certain time  $t$  can be calculated numerically, employing the classical equations of motion subject to given starting conditions at time  $t_0$ . Therefore, the time interval  $[t_0, t]$  is divided into  $N$  small time steps  $dt$  and

$$t = t_0 + N dt. \quad (3.1)$$

Runge-Kutta methods, in general, employ a Taylor expansion as

$$q(t + dt) = q(t) + \dot{q}(t)dt + \frac{1}{2}\ddot{q}(t)dt^2 + \dots = \sum_{n=0}^{\infty} \frac{1}{n!} \frac{\partial^n q}{\partial t^n}(t) dt^n. \quad (3.2)$$

Keeping only the linear term in the expansion leads to the Euler method, as already stated in section 2.1:

$$q(t + dt) = q(t) + \dot{q}(t)dt \quad (3.3)$$

$$\dot{q}(t + dt) = \dot{q}(t) + \ddot{q}(t)dt = \dot{q}(t) + \frac{F}{m}dt = \dot{q}(t) - \frac{\partial V}{\partial q} dt. \quad (3.4)$$

If intermediate points at  $t + \frac{1}{2}dt$  are employed, the accuracy can be improved by one order. This method is called second-order Runge-Kutta algorithm or leap-frog scheme [49] and the positions of the particle can be calculated iteratively

$$q(t + \frac{1}{2}dt) = q(t) + \frac{1}{2}\dot{q}(t)dt \quad (3.5)$$

$$\dot{q}(t + \frac{1}{2}dt) = \dot{q}(t) + \frac{1}{2} \frac{-\frac{\partial V(q(t))}{\partial q}}{m} dt \quad (3.6)$$

$$q(t + dt) = q(t) + \dot{q}(t + \frac{1}{2}dt)dt \quad (3.7)$$

$$\dot{q}(t + dt) = \dot{q}(t) + \frac{-\frac{\partial V(q(t+\frac{1}{2}dt))}{\partial q}}{m} dt, \quad (3.8)$$

where the classical equations of motion are employed for a particle of mass  $m$ , moving in an external potential  $V$ .

## 3.2 Short-time propagator

The time evolution operator  $\hat{U}(t, t_0)$  maps the state vector at time  $t_0$  to a new vector at time  $t$ . It is analytically exact to split the operator into a product of propagators for small time intervals

$$\hat{U}(t, t_0) = \Pi_n \hat{U}(t_n + dt, t_n). \quad (3.9)$$

In section 2.2, it was shown that

$$\hat{U}(t, t_0) = \mathcal{T} e^{-\frac{i}{\hbar} \int_{t_0}^t \hat{H}(t') dt'}. \quad (3.10)$$

Within one time interval, the integral expression can be approximated by

$$\hat{U}(t_n + dt, t_n) = e^{-\frac{i}{\hbar} \int_{t_n}^{t_n+dt} \hat{H}(t') dt'} \approx e^{-\frac{i}{\hbar} \hat{H}(t) dt}, \quad (3.11)$$

if the time step  $dt$  is small enough. To reach the desired time  $t$ , the short-time propagator  $e^{-\frac{i}{\hbar} \hat{H}(t) dt}$  has to be applied iteratively. This implies an inherent time ordering and the corresponding operator  $\mathcal{T}$  is not necessary.

Although numerical methods exist, which do not rely on short-time propagator schemes (see the reviews by Leforestier et al. [50] and Kosloff [51, 52]), here, this idea is employed within the so-called split-operator technique as is explained in the next section.

## 3.3 Split-operator technique

The short-time propagator  $e^{-\frac{i}{\hbar} \hat{H} dt}$  depends on the system's Hamiltonian, which consists of the kinetic energy operator  $\hat{T}$  and the potential energy operator  $\hat{V}$ . Because  $\hat{T}$  contains derivatives with respect to the spatial coordinates, and  $\hat{V}$  directly depends on the coordinates, a separate treatment of the kinetic part and the potential part of the propagator is advantageous. As  $\hat{T}$  and  $\hat{V}$  do not commute, a splitting contains an second-order error

$$e^{-\frac{i}{\hbar} (\hat{T} + \hat{V}) dt} = e^{-\frac{i}{\hbar} \hat{T} dt} e^{-\frac{i}{\hbar} \hat{V} dt} + \mathcal{O}(dt^2). \quad (3.12)$$

This can easily be verified by a comparison of Taylor expansions of the left-hand side

$$e^{-\frac{i}{\hbar}\hat{H}dt} = \sum_{n=0}^{\infty} \frac{\left(-\frac{i}{\hbar}dt\right)^n}{n!} \hat{H}^n \quad (3.13)$$

and the right-hand side.

In the split-operator technique [53, 54] used in this work, the accuracy is improved by a symmetric splitting of the form

$$e^{-\frac{i}{\hbar}(\hat{T}+\hat{V})dt} = e^{-\frac{1}{2}\frac{i}{\hbar}\hat{T}dt} e^{-\frac{i}{\hbar}\hat{V}dt} e^{-\frac{1}{2}\frac{i}{\hbar}\hat{T}dt} + \mathcal{O}(dt^3), \quad (3.14)$$

which contains only a third-order error [55]. The latter can be neglected for a short time step  $dt$ .

The derivatives of the kinetic energy operator are evaluated in momentum space, employing the Fourier decomposition of the wave function

$$\Psi(P) = \frac{1}{\sqrt{2\pi}} \int_{-\infty}^{\infty} dR \Psi(R) e^{-i P R}, \quad (3.15)$$

so that

$$\begin{aligned} e^{-\frac{i}{\hbar}\hat{T}dt} \Psi(P) &= e^{-\frac{i}{\hbar}\frac{\hat{p}^2}{2m}dt} \frac{1}{\sqrt{2\pi}} \int_{-\infty}^{\infty} dR \Psi(R) e^{-i P R} \\ &= \frac{1}{\sqrt{2\pi}} \int_{-\infty}^{\infty} dR \Psi(R) e^{-\frac{i}{\hbar}\frac{\hat{p}^2}{2m}dt} e^{-i P R} \\ &= \frac{1}{\sqrt{2\pi}} \int_{-\infty}^{\infty} dR \Psi(R) e^{-\frac{i}{\hbar}\frac{P^2}{2m}dt} e^{-i P R} \\ &= e^{-\frac{i}{\hbar}\frac{P^2}{2m}dt} \Psi(P). \end{aligned} \quad (3.16)$$

In the penultimate step, it was used that  $e^{-i P R}$  is an eigenfunction to the momentum operator  $\hat{p}$  and thus,

$$\hat{p}e^{-i P R} = P e^{-i P R}. \quad (3.17)$$

The result for  $e^{\lambda\hat{p}^2}e^{-i P R}$  can then be derived from a Taylor expansion

$$\begin{aligned} e^{\lambda\hat{p}^2}e^{-i P R} &= 1e^{-i P R} + \lambda\hat{p}^2e^{-i P R} + \frac{1}{2}(\lambda\hat{p}^2)^2e^{-i P R} + \dots \\ &= 1e^{-i P R} + \lambda P^2e^{-i P R} + \frac{1}{2}(\lambda P^2)^2e^{-i P R} + \dots \\ &= e^{\lambda P^2}e^{-i P R} \end{aligned} \quad (3.18)$$

The change of the wavefunction representation from coordinate to momentum space and vice versa is performed numerically with fast Fourier transform (FFT) algorithms. The wave function is described here on a discretized grid. A FFT then needs  $K \log(K)$  operations for the transform, where  $K$  is the number of points on the grid, in contrast to a scaling of  $K^2$  for a naive implementation of the transform. Here, the freely available FFTW package [56] was used.

### 3.4 Relaxation method

An advantage of the split-operator technique is, that with slight modifications the propagation algorithm can be used to calculate eigenstates. The procedure is then called relaxation method [57]. Here, the time step  $dt$  is replaced by  $-i dt$ , i.e. it is propagated with imaginary time. The starting point is an almost arbitrary function  $\psi$  (it may not be orthogonal to the eigenfunctions). Because the yet unknown eigenstates  $\phi_n$  with eigenenergies  $E_n$  form an orthonormal basis,  $\psi$  can be expanded as

$$\psi = \sum_{n=0}^{\infty} c_n \phi_n, \quad (3.19)$$

where

$$c_n = \langle \phi_n | \psi \rangle. \quad (3.20)$$

Application of the propagator now yields

$$\psi(t + dt) = \sum_n e^{-\frac{i}{\hbar} E_n dt} \langle \phi_n | \psi \rangle \phi_n. \quad (3.21)$$

In other words, each eigenstate  $\phi_n$  is damped via  $e^{-\frac{i}{\hbar} E_n dt}$  at a rate corresponding to its own eigenenergy  $E_n$  (For negative  $E_n$  it is not damped but enhanced). Therefore, the wave function has to be re-normalized after every propagation step in order not to become zero (or infinity, if negative eigenenergies are included). Then, in the limit of infinite times, the amplitude  $c_0$  of the eigenstate with lowest eigenenergy  $E_0$  approaches the value of 1 and hence, the ground state has been obtained. This is illustrated in Fig. 3.1 for the vibrational ground state of a Morse oscillator.

Since infinite times are not accessible in reality, the imaginary propagation has

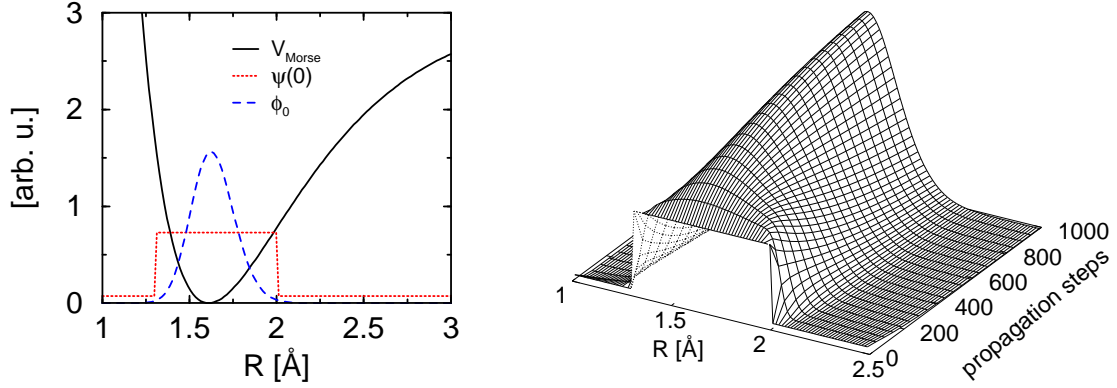


Figure 3.1: On the left-hand side, a Morse potential  $V_{Morse}$ , the initial arbitrary wave function  $\psi(0)$  (chosen as a rectangular function) and the converged ground state  $\phi_0$  are shown. On the right-hand side, the damping process from the rectangular function towards the ground state is depicted.

to be stopped, when the wave function is accurate enough. As convergence criterion, the change of the energy expectation value in time is adopted. It can be easily obtained from

$$\langle \psi(t+dt) | \psi(t+dt) \rangle = \langle e^{-\frac{1}{\hbar} \hat{H} dt} \psi(t) | e^{-\frac{1}{\hbar} \hat{H} dt} \psi(t) \rangle \quad (3.22)$$

$$\Rightarrow \langle \psi(t+dt) | \psi(t+dt) \rangle = \lim_{t \rightarrow \infty} \langle e^{-\frac{1}{\hbar} E dt} \psi(t) | e^{-\frac{1}{\hbar} E dt} \psi(t) \rangle \quad (3.23)$$

$$\Rightarrow e^{-\frac{2}{\hbar} E dt} = \frac{\langle \psi(t+dt) | \psi(t+dt) \rangle}{\langle \psi(t) | \psi(t) \rangle} \quad (3.24)$$

$$\Rightarrow E = -\frac{\hbar}{2dt} \ln \frac{\langle \psi(t+dt) | \psi(t+dt) \rangle}{\langle \psi(t) | \psi(t) \rangle}, \quad (3.25)$$

The difference of the energy  $E$  and the stored  $E$  of the time step before is compared to a threshold. If the difference is smaller than the threshold, the calculation is converged according to the criterion.

Afterwards, higher eigenstates can be evaluated by projecting out the  $m$  already found eigenstates in every time step

$$\psi' = \psi - \sum_{n=0}^m \langle \phi_n | \psi \rangle \phi_n. \quad (3.26)$$

Sometimes, it is reported, that the relaxation method only works for a positive spectrum of eigenenergies. It is stressed here, that this statement is wrong.

### 3.5 The rotational degree of freedom

The above can be directly implemented for fixed orientation of a molecule in the laboratory frame. If the rotational degree of freedom is taken into account, usually Euler angles are employed to describe the interaction of a field with a molecule.

In the case of a linear molecule (symmetric top) interacting with a linearly polarized field, the interaction term depends only on one angle, the polar Euler angle  $\theta$  between the field polarization vector and the dipole moment vector [58]. Here, the field is taken to be polarized along the z-axis of the laboratory frame. To define the direction of the dipole moment completely respective to the field, additionally the angle  $\varphi$ , which specifies a rotation in the xy-plane, would be necessary. But due to the cylindrical symmetry of the field, the angle  $\varphi$  can be neglected. Only when calculating spatial integrals (e.g. expectation values), the factor of  $2\pi$  remains according to

$$\int_0^{2\pi} d\varphi = 2\pi. \quad (3.27)$$

To keep track of the population of rotational levels, the wavefunction is expanded into spherical harmonics  $Y_{j,m_j}$ . Due to the polarization of the field along the z-axis, the selection rule  $\Delta m_j = 0$  is obtained [59]. Thus, all  $m_j$  can be treated separately and for simplicity,  $m_j$  is set to zero. Under these conditions, the spherical harmonics only depend on  $j$  and  $\theta$ . The basis set expansion of the wavefunction then reads

$$\Psi(R, \theta, t) = \sum_j \chi_j(R, t) Y_{j,0}(\theta, 0). \quad (3.28)$$

Here,  $\Psi(R, \theta, t)$  is the reduced wavefunction. The total wavefunction  $\Phi(R, \theta, t)$  is obtained via the relation

$$\Psi(R, \theta, t) = R \cdot \Phi(R, \theta, t) \quad (3.29)$$

This representation simplifies the application of the Hamiltonian in spherical coordinates. The Hamiltonian is then of the form

$$\hat{H} = \hat{T}(R) + \hat{T}(J) + \hat{V}(R) + \hat{W}(t), \quad (3.30)$$

where the interaction with the external field is

$$\hat{W}(t) = -\mu(R)E(t) \cos \theta \quad (3.31)$$

and the angular kinetic energy operator is defined as

$$\hat{T}(J) = \frac{\hat{J}^2}{2mR^2}. \quad (3.32)$$

Here, the angular momentum operator has the form

$$\hat{J}^2 = -\hbar^2 \left( \frac{\partial^2}{\partial \theta^2} + \cot \theta \frac{\partial}{\partial \theta} + \frac{1}{\sin^2 \theta} \frac{\partial^2}{\partial \varphi^2} \right), \quad (3.33)$$

which reduces to  $\hat{J}^2 = \hbar^2 j(j+1)$  in the case of acting on its eigenfunctions, i.e. spherical harmonics.

Employing the split-operator method (see section 3.3), the propagators for a short time interval  $\Delta t$  are split, in a first step, as

$$U(t) = e^{-i\hat{T}(R)\frac{\Delta t}{2}} e^{-i[\hat{V}(R)+\hat{T}(J)+\hat{W}(t)]\Delta t} e^{-i\hat{T}(R)\frac{\Delta t}{2}}. \quad (3.34)$$

The action of the operators containing  $\hat{T}(R)$  are evaluated in momentum space. Additionally, the following splitting is performed

$$e^{-i[\hat{V}(R)+\hat{T}(J)+\hat{W}(t)]\Delta t} = e^{-i[\hat{V}(R)+\hat{T}(J)]\frac{\Delta t}{2}} e^{-i\hat{W}(t)\Delta t} e^{-i[\hat{V}(R)+\hat{T}(J)]\frac{\Delta t}{2}}. \quad (3.35)$$

In applying the operator containing the sum  $[\hat{V}(R) + \hat{T}(J)]$  to the wave function (Eq. 3.28), the  $j$ -th expansion term is multiplied by  $e^{-i\left[\hat{V}(R) - \frac{\hbar^2 j(j+1)}{2mR^2}\right]\frac{\Delta t}{2}}$ . The matrix representation (with respect to the angular basis functions) of the dipole interaction exponential is of tri-diagonal form and an additional splitting is introduced as

$$e^{-i\mathbf{W}(t)\Delta t} = e^{i\mu(R)E(t)\mathbf{W}_1\frac{\Delta t}{2}} e^{i\mu(R)E(t)\mathbf{W}_2\Delta t} e^{i\mu(R)E(t)\mathbf{W}_1\frac{\Delta t}{2}}. \quad (3.36)$$

The matrices  $\mathbf{W}_n$  are defined as

$$\mathbf{W}_1 = \begin{pmatrix} 0 & c_1^+ & 0 & 0 & 0 & \dots \\ c_2^- & 0 & 0 & 0 & 0 & \dots \\ 0 & 0 & 0 & c_3^+ & 0 & \dots \\ 0 & 0 & c_4^- & 0 & 0 & \dots \\ 0 & 0 & 0 & 0 & 0 & \dots \\ \vdots & \vdots & \vdots & \vdots & \vdots & \ddots \end{pmatrix}, \quad \mathbf{W}_2 = \begin{pmatrix} 0 & 0 & 0 & 0 & 0 & \dots \\ 0 & 0 & c_2^+ & 0 & 0 & \dots \\ 0 & c_3^- & 0 & 0 & 0 & \dots \\ 0 & 0 & 0 & 0 & c_4^+ & \dots \\ 0 & 0 & 0 & c_5^- & 0 & \dots \\ \vdots & \vdots & \vdots & \vdots & \vdots & \ddots \end{pmatrix}. \quad (3.37)$$

Here, the following properties of the spherical harmonics are used:

$$\cos \theta Y_{j,0}(\theta, 0) = c_j^+ Y_{(j+1),0}(\theta, 0) + c_j^- Y_{(j-1),0}(\theta, 0), \quad (3.38)$$

with the coefficients

$$c_j^+ = \frac{(j+1)}{\sqrt{(2j+1)(2j+3)}}, \quad c_j^- = \frac{j}{\sqrt{(2j+1)(2j-1)}}. \quad (3.39)$$

The splitting algorithm of Eqs. (3.36, 3.37) allows for an analytical evaluation of the exponential propagators using the formula [60]

$$\exp \left[ -i\lambda \begin{pmatrix} 0 & c \\ c & 0 \end{pmatrix} \right] = \begin{pmatrix} \cos(\lambda c) & -i \sin(\lambda c) \\ -i \sin(\lambda c) & \cos(\lambda c) \end{pmatrix}, \quad (3.40)$$

where additionally, the property  $c_j^+ = c_{j+1}^-$  is used. Thus, two adjacent expansion terms are mixed within each propagation step by a matrix multiplication.

### 3.6 Simpson integral

If an integral is evaluated numerically, the area under a curve interval is divided into  $n$  subintervals of width  $h$ . The easiest method is to build the Riemann sum, where the exact form of the subdivisions is approximated by rectangles. Here, a large number of subintervals is needed to obtain converged results.

Various techniques exist to improve accuracy with less subdivisions. One of these is the so-called Simpson method, where two subdivisions are considered together. Two subintervals define three points with the respective values  $y_0$ ,  $y_1$  and  $y_2$  on the exact curve. The latter is now approximated by a parabola through the three points. The area under the parabola is evaluated with Stirling's formula and yields the integral value  $S$  for the two subintervals [61]

$$S = h \left( \frac{1}{3}y_0 + \frac{4}{3}y_1 + \frac{1}{3}y_2 \right). \quad (3.41)$$

If this procedure is repeated for the remaining subdivisions, the result is the Simpson rule [62]

$$S = \frac{h}{3} \sum_{i=0}^{\frac{n}{2}-1} (y_{2i} + 4y_{2i+1} + y_{2i+2}) + \mathcal{O}(h^4). \quad (3.42)$$

To build subinterval pairs, an even number of subintervals is necessary. For an odd number, the last subinterval can be added according to

$$S_n = \frac{h}{12} (-y_{n-2} + 8y_{n-1} + 5y_n). \quad (3.43)$$

The Simpson rule was needed especially for the calculation of integrals with spherical harmonics of high quantum number in this work.



## 4 Control theories - A short overview

The control of chemical reactions and molecular dynamics with laser light is in the focus of interest since the 1980s. An existence proof was given, that provides sufficient (but not necessary) conditions for complete control [63]. Various techniques and theories were proposed, but we are still at the very beginning of what is dreamed of or what has not even been thought about, yet. Here, the prevailing control methods are summarized.

### 4.1 Brumer-Shapiro quantum interference

One of the first control theories was proposed by Brumer and Shapiro [4, 64]. They suggested the coupling of degenerate final states by two laser pulses of different

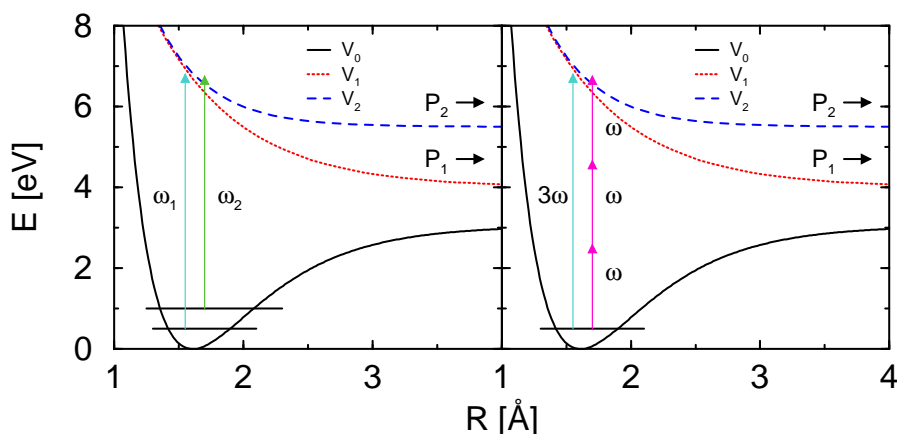


Figure 4.1: In the original Brumer-Shapiro control scheme (left-hand side) a preliminary pulse (not shown) excites two vibrational states. From there, the transfer to  $V_1$  or  $V_2$  is steered by the relative phase of the two control lasers with  $\omega_1$  and  $\omega_2$ . On the right-hand side, the simplified control scheme with one-photon (frequency of  $3\omega$ ) and three-photon absorption (frequency of  $\omega$ ) is shown.

frequency. The resulting phase of the laser field then should interfere constructively with the phase of the wave packet in one of the final states and destructively with the one in the other.

An example is depicted in Fig. 4.1. In the original scheme, a preliminary (infra-red) pulse generates population in both the vibrational groundstate and a vibrationally excited state. From these two levels, the control pulses create population in the two exit channels. By varying the relative phase of the two pulses, an excess of either product  $P_1$  or  $P_2$  is induced.

The scheme was simplified later on, in a way that no preliminary pulse is needed anymore [65]. The interaction of the initial state with a final state stems from one-photon and three-photon processes (see Fig. 4.1).

The Brumer-Shapiro control theory has also been verified experimentally [66, 67].

## 4.2 STIRAP

The “stimulated Raman adiabatic passage” (STIRAP) was proposed and experimentally implemented by Bergmann and coworkers [68, 69]. Here, a complete population transfer from an initial state  $|1\rangle$  to a final state  $|3\rangle$  is achieved by two overlapping nanosecond pulses. The population transfer is achieved via an intermediate state  $|2\rangle$  by a counter-intuitive pulse sequence. The Stokes pulse, which

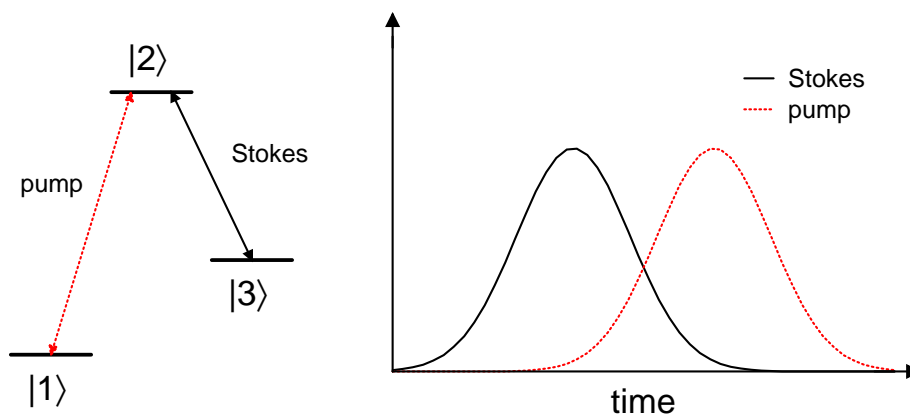


Figure 4.2: With the STIRAP method, complete population transfer from initial state  $|1\rangle$  to final state  $|3\rangle$  is possible. The states are coupled by two overlapping nanosecond pulses (pump pulse and Stokes pulse), which are applied in a counter-intuitive way. The transient population of the intermediate state  $|2\rangle$  remains zero.

exhibits approximately the resonance frequency between  $|2\rangle$  and  $|3\rangle$ , precedes the pump pulse (see Fig. 4.2). As a consequence, the intermediate state  $|2\rangle$  is never populated.

### 4.3 Tannor-Kosloff-Rice pump-dump

Within the Tannor-Kosloff-Rice scheme, different chemical products are generated by controlling the delay between two ultrashort laser pulses [70, 71]. The first (pump) pulse creates a wavepacket in an excited state. The wavepacket can then be dumped after different propagation times back to the groundstate. Depending on the location of the excited-state wavepacket at the pump-dump delay-time, different exit channels are reached.

This pump-dump scheme is illustrated in Fig. 4.3. Here, the dissociation of a

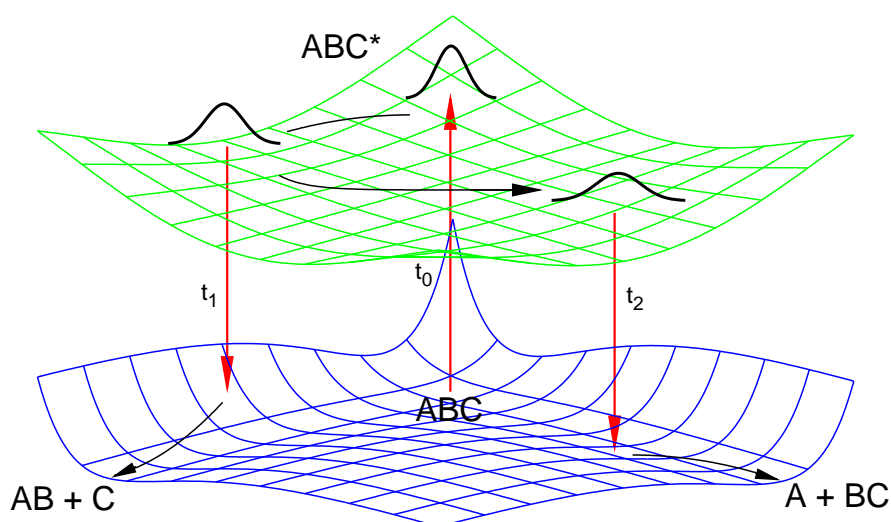


Figure 4.3: The Tannor-Kosloff-Rice scheme is shown for a molecule  $ABC$ . At time  $t_0$  a pump pulse creates a wavepacket in the excited state. A dump pulse at either time  $t_1$  or time  $t_2$  then leads to the population of different exit channels in the groundstate. Thus, a product of either  $AB + C$  or  $A + BC$  can be controlled by the delay time between the pump- and the dump-pulse.

molecule  $ABC$  into either  $AB + C$  at time  $t_1$ , or  $A + BC$  at time  $t_2$ , is triggered. With the availability of femtosecond laser pulses, experiments realizing the Tannor-Kosloff-Rice scheme were carried out [72, 73].

## 4.4 Chirping

Further development of the control techniques mentioned above resulted in not only controlling the delay time or relative phase of laser pulses, but also their momentary frequency. With these chirped pulses, electronic excitations were investigated both theoretically and experimentally, see e.g. Ref. [74, 75]. Another interesting application is the control of vibrational excitations via ladder-climbing processes. Both theoretical [76] and experimental [77] research was carried out with these frequency-swept infrared pulses.

In the schemes mentioned in the paragraphs above, a single parameter has to be adjusted. With the use of chirped pulses, several parameters can be varied independently (see section 2.3.1) and have to be optimized at the same time. Therefore, more complex theories were developed.

## 4.5 Genetic algorithms and feedback control

Genetic algorithms systematically use random numbers to find an optimal set of parameters for a given problem. They were not developed especially for laser control, but for various optimization procedures as soon as computers were available (a well-known example is the travelling salesman problem, where a salesman must visit every city in his territory exactly once and then return to the starting point at minimum total travelling expenses) [78].

The general structure of such a program is as follows:

- start with several sets of random parameters, which define a solution to the given problem
- evaluate the (presumably not optimal) result for each set and store the best set
- initialize a new generation of sets from random numbers, changing single

parameters within a copy of the stored best set of the generation before (mutation), exchanging parameters against each other within another copy (crossover), ...

- evaluate the result for each new set, compare it to the stored result of the momentary best set and eventually store a better one
- repeat the last two points until a predefined target is reached.

These evolution programs are not only employed for theoretical investigations, but they are also the prevailing method for experimental laser control [79–81]. The latter is also termed adaptive quantum control or feedback control and was introduced by Judson and Rabitz [82].

An example is shown in Fig. 4.4. Here, the evaluation of the result takes place with a detector, e.g. a time-of-flight (TOF) mass spectrometer. The detector then passes a signal (feedback) to a computer, which adjusts different pixels of a liquid-crystal display (LCD) according to a genetic algorithm. By applying different voltages, dif-

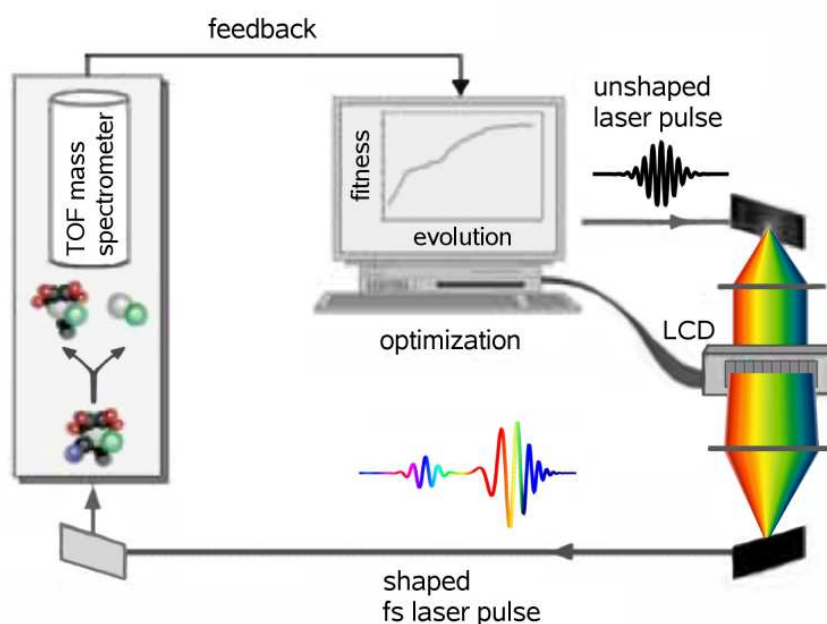


Figure 4.4: An example of an experimental setup for feedback control is shown (compare Ref. [80]). A computer adjusts a pulse shaper (i.e. the LCD). In this way, a tailored pulse is created, which dissociates a molecule. The fragments are measured by a detector, which then passes a feedback to the computer.

ferent refractive indices are achieved in the LCD pixels, and thus, different phases are applied to different colors of the spatially dispersed laser pulse. If the laser beam is recollimated afterwards, a shaped pulse is obtained. The tailored pulse then interacts with a molecular sample and e.g. induces fragmentation. The result is recorded by the detector, which closes the loop. Therefore, closed-loop learning algorithm is also employed as keyword.

## 4.6 Optimal control theory

Optimal control theory (OCT) was developed by Tannor, Kosloff, Rice et al. [70, 83], by Rabitz et al. [84–86] and by Manz et al. [87]. For a review see e.g. Ref. [2]. OCT should not be confused with the term “optimal control” in experimental papers, which is often used as synonym for feedback control.

Optimal control theory relies on a purely mathematical ansatz to find a field, which yields a predefined target state  $|\Phi\rangle$  at a specified final time  $t_f$ . Starting from an initial state  $|\Psi(t_0)\rangle$  of the system at time  $t_0$ , the objective is to maximize the overlap

$$j = |\langle\Phi|\Psi(t_f)\rangle|^2. \quad (4.1)$$

To give a physical meaning, some conditions have to be included in the mathematical optimization process. The two elementary constraints are the obedience of  $|\Psi\rangle$  to the time-dependent Schrödinger equation (assume a time-dependent interaction of  $-\mu E(t)$ )

$$\left(i\hbar\frac{\partial}{\partial t} - \hat{H}(t)\right)|\Psi\rangle = 0 \quad (4.2)$$

and a fixed total energy  $I$  of the laser field  $E(t)$

$$\int_{t_0}^{t_f} dt |E(t)|^2 - I = 0. \quad (4.3)$$

The maximization of  $j$  with the above constraints can be transformed to an unconstrained problem using Lagrange multipliers  $\chi$  and  $\lambda$ . The resulting objective

$$\begin{aligned} J = & |\langle\Phi|\Psi(t_f)\rangle|^2 + \lambda \left[ \int_{t_0}^{t_f} dt |E(t)|^2 - I \right] \\ & + \frac{i}{\hbar} \int_{t_0}^{t_f} dt \left[ \langle\chi | \left(i\hbar\frac{\partial}{\partial t} - \hat{H}(t)\right) |\Psi\rangle - \langle\Psi | \left(i\hbar\frac{\partial}{\partial t} - \hat{H}(t)\right) |\chi\rangle \right] \end{aligned} \quad (4.4)$$

is maximized by the variational approach  $\delta J = 0$  [83].

Firstly, this leads to

$$\left(i\hbar\frac{\partial}{\partial t} - \hat{H}(t)\right) |\chi\rangle = 0 \quad (4.5)$$

with the final condition

$$|\chi(t_f)\rangle = \langle\Phi | \Psi(t_f)\rangle |\Phi\rangle. \quad (4.6)$$

As a consequence,  $|\chi(t)\rangle$  can be obtained by a propagation backwards in time, as soon as  $|\chi(t_f)\rangle$  is evaluated via Eq. (4.6) from the forward propagation of  $|\Psi(t)\rangle$  until time  $t_f$ .

The second equation following from  $\delta J = 0$  is

$$\begin{aligned} E(t) &= \frac{i}{\lambda} [\langle\chi|\mu|\Psi\rangle + \langle\Psi|\mu|\chi\rangle] \\ &= \frac{O(t)}{\lambda}. \end{aligned} \quad (4.7)$$

Once,  $O(t)$  has been found, the yet unknown real Lagrange multiplier  $\lambda$  can be evaluated from Eq. (4.3) as

$$\lambda = \pm \sqrt{\frac{1}{I} \int_{t_0}^{t_f} dt |O(t)|^2}. \quad (4.8)$$

Hence, OCT can be implemented numerically as follows:

- guess an initial laser field  $E(t)$
- propagate  $|\Psi\rangle$  to time  $t_f$  using the given  $E(t)$
- project  $|\Phi\rangle$  onto  $\Psi(t_f)$  to get  $|\chi(t_f)\rangle$
- propagate  $\chi$  backwards to time  $t_0$  (propagate  $|\Psi\rangle$  backwards as well, to avoid storing or memorizing the complete  $|\Psi(t)\rangle$  from forward propagation)
- during this propagation evaluate  $O(t)$  and store it
- after backwards propagation, calculate  $\lambda$  and renormalize  $O(t)$  with it, to yield a new  $E(t)$
- repeat the last five steps until convergence is achieved.

Although OCT is often referred to as global optimization procedure, it is only global in time [7]. Other control methods may still yield a “more optimal” field, because OCT may be trapped in a local maximum (depending on the initially guessed field).

## 4.7 Local control theory (LCT)

Local control theory was invented by Tannor, Kosloff and coworkers [88] and a little later, independently by Rabitz and coworkers, where it is called tracking [89–91]. Here, the control field is determined from the system’s dynamics at every instant in time and immediately fed back into the dynamics. Therefore, it can be implemented in the laboratory through automated experiments, in principle [7]. The laser field is derived from the rate  $\frac{d\langle\hat{A}\rangle}{dt}$  of a target expectation value  $\langle\hat{A}\rangle$  (see next chapter for details), where the central equation is

$$\frac{d\langle\hat{A}\rangle}{dt} = \frac{i}{\hbar}\langle\Psi(t)|[\hat{H}(t), \hat{A}]\Psi(t)\rangle, \quad (4.9)$$

or variants thereof.

The field is local in time, since it is determined to achieve a monotonic increase (decrease, constant) in the desired objective. As the field directly stems from the dynamics, it is very close to intuition and in most cases easily understandable. For example, the STIRAP scheme automatically emerged from the local optimization and was extended to an N-level system [92]. Local control was also formulated within the density matrix approach [93, 94]. An extension for controlling not only the field’s amplitude but also the phase was implemented for quantum computing [95, 96]. Various other applications can be found in the literature (see e.g. references [97–107]).

Since local control theory is the method used in this work, it is discussed in more detail in the next chapter.



## 5 Local control theory revisited

In local control theory (LCT), the shape of a laser field is determined by the system's dynamics. The analytical expression is derived from the rate  $\frac{d\langle\hat{A}\rangle}{dt}$  of a target expectation value  $\langle\hat{A}\rangle$ . In case of a time-independent operator  $\hat{A}$ , this time derivative can be evaluated according to:

$$\begin{aligned}
 \frac{d\langle\hat{A}\rangle}{dt} &= \frac{d}{dt} \langle\Psi(t) | \hat{A} | \Psi(t)\rangle \\
 &= \left\langle \frac{d}{dt} \Psi(t) | \hat{A} | \Psi(t)\right\rangle + \left\langle \Psi(t) | \hat{A} | \frac{d}{dt} \Psi(t)\right\rangle \\
 &= \frac{i}{\hbar} \langle\Psi(t) | \hat{H}(t)\hat{A} | \Psi(t)\rangle - \frac{i}{\hbar} \langle\Psi(t) | \hat{A}\hat{H}(t) | \Psi(t)\rangle \\
 &= \frac{i}{\hbar} \langle\Psi(t) | [\hat{H}(t), \hat{A}] | \Psi(t)\rangle,
 \end{aligned} \tag{5.1}$$

where the product rule was used in a first step and the time-dependent Schrödinger equation  $\frac{d}{dt}\Psi(t) = -\frac{i}{\hbar}\hat{H}(t)\Psi(t)$  was inserted in a second step. The time-dependent Hamiltonian is taken to consist of the time-dependent interaction  $\hat{W}(t) = -\mu E(t)$  and the Hamiltonian of the unperturbed system  $\hat{H}_0$ . As a consequence, the expectation value of the commutator can be split up into two parts

$$\begin{aligned}
 \frac{i}{\hbar} \langle\Psi(t) | [\hat{H}(t), \hat{A}] | \Psi(t)\rangle &= \frac{i}{\hbar} \langle\Psi(t) | [\hat{H}_0, \hat{A}] | \Psi(t)\rangle \\
 &\quad + \frac{i}{\hbar} \langle\Psi(t) | [\hat{W}(t), \hat{A}] | \Psi(t)\rangle.
 \end{aligned} \tag{5.2}$$

In several cases, the commutator  $[\hat{H}_0, \hat{A}]$  vanishes or can be neglected. The remaining term then yields

$$\frac{d\langle\hat{A}\rangle}{dt} = E(t) \frac{i}{\hbar} \langle\Psi(t) | [-\mu, \hat{A}] | \Psi(t)\rangle. \tag{5.3}$$

If the objective is either a positive or negative rate, the field can be chosen as

$$E(t) = \begin{cases} +\lambda \frac{i}{\hbar} \langle\Psi(t) | [-\mu, \hat{A}] | \Psi(t)\rangle & \text{for a monotonic increase of } \langle\hat{A}\rangle \\ -\lambda \frac{i}{\hbar} \langle\Psi(t) | [-\mu, \hat{A}] | \Psi(t)\rangle & \text{for a monotonic decrease of } \langle\hat{A}\rangle \end{cases} \tag{5.4}$$

where  $\lambda$  can be e.g. a positive scaling factor or an envelope function. The reason for this choice of the field becomes clear, if Eq. (5.4) is inserted into Eq. (5.3), which yields

$$\frac{d\langle\hat{A}\rangle}{dt} = \begin{cases} +\lambda \left( \frac{i}{\hbar} \langle \Psi(t) | [-\mu, \hat{A}] | \Psi(t) \rangle \right)^2 \geq 0 \\ -\lambda \left( \frac{i}{\hbar} \langle \Psi(t) | [-\mu, \hat{A}] | \Psi(t) \rangle \right)^2 \leq 0. \end{cases} \quad (5.5)$$

It follows, that the rate then is represented by the square of the expectation value of the commutator, which is always larger than or equal to zero for  $+\lambda$  (smaller than zero for  $-\lambda$ ). The latter conclusion is valid, due to the lemma, that the expectation value of a Hermitian operator is purely real [108] (and thus,  $\frac{d\langle\hat{A}\rangle}{dt}$  is real-valued). Another way of putting this, uses that a commutator is anti-Hermitian. With the lemma, that the expectation value of an anti-Hermitian operator, defined by  $C = -C^\dagger$ , is purely imaginary [108], the same result is obtained.

If the commutator  $[\hat{H}_0, \hat{A}]$  does not vanish, the field can be determined as

$$E(t) = \lambda \frac{\frac{i}{\hbar} \langle \Psi(t) | [\hat{H}_0, \hat{A}] | \Psi(t) \rangle}{\frac{i}{\hbar} \langle \Psi(t) | [-\mu, \hat{A}] | \Psi(t) \rangle} \quad (5.6)$$

where

- for a monotonic increase of  $\langle\hat{A}\rangle$ ,  $\begin{cases} \lambda > -1 & \text{if } \frac{i}{\hbar} \langle \Psi(t) | [\hat{H}_0, \hat{A}] | \Psi(t) \rangle > 0 \\ \lambda < -1 & \text{if } \frac{i}{\hbar} \langle \Psi(t) | [\hat{H}_0, \hat{A}] | \Psi(t) \rangle < 0 \end{cases}$
- for a constant  $\langle\hat{A}\rangle$ ,  $\lambda = -1$
- for a monotonic decrease of  $\langle\hat{A}\rangle$ ,  $\begin{cases} \lambda < -1 & \text{if } \frac{i}{\hbar} \langle \Psi(t) | [\hat{H}_0, \hat{A}] | \Psi(t) \rangle > 0 \\ \lambda > -1 & \text{if } \frac{i}{\hbar} \langle \Psi(t) | [\hat{H}_0, \hat{A}] | \Psi(t) \rangle < 0. \end{cases}$

From the latter inequalities, it can be seen, that the to some extent general procedure has to be adjusted according to the respective target. The following examples illustrate the proceeding necessary for the treated problems in this work.

## 5.1 Energy objective

If energy is to be pumped into the system (heating) or taken away (cooling), the expectation value of the unperturbed system's Hamiltonian  $\hat{H}_0$  is regarded. Its

time derivative

$$\begin{aligned}
\frac{d\langle\hat{H}_0\rangle}{dt} &= \frac{i}{\hbar} \left\langle \Psi(t) \left| [\hat{H}(t), \hat{H}_0] \right| \Psi(t) \right\rangle \\
&= E(t) \frac{i}{\hbar} \left\langle \Psi(t) \left| [-\mu, \hat{T}] \right| \Psi(t) \right\rangle \\
&= E(t) \frac{\hbar}{i2m} \left\langle \Psi(t) \left| \left( \frac{d^2\mu}{dR^2} + 2\frac{d\mu}{dR} \frac{d}{dR} \right) \right| \Psi(t) \right\rangle
\end{aligned} \tag{5.7}$$

then should be positive for a heating (negative for a cooling) at all times. Therefore, the field is chosen as

$$E(t) = \lambda \frac{i\hbar}{2m} \left\langle \Psi(t) \left| \left( \frac{d^2\mu}{dR^2} + \frac{d\mu}{dR} \frac{d}{dR} \right) \right| \Psi(t) \right\rangle, \tag{5.8}$$

where  $\lambda$  is a positive constant for the heating case (negative for cooling).

In the special case of a linear dipole moment, i.e.  $\mu = q R$ , equation (5.7) is simplified to

$$\begin{aligned}
\frac{d\langle\hat{H}_0\rangle}{dt} &= E(t) \frac{\hbar}{i2m} \left\langle \Psi(t) \left| 2q \frac{d}{dR} \right| \Psi(t) \right\rangle \\
&= E(t) \frac{q}{m} \langle \Psi(t) | \hat{p} | \Psi(t) \rangle
\end{aligned} \tag{5.9}$$

and consequently, the field is chosen as

$$E(t) = \begin{cases} +\lambda \langle \hat{p} \rangle & \text{(heating)} \\ -\lambda \langle \hat{p} \rangle & \text{(cooling)}. \end{cases} \tag{5.10}$$

## 5.2 Vibrational eigenstate objective

If the target is a single vibrational state  $|\phi_t\rangle$ , the projector  $|\phi_t\rangle\langle\phi_t|$  onto this eigenstate is the operator of interest. The rate is then

$$\begin{aligned}
\frac{d\langle|\phi_t\rangle\langle\phi_t| \rangle}{dt} &= \frac{i}{\hbar} \left\langle \Psi(t) \left| [\hat{H}(t), |\phi_t\rangle\langle\phi_t|] \right| \Psi(t) \right\rangle \\
&= E(t) \frac{i}{\hbar} \left\langle \Psi(t) \left| [-\mu, |\phi_t\rangle\langle\phi_t|] \right| \Psi(t) \right\rangle \\
&= E(t) \frac{2}{\hbar} \Im \langle \Psi(t) | \mu | \phi_t \rangle \langle \phi_t | \Psi(t) \rangle
\end{aligned} \tag{5.11}$$

and the field becomes

$$E(t) = +\lambda \Im \langle \Psi(t) | \mu | \phi_t \rangle \langle \phi_t | \Psi(t) \rangle. \tag{5.12}$$

From this analytical form it becomes obvious, that some overlap between the wavepacket  $\Psi(t)$  and the target state  $|\phi_t\rangle$  must exist at the beginning. Otherwise the field remains zero. This problem is overcome e.g. by a so-called seed pulse, which transfers a negligible amount of population to the desired state. However, it is important to note, that in an experiment the seed pulse would not be necessary, if the calculated control field was applied.

### 5.3 Electronic state objective

If population is to be transferred from an electronic state  $|1\rangle$  to another electronic state  $|2\rangle$ , the procedure is similar as with the vibrational eigenstate objective. The expectation value of the projector  $|2\rangle\langle 2|$  onto the chosen final state is differentiated by time. In this case, the wavefunction consists of two parts belonging to the respective electronic state

$$|\Psi(t)\rangle = \psi_1|1\rangle + \psi_2|2\rangle. \quad (5.13)$$

The Hamiltonian now reads

$$\hat{H}(t) = |1\rangle(\hat{T}+V_1)\langle 1| + |1\rangle(-\mu_{12} E(t))\langle 2| + |2\rangle(-\mu_{12} E(t))\langle 1| + |2\rangle(\hat{T}+V_2)\langle 2| \quad (5.14)$$

with the potential energy  $V_n$  in state  $|n\rangle$  ( $n = 1, 2$ ) and the transition dipole moment  $\mu_{12}$ . The time derivative of the target is then evaluated according to

$$\begin{aligned} \frac{d\langle 2|2\rangle}{dt} &= \frac{i}{\hbar} \left( \langle 1| \psi_1^* + \langle 2| \psi_2^* \right) [\hat{H}(t), |2\rangle\langle 2|] \left( \psi_1 |1\rangle + \psi_2 |2\rangle \right) \\ &= \frac{2}{\hbar} E(t) \Im \langle \psi_1 | \mu_{12} | \psi_2 \rangle \end{aligned} \quad (5.15)$$

where  $\langle n|m\rangle = \delta_{nm}$  was used. As a consequence, the control field takes the form

$$E(t) = \lambda \Im \langle \psi_1 | \mu_{12} | \psi_2 \rangle. \quad (5.16)$$

### 5.4 Energy objective including rotation

The above objectives are discussed for fixed orientation of the molecule with respect to the laser polarization. If the rotational degree of freedom is taken into account, slight variations are encountered.

As stated above (section 3.5), the interaction takes the form  $W(t) = -\mu E(t) \cos \theta$ .

The rate expression for a diatomic molecule's vibrational energy  $\hat{H}_{vib}$  now results in (assuming a linear dipole moment)

$$\begin{aligned}\frac{d\langle\hat{H}_{vib}\rangle}{dt} &= E(t)\frac{\hbar}{i2m}\left\langle\Psi(t)\left|2q\frac{\partial}{\partial R}\right|\Psi(t)\right\rangle \\ &= E(t)\frac{q}{m}\langle\Psi(t)|\hat{p}\cos\theta|\Psi(t)\rangle\end{aligned}\quad (5.17)$$

and consequently, the field is chosen as

$$E(t) = \begin{cases} +\lambda \langle\hat{p}\cos\theta\rangle & \text{(heating)} \\ -\lambda \langle\hat{p}\cos\theta\rangle & \text{(cooling)}. \end{cases}\quad (5.18)$$

Due to the  $\cos\theta$ -term, this field usually is zero, when starting from the groundstate. In this case, a seed pulse is needed in order to achieve active control.

## 5.5 Orientation objective

If an orientation of the molecule with respect to the laser polarisation should be achieved, the target is chosen as  $\langle\hat{J}^2\rangle$ . The reason for this choice is, that a superposition of a large number of rotational eigenstates  $j$  results in an orientation. The latter can be verified by the means of a Fourier series, where a localized function can be approximated by the superposition of e.g. trigonometric functions [109]. Here, the superposition of more and more angular free-rotor states leads to an object localized in the angular degree of freedom. Thus, the increase of the expectation value of the angular momentum operator  $\langle\hat{J}^2\rangle$  is a sufficient condition for an orientation.

The time derivative of the target is then evaluated for a diatomic molecule according to

$$\begin{aligned}\frac{d\langle\hat{J}^2\rangle}{dt} &= E(t) i\hbar\left\langle\Psi(t)\left|\mu\left[\cos\theta,\left(\frac{\partial^2}{\partial\theta^2}+\cot\theta\frac{\partial}{\partial\theta}\right)\right]\right|\Psi(t)\right\rangle \\ &= E(t)\frac{2\hbar}{i}\left\langle\Psi(t)\left|\mu\left(\cos\theta+\sin\theta\frac{\partial}{\partial\theta}\right)\right|\Psi(t)\right\rangle.\end{aligned}\quad (5.19)$$

As a consequence, the control field is chosen as

$$E(t) = \lambda \Im\left\langle\Psi(t)\left|\mu\left(\cos\theta+\sin\theta\frac{\partial}{\partial\theta}\right)\right|\Psi(t)\right\rangle\quad (5.20)$$

to ensure a rate, which is larger than zero.



# 6 Laser control of the NaI molecule

One of the first molecules studied with femtosecond time resolution was sodium iodide (see e.g. the seminal work by Zewail et al. [110, 111]). A lot of data is available for this molecule, which builds an excellent basis for further studies. Here, sodium iodide is chosen as model system for laser control. For related work on NaI control, see Refs. [112–117].

As mentioned in section 2.5, the potentials of NaI can be described in the adiabatic (index  $a$ ) or the diabatic (index  $d$ ) picture. In the literature, the analytic form of the curves in the diabatic representation can be found [118]. Here, the potential  $V_1^d$  of the ionic groundstate  $|1\rangle$  is given as

$$V_1^d = \left[ A_1 + \left( \frac{B_1}{R} \right)^8 \right] \cdot e^{-\frac{R}{\rho}} - \frac{e^2}{R} - \frac{e^2(\lambda^+ + \lambda^-)}{2R^4} - \frac{C_1}{R^6} - \frac{2e^2\lambda^+\lambda^-}{R^7} + \Delta E_1 \quad (6.1)$$

The values of the parameters as well as the constants from the following equations can be found in Tab. 6.1. The character of the first excited state  $|2\rangle$  is neutral and its potential

$$V_2^d = A_2 e^{-\beta_2(R-R_0)} + \Delta E_2 \quad (6.2)$$

is dissociative. It shows a non-adiabatic coupling to the groundstate, which can be modeled by the coupling function

$$V_{12}^d = A_{12} e^{-\beta_{12}(R-R_c)^2}, \quad (6.3)$$

which is chosen as a gaussian to fit the energy gap of 0.11 eV of the avoided crossing at  $\approx 7 \text{ \AA}$  in the adiabatic representation [118]. A second excited state is involved in some of the following setups. Because it shows no coupling to one of the other states, its form is identical in the diabatic as well as in the adiabatic picture [119]:

$$V_3 = A_3 [1 - e^{-\beta_3(R-R_{e3})}]^2 - A_3 + \Delta E_3 \quad (6.4)$$

Table 6.1: Parameters for the NaI potentials.

$V_1^d$		$V_2^d$		$V_{12}$		$V_3$	
$A_1$ [eV]	2760	$A_2$ [eV]	0.813	$A_{12}$ [eV]	0.055	$A_3$ [eV]	0.06572
$B_1$ [ $\text{eV}^{\frac{1}{8}} \text{\AA}$ ]	2.398	$\beta_2$ [ $\text{\AA}^{-1}$ ]	4.08	$\beta_{12}$ [ $\text{\AA}^{-2}$ ]	0.6931	$\beta_3$ [ $\text{\AA}^{-1}$ ]	1.8
$C_1$ [ $\text{eV} \text{\AA}^6$ ]	11.3	$R_0$ [ $\text{\AA}$ ]	2.67	$R_c$ [ $\text{\AA}$ ]	6.93	$R_{e3}$ [ $\text{\AA}$ ]	3.4
$\lambda^+$ [ $\text{\AA}^3$ ]	0.408	$\Delta E_2$ [eV]	4.086			$\Delta E_3$ [eV]	6.191
$\lambda^-$ [ $\text{\AA}^3$ ]	6.431						
$\rho$ [ $\text{\AA}$ ]	0.3489						
$\Delta E_1$ [eV]	4.086						

The potential curves are depicted in Fig. 6.1.

The permanent dipole moment of the first excited state in the adiabatic representation was taken from a figure in Ref. [120]. It can be approximated by the analytic form

$$\begin{array}{l|l} R < R_I & \mu_2^a = 0.0 D \\ R_I \leq R \leq R_{II} & \mu_2^a = A_I \cdot e^{-\beta_I \cdot (R - R_{III})^2} - B_I \\ R_{II} < R & \mu_2^a = A_{II} \cdot R \end{array}$$

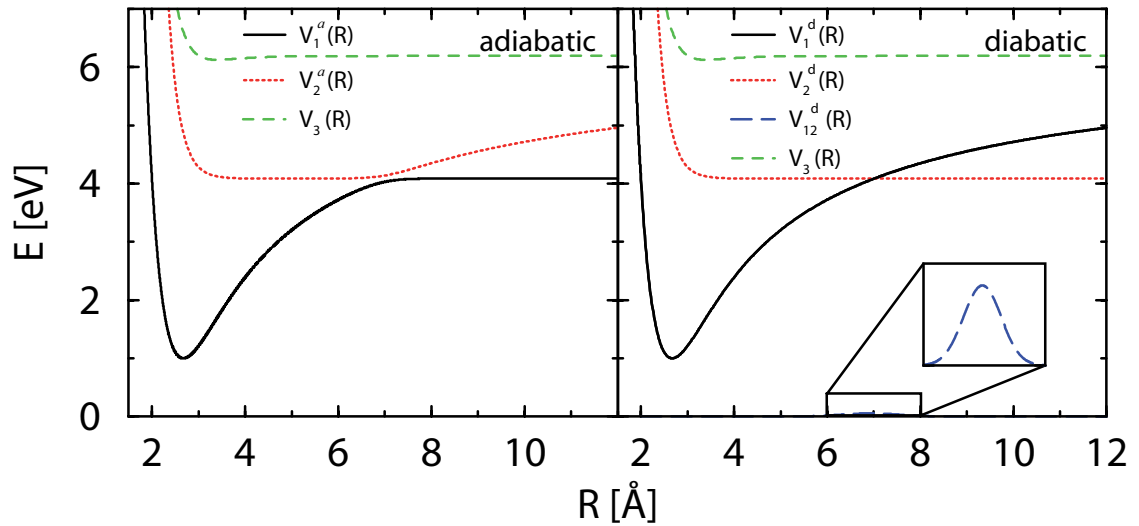


Figure 6.1: Potentials of sodium iodide. Left: Adiabatic curves. Right: Diabatic curves.



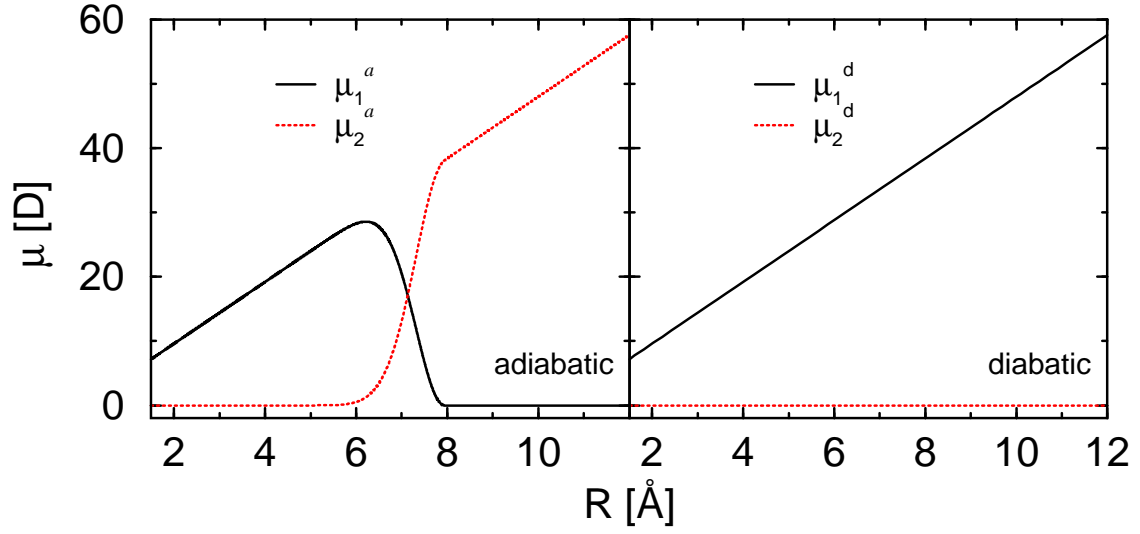


Figure 6.2: Permanent dipole moments. Left: Adiabatic dipole moments for the groundstate and the first excited state. Right: Diabatic curves, where the ionic nature of the diabatic groundstate and the neutral character of the excited state gets clear.

The adiabatic dipole moment  $\mu_1^a$  of the groundstate is then calculated by subtracting this  $\mu_2^a$  from the diabatic dipole moment  $\mu_1^d$  of the groundstate

$$\mu_1^a = \mu_1^d - \mu_2^a, \quad (6.5)$$

where

$$\mu_1^d = A_{II} \cdot R. \quad (6.6)$$

Table 6.2: Parameters for the dipole moments.

$\mu_2^a$ and $\mu_1^d$	
$R_I$ [Å]	5.000
$R_{II}$ [Å]	7.939
$R_{III}$ [Å]	8.000
$A_I$ [D]	38.262
$\beta_I$ [Å <sup>-1</sup> ]	0.567
$B_I$ [D]	$2.485 \cdot 10^{-3}$
$A_{II}$ [D Å <sup>-1</sup> ]	4.803 <sup>a</sup>

<sup>a</sup>Note, that this value equals 1 a.u.

The diabatic dipole moment of the excited state is small and consequently set to zero. The different dipole moments are displayed in Fig. 6.2.

## 6.1 Heating and cooling within an electronic state

In the first numerical example, the NaI molecule is excited from the groundstate by a femtosecond pulse into  $V_2^a$ . Within a simplified model, the predissociation channel, being effective through the non-adiabatic coupling at a distance of 7 Å, is ignored. In the excited state, either a heating or a cooling process is triggered by a control field, which is determined according to local control theory. Such processes occurring in molecules have been discussed in connection with, e.g., IR multiphoton dissociation [76, 121], and cooling of the internal degrees of freedom [93, 122].

The excited-state wave packet is prepared by a 50 fs pulse (full width at half maximum of the Gaussian field envelope) with a wavelength of 310 nm from the electronic ground state. This excitation is calculated within perturbation theory. The potential curve  $V_2^a(R)$  of the excited adiabatic state, where the dynamics takes place, is displayed in Fig. 6.3. The heating process, finally leading to dissociation, and the cooling process are illustrated schematically.

On account of the covalent character of the excited electronic state at small dis-

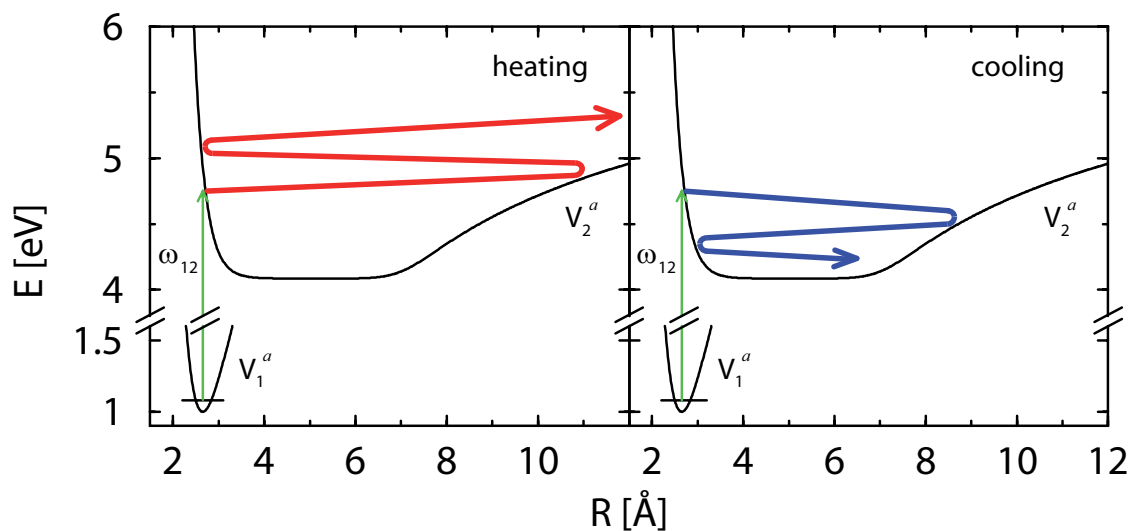


Figure 6.3: Scheme of a heating (left panel) and a cooling (right panel) process in the first excited state of sodium iodide.

tances,  $\mu_2^a(R)$  is negligibly small for  $R$  smaller than 6 Å and increases linearly for larger  $R$  (see Fig. 6.2). This behavior stems from the fact that at larger bond distances the character of the electronic state changes from covalent to ionic due to the avoided crossing. Thus, the model system is characterized by the Hamiltonian

$$\begin{aligned}\hat{H} &= -\frac{\hbar^2}{2m} \frac{d^2}{dR^2} + V_2^a(R) - \mu_2^a(R)E(t) \\ &= \hat{H}_0 - \mu_2^a(R)E(t),\end{aligned}\tag{6.7}$$

where the reduced mass  $m$  of NaI is 19.464 u (relative atomic mass units) and  $\hat{H}_0$  is the Hamiltonian of the unperturbed system.

The control target is either excited-state dissociation or a vibrational cooling. Therefore, the field  $E(t)$  is determined according to the energy objective (see section 5.1). Because of the shape of the dipole moment  $\mu_2^a(R)$ , the simplified approach, where the field is determined from the momentum expectation value  $\langle \hat{p} \rangle$ , can be applied. As a consequence, the control field is calculated at each time-step as

$$E(t) = \lambda \langle \hat{p} \rangle,\tag{6.8}$$

where the scaling parameter  $\lambda$  is chosen negatively for a cooling and positively for a heating process.

### 6.1.1 Heating

The heating process is illustrated in Figs. 6.4 and 6.5 for different scaling parameters  $\lambda$ . They are chosen as  $\lambda = 1 \cdot 10^{-6}$  a.u.,  $4 \cdot 10^{-6}$  a.u. and  $10 \cdot 10^{-6}$  a.u. The case without control field ( $\lambda = 0$  a.u.) is shown on the left-hand side in Fig. 6.4 for comparison.

In the upper panels, the control fields are depicted, respectively. Note that, because the field  $E(t)$  is scaled with the mean momentum, the amplitude  $E_0$  is actually much stronger than  $\lambda$ . For the highest value of  $\lambda = 10 \cdot 10^{-6}$  a.u., the maximum field strength is about  $5 \cdot 10^{-4}$  a.u., which corresponds to  $\sim 2.6 \cdot 10^8 \frac{V}{m}$  or an intensity of  $\sim 8.8 \cdot 10^9 \frac{W}{cm^2}$ . The fields are set to zero as soon as dissociation (lowest panels) sets in.

Dissociation is assumed to take place as soon as a bond length of  $R_{diss} = 37.5$  Å

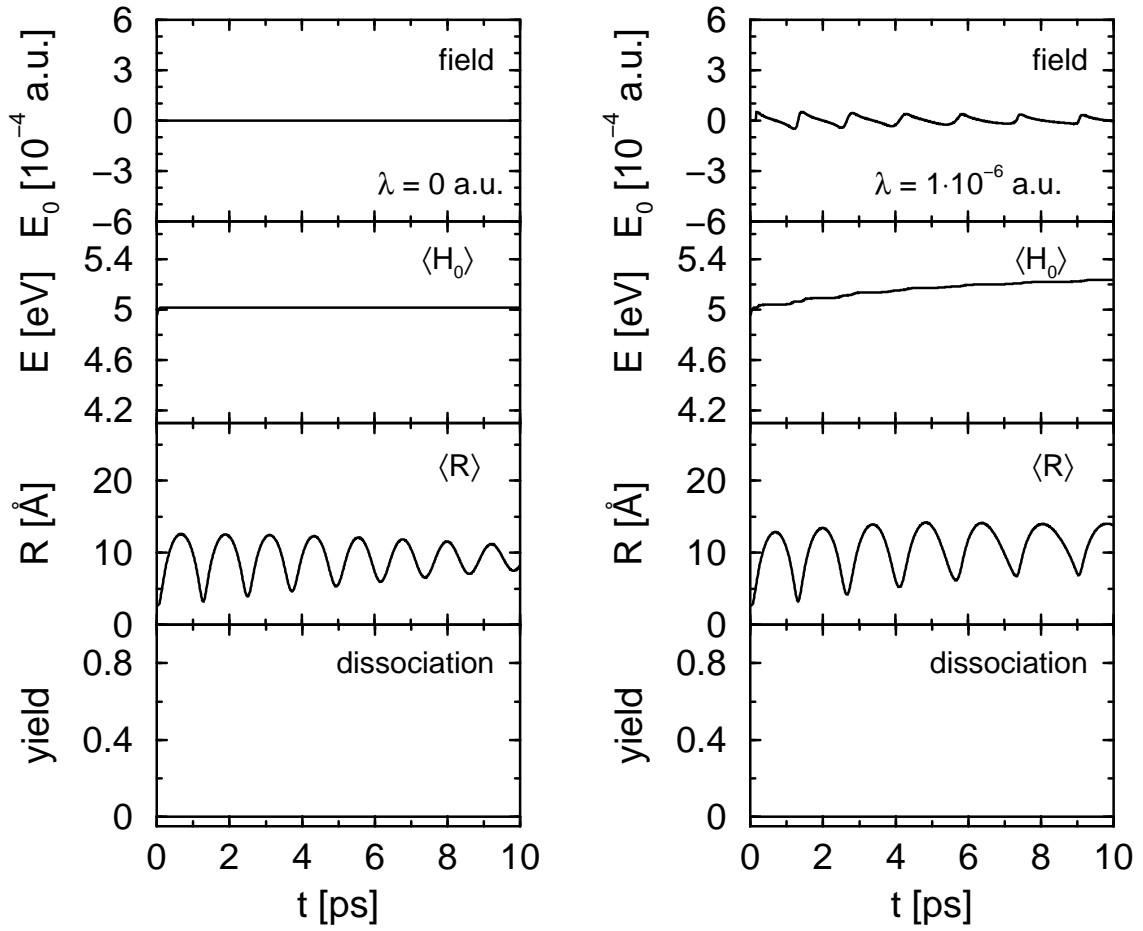


Figure 6.4: Heating of the NaI molecule. The upper panels contain the fields as constructed from the momentum changes in the system (see Eq. (6.8)) calculated for different coupling parameters (compare also Fig. 6.5). Here,  $\lambda = 1 \cdot 10^{-6}$  a.u. (right-hand side) and  $\lambda = 0$  a.u. (left-hand side), for comparison, are displayed. Also shown are the expectation values of the system's energy  $\langle H_0 \rangle$  and of the bond-length  $\langle R \rangle$  in the different cases. The lower panels display the dissociation yield.

is reached. Parts of the wavepacket exceeding this value are smoothly removed by an optical potential [123–127]. In other words, the wavefunction is multiplied with a cut-off function, which decays in a half-gaussian shape from 1 to 0 over a spatial interval of  $2 \text{ \AA}$  starting at  $R_{diss} = 37.5 \text{ \AA}$ . The dissociation yield is calculated in every time step by spatial integration over the removed wave-packet parts. The overall yield is then computed as the sum of those integrals. The dissociation yields for the different  $\lambda$  are shown in the lowest panels of figures 6.4 and 6.5.

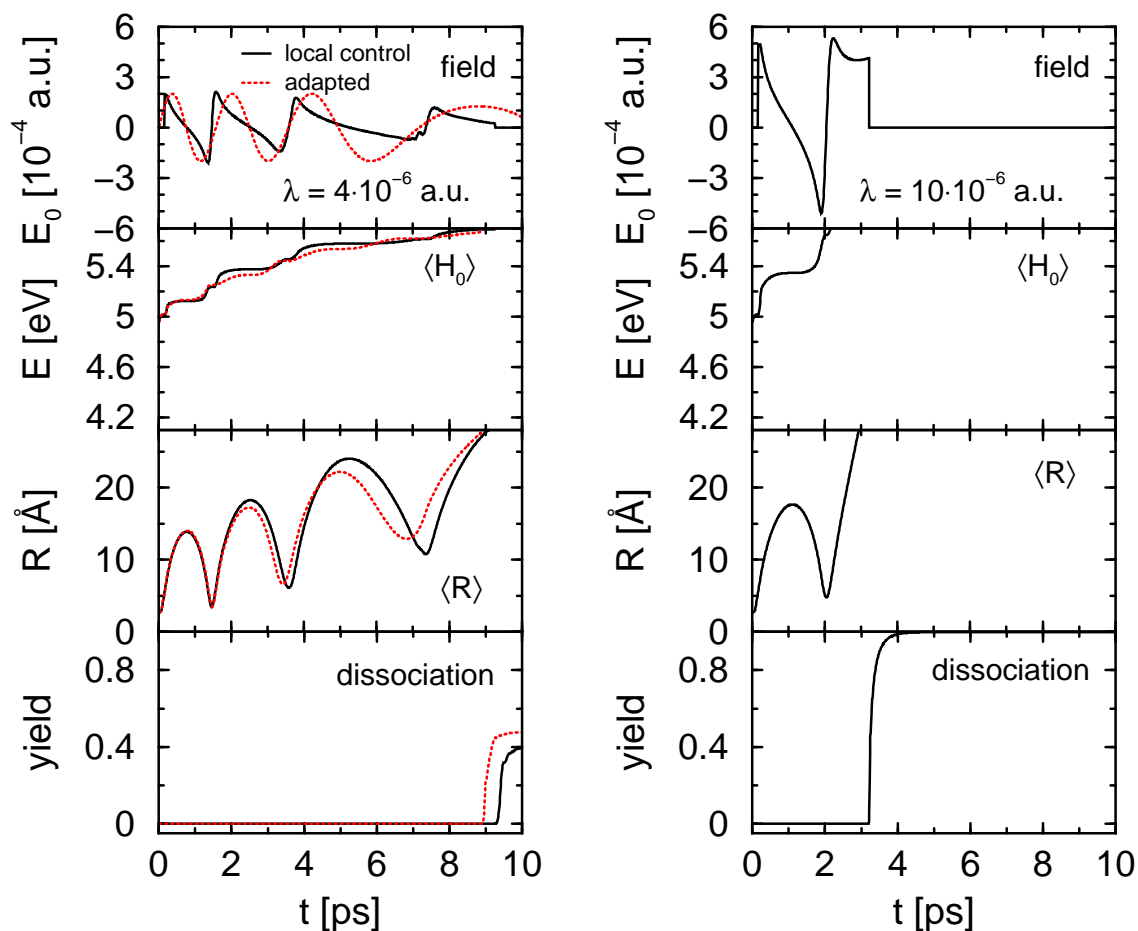


Figure 6.5: Field induced dissociation of NaI. The same values as in Fig. 6.4 are shown for  $\lambda = 4 \cdot 10^{-6}$  a.u. (left-hand side) and  $\lambda = 10 \cdot 10^{-6}$  a.u. (right-hand side). The left-hand side also contains the chirped field as given in Eq. 6.9, which is adapted to resemble the local control field. The corresponding expectation values are displayed in dotted lines.

Additionally, the energy expectation values  $\langle H_0 \rangle$  of the unperturbed system and the bond-length expectation values  $\langle R \rangle$  are depicted in the middle panels, as indicated. They are shown until dissociation sets in.

From the figures and from the definition of the control field, it emerges, that the heating process can be imagined as an in-phase-driven oscillator. With increasing energy, the vibrational amplitude increases and consequently, the frequency of the field becomes smaller. Thus, a down-chirp is expected and readily found. The quantum-mechanical analogon to the classical phenomenon of an in-phase-driven

oscillator is also well-known as ladder-climbing [76, 77, 121]. Here, the vibrational levels are seen as rungs of a ladder, which are climbed by the system via consecutive transitions induced by the field.

In what follows, the influence of the different intensities is discussed in detail. The case with the smallest scaling factor of  $\lambda = 1 \cdot 10^{-6}$  a.u. is regarded first (Fig. 6.4, right-hand side). A deposit of energy is clearly visible from the rise of the energy expectation value  $\langle H_0 \rangle$ . The bond-length expectation value reflects a vibrational motion with increasing amplitude and decreasing frequency, as expected from the classical arguments given above. Nevertheless, the control field is too weak to induce dissociation. At later times (not shown), the wave packet is de-localized over the potential well. This is accompanied by a mean momentum of zero. Thus, the spreading prevents that any more energy can be pumped into the system by a field defined according to Eq. (6.8).

Choosing only a slightly more intense field with  $\lambda = 4 \cdot 10^{-6}$  a.u. (Fig. 6.5, left-hand side), has the effect, that three vibrational periods are performed until fragmentation starts being effective. The increasing amplitude of the vibrational motion gets even more distinct. But due to wave-packet dispersion, only about 40% of the molecules undergo dissociation.

The limiting case, where the dissociation yield is 100 %, is obtained, choosing the parameter  $\lambda = 10 \cdot 10^{-6}$  a.u. (Fig. 6.5, right-hand side). Here, the absorption of energy is so effective that the initial wave packet reaches the dissociation channel only after one vibrational period.

The fields, as derived from the dynamics, have a somewhat complicated appearance. They should be regarded as theoretically derived fields to be approximated by simpler fields, which can be produced in the laboratory. As an example, the case of  $\lambda = 4 \cdot 10^{-6}$  a.u. (Fig. 6.5, left-hand side) is chosen. To a good approximation the field can be represented as

$$E(t) = E_0 \cos(\omega t + \alpha t^2 + \beta t^3 + \delta) \quad (6.9)$$

with  $\omega = 1.06 \cdot 10^{-4}$  a.u. and  $\delta = \frac{3}{2} \pi$ . The chirp parameters were chosen as  $\alpha = -1.4 \cdot 10^{-10}$  a.u. and  $\beta = -1 \cdot 10^{-17}$  a.u. The such parameterized field is included in the figure (dotted/red line). Employing this negatively chirped field, a

dissociation yield of roughly 45% is found, which even exceeds the results from the LCT field. This proves that indeed a reasonably smooth field may be derived from the quantum dynamics being as effective as the momentum scaled field of Eq. (6.8). The slightly better results of the smooth field show, that LCT may not provide the optimal field, as already stated by Tannor and coworkers [7]. Nevertheless, very efficient fields evolve, that can be clearly interpreted on a physical basis, where the latter is often not the case for other control algorithms.

### 6.1.2 Cooling

Due to the form of the control field equation, an out-of-phase-driven oscillator is expected for the cooling case. Here, the field should exhibit an up-chirp, as is clearly the case for  $\lambda = -1 \cdot 10^{-6}$  a.u. Regarding  $\langle H_0 \rangle$ , it can be seen, that a cooling is achieved. Also, the amplitude of the vibrational motion decreases and its frequency increases as can be anticipated from the classical argumentation.

For higher intensities of the field ( $\lambda = -4 \cdot 10^{-6}$  a.u.,  $-10 \cdot 10^{-6}$  a.u.), the up-chirp is visible at early times, but becomes less pronounced later on. This is due to the additional wave-packet dispersion introduced by the control field. Nevertheless, the cooling is very effective as can be seen from the energy expectation values  $\langle H_0 \rangle$ .

The rather irregular fields derived from LCT once again can be replaced by simpler fields to be produced in the laboratory. As an example, the case of  $\lambda = -4 \cdot 10^{-6}$  a.u. (Fig. 6.6, lower left-hand side) is chosen. The local control field can be fitted according to

$$E(t) = E_0 \cos(\omega t + \alpha t^2 + \beta t^3 + \delta) e^{-\xi(t-t_0)^2} \quad (6.10)$$

with  $\omega = 9.5 \cdot 10^{-5}$  a.u. and  $\delta = -0.3 \pi$ . The chirp parameters were chosen as  $\alpha = 5 \cdot 10^{-10}$  a.u. and  $\beta = -7.8 \cdot 10^{-16}$  a.u., while  $t_0 = 0$  and  $\xi = 1.17 \cdot 10^{-11}$  a.u. for the gaussian envelope. The such parameterized field is included in the figure (dotted/red line). In comparing the bond length with the energy expectation value, the conclusion can be drawn, that the chirped cosine field is equally effective as the momentum scaled one. This again proves, that practicable control fields can be derived from the system's dynamics.

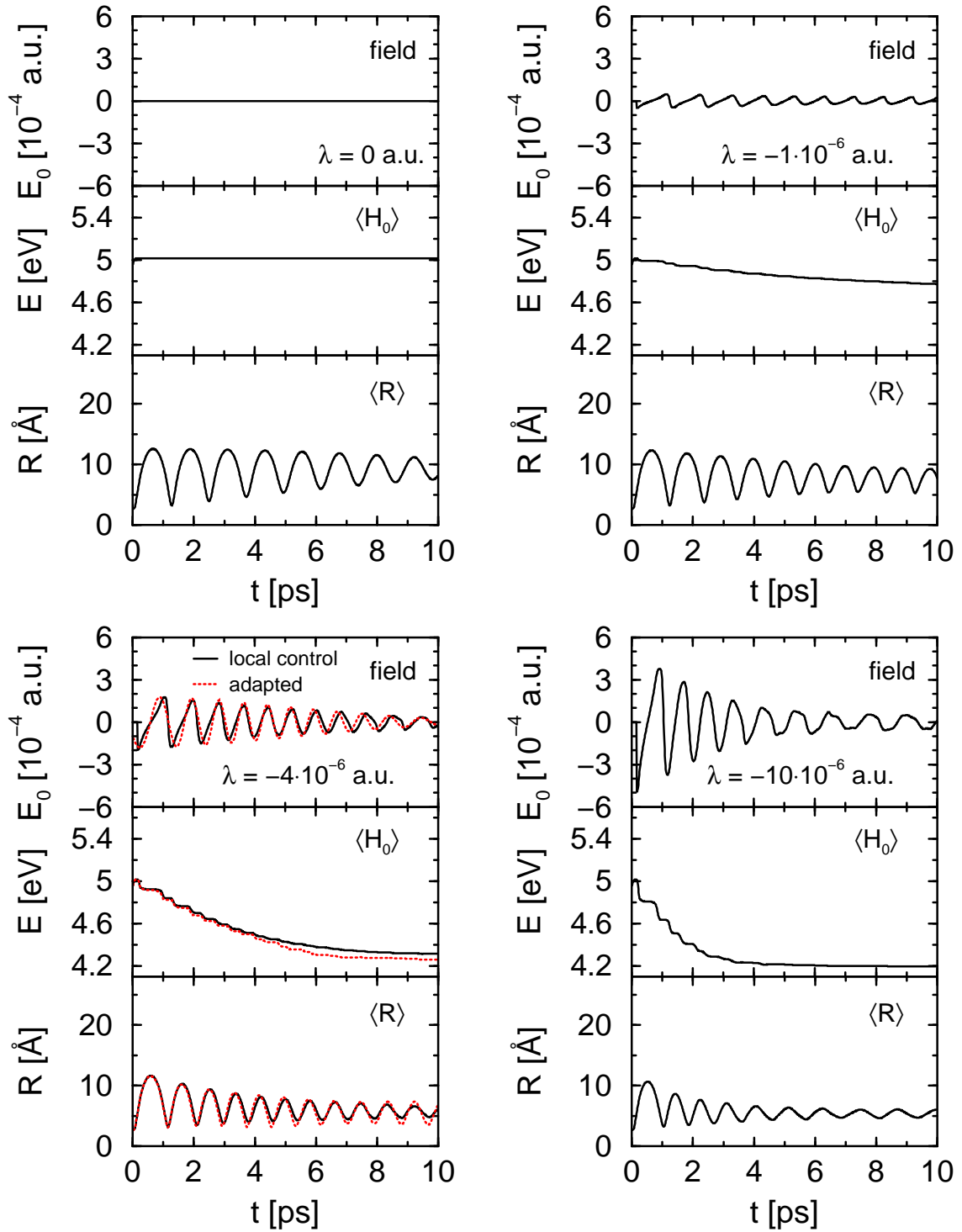


Figure 6.6: Cooling of the NaI molecule. The control fields (upper panels) are constructed from the momentum expectation value for different scaling parameters as indicated. Also, the expectation values of the system's energy  $\langle H_0 \rangle$  (middle panels) and of the bond-length  $\langle R \rangle$  (lower panels) are displayed for the respective cases. Additionally, a smooth field derived from a chirped cosine (Eq. (6.10)) and the corresponding expectation values are shown on the lower left-hand side (dotted/red lines). The former is adapted to resemble the local control field for  $\lambda = -4 \cdot 10^{-6}$  a.u.



## 6.2 Dissociation and Predissociation

In the previous section, the non-adiabatic coupling to the groundstate was ignored. Proceeding to a more realistic description, the resulting predissociation channel is now included. Once again, the heating case is regarded. However, not only excited-state dissociation, but the ratio of excited-state dissociation versus predissociation is of interest, here. A different target is pursued with the cooling fields. A decline of the predissociation is expected in this case. The results are compared to predictions from the Landau-Zener theory (see section 2.6). There exist several studies of the control of predissociation dynamics in the NaI molecule [59, 112, 113, 115, 116]. The present study differs from the above mentioned work in the way, the control fields are constructed.

The initial wave packet is prepared as described previously within perturbation theory. This packet performs a vibrational motion in the upper potential well but, due to the existence of the non-adiabatic coupling, curve crossing processes become effective each time the packet approaches the coupling region, finally leading to a complete predissociation. According to the Landau-Zener formula

$$P^{LZ} = e^{-\pi^2 \frac{\Delta E_c^2}{v \hbar \Delta F_c}}, \quad (6.11)$$

the probability for a transition from one adiabatic state to another, or in this case, the predissociation yield depends on the energy gap  $\Delta E_c$  between the adiabatic curves at the crossing point  $R_c$  and the velocity  $v$  of the wave packet in this region. These parameters are influenced by the control field. At the first glance, a higher predissociation yield is expected from a heating field due to an acceleration of the wave packet. In contrast, with decreasing velocity  $v$  induced by a cooling field, the predissociation yield should approach zero. These processes are sketched in Fig. 6.7.

The adiabatic potential curves  $V_n^a$  ( $n = 1, 2$ ) are constructed from the diabatic potentials introducing a potential coupling  $V_{12}$ . The Hamiltonian of the unperturbed system, within the diabatic representation, reads:

$$\mathbf{H}^d = \begin{pmatrix} \hat{T} & 0 \\ 0 & \hat{T} \end{pmatrix} + \begin{pmatrix} V_1^d(R) & V_{12} \\ V_{12} & V_2^d(R) \end{pmatrix} \quad (6.12)$$

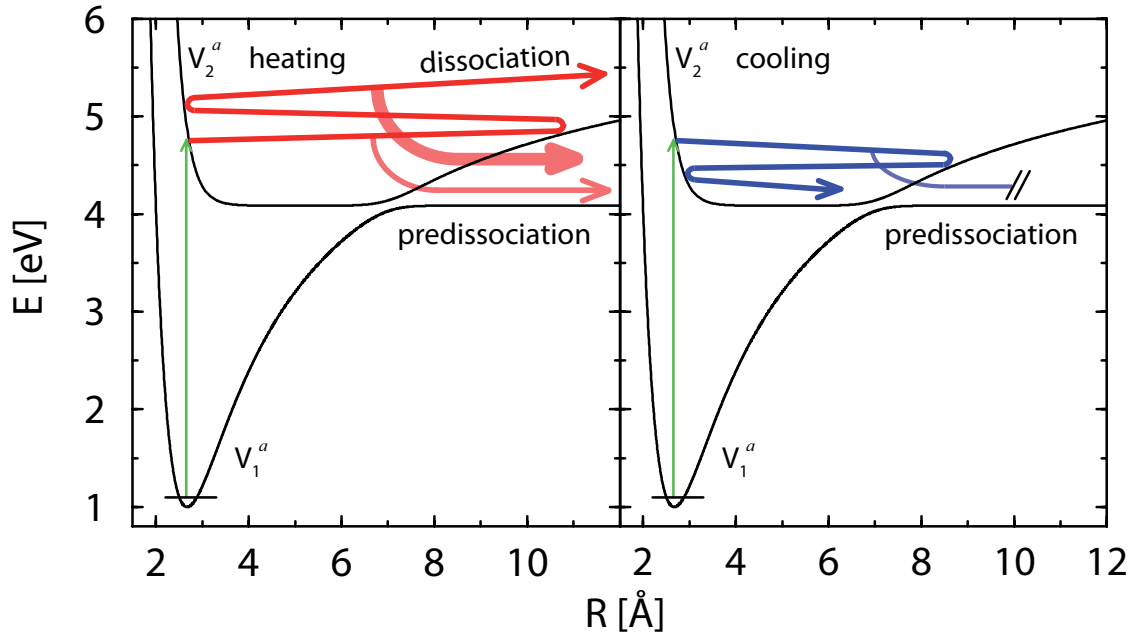


Figure 6.7: Scheme of a heating (left panel) and a cooling (right panel) process. In the heating case, predissociation is enhanced until excited-state dissociation sets in. In this way, the ratio between neutral ( $\text{Na} + \text{I}$ ) and ionic ( $\text{Na}^+ + \text{I}^-$ ) products can be influenced. Regarding the cooling, predissociation is suppressed.

where  $\hat{T}$  is the kinetic energy operator.

The interaction with the external heating/cooling field is given by the dipole coupling-term of the form

$$W_n^a = -\mu_n^a(R) E(t). \quad (6.13)$$

To arrive at a description in adiabatic states and to apply the adiabatic dipole moments  $\mu_n^a$ , the short-time propagator, acting at time  $t$  on the two-component nuclear wave function is approximated as

$$\mathbf{U}_{12} = e^{-i\mathbf{T}\frac{\Delta t}{2}} \mathbf{A}^T e^{-i\mathbf{V}_W^a \Delta t} \mathbf{A} e^{-i\mathbf{T}\frac{\Delta t}{2}}. \quad (6.14)$$

The matrix  $\mathbf{A}(R)$  (where  $\mathbf{A}^T$  is its transposed) diagonalizes the diabatic potential matrix appearing in Eq. (6.12). The resulting matrix  $\mathbf{V}_W^a$  contains the sum of the adiabatic potentials  $V_n^a(R)$  and the interaction term  $W_n^a(R, t)$  as diagonal matrix elements

$$\mathbf{V}_W^a = \begin{pmatrix} V_1^a + W_1^a & 0 \\ 0 & V_2^a + W_2^a \end{pmatrix}. \quad (6.15)$$

The expression for the propagator is valid in the limit that the electric field can be regarded as constant within the small time interval  $\Delta t$  [128]. This is the case, as  $E(t)$  is again derived in every time step from the momentum in the upper adiabatic state

$$E(t) = \lambda \langle \hat{p}_2^a \rangle. \quad (6.16)$$

The dissociation yield in the excited adiabatic state is calculated as described in the previous section. Additionally, the predissociation yield is computed in a similar way. Here, the optical potential, which cuts parts of the two-component wave function in the adiabatic groundstate, starts to act at a distance  $R_{prediss} = 9.5 \text{ \AA}$ .

### 6.2.1 Na + I vs. Na<sup>+</sup> + I<sup>-</sup>

First, the case of a heating field is treated. The control fields for different parameters  $\lambda$  are shown in Fig. 6.8a. The numbers (s) in the figure correspond to values of  $\lambda = s \cdot 10^{-6}$  a.u. From the figure, it can be taken, that the frequency of the fields decreases in time. This again hints at an enlarged amplitude of the vibrational motion, as shown in the previous section for the simplified model.

The panels (b) display the time-dependent energy expectation values

$$\langle H_0 \rangle = \frac{\langle \Psi(t) | \mathbf{H}^d | \Psi(t) \rangle}{\langle \Psi(t) | \Psi(t) \rangle}. \quad (6.17)$$

Here,  $\Psi(t)$  denotes the part of the two-component wave function which has not disappeared into the reaction channels. From the energy expectation values, it is seen that with increasing field strength the energy deposition is effectively enhanced. The heating of the system has the consequence that the average velocity of the relative motion is increased. As stated above, this increases the transition probability, so that predissociation is enhanced. The percentage of molecules, which undergo predissociation and turn to the neutral fragments Na + I, is displayed in panels (c). Nevertheless, as more and more energy is absorbed from the control field, the total energy is approaching the dissociation limit in the excited electronic state occurring at a value of about 5.7 eV. Molecules exceeding this energy fragment into the ionic products Na<sup>+</sup> + I<sup>-</sup>. The respective dissociation yields are shown in panels (d).

Regarding the cases of different field strengths, the following effects are found. For the weakest field ( $s = 1$ , straight/dark red line) no dissociation is found in the

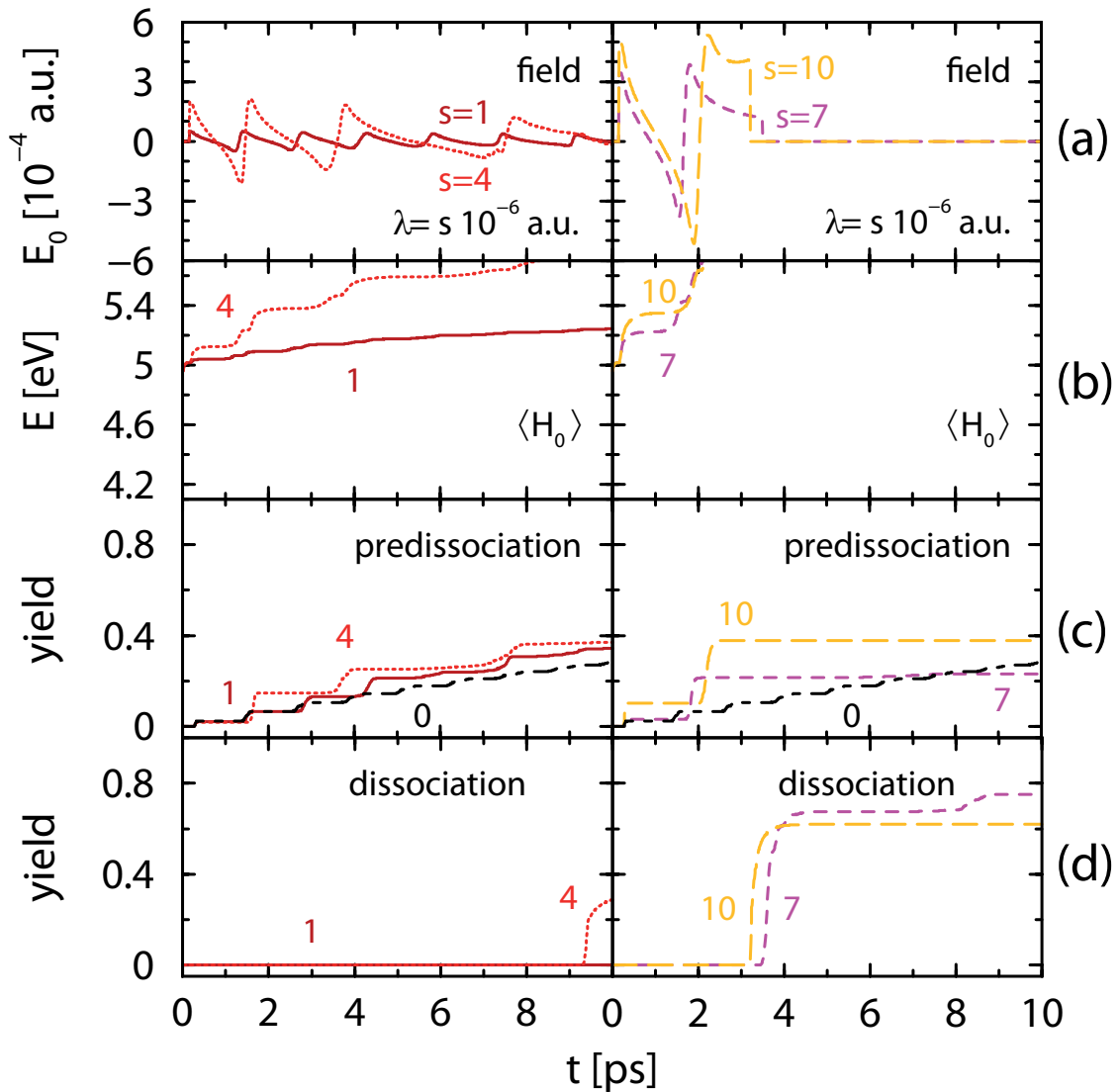


Figure 6.8: Heating. Panels (a) show the control fields for various scaling factors  $\lambda = s \cdot 10^{-6}$  a.u., where  $s = 1, 4, 7$  or  $10$ . Below, the respective energy expectation values  $\langle H_0 \rangle$  are displayed (panels (b)). In the lowest panels (d), the excited-state dissociation yields are depicted, where the resulting fragments are  $\text{Na}^+ + \text{I}^-$ . In panels (c), the yield for the fragments  $\text{Na} + \text{I}$  according to a predissociation mechanism can be found. Here, the predissociation yield in the fieldless case is additionally shown for comparison.

displayed time interval. Regarding the predissociation process, it is seen that the predissociation yield at  $t = 10$  ps is enhanced as compared to the zero-field case (dot-dashed/black line).

Increasing the field strength by a factor of 4 (dotted/red line) results in an even larger yield at shorter times. However, this value becomes smaller than the one obtained at zero field at later times (not shown). The reason is that, if no field is present, all laser excited molecules undergo predissociation in the limit of infinite times, which is not the case if excited-state fragmentation occurs. The latter is taking place for  $s = 4$  shortly before 10 ps, as can be seen from the panels (d), left-hand side.

A higher field strength ( $s = 7$ , dashed/violet line) results in a higher ratio of dissociation/predissociation, i.e. more fragments are produced via excited-state dissociation. Here, the dissociation process of nearly all still-bound molecules sets in already at about 3.5 ps, which is shown in panels (d) on the right. Consequently, also the respective predissociation yield does not increase visibly afterwards.

For an even higher field strength of  $s = 10$  (long-dashed/orange line), the ratio of dissociation/predissociation gets lower again. Although the dissociation limit is reached somewhat earlier (shortly after 3 ps) than in the case with  $s = 7$ , more molecules have undergone predissociation until that time.

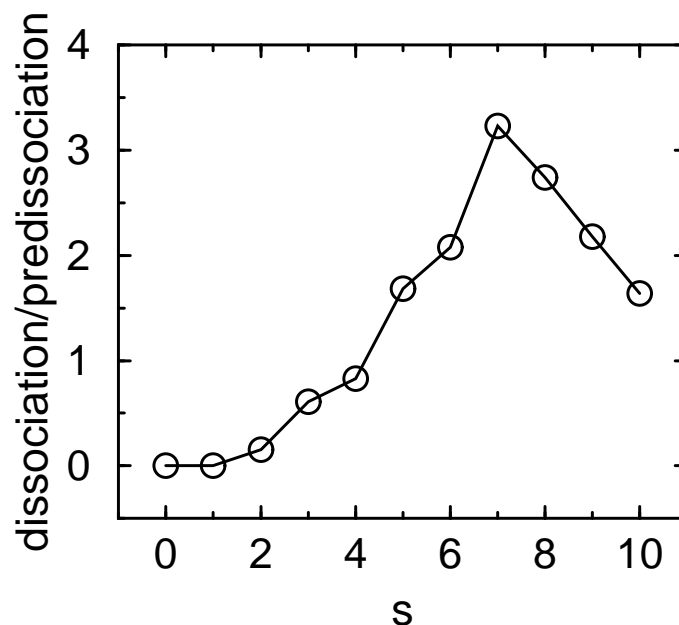


Figure 6.9: The ratio of dissociation/predissociation is plotted against  $s$ , where  $\lambda = s \cdot 10^{-6}$  a.u.

This trend of the dissociation/predissociation ratio is visualized in Fig. 6.9, where also intermediate values  $s$  have been considered additionally to the ones discussed above. The picture implies, that an optimal value of the field strength exists for the given problem. Here, the best scaling factor is  $\lambda = 7 \cdot 10^{-6}$  a.u. To find out the reasons for this behaviour, the Landau-Zener theory is helpful.

The predissociation yield  $P$  after passing the crossing point  $R_c$  for the first time (around 250 fs) is compared to results  $P^{LZ}$  obtained within the Landau-Zener theory, see Tab. 6.3. In calculating  $P^{LZ}$ , the values  $\Delta E_c$ ,  $\Delta F_c$  and the velocity  $v$  are evaluated from the expectation values of the bond length  $\langle R \rangle$  and the momentum  $\langle p \rangle$  in the excited adiabatic state. Here,  $\Delta E_c$  and  $\Delta F_c$  are modified by the external field, see below. All quantities are determined at the time  $t_c$  when the population in the adiabatic groundstate, being zero initially, assumes half of the value which is reached after the first crossing process.

Table 6.3: Transition probabilities  $P^{LZ}$  derived from Landau-Zener theory are compared to those obtained from the numerical calculations ( $P$ ) for a heating field.

$\lambda$	$P^{LZ}$	$P$	$\Delta F_c$ [a.u.]	$\Delta E_c$ [a.u.]	$v$ [a.u.]
0.	0.041	0.023	$5.914 \cdot 10^{-3}$	$4.002 \cdot 10^{-3}$	$1.334 \cdot 10^{-3}$
1.	0.034	0.021	$5.860 \cdot 10^{-3}$	$4.111 \cdot 10^{-3}$	$1.339 \cdot 10^{-3}$
4.	0.019	0.019	$5.683 \cdot 10^{-3}$	$4.415 \cdot 10^{-3}$	$1.357 \cdot 10^{-3}$
7.	0.011	0.032	$5.494 \cdot 10^{-3}$	$4.659 \cdot 10^{-3}$	$1.375 \cdot 10^{-3}$
10.	0.004	0.102	$5.356 \cdot 10^{-3}$	$5.177 \cdot 10^{-3}$	$1.394 \cdot 10^{-3}$

Regarding Tab. 6.3, it is obvious, that considering only the velocity, as presumed in the simple sketch in Fig. 6.7, is not sufficient. The results crucially depend on the modification of the energy gap

$$\Delta E_c = [(V_2^a + W_2^a) - (V_1^a + W_1^a)]_{R_c} \quad (6.18)$$

by the external field (and consequently also its derivative  $\Delta F_c$ ). The heating field induces a larger gap and a smaller force term  $\Delta F_c$ , yielding a smaller transition probability  $P^{LZ}$  than in the field free case. This is the opposite of the behaviour according to the velocity argumentation.

From Tab. 6.3, it can be taken that the Landau-Zener theory produces the tendency of a decreasing transition probability for increasing field strength. This is also found numerically for the smaller scaling parameters  $\lambda$ . However, for larger scaling parameters, no agreement is found. In that case, the intense field modifies the potential curves strongly so that only minor modifications in the bond length taken to determine the gap  $\Delta E_c$  and the force term  $\Delta F_c$  result in quite different numbers for  $P^{LZ}$ .

## 6.2.2 Suppressing predissociation

In order to suppress the predissociation process, the field is determined from Eq. (6.16), employing a negative  $\lambda$  to induce a cooling within the excited state. The control fields for different parameters  $\lambda = s \cdot 10^{-6}$  a.u. are shown in Fig. 6.10. The fields shows regular oscillations which reflect the vibrational period of the quasi-bound motion in the excited state. It is seen that the amplitude decreases as a function of time. This is much more pronounced in the case of the stronger fields. At about 10 ps, the fields exhibit only minor deviation from a value of zero. Because the field is directly proportional to the expectation value of the momentum, the decrease of amplitude hints at a decrease in momentum, in the average. Thus, classically speaking, the motion loses kinetic energy and becomes more and more constrained to take place close to the bottom of the potential well. That this is indeed the case can be taken from Fig. 6.10, middle panels, which displays the time-dependent energy expectation values  $\langle H_0 \rangle$ , computed according to Eq. (6.17).

For the weakest field, the energy diminishes steadily in the time interval displayed (and also at longer times, which are not shown). Increasing the field strength results in a large loss of energy within the first 5 ps, and afterwards the energy stays nearly constant. Note, that the energy of the predissociation channel (leading to fragmentation into Na and I) corresponds to a value of  $\sim 4.1$  eV.

The effective cooling indeed leads to a stabilization of the laser-excited molecules. This is illustrated in the lower panel of Fig. 6.10, which contains the predissociation yields. It is seen that, at longer times, the yields are lower as compared to the case of the unperturbed molecule which is also shown, for comparison. However, it is not found that the number of stabilized molecules scales directly with the field

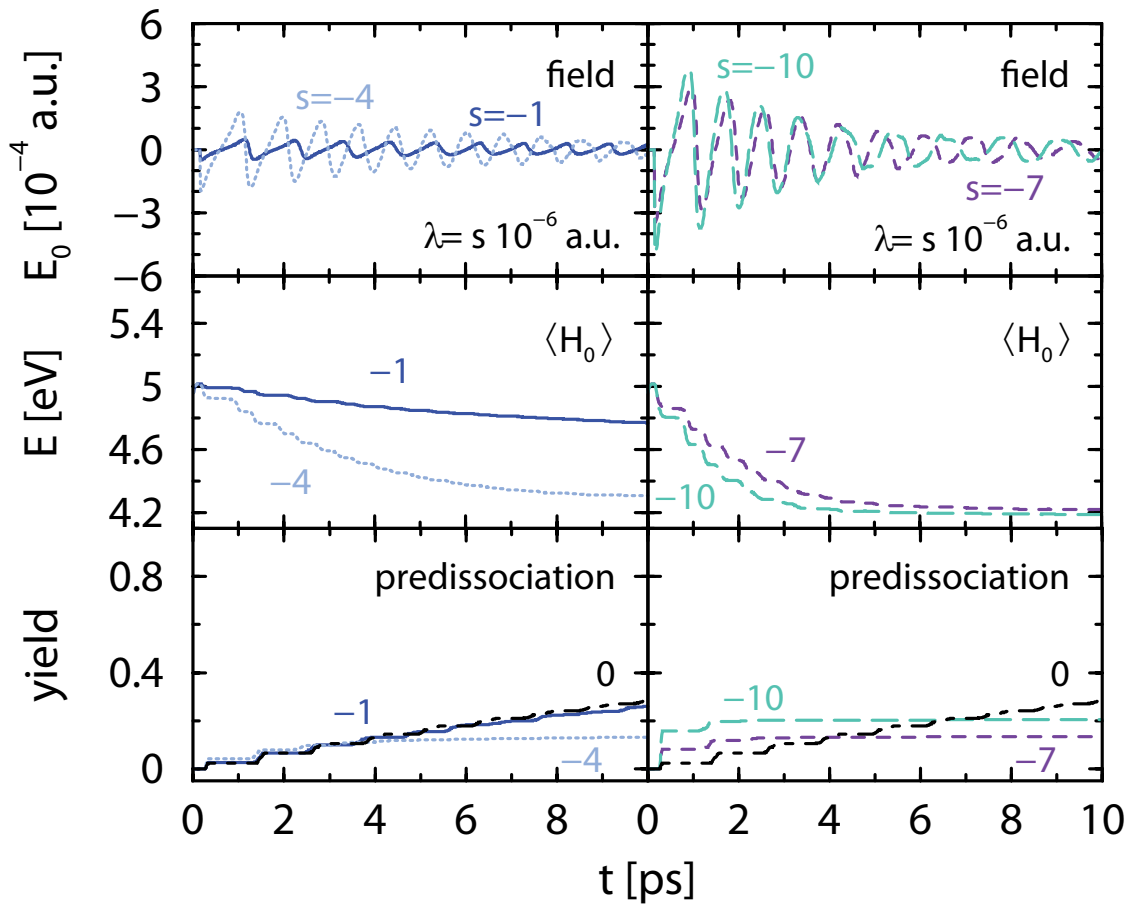


Figure 6.10: Cooling. The control fields for various scaling factors  $\lambda = s \cdot 10^{-6}$  a.u. are displayed in the upper panel. The parameter  $s$  is chosen as  $-1$ ,  $-4$ ,  $-7$  or  $-10$ . Below, the respective energy expectation values  $\langle H_0 \rangle$  are shown. In the lower panels, the predissociation yields for the different cases can be found. Here, the curve for the field free case is additionally shown for comparison.

strength, as could be expected from the Landau-Zener formula taking only the diminished velocity into account. From the cases presented in the figure, the weakest field of  $\lambda = -1 \cdot 10^{-6}$  a.u. (straight/blue line) results in slightly less predissociation than the field free case (dot-dashed/black line). The choice of  $\lambda = -4 \cdot 10^{-6}$  a.u. represents a field for which only 15% of the molecules decay via predissociation. This yield is even less for  $\lambda = -7 \cdot 10^{-6}$  a.u., while choosing the most intense field ( $\lambda = -10 \cdot 10^{-6}$  a.u.) leads to a higher decay of 20%.

To explain this trend, the modifications of the potential gap  $\Delta E_c$  and the force



term  $\Delta F_c$  (see Eqs. (6.11) and (6.18)) through the external field have to be considered. A closer inspection of the  $s = -10$  predissociation yield in Fig. 6.10 shows that at a time of 250 fs, when the excited-state wave packet reaches the crossing region for the first time, almost all of the fragments are built so that afterwards, the respective yield is nearly constant. At early times cooling is not yet very effective and thus the main deviation from the field free case is to be expected to originate from the field induced changes of the potential energy curves. However, at later times the field intensity approaches zero and the potential gap is only slightly influenced, while the cooling has then taken effect.

Table 6.4: Transition probabilities  $P^{LZ}$  derived from Landau-Zener theory are compared to those obtained from the numerical calculations ( $P$ ) for a cooling field.

$\lambda$	$P^{LZ}$	$P$	$\Delta F_c$ [a.u.]	$\Delta E_c$ [a.u.]	v [a.u.]
0	0.041	0.023	$5.914 \cdot 10^{-3}$	$4.002 \cdot 10^{-3}$	$1.334 \cdot 10^{-3}$
-1.	0.050	0.026	$5.972 \cdot 10^{-3}$	$3.894 \cdot 10^{-3}$	$1.328 \cdot 10^{-3}$
-4.	0.085	0.043	$6.138 \cdot 10^{-3}$	$3.558 \cdot 10^{-3}$	$1.311 \cdot 10^{-3}$
-7.	0.134	0.080	$6.294 \cdot 10^{-3}$	$3.230 \cdot 10^{-3}$	$1.297 \cdot 10^{-3}$
-10.	0.181	0.159	$6.428 \cdot 10^{-3}$	$2.997 \cdot 10^{-3}$	$1.285 \cdot 10^{-3}$

The conclusions derived for early times can be verified in comparing the numerically calculated transition probabilities  $P$  to the ones obtained from the Landau-Zener formula  $P^{LZ}$ , which are collected in Tab. 6.4. As can be taken from the table, the Landau-Zener theory describes the numerically found trends very well, namely that with increasing field strength the transition probability increases. Regarding the numbers which enter into the expression for  $P^{LZ}$ , it is seen that the main effect here stems from the modification of the potential gap, whereas the changes in velocity due to the cooling are, at this early time, of minor importance. Regarding the whole process, the control fields are able to suppress the decay via predissociation.

To summarize, the decay rates for the predissociation process are modified to a great extent. In discussing the decay mechanisms of NaI interacting with control fields, one has to take the internal energy as well as the Stark shifts of the coupled potentials into account. On one hand, the energy transfer influences the average relative velocity, and on the other hand, the external field modifies the potential curves in the crossing region. The interplay of both effects determine the time-

dependence of the product yields.

### 6.3 Complete control of NaI

In the first two sections of this chapter, local control of NaI was achieved, where first an adiabatic approach neglecting predissociation was employed. Then, an extended study incorporated the bound-to-continuum coupling. In both investigations, a pump laser initiates a population transfer from the electronic ground state to an excited state. The control scheme then is applied only to the (eventually small) fraction of molecules excited in the pump transition. This control scheme is incomplete in the sense that the remaining ground-state population is not properly taken into account. Instead, the objective should be to dissociate as many molecules as possible. Therefore, it is necessary to both depopulate the ground state and induce the excited-state dissociation.

A possible excitation scheme is presented in Fig. 6.11. There, the field  $E_1(t)$  depletes the ground state  $|1\rangle$ , and absorption of photons from the second field  $E_2(t)$  leads to excited-state dissociation (in state  $|2\rangle$ ). However, the fragmentation within the electronic ground state is a competing process. Because the amount of fragments entering the predissociation channel might be substantial, it is properly taken into account.

As in the previous section 6.2, the Hamiltonian of the unperturbed system is given by Eq. (6.12) within the diabatic representation. In contrast, the interaction with the external field

$$W_{nm}^a = -\mu_{nm}^a(R) E(t). \quad (6.19)$$

is applied in the adiabatic representation. Here, the transition dipole moments  $\mu_{12}^a$  and  $\mu_{21}^a$  are set to a constant value of 1 a.u. The permanent dipole moments  $\mu_{11}^a$  and  $\mu_{22}^a$  are taken from Ref. [120], as shown in Fig. 6.2 (p. 55). Like stated in the previous section, the matrix  $\mathbf{A}(R)$  diagonalizes the diabatic potential matrix from Eq. (6.12). Afterwards, the interaction with the external field is applied in the adiabatic representation. Due to the non-zero transition dipole moment, the

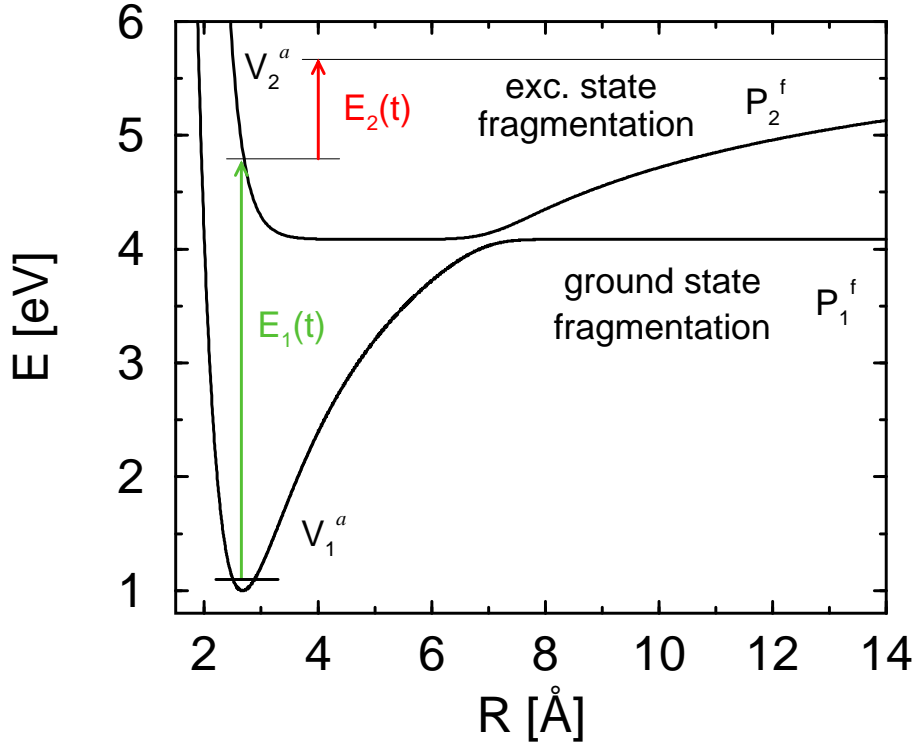


Figure 6.11: Excitation scheme for the control of excited-state dissociation in the NaI molecule. An electric field  $E_1(t)$  depletes the electronic ground state  $|1\rangle$ , and another field  $E_2(t)$  serves the purpose to deposit energy in molecules being prepared in the excited state  $|2\rangle$ . The ground-state dissociation is a competing process which is triggered by non-adiabatic potential- and also field-coupling.

resulting interaction matrix  $\mathbf{V}_W^a$  is not diagonal, anymore. It reads

$$\mathbf{V}_W^a = \begin{pmatrix} V_1^a + W_{11}^a & W_{12}^a \\ W_{21}^a & V_2^a + W_{22}^a \end{pmatrix}. \quad (6.20)$$

Therefore, the part of the propagator containing this matrix has to be applied as follows. Due to  $W_{12}^a = W_{21}^a$ , the equality

$$e^{-i \begin{pmatrix} V_1^a + W_{11}^a & W_{12}^a \\ W_{21}^a & V_2^a + W_{22}^a \end{pmatrix} \Delta t} = \begin{pmatrix} \cos([V_1^a + W_{11}^a] \Delta t) & -i \sin(W_{12}^a \Delta t) \\ -i \sin(W_{12}^a \Delta t) & \cos([V_2^a + W_{22}^a] \Delta t) \end{pmatrix} \quad (6.21)$$

holds true. The right-hand side can now easily be multiplied with the two-component wave function in order to propagate with the potential and the interaction part.

This somewhat complicated procedure is necessary to get a description in adiabatic states.

The electric field  $E(t)$  is determined from local control theory. A depopulation of the ground state  $|1\rangle$  is effective if a control field  $E_1(t)$  is determined such, that the rate of population transfer to the excited state is positive at all times. For this purpose, the projector  $A_2 = |2\rangle\langle 2|$  is defined, acting on the two-component wave function

$$|\psi(t)\rangle = \psi_1(R, t) |1\rangle + \psi_2(R, t) |2\rangle, \quad (6.22)$$

where  $\psi_n(R, t)$  is the vibrational wave function in state  $|n\rangle$ . One then calculates the excited-state population as

$$P_2^{tot}(t) = \langle \psi(t) | A_2 | \psi(t) \rangle = \langle \psi_2(t) | \psi_2(t) \rangle, \quad (6.23)$$

where the brackets denote integration over the nuclear coordinate  $R$ . The rate Eq. (5.1), p. 47, now takes the form (compare also section 5.3, p. 50)

$$\begin{aligned} \frac{dP_2^{tot}(t)}{dt} &= -\frac{2}{\hbar} \Im \langle \psi_1(t) | V_c - E_1(t) \mu_{12} | \psi_2(t) \rangle \\ &\approx \frac{2}{\hbar} E_1(t) \Im \langle \psi_1(t) | \mu_{12} | \psi_2(t) \rangle, \end{aligned} \quad (6.24)$$

where  $\Im$  denotes the imaginary part. Here, the contribution containing the matrix element of the potential coupling  $V_c(R)$  is neglected. This is a good approximation (a fact which was checked upon numerically), because the ground-state wave packet hardly has any overlap with the coupling element, the latter being localized around 7 Å.

In what follows, the field  $E_1(t)$  is chosen as

$$E_1(t) = \lambda_1 \Im \langle \psi_1(t) | \mu_{12} | \psi_2(t) \rangle. \quad (6.25)$$

For a positive scaling factor  $\lambda$ , the field then ensures a positive rate of population transfer. It is to be noted that Eq. (6.25) only delivers a non-zero field if a small amount of population is launched into the excited state initially. Therefore one usually employs an arbitrary 'seed pulse' preceding the control field [129].

The excited-state dissociation proceeds only if the energy in the excited state is

larger than the dissociation energy. Therefore, a second control field  $E_2(t)$  is constructed in the same manner as in the previous two sections and is taken as ( $\lambda_2 > 0$ ):

$$E_2(t) = \lambda_2 \Im \langle \psi_2(t) | [\mu_{22}(R), T(R)] | \psi_2(t) \rangle, \quad (6.26)$$

which ensures that the energy rate in the excited state is positive at all times (note, that the expectation value of the commutator is a purely imaginary number).

There are two strategies which emerge for the purpose to induce the excited-state dissociation. One could first apply the field  $E_1(t)$  and transfer as much population to the excited state as possible. Subsequently, the field  $E_2(t)$  is used to fragment the molecule.

Alternatively, the two field components could be constructed and applied simultaneously which, in general, should give a different yield of excited-state fragments.

First, the two-step process is discussed, where, starting from the vibrational ground state in  $|1\rangle$ , a population transfer to the excited state  $|2\rangle$  is triggered by the field  $E_1(t)$ , determined from Eq. (6.25). In order to start the algorithm, a low intensity Gaussian seed pulse is applied which puts a negligible amount of population in the excited state. The prepared wave packet moves outward and returns to the Franck-Condon region at about 1 ps. It is only then, that there is an overlap with the ground-state wave packet and, according to Eq. (6.25), the field  $E_1(t)$  starts deviating from zero. This can be seen in Fig. 6.12, lower panel, which displays the control field. In the calculation, a scaling factor of  $\lambda_1 = 5 \cdot 10^{-3}$  a.u. is employed. At times smaller than 5 ps, one observes a train of pulses with increasing overall intensity. The temporal separation of the peaks reflects the periodicity of the vibrational wave-packet motion in the excited state. The fast oscillations, on the other hand, are determined from phase factors containing the energy difference between excited and ground-state levels [101]. It is thus clearly seen that the dynamics – at each time-step – determines the field, which in turn influences the system to achieve a predefined objective.

The middle panel of Fig. 6.12 shows the ground- and excited-state population, as indicated. They are calculated as

$$P_n(t) = \int_0^\infty dR |\psi_n(R, t) f_w(R)|^2. \quad (6.27)$$

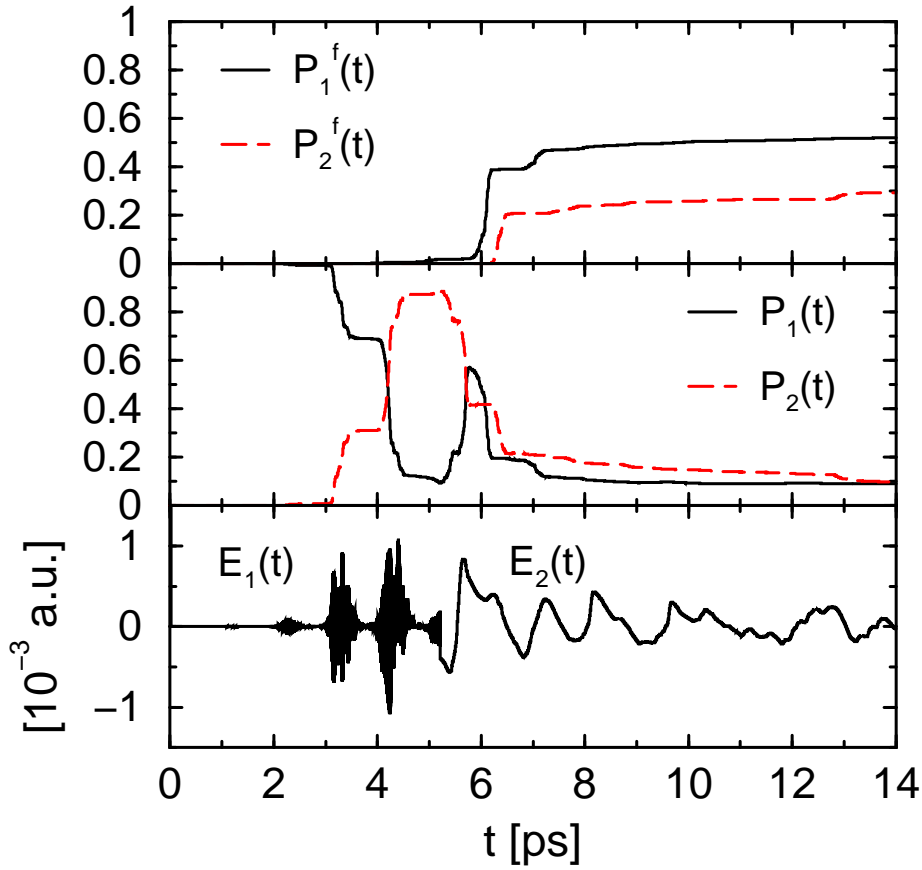


Figure 6.12: Control of excited-state fragmentation by successive application of two fields. The fields are displayed in the lower panel, where  $E_1(t)$  is switched off at 5 ps and  $E_2(t)$  interacts only afterwards. The bound-state population  $P_n(t)$  in the state  $|n\rangle$  ( $n=0,1$ ) are shown (middle panel) as well as the respective fragmentation yields  $P_n^f(t)$  (upper panel).

Here, a window function  $f_w(R)$  is employed which assumes a value of  $f_w(R)=1$  for bond-lengths smaller than  $R_w=22.5 \text{ \AA}$ , and then decreases to zero in an interval of  $2 \text{ \AA}$ . This corresponds to absorbing boundary conditions [123–127]. The ground- and excited-state fragmentation yields are obtained as

$$P_n^f(t) = \int_0^{\infty} dR |\psi_n(R, t) (1 - f_w(R))|^2. \quad (6.28)$$

As can be taken from Fig. 6.12, the ground-state population  $P_1(t)$  decreases in steps, which is accompanied by the increase of  $P_2(t)$ . This takes place until a time of  $\sim 5$  ps when the excited state is populated to 89 %. Afterwards, the field  $E_1(t)$

is artificially switched off and the second field  $E_2(t)$  is turned on. The latter is determined from Eq. (6.26) with a scaling factor of  $\lambda_2 = 2 \cdot 10^{-5}$  a.u. Around 6 ps, the excited-state population drops which, however, is not due to excited-state fragmentation. Instead transitions to the ground state are induced by both, the potential- and the field coupling, where the latter induces most of the transfer. As a consequence, the ground-state population first increases and then decreases, when predissociation becomes effective. This can be taken from the ground-state fragmentation yield  $P_1^f(t)$  shown in the upper panel of Fig. 6.12. Shortly after 6 ps, the heating field  $E_2(t)$  which follows the vibrational wave packet motion in the excited state, has pumped enough energy into the system, that excited-state fragmentation can – partly – take place. The yield  $P_2^f(t)$  increases and settles to about 30 % asymptotically. The remaining population is trapped in the ground state or, in the long-time limit, undergoes ground-state dissociation.

Now, the case where the total control field  $E(t)$  is composed of both components is discussed, i.e.  $E(t) = E_1(t) + E_2(t)$ . In Fig. 6.13, results are presented where the same scaling factors as in the calculation leading to the results displayed in Fig. 6.12 are employed. Naturally, now the field is of a more complicated structure than before. Therefore, the two components of the total field are displayed separately in the lower panels of the figure. Note, that the field  $E_1(t)$  is constructed to increase the excited-state population and also, the second field  $E_2(t)$  is determined to increase the average energy in the excited state. However, because the sum of both fields interacts with ground- and excited-state molecules, this total field not necessarily is able to accomplish both tasks simultaneously. Thus, the population  $P_2(t)$  does not increase monotonically as can be taken from the figure. At the end of the displayed time interval (15 ps), the ground-state (bound) population  $P_1(t)$  is close to zero, whereas still about 50 % is bound in the excited state. On the other hand, the ground- and excited-state fragmentation yields are equal, see the upper panel of the figure. At longer times (not shown), the yield  $P_2^f(t)$  does not change anymore settling to a yield of 30 %, which means that the effect of the perturbation by the external field is negligible. On the other hand, due to the non-adiabatic coupling, the still bound parts of the wave packet  $\psi_1(t)$  end up in the predissociation channel, so that  $P_1^f(t)$  keeps growing. As compared to the case treated before, the simultaneous action of the control fields results in roughly the same target-state population.

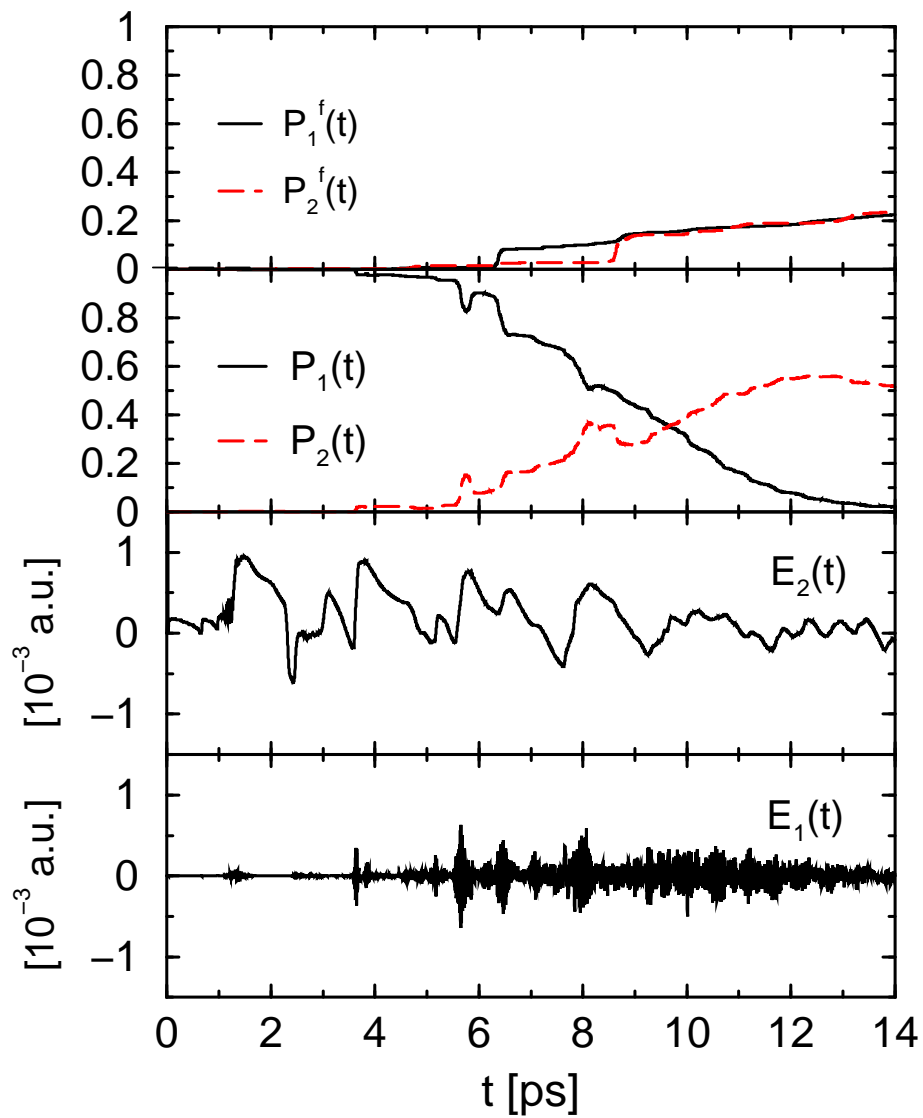


Figure 6.13: Control of excited-state fragmentation by simultaneous application of fields. Shown are the time-dependent dissociation yields in the two electronic states (upper panel), the bound state fractions  $P_n(t)$ , and the two electric field components (lower panels).

The branching ratio can be modified by changing the intensity of the two field components  $E_n(t)$ . In fact, the values of the strength parameters  $\lambda_1$  and  $\lambda_2$  are the only free parameters in the algorithm of local control. In what follows, we only discuss the case where the scaling factor  $\lambda_1$  is increased by a factor of two ( $\lambda_1 = 1 \cdot 10^{-2}$  a.u.). The results of the respective calculation are collected in Fig. 6.14. Here,



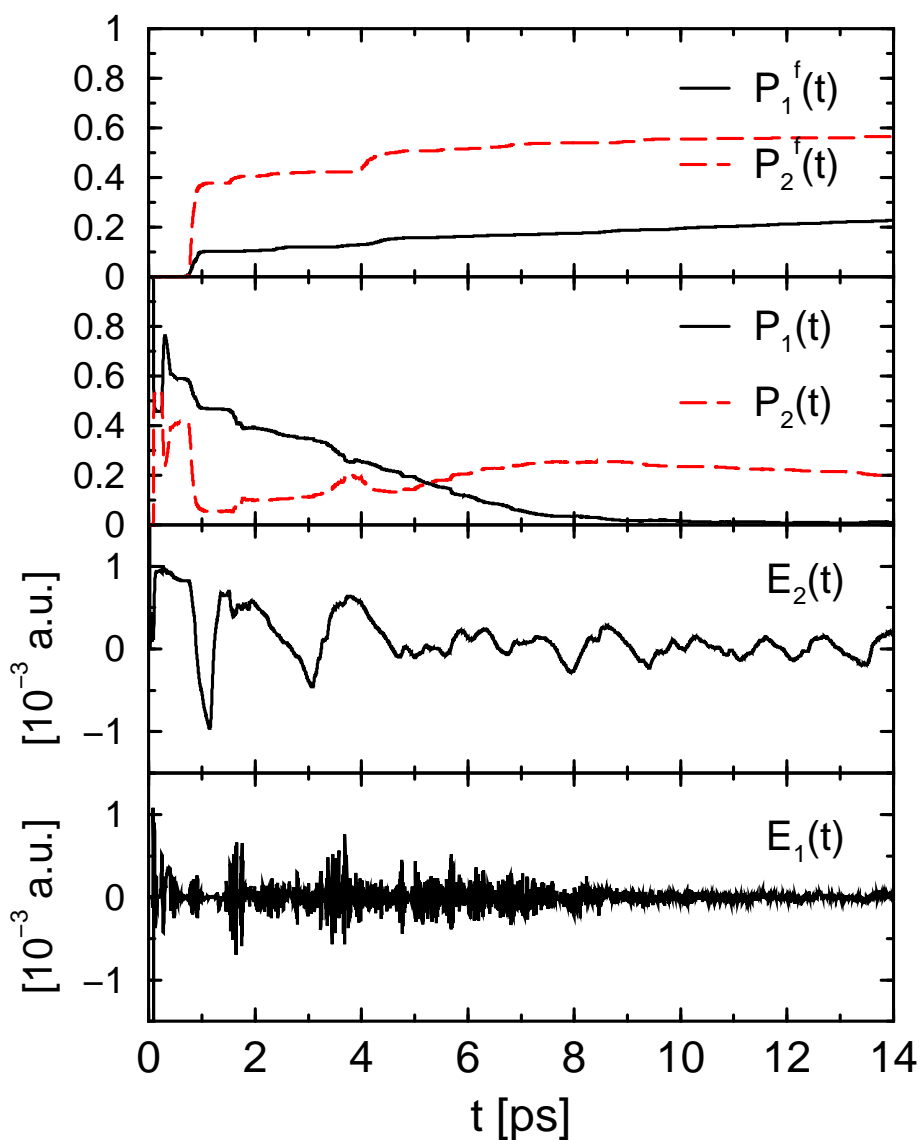


Figure 6.14: Same as Fig. 6.13 but for a larger scaling factor  $\lambda_1$ .

already at early times, a large population transfer between the two electronic states takes place. Also, fragmentation sets in shortly after 1 ps. The target channel then is populated to about 50 % asymptotically. Additional calculations show, that also in the case of the sequential application of the two control fields, the chosen value of  $\lambda_1$  results in the production of half of the molecules in the excited-state fragmentation channel. Various calculations were performed with different values of both parameters  $\lambda_n$  and found that, within the parameter range investigated, the yield was never substantially larger than 50 %. Although an exploration of parameter

space or the use of other control schemes might lead to higher yields, this number is to be considered as excellent.

# 7 Vectorial properties: ro-vibrational dynamics in external fields

The role of the rotational degree of freedom is pursued in the following. The regarded systems now include explicitly vectorial properties like e.g. the orientation of a molecule in the laboratory. First in this chapter, the ro-vibrational dynamics of sodium iodide is investigated in static electric fields. The second part deals with the interplay of rotations and local control theory.

In general, one distinguishes molecular orientation and alignment. Formally, orientation can be described by an arrow pointing in a certain direction, while alignment refers to a situation, where a double-headed arrow reflects the circumstances. In the latter case, a distinction between head and tail is impossible. Orientation is achieved e.g. by static electric fields, whereas laser fields usually only create alignment due to their oscillatory nature.

## 7.1 Predissociation in a static electric field

In this section, the rotational-vibrational dynamics of sodium iodide in a static electric field is investigated. Therefore, the same potential curves and dipole moments as in the previous chapter 6 are used. There, it was shown, that the electronic ground state of NaI is of ionic character and, accordingly, has a large permanent dipole moment. As a consequence, when an electric field is applied, a large torque is experienced by those molecules which are not oriented along the field direction. This makes the molecule an ideal candidate to study orientation effects induced by external fields [59, 130–132]; for an overview on recent efforts to align molecules, see the article by Stapelfeldt and Seideman [58].

In a former study, the rotational-vibrational dynamics of NaI in a static electric field after femtosecond excitation was investigated [133]. Whereas the preliminary study ignored the predissociation channel, the present work aims at a complete description of the dynamics including the coupling to the dissociation continuum.

### 7.1.1 The model system

The pump excitation prepares a wave packet in the covalent branch of the excited-state potential. Because of the vanishing dipole moment, it performs an unperturbed motion until the crossing region is reached. Then, moving to larger distances in the ionic branch, a strong perturbation by the external field is switched on. This modulation of the interaction energy with the vibrational period resembles a train of ‘half cycle pulses’ [133]. Note, that despite this resemblance, the Hamiltonian is time-independent after the pump laser is switched off. The calculations are performed to simulate polarization sensitive real-time measurements, which are able to detect the orientational dynamics.

The present model consists of three electronic states  $|n\rangle$  ( $n=1,2,3$ ). The respective adiabatic potential energy curves  $V_n^a(R)$  are displayed in Fig. 6.1, left-hand side (p. 54). In the numerical treatment, intersecting (diabatic) potential curves  $V_n^d(R)$  are used (see Fig. 7.1). Additionally, an off-diagonal potential matrix element  $V_{12}(R)$  is introduced to account for the coupling between the ground state and the first excited state.

The potentials and the corresponding wave functions are related by unitary transformations with the matrix  $\mathbf{A}$  diagonalizing the diabatic potential matrix:

$$\mathbf{A} = \begin{pmatrix} \cos \gamma(R) & -\sin \gamma(R) \\ \sin \gamma(R) & \cos \gamma(R) \end{pmatrix}, \quad (7.1)$$

where the function  $\gamma(R)$  is given as

$$\gamma(R) = \frac{1}{2} \arctan \left( \frac{2V_{12}(R)}{V_1^d(R) - V_2^d(R)} \right). \quad (7.2)$$

The Hamiltonian describing the nuclear motion in the diabatic electronic states  $|1\rangle$  and  $|2\rangle$  reads (atomic units are employed in what follows):

$$\mathbf{H}^d = \begin{pmatrix} T(R) + \frac{j^2}{2mR^2} & 0 \\ 0 & T(R) + \frac{J^2}{2mR^2} \end{pmatrix} + \begin{pmatrix} V_0^d(R) & V_c(R) \\ V_c(R) & V_1^d(R) \end{pmatrix}. \quad (7.3)$$

Here,  $T(R)$  is the nuclear vibrational kinetic energy operator,  $\mathbf{J}$  is the angular momentum operator and  $m$  is the reduced mass.

In a static electric field with field strength  $E_s$  and a polarization vector  $\vec{\epsilon}_s$  pointing along the  $z$ -axis, the Hamiltonian includes the interaction energy in the adiabatic state  $|n\rangle$  as:

$$W_{ns}^a(R, \theta) = -E_s \mu_n^a(R) \cos \theta, \quad (7.4)$$

where  $\mu_n^a(R) \cos \theta$  is the projection of the permanent (adiabatic) dipole moment on the field polarization. The dipole moments  $\mu_n^a(R)$  are displayed in Fig. 6.2, left-hand side (p. 55).

The time-dependent Schrödinger equation is solved for the motion of NaI in the coupled states  $|1\rangle$  and  $|2\rangle$ , interacting with the static electric field. Therefore, the reduced wave function  $\psi(R, \theta, t) = R\Phi(R, \theta, t)$ , where  $\Phi(R, \theta, t)$  is the complete wave function, is represented on a spatial grid in the coordinates  $R$  and  $\theta$ . The short-time propagator is written as

$$\mathbf{U}_{12}^d(\lambda) = e^{\lambda\mathbf{T}(R)/4} e^{\lambda\mathbf{T}(J)/2} e^{\lambda\mathbf{T}(R)/4} (\mathbf{A}^t e^{\lambda\mathbf{V}_s^a(R, \theta)} \mathbf{A}) e^{\lambda\mathbf{T}(R)/4} e^{\lambda\mathbf{T}(J)/2} e^{\lambda\mathbf{T}(R)/4}, \quad (7.5)$$

where  $\lambda = -i\Delta t$  and  $\Delta t$  is a short time step. The matrices appearing in the exponentials have the following elements:

$$(\mathbf{T}(R))_{nm} = -\frac{1}{2m} \frac{\partial^2}{\partial R^2} \delta_{nm}, \quad (7.6)$$

$$(\mathbf{T}(J))_{nm} = \frac{\hat{J}^2}{2mR^2} \delta_{nm}, \quad (7.7)$$

$$(\mathbf{V}_s^a(R, \theta))_{nm} = \{V_n^a(R) - E_s \mu_n^a(R) \cos \theta\} \delta_{nm}. \quad (7.8)$$

This splitting of the propagator is exact to the order of  $(\Delta t)^3$  [55].

In applying the propagator to the diabatic wave functions, the action of the operators containing  $\mathbf{T}(R)$  is evaluated in momentum space [53]. In order to apply the exponential kinetic angular operator  $e^{\lambda\mathbf{T}(J)/2}$ , the coordinate space wave function, at each time step, is expanded into spherical harmonics  $Y_{J,0}(\theta, 0)$  as

$$\psi_n^d(R, \theta) = \sum_J a_{nJ}^d(R) Y_{J,0}(\theta, 0), \quad (7.9)$$

so that each expansion coefficient is multiplied by  $e^{\lambda J(J+1)/(2mR^2)}$ . Afterwards, a re-summation is performed. The action of the exponentials containing the potential-

and interaction energy amounts to a multiplication of the spatial wave function by phase factors at each grid point. To avoid reflections at the grid boundary, an optical potential is introduced in the dissociation channel [123–127].

The propagation scheme yields time-dependent wave functions  $\psi_n^k(R, \theta, t)$  ( $k = a, d; n = 1, 2$ ) in the two adiabatic/diabatic states of the molecule. Below, radial densities are regarded which are defined as

$$\rho_n^k(R) = 2\pi \int d\theta \sin \theta |\psi_n^k(R, \theta, t)|^2. \quad (7.10)$$

Likewise, angular densities are defined as

$$\rho_n^k(\theta) = \int dR \sin \theta |\psi_n^k(R, \theta, t)|^2. \quad (7.11)$$

Instead of inspecting the coordinate- and time-dependent wave functions, the dynamics of the system is much simpler illustrated in terms of the above defined densities.

The quantum dynamics of NaI is followed in real time using a pump-probe scheme as sketched in Fig. 7.1. In a first step, a vibrational wave packet is prepared upon

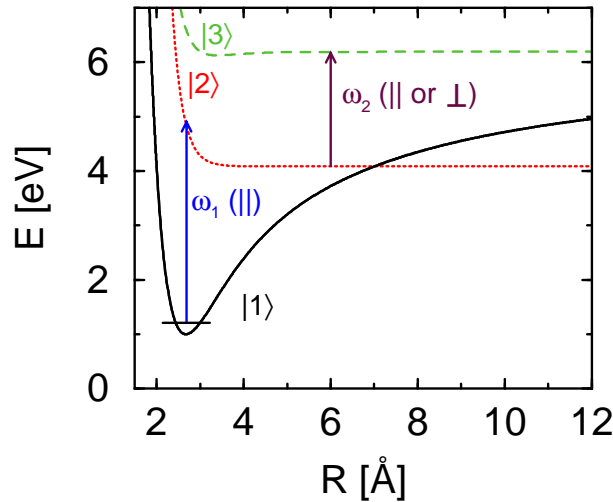


Figure 7.1: Pump-probe scheme of NaI. Transitions are induced by pulses with frequencies  $\omega_1$  and  $\omega_2$ , where the latter pulse can be polarized either parallel (||) or perpendicular ( $\perp$ ) to the molecular axis.

one-photon absorption described within first-order perturbation theory:

$$\begin{pmatrix} \psi_1^d(R, \theta, t) \\ \psi_2^d(R, \theta, t) \end{pmatrix}^t = \frac{E_1^0}{2i} \mathbf{U}_{12}(t) \int_{-\infty}^{\infty} d\tau g_1(\tau) e^{-i\omega_1\tau} \mathbf{U}_{12}(-\tau) \vec{\epsilon}_1 \vec{\mu}_{12} \begin{pmatrix} e^{-iE_{10}\tau} \psi_{10}(R, \theta) \\ 0 \end{pmatrix}. \quad (7.12)$$

The pump pulse is characterized by its field strength  $E_1^0$ , polarization vector  $\vec{\epsilon}_1$ , frequency  $\omega_1$  and the pulse shape  $g_1(\tau)$ . The initial wave function  $\psi_{10}(R, \theta)$  of energy  $E_{10}$  is an eigenstate of the ground-state Hamiltonian including the interaction with the external field (see Sec. 7.1.2), and  $\vec{\mu}_{12}$  denotes the transition dipole-moment for the  $|2\rangle \leftarrow |1\rangle$  electronic transition.

At time  $T$ , the probe pulse induces a transition to the electronic state  $|3\rangle$ , see Fig. 7.1. The wave function in the latter state is as well determined within first-order perturbation theory. This is appropriate because weak fields and non-overlapping pulses are regarded. In calculating the transient signals only probe transitions originating in state  $|2\rangle$  are included so that one finds

$$\psi_3^d(R, \theta, t) = \frac{E_2^0}{2i} U_3(t - T) \int_{-\infty}^{\infty} d\tau g_2(\tau) e^{-i\omega_2\tau} U_3(-\tau) \begin{pmatrix} 0 \\ \vec{\epsilon}_2 \vec{\mu}_{23} \end{pmatrix} \mathbf{U}_{12}(\tau) \begin{pmatrix} \psi_1^d(R, \theta, T) \\ \psi_2^d(R, \theta, T) \end{pmatrix}, \quad (7.13)$$

where the probe-pulse parameters are labeled with index 2. The pump-probe signal, consisting of the total fluorescence from state  $|3\rangle$ , is assumed to be proportional to the population in that state yielding the signal

$$S(T) = \langle \psi_3^d(R, \theta, T) | \psi_3^d(R, \theta, T) \rangle, \quad (7.14)$$

where the bra-kets denote integration over the coordinates  $R$  and  $\theta$ . In calculating the signals  $S(T)$ , all transition dipole moments are set to a constant (Condon approximation).

For the polarizations of pump- and probe lasers, two configurations are considered. In the first one ( $\parallel$ ), the polarization vectors of both pulses are parallel to  $\epsilon_s$ .

Alternatively, the second configuration ( $\perp$ ) corresponds to a pump laser polarized along the  $z$ -axis and a probe laser polarized perpendicular to this direction. Thus, for the pump-transitions one has  $\vec{\epsilon}_1 \vec{\mu}_{12} = \mu_{12} \cos \theta$ , which enters into Eq. (7.12). Because the  $|3\rangle \leftarrow |2\rangle$  transition is a parallel transition, Eq. (7.13) contains the scalar products

$$\vec{\epsilon}_2 \vec{\mu}_{23} = \mu_{23} \cos \theta \quad (\parallel), \quad (7.15)$$

$$\vec{\epsilon}_2 \vec{\mu}_{23} = \mu_{23} \sin \theta \cos \varphi \quad (\perp), \quad (7.16)$$

for parallel and perpendicular pump-probe arrangements, respectively. Thus, dependent on the relative choice of the laser polarization vectors, two different pump-probe signals  $S_{pp}$  ( $pp = \parallel, \perp$ ) are obtained.

The above is directly valid, when the parallel arrangement is encountered. For the perpendicular case, actually it would be necessary to consider the Euler angle  $\varphi$  and the quantum number  $m_l$ , but this can be circumvented by a neglect of the kinetic energy during the probe pulse. Within this approximation, it is assumed, that the orientation of the molecule is fixed during the short probe interaction. The term, where the kinetic energy is ignored, is defined as approximation function  $I$ . Thus, Eq. (7.13) can be rewritten as

$$\begin{aligned} \psi_3^d(R, \theta, t) &= \psi_3^a(R, \theta, t) \approx \vec{\epsilon}_2 \vec{\mu}_{23} \psi_2^a(R, \theta, T) \int_{-\infty}^{\infty} d\tau g_2(\tau) e^{i(V_3(R) - (V_2^a(R) - W_{2s}^a(R, \theta)) - \omega_2)\tau} \\ &= \vec{\epsilon}_2 \vec{\mu}_{23} \psi_2^a(R, \theta, T) I(R, \theta, T), \end{aligned} \quad (7.17)$$

where the solution to the approximated integral is

$$I(R, \theta, T) = \sqrt{\frac{\pi}{\alpha_2}} e^{-\frac{(V_3(R) - (V_2^a(R) - W_{2s}^a(R, \theta)) - \omega_2)T}{4\alpha_2}} \quad (7.18)$$

with  $\alpha_2$  being the exponential factor from the gaussian envelope function  $g_2$ .

Now, the signal from the parallel pump-probe arrangement is easily obtained as

$$S_{\parallel}(T) = \boxed{2\pi} \int_0^{\pi} \sin \theta d\theta \int_0^{\infty} dR \boxed{\cos^2 \theta} |I(R, \theta, T) \psi_2^a(R, \theta, T)|^2, \quad (7.19)$$

which yields exactly the same curve as calculated within pure perturbation theory, apart from a proportionality factor (differences to  $S_{\perp}(T)$  have been emphasized



with boxes).

Thus, also the signal from the perpendicular case can be evaluated using  $I(R, \theta, T)$ . Here, neither  $\psi_2^a$  nor  $I$  depend on the Euler angle  $\varphi$ . The only remaining term is  $\cos \varphi$  from the projection of the dipole moment on the polarization vector (see Eq. (7.16)). According to

$$\int_0^{2\pi} d\varphi \cos^2 \varphi = \left[ \frac{1}{2}\varphi + \frac{1}{4} \sin(2\varphi) \right]_0^{2\pi} = \pi \quad (7.20)$$

integration over the whole space yields a factor  $\pi$  instead of  $2\pi$ , as before. For the signal of the perpendicular arrangement, this leads to

$$S_{\perp}(T) = \boxed{\pi} \int_0^{\pi} \sin \theta \, d\theta \int_0^{\infty} dR \boxed{\sin^2 \theta} |I(R, \theta, T) \psi_2^a(R, \theta, T)|^2. \quad (7.21)$$

In order to experimentally detect the degree of molecular orientation, a polarization sensitive experiment is suggested. If, for a fixed pump-pulse polarization and time-delay, a probe excitation within the parallel and also perpendicular configuration is performed, the ratio of the two signals is determined as

$$A(T) = \frac{S^{\parallel}(T) - 3S^{\perp}(T)}{S^{\parallel}(T) + 3S^{\perp}(T)}. \quad (7.22)$$

The definition of the signal ratio  $A(T)$  accounts for the following situation: in the field-free case and starting from the rotational ground state before the pump-excitation, the signal  $S^{\parallel}$  is a factor of 3 larger than the signal  $S^{\perp}$ , so that  $A(T)$  vanishes identically. The reason for the factor of 3 is easily found, when the distribution of the wave function  $\psi_2^a$  in  $\theta$  is considered. Due to starting in  $J = 0$  in the groundstate, the selection rule  $\Delta J = \pm 1$  leads to  $\psi_2^a$  being localized completely in  $J = 1$ , which is proportional to  $\cos \theta$ . With Eqs. (7.19) and (7.21), the following proportionalities emerge for the fieldfree case:

$$S_{\parallel} \sim 2\pi \int_0^{\pi} d\theta \sin \theta \cos^2 \theta |\cos \theta|^2 = \frac{12}{15}\pi \quad (7.23)$$

$$S_{\perp} \sim \pi \int_0^{\pi} d\theta \sin^3 \theta |\cos \theta|^2 = \frac{4}{15}\pi, \quad (7.24)$$

where the factor of 3 is obvious. This is, however, different in the case where the molecule is pre-oriented in the static field, see the discussion in the next section. For a perfect orientation the signal  $S^\perp(T)$  is identically zero and  $A(T)$  assumes a value of one.

### 7.1.2 Pendular states

The large dipole moment of NaI in its electronic ground state leads to a strong orientation, if an external electric field is applied. The molecular eigenfunctions

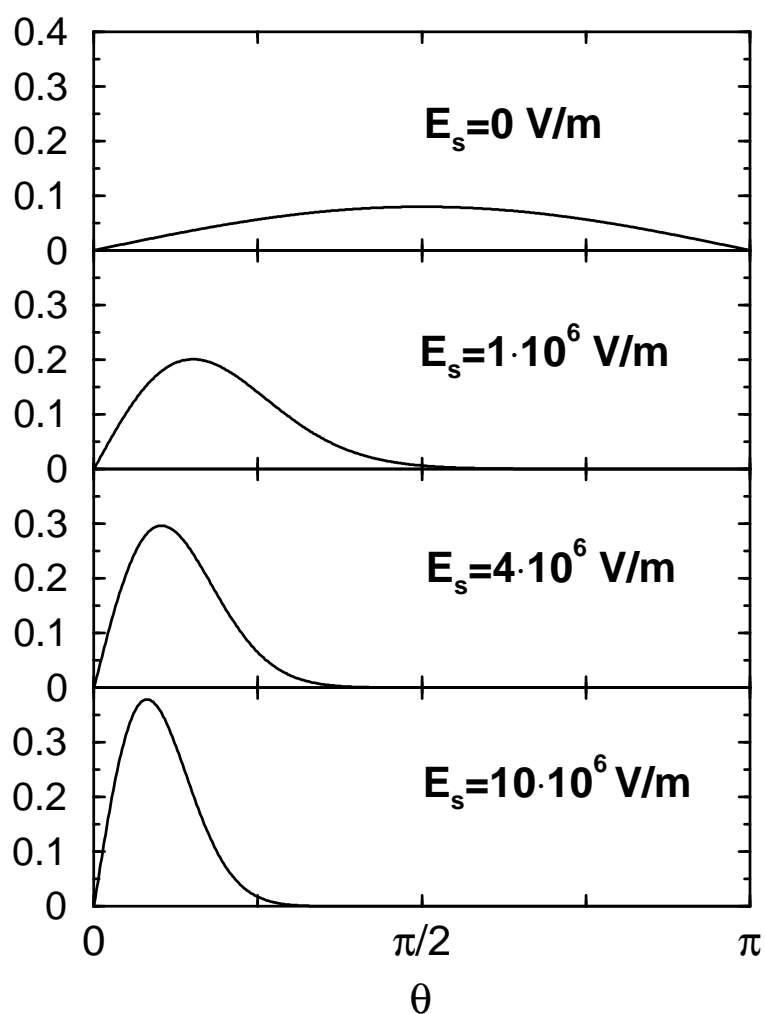


Figure 7.2: Angular densities in the electronic ground state, calculated for different field strengths, as indicated. With increasing field strength, the degree of orientation in the direction of the applied static field ( $\theta = 0$ ) increases.

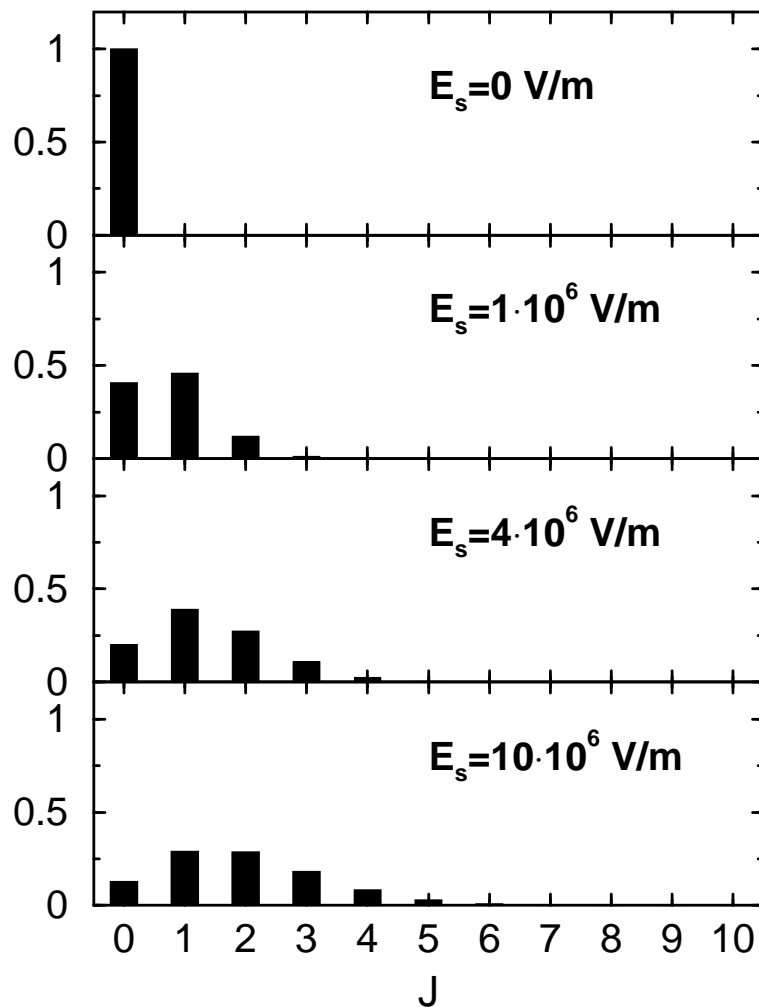


Figure 7.3: Decomposition of the ground-state wave function in the static field in terms of free rotor states with quantum number  $J$ . With increasing field strength, the number of populated rotor states increases.

in the field, concerning the angular degree of freedom, are linear superpositions of free-rotor states, i.e. pendular states [134].

To demonstrate the influence of the static field on the eigenfunctions of NaI, the stationary Schrödinger equation

$$\{T(R) + T(J) + V_1^a(R) + W_s^a(R, \theta)\} \psi_1^a(R, \theta) = E \psi_1^a(R, \theta), \quad (7.25)$$

is solved for various values of the field strength  $E_s$  yielding different ground-state wave functions  $\psi_{10}^a(R, \theta)$  with energies  $E_0$ . The orientational effect caused by the external field is illustrated in Fig. 7.2 containing ground-state angular densities as

defined in Eq. (7.11). Because, for zero field strength, the ground state is spherically symmetric, the density exhibits a  $\sin\theta$ -distribution. Already for a moderate field of  $1 \cdot 10^6$  V/m, the maximum of the density shifts to values below  $45^\circ$  and with increasing field strength the distribution is confined to smaller angles. Employing the decomposition of Eq. (7.9) for the adiabatic ground-state wave function, the populations in different angular momentum states  $Y_{J,0}$  is calculated as

$$P_{0J}^a = \int dR |a_{0J}^a(R)|^2. \quad (7.26)$$

The populations  $P_{0J}^a$  are calculated for the set of field strengths indicated in Fig. 7.3. It is found that, in going from the unperturbed case ( $E_s = 0$ ), where only the  $J=0$  state is populated, to high field strength, the  $J$ -distribution becomes broader. For a field strength of  $E_s = 10 \cdot 10^6$  V/m, seven angular momentum states are populated having a distribution with a maximum at  $J=2$ . Thus, the superposition of more and more angular free-rotor states goes along with the preparation of a rotational wave packet, i.e. an object localized in the angular degree of freedom.

### 7.1.3 Quantum dynamics

The coupled rotational, vibrational and predissociation dynamics of NaI in static electric fields is discussed in the following. First, a field strength of  $10 \cdot 10^6$  V/m is considered. Femtosecond excitation with a 50 fs Gaussian pulse at 310 nm produces a ro-vibrational wave packet performing a quasi-bound motion in the coupled electronic states  $|1\rangle$  and  $|2\rangle$ . The respective (diabatic) radial densities are depicted in Fig. 7.4.

They do not deviate much from those calculated in the field-free case discussed in former work [118], indicating that the vibrational dynamics is not influenced strongly by the external field. At early times, one observes a vibrational motion which is accompanied by a loss of probability density into the dissociation channel. Due to the off-diagonal potential coupling a population transfer between the two electronic states occurs twice every vibrational period. After several picoseconds, the wave packet has spread and fills the entire upper adiabatic potential.

The angular density dynamics is illustrated in Fig. 7.5. Initially, the dis- and re-appearance of density in the respective states reflects the curve-crossing vibrational dynamics. It is seen that at a time of  $\sim 5.5$  ps, the orientation is strongest

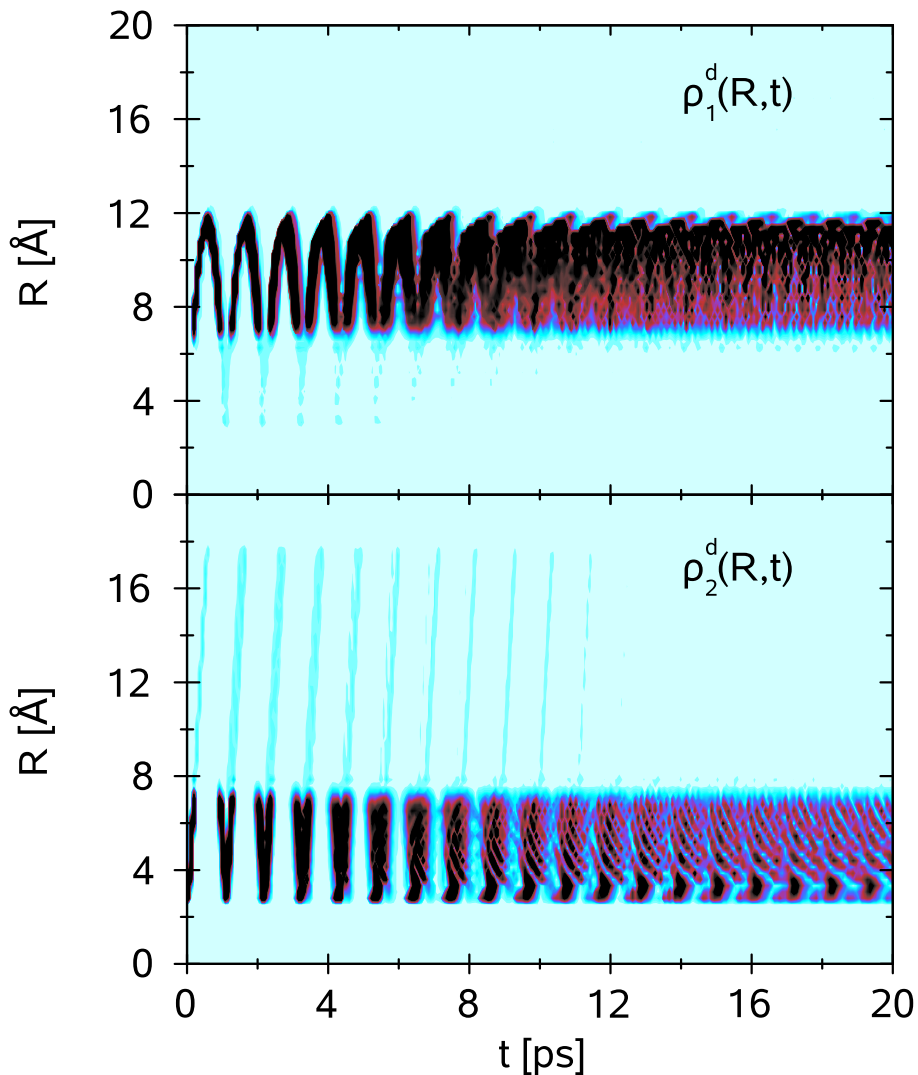


Figure 7.4: Dynamics of radial densities in the diabatic ground state  $|1\rangle$  and excited state  $|2\rangle$ , calculated for a static field strength of  $10 \cdot 10^6$  V/m. The vibrational motion is accompanied by a predissociation process.

but then, the angular distribution broadens again. A second focusing at small angles can be observed shortly after 16 ps. Thus, the angular densities exhibit a rotational motion with a period of about 11 ps (for a field strength of  $10 \cdot 10^6$  V/m). For a weaker external field the time-scale for the rotational motion changes. At a value of  $E_s = 4 \cdot 10^6$  V/m, the rotational period increases to about 18 ps, and the density is broader as compared to the situation where the stronger field is present. With increasing field strength, the Stark effect shifts the energy levels more apart from each other [134] so that the rotational period becomes smaller. In both cases regarded above, the static field potential confines the angular motion

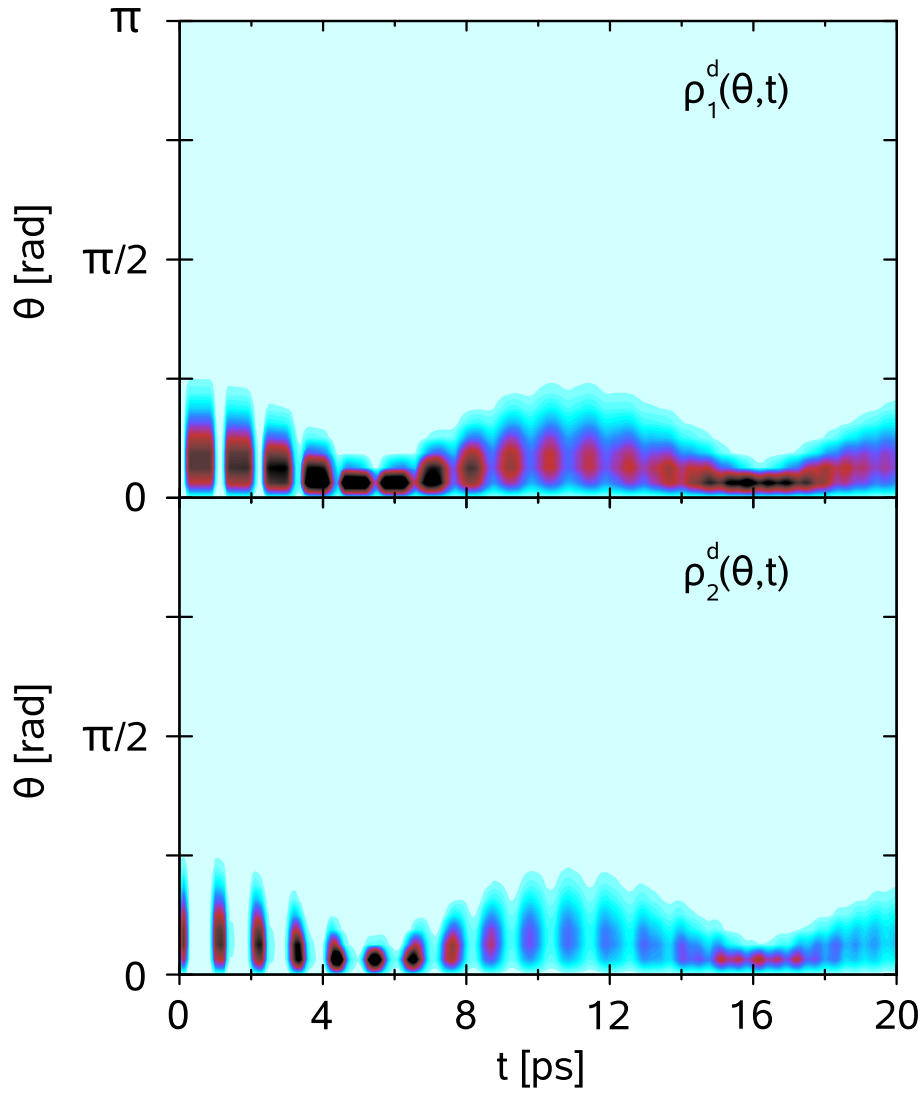


Figure 7.5: Dynamics of the angular densities in the diabatic ground and excited state for a static field strength of  $10 \cdot 10^6$  V/m. A rotational motion takes place with an overall period of  $\sim 11$  ps.

drastically so that the strong field limit, where the Stark energies become those of a two-dimensional oscillator, is reached [134].

It is instructive to make contact to the concept of a mean rotational period in terms of free rotor states. Therefore, at any time  $t$ , the state  $J_{max}$  with the maximal population  $P_{1J}^a(t)$  (see Eq. (7.26)) and period

$$T_{free} = \frac{2\pi}{E(J_{max}) - E(J_{max} - 1)} = \frac{2\pi m \langle R(t) \rangle_1^2}{J_{max}}, \quad (7.27)$$

is calculated, where  $E(J)$  is the rotational energy for the quantum number  $J$  and  $\langle R(t) \rangle_1$  is the expectation value of the vibrational coordinate in state  $|1\rangle$ .

In Fig. 7.6, several quantities are displayed which together give a complete picture of the quantum dynamics of the system (for a field strength of  $10 \cdot 10^6$  V/m). Panel (a) of Fig. 7.6 contains the expectation value of  $\cos \theta$ , which serves as a measure for orientation. This curve exhibits the periodicity (11 ps) of the pendular motion, as is seen in the angular densities and also in  $J_{max}$ . Thus, around  $t = 5.5$  ps and 16.5 ps maximal orientation is assumed.

As was already shown (see Sec. 7.1.2), maximal orientation corresponds to maximal population of  $J$ -states. Consequently, in panel (d), the time-dependence of the rotational quantum number  $J_{max}$  is depicted. Here, the population of free rotor states varies from  $J_{max} = 2$  to 8, exhibiting the characteristic period of  $\sim 11$  ps.

The average rotational period  $T_{free}$  is shown in panel (c) of Fig. 7.6. It assumes values in the range between 20 ps and 700 ps. The function is modulated with a higher frequency corresponding to the oscillations as seen in the angular densities (Fig. 7.5). The faster oscillations stem from the vibrational motion which enter into  $T_{free}(t)$  via the bond length expectation value  $\langle R(t) \rangle_1$ . To document this relationship the latter is shown in panel (b) of the figure. As is expected classically, at times when the wave packet is located at small bond lengths, a faster rotation occurs which becomes slower with increasing bond length. At times around 20 ps, where a large dispersion of the vibrational wave packet is present, the bond length expectation-value settles to a constant and the vibrational dynamics is no longer reflected in the rotational period.

This classical argumentation is supported in Fig. 7.7, where the expectation values  $\langle \cos \theta \rangle$  and  $\langle R \rangle_1$  are compared to  $R$  and  $\cos \theta$  from a classical trajectory. The field strength is set to  $E_s = 10 \cdot 10^6$  V/m, leading to a libration with a period of  $\sim 11$  ps, as stated above. This pendular motion (Fig. 7.7, upper panel) is modulated with the vibrational period (compare lower panel). While in the classical case the modulation is pertained at all times, it vanishes for the quantum system due to wave packet dispersion.

To summarize the conclusions, which can be taken from Fig. 7.6, the population of different free rotor states  $Y_{J,0}$  varies periodically with time. Accordingly, the rotational period, defined in terms of free rotor states, changes. Also, the vibrational wave-packet motion, modulating the average bond length periodically, influences

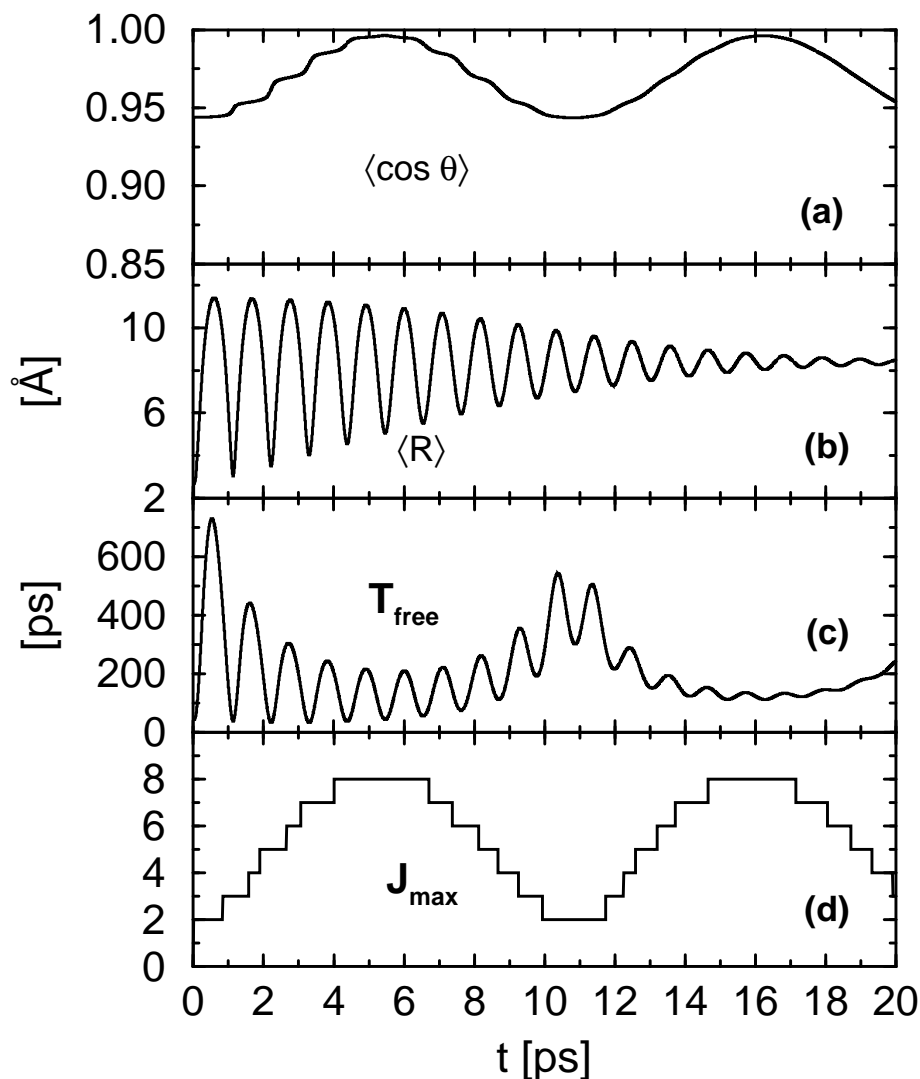


Figure 7.6: Ro-vibrational dynamics in a static field of strength  $10 \cdot 10^6$  V/m: the different panels exhibit various characteristics of the wave-packet motion. Panel (a) shows the expectation value of  $\cos \theta$  which measures the degree of orientation. For a value of  $\langle \cos \theta \rangle = 1$ , perfect orientation along the axis of the applied static field is assumed. The expectation value of  $\cos \theta$  is modulated with the frequency of the vibrational motion, as can be taken from panel (b), containing the bond length expectation-value. The latter also enters directly into the rotational period  $T_{free}$ , assuming values up to 700 ps, is displayed in panel (c). Panel (d) contains the quantum number  $J_{max}$  of the free rotor state with the largest population.



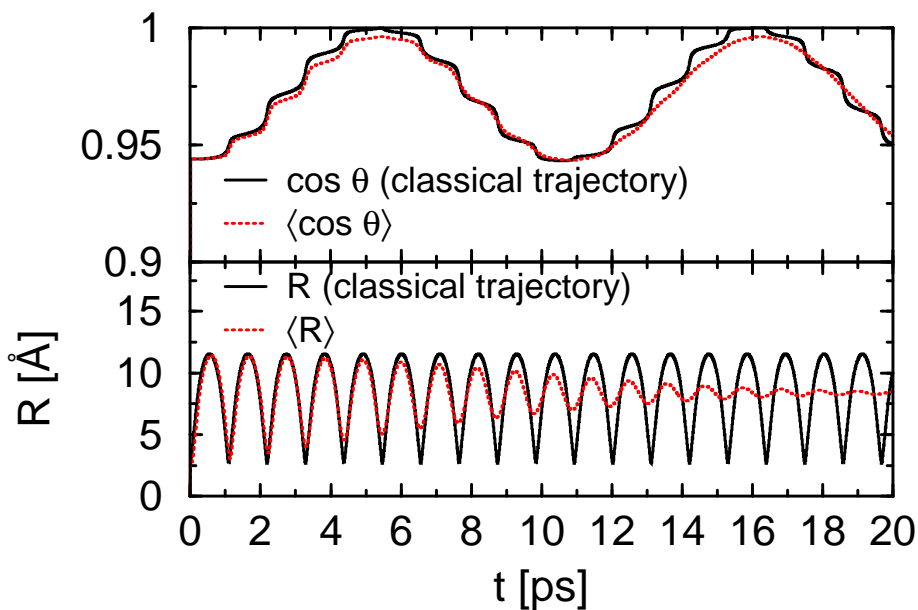


Figure 7.7: Comparison of quantum and classical calculation. The upper panel shows the expectation value of  $\cos \theta$  (dotted/red line) and  $\cos \theta$  from a classical trajectory (solid/black line). Both exhibit a pendular motion, which is modulated with the vibrational period. The latter can be taken from the bond length expectation value (dotted/red line) or the trajectory's  $R$  (solid/black line) displayed in the lower panel.

the free rotor distribution essentially. If many angular momenta are excited, the degree of orientation of the molecule is large, whereas a distribution of only a few rotational states leads to a loss of orientation.

To investigate the influence of the static field on the predissociation yield, the latter is calculated as a function of time and for various field strengths ranging from zero to  $10 \cdot 10^6$  V/m. Higher fields were not regarded because, due to electric charge effects, they cannot be realized for NaI under normal gas-phase experimental conditions [135]. The yield is obtained from the norm of the fraction of  $\psi_1^d$  moving into the dissociation channel. It is found that the predissociation yield is nearly independent of the applied field, for the field strengths regarded. It has to be kept in mind that the employed model assumes that the electronic structure, i.e. the potential curves and non-adiabatic coupling, are independent of the strength of the applied field [136], the latter appearing only in the additional interaction term in the nuclear Hamiltonian.

### 7.1.4 Pump-probe spectroscopy

Pump-probe spectra for the parallel and perpendicular configuration are calculated for a 50 fs pump- and a 10 fs probe pulse at wavelengths of 310 nm and 612 nm, respectively. The spectra are presented in Figs. 7.8-7.9 for three different field strengths and also the field free case. The figures document that the interaction with the field changes the intensity but not the overall appearance of the transient features. Because the probe-pulse wavelength is chosen such that the bound-state motion of the wave packet is detected, one observes a progression of peaks separated by the mean vibrational period in the upper adiabatic potential well [110, 111]. The

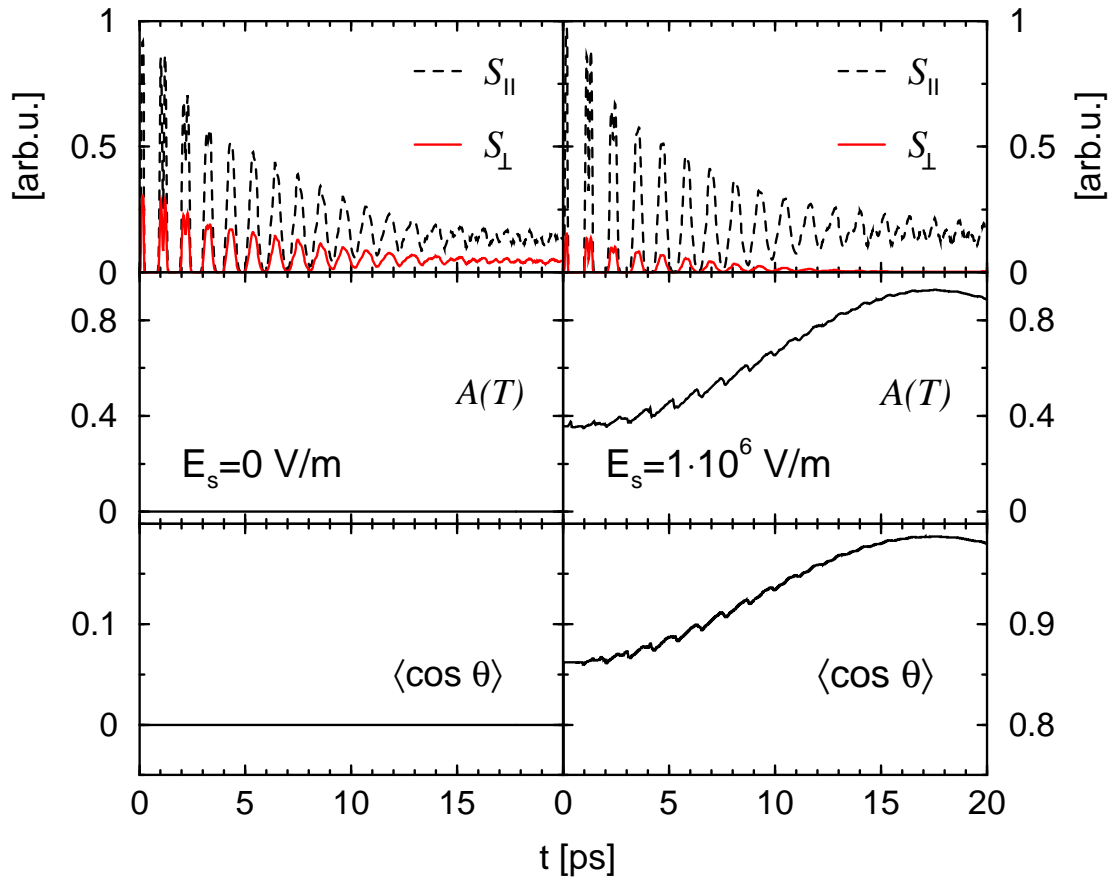


Figure 7.8: Pump-probe spectra calculated for parallel (dashed/black line) and perpendicular (solid/red line) detection geometry are shown in the upper panels for the field free case (left-hand side) and  $E_s = 1 \cdot 10^6$  V/m (right-hand side). In the middle panels, the ratio of the signals  $A(T)$  is displayed and compared to the expectation value of  $\cos \theta$  (lower panels).

peak height decreases due to dispersion of the packet on one hand, and to the loss of probability into the dissociation channel, on the other.

For all field strengths, the signal  $S_{\perp}(T)$  is much smaller than the one obtained in the ( $\parallel$ ) configuration but the shapes of the curves are very similar. With increasing field strength the ratio of the signals becomes larger, which is revealed more clearly in the respective middle panels, containing the signal ratio  $A(T)$  defined in Eq. (7.22). Because the signals are zero for many delay times, the ratio is calculated at the peaks of the transient signals only. It is seen that  $A(T)$  varies as a function of

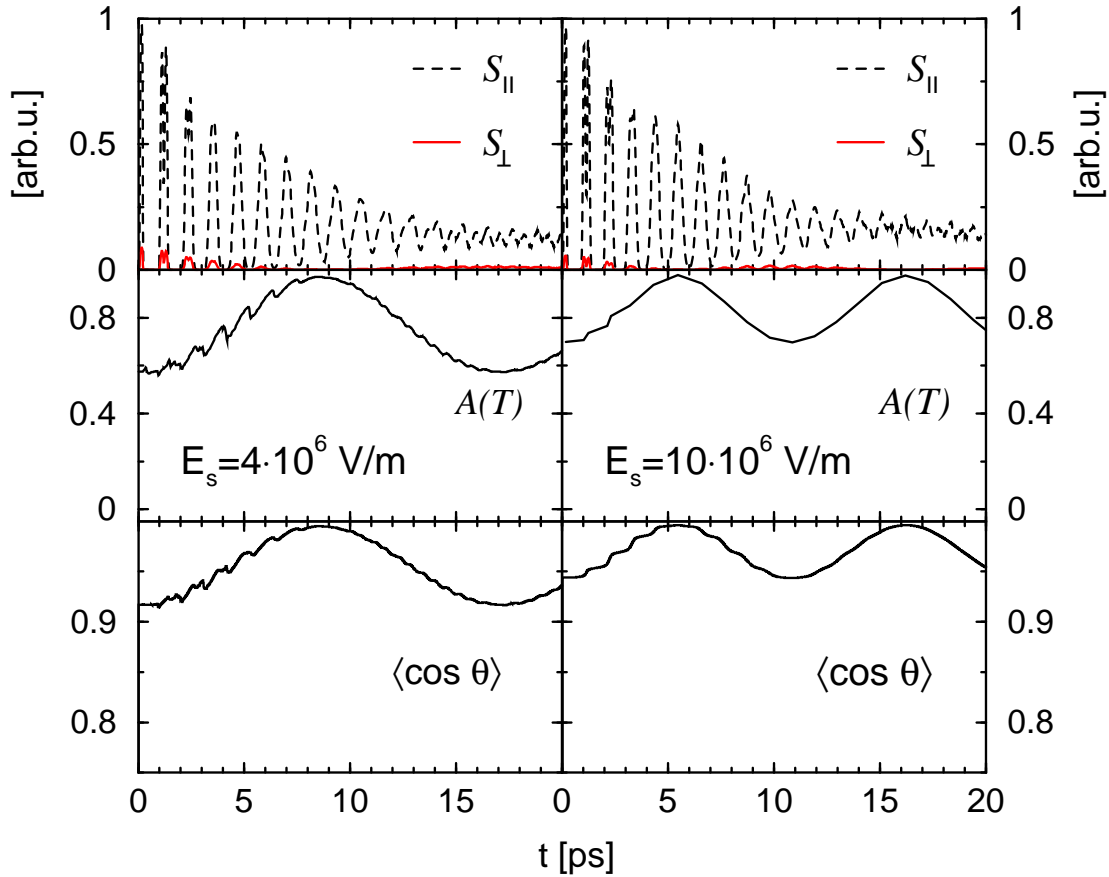


Figure 7.9: The same as Fig. 7.8, but for  $E_s = 4 \cdot 10^6$  V/m (left-hand side) and  $E_s = 10 \cdot 10^6$  V/m (right-hand side). The ratio  $A(T)$  (middle panels) is calculated at the maxima of the transient signals. An excellent agreement with the expectation value of  $\cos \theta$  (lower panels) is found. This proves that the rotational motion can be observed with the suggested polarization sensitive pump-probe setup.

time and maps the pendular motion of the molecule. The time-dependence of the signal ratio directly reflects the degree of orientation, ranging from a perfect orientation ( $A(T)=1$ ) to some field-dependent minimum value. The latter increases with increasing strength of the perturbation due to the pre-orientation of the molecule before the pulse interaction starts. This is also reflected in the expectation value  $\langle \cos \theta \rangle$ , which is displayed in the lower panels for comparison.

Altogether, polarization sensitive pump-probe experiments are simulated, where a time-delayed probe pulse initiates a transition to a higher electronic state and a fluorescence yield is detected as a function of the time delay. Performing such an experiment with probe-pulse polarization vectors chosen to be either parallel or perpendicular to the static field direction leads to different signals. The ratio of the latter directly monitors the rotational motion of the molecule which thus allows for a real-time observation of field induced orientational dynamics.

## 7.2 LCT - the rotational degree of freedom

In chapter 6, it was shown, that active control of elementary processes taking place in molecules can be realized with coherent radiation. There, all studies were performed for a fixed molecular orientation. It could be shown that the obtained fields are very effective in inducing the fragmentation of sodium iodide. Treating the same model system, here the question is asked, in how far this still holds if the rotational degree of freedom is included.

Although several papers discussed the effect of an orientation on the controllability of internal dynamics [103, 137–139], the entanglement of vibrational-rotational motion and control field has not been investigated in much detail. An exception is the work of Hornung and de Vivie-Riedle [140] who studied this interplay in connection with optimal control theory (OCT, see Sec. 4.6).

In this case, local control theory (LCT, see chapter 5) is incorporated in the context

of molecular rotation. As model system, sodium iodide is chosen once more, as the comparison to the previous results is facilitated in this way. The same excitation scheme as on the left-hand side of Fig. 6.3 (p. 56) is applied, where a femtosecond laser pulse ( $E_{12}(t)$ ) prepares an excited-state wave packet in state  $|2\rangle$ . The non-adiabatic coupling which finally leads to the decay of the excited-state complex, is switched off, so that the rotational-vibrational motion only in the adiabatic first excited state is treated. The objective of the control process is to construct a field  $E(t)$ , which pumps energy into the system until dissociation in ionic fragments  $\text{Na}^+$  and  $\text{I}^-$  occurs. Thus, the situation where an infrared (IR) control field interacts with the permanent dipole moment of the molecule in the excited state is investigated.

The Hamiltonians of the unperturbed molecule are of the form (atomic units are employed in what follows)

$$H_n = -\frac{1}{2m} \frac{\partial^2}{\partial R^2} + \frac{\hat{J}^2}{2mR^2} + V_n(R) = T(R) + T(J) + V_n(R), \quad (7.28)$$

where  $V_n(R)$  is the potential energy curve in state  $|n\rangle$  ( $n = 1, 2$ ) (compare also Eq. (3.30), p. 36). As mentioned above, the non-adiabatic coupling present in the molecule around a distance of 7 Å is ignored.

The femtosecond excitation from the initial state  $\psi_i$  in the electronic ground state is treated within first order perturbation theory. For times  $t$  after the pump interaction, the prepared rotational-vibrational wave packet  $\psi_2$  in the excited state reads

$$\psi_2(t) = U_2(t)\psi_2(0) = U_2(t) \left\{ \frac{1}{i} \int_{-\infty}^{+\infty} dt' U_2(-t') W_{12}(t') U_1(t') \psi_i \right\}, \quad (7.29)$$

where  $U_n(t)$  is the propagator for the nuclear motion in state  $|n\rangle$ . The pump-pulse interaction is of the dipole form

$$W_{12}(t) = -\frac{1}{2} \mu_{12} \cos \theta g_{12}(t) e^{-i\omega_{12}t}, \quad (7.30)$$

with the frequency  $\omega_{12}$ , the pulse envelope  $g_{12}(t)$ , and the transition dipole moment  $\mu_{12}$ . The latter is set to a constant in the numerical calculation. The angle  $\theta$  describes the orientation of the dipole moment with respect to the laser field, which

is polarized along the  $z$ -axis.

Defining the objective to induce an effective excited-state fragmentation, a control field is to be determined. The corresponding interaction energy  $W(t)$  is taken as

$$W(t) = -\mu_2(R) \cos \theta E(t), \quad (7.31)$$

where  $\mu_2(R)$  is the modulus of the dipole moment in state  $|2\rangle$ , and  $E(t)$  describes the time dependence of the control field which is polarized along the  $z$ -direction. The dipole moment is parameterized as described in Chap. 6.

For the propagation, the scheme discussed in Sec. 3.5 is used, where the excited-state wave function is expanded in terms of spherical harmonics.

### 7.2.1 Fixed orientation

In order to understand the role of orientation for the purpose of local control, the rotationless case is recalled first. It is formally obtained by fixing the angle  $\theta$  to a constant value  $\theta_0$ . Within this ‘sudden approximation’ [141], the angular momentum term vanishes from  $H_n$  in Eq. (7.28).

As was shown in Sec. 6.1.1, fields constructed from the dynamical response of the system effectively induce an excited-state dissociation, however, under the assumption of a perfect molecular orientation. There, the angle was fixed as  $\theta_0 = 0$  so that the dipole moment was assumed to point along the  $z$ -axis. Molecules, oriented at different angles experience a weaker field. This is the reason why for a randomly oriented sample of molecules the dissociation yield should be drastically decreased, when applying the same fields. In order to seek for new solutions to the extended problem, the coupled rotational-vibrational dynamics is explored in what follows.

### 7.2.2 Rotational-vibrational dynamics

The rotational degree of freedom is now taken into consideration. At first, the efficiency of the control fields obtained for fixed orientation is tested within the extended model. Thus, the fields obtained for  $\lambda = 10 \cdot 10^{-6}$  a.u. (compare Fig. 6.5, p. 59) and the chirped cosine, adapted to fit  $\lambda = 4 \cdot 10^{-6}$  a.u., were employed as

control fields  $E(t)$ . These fields and the corresponding results for the rotational-vibrational dynamics are depicted in Fig. 7.10.

As expected, the dissociation yield decreases, if compared to the cases of fixed

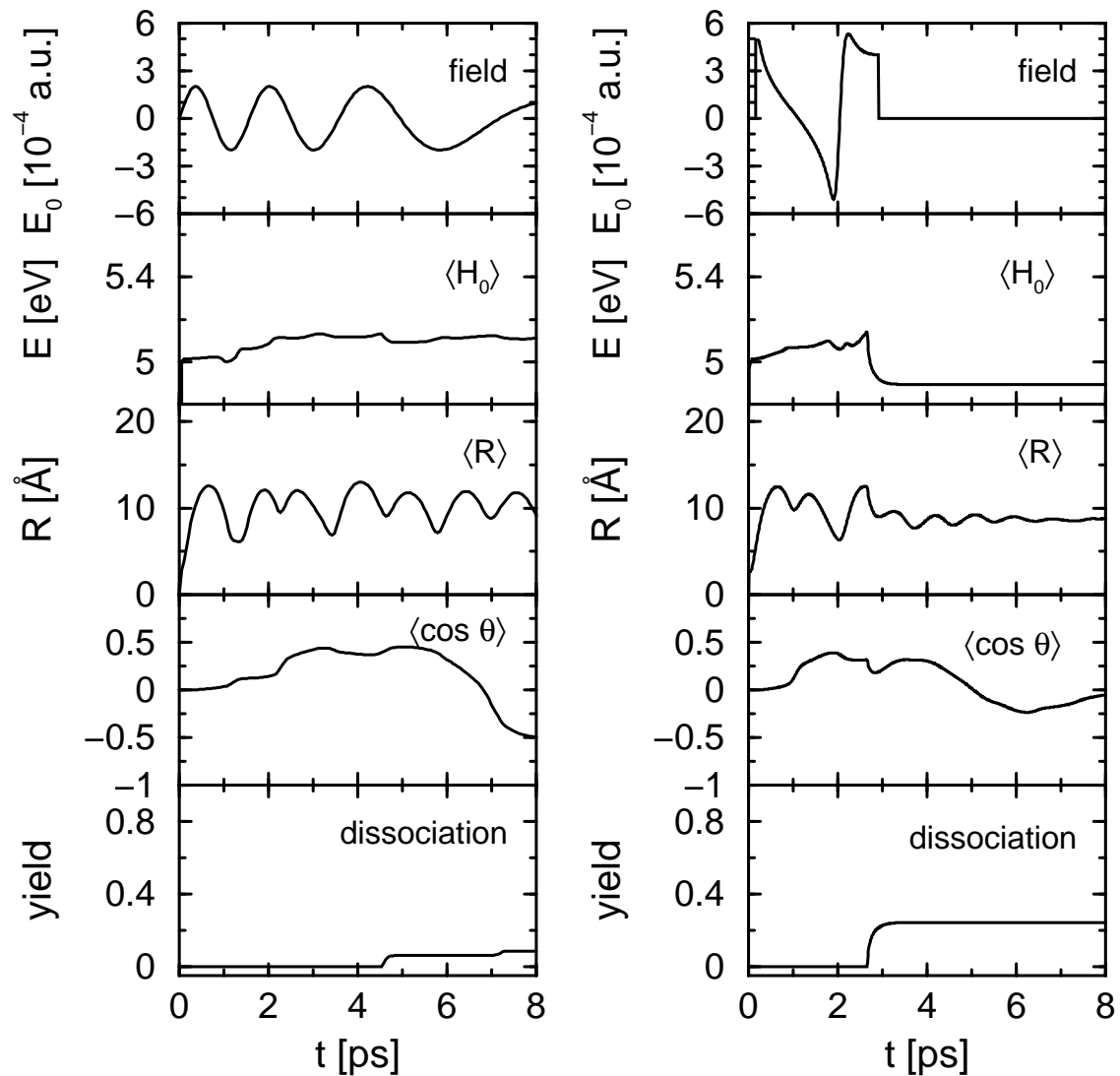


Figure 7.10: Rotational-vibrational dynamics of NaI for control fields obtained from fixed orientation. The upper panels contain the fields as calculated without the rotational degree of freedom (compare Fig. 6.5, p. 59). Here, the cases with  $\lambda = 10 \cdot 10^{-6}$  a.u. (right-hand side) and the chirped cosine fitted to  $\lambda = 4 \cdot 10^{-6}$  a.u. (left-hand side) are displayed. Also shown are the expectation values of the system's energy  $\langle H_0 \rangle$ , of the bond-length  $\langle R \rangle$  and  $\langle \cos \theta \rangle$  in the different cases as indicated. The lower panels display the dissociation yield.

orientation. Especially for  $\lambda = 10 \cdot 10^{-6}$  a.u. (right-hand side, Figs. 6.5 and 7.10), where the fragmentation yield was almost 100 %, now only 24 % of the molecules undergo dissociation. Here, the fragmentation yield is defined as

$$F_{frag}(t) = \int_0^{\infty} dR |\psi_1(R, t) w(R)|^2, \quad (7.32)$$

where  $w(R)$  is a window function assuming a value of zero for  $R \leq R_d = 22.5 \text{ \AA}$  and increasing within  $2 \text{ \AA}$  to a constant value of one for larger distances. In passing, note that a cut-off function ( $w_c(R) = 1 - w(R)$ ) is applied at each time step of the numerical propagation, thus removing the outgoing probability density flux (absorbing boundary conditions [124–126]). The expectation values displayed in the various figures are then only calculated with wave functions located at distances below  $R_d$ . This is the reason why e.g. the expectation value of the system's energy drastically decreases, when dissociation sets in, see  $\langle H_0 \rangle$  on the right-hand side of Fig. 7.10 around 2.7 ps.

Until the beginning of fragmentation, the energy expectation value increases for the regarded fields, also with molecular rotation included in the calculations. Nevertheless, it is already obvious, that the heating is not as effective as in the rotationless cases, because now the increase is not monotonic anymore. Additionally, the expectation value of the bond-length shows a rather complicated structure compared to the clearly increasing amplitude for fixed orientation.

As already mentioned in the last section, the expectation value of  $\cos \theta$  is taken as measure of orientation. This value has of course no counter part in the rotationless calculations. Nevertheless, it is interesting to see, that an orientation is transiently achieved to some extent by the control fields. The reason is, that not only vibrationally excitation is performed, but also higher free-rotor states are excited. Note, that rotational states up to  $J = 290$  are significantly populated for the field with  $\lambda = 10 \cdot 10^{-6}$  a.u. Due to the longer interaction time, states even up to  $J = 360$  are excited by the weaker field fitted to  $\lambda = 4 \cdot 10^{-6}$  a.u.

In order to obtain a higher dissociation yield, the expression leading to the field definition within local control theory has to be adapted to include rotations. It is reasonable, because an energy absorption in the vibrational degree of freedom is responsible for the bond rupture, to use the operator  $H_{vib} = H_1 - T(J)$  in the rate



equation (Eq. (5.1), p. 47) to obtain

$$\begin{aligned} \frac{d\langle H_{vib} \rangle_t}{dt} = & i\langle \psi(t) | [T(J), T(R)] | \psi(t) \rangle \\ & - iE(t) \langle \psi(t) | [\mu_1(R) \cos \theta, T(R)] | \psi(t) \rangle. \end{aligned} \quad (7.33)$$

The first term in the latter equation can be estimated to be negligible (a fact which was checked upon numerically), because it scales with  $1/m^2$  and also, the commutator involves terms scaling with  $R^{-3}$  and  $R^{-4}$ . As a consequence, it is dropped in the construction of the control field. Employing the (linear) properties of the dipole moment (see Chap. 6), one then arrives at the following equation:

$$\frac{d\langle H_{vib} \rangle_t}{dt} = \frac{E(t)}{m} \langle \psi(t) | P \cos \theta | \psi(t) \rangle. \quad (7.34)$$

Starting in an initial rotational eigenstate  $Y_{J,0}$ , the one-photon (weak field) femtosecond excitation from the electronic ground state prepares a linear combination of rotational states with quantum numbers  $J \pm 1$ . It is interesting to note that, as a consequence of this property (see Eq. (3.38)), the energy rate (Eq. (7.34)) is zero initially. The same actually applies as well, if a strong pump pulse is employed. Because only the combined absorption and emission of an odd number of photons leads to a change in the excited-state population, the excited rotational states always belong to quantum numbers which are odd for an initial state with even  $J$  and belong to even values of  $J$  for an odd initial quantum number. The presence of the  $\cos \theta$  then, taking Eq. (3.38) into account, makes the expectation value identical to zero. It is only after the angular dependent interaction due to the (IR) control field has acted for a time, long enough to prepare an excited-state wave packet containing angular momenta with even and odd quantum numbers, the rate starts to deviate from zero. For the construction of the control field it is then not possible to choose the control field according to

$$E(t) = \lambda \langle \psi(t) | P \cos \theta | \psi(t) \rangle \quad (7.35)$$

initially, because then the field remains identically zero. Note that this holds also, if one starts from a thermal distribution of initial rotational states.

As a control field defined according to Eq. (7.35) cannot be applied directly without any auxiliary means, different strategies are discussed. In a straightforward approach, the field is chosen in analogy to the case of fixed orientation as

$$E(t) = \lambda \langle P \rangle_t = \lambda \sum_J \langle \psi_J(R, t) | P | \psi(R, t) \rangle. \quad (7.36)$$

Adopting this construction scheme yields the results presented in Fig. 7.11, where a strength parameter of  $\lambda = 10 \cdot 10^{-6}$  a.u. is employed. At shorter times, the control field (panel (a)) resembles the one found for fixed orientation (see Fig. 7.10). The expectation value of  $\cos \theta$  though demonstrates, that the molecular sample is not oriented (panel (d)). After 2000 fs, oscillations are seen in the field, which hint at a

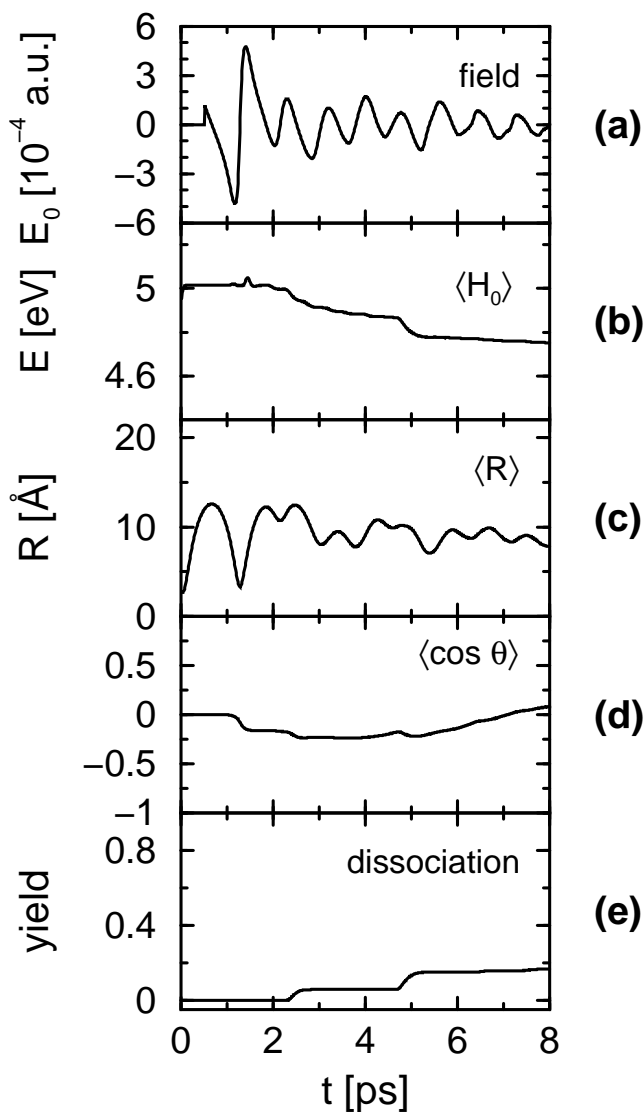


Figure 7.11: Local control including rotational motion. Here the control field (panel (a)) is constructed from the expectation value of the radial momentum operator  $P$ . Panels (b), (c), (d) and (e) show the expectation value of the vibrational Hamiltonian, the bond-length expectation value, the expectation value of  $\cos \theta$  and the fragmentation yield, respectively.

more or less regular variation of the radial momentum. The coordinate expectation value (panel (c)), however, does not support the picture of a vibrational motion performed by a localized wave packet. Also, because its value does not exceed a distance of 15 Å, fragmentation seems not to take place (note, that the cut-off function removes only parts of the wave packet which are localized at distances larger than  $R_d = 22.5$  Å). This is not correct as can be taken from the fragmentation yield displayed in panel (e) of the figure which shows that at 6000 fs 15 % of the molecules have undergone dissociation.

It is noteworthy that, in the average, the energy in the system is decreasing rather than increasing (see panel (b)). A conclusion evolving from Fig. 7.11 is, that the control field constructed via Eq. (7.36) is not efficient in obtaining a good fragmentation yield. Rather, the average effect is, that the field acts as a cooling field, which takes away energy from the system.

In order to illustrate the quantum dynamics in the present case, Fig. 7.12 displays the bound state part of the radial density

$$\rho(R, t) = 2\pi \int d\theta \sin \theta |\psi(R, \theta, t)|^2. \quad (7.37)$$

Note, that the figure exhibits the density also during the time the pump-process takes place. After the process is terminated it is a rather localized function ( $\sim 2$  Å). It can be taken from the figure that after 1700 fs, the density splits into two parts, one part moving out into the dissociation channel and another part performing a bound state motion. The observed splitting explains the partly induced fragmentation. Also, the amplitude of the bound state motion decreases which hints at a loss of vibrational energy. To rationalize the splitting of the wave packet we regard the angular density

$$\rho(\theta, t) = \int dR \sin \theta |\psi(R, \theta, t)|^2, \quad (7.38)$$

which is shown in Fig. 7.12, lower panel. Because the femtosecond excitation from the ground state starts from the  $Y_{0,0}$  rotational eigenstate, the initial excited-state rotational functions is  $Y_{1,0}$ , i.e. proportional to the  $\cos \theta$  function. As an overall trend, one sees that the angular density is depleted for angles lower than  $\pi/2$  and an orientation around  $\pi$  takes place as a function of time. That the angular distribution is directly connected to the splitting of the radial wave packet can be

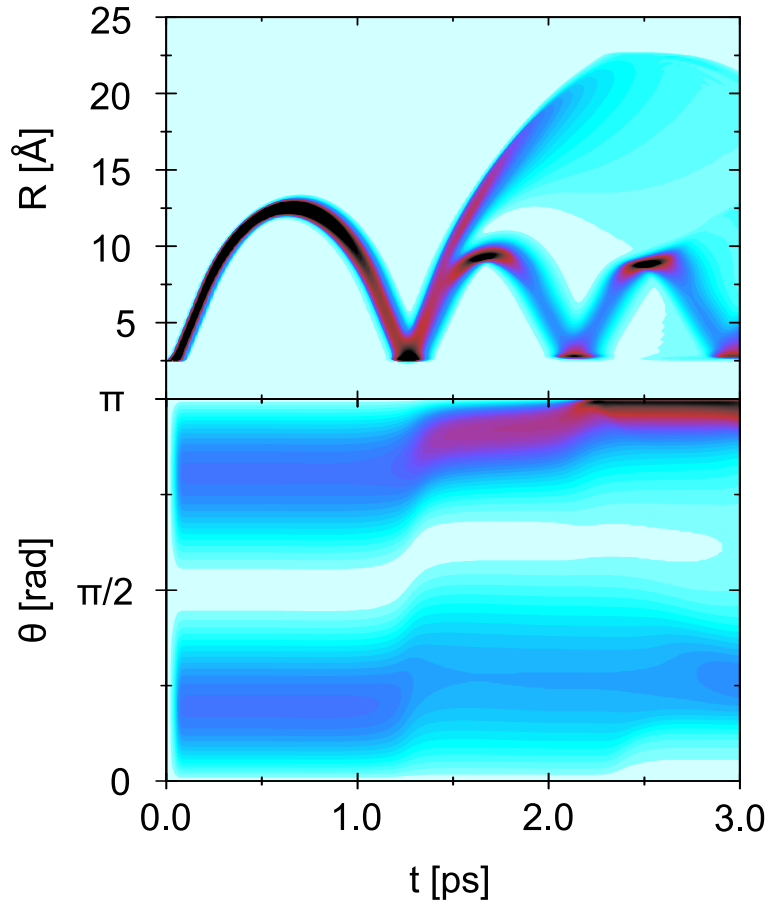


Figure 7.12: Local control including rotational motion. The radial (upper panel) and angular densities (lower panel) are displayed for times up to 3000 fs.

rationalized employing classical arguments. The classical force associated with the external field and acting along the bond coordinate  $R$  is

$$F_R(t) = -\frac{\partial W(t)}{\partial R} = \cos(\theta(t)) P(t), \quad (7.39)$$

where we used  $d\mu_1(R)/dR = 1$  (in atomic units), and  $P(t)$  is the canonical momentum associated with  $R$ . The initial classical distribution in the angular degree of freedom involves angles larger than and smaller than  $\pi/2$ . As a consequence, trajectories starting at angles smaller than  $\pi/2$  (where  $\cos(\theta(t))$  is positive), and moving towards larger distances, experience an additional positive force by the field which, at least partly, induces dissociation. On the other hand, the orbits starting with angles between  $\pi/2$  and  $\pi$ , where  $\cos(\theta(t))$  is negative, experience an attractive force which reduces the radial energy. Thus, in the present example, it is

found that the inclusion of the angular degree of freedom results in a complicated field-molecule energy transfer and the efficiency of the local control algorithm is diminished.

### 7.2.3 Rotational-vibrational dynamics in a static field

Next, the case is discussed, where the control field is constructed from the formula

$$E(t) = E_0 \langle \psi(t) | P \cos \theta | \psi(t) \rangle, \quad (7.40)$$

so that, under the assumptions leading to Eq. (7.34), the energy rate is positive. As is noted above, in order that the expectation value in Eq. (7.40) deviates from zero, it is necessary that rotational eigenstates  $Y_{J,0}$  with even and odd quantum numbers are populated. This can be achieved by applying an additional static electric field to the system resulting in the interaction energy

$$W_{ns} = -\mu_n(R) E_s \cos \theta, \quad (7.41)$$

where  $E_s$  is the field strength and the static field points along the  $z$ -axis. Because of the large dipole moment of the NaI molecule, the interaction leads to a preorientation in the electronic ground state before the femtosecond excitation takes place, i.e. a ‘pendular state’ [134]. This orientation goes in hand with the population of angular momentum states and with increasing field strength  $E_s$ , higher angular momentum states are excited. This, of course, has consequences for the fragmentation dynamics in the control field. Figure 7.13 collects the numerical results obtained for different values of  $E_s$ . Note that the irregularities in the various expectation values stem from the removal of the outgoing flux which leaves only the bound-state fraction of the wave functions for their calculation.

From the energy expectation values, it is seen that with increasing field strength the energy deposition becomes more effective (panel (b)). This is as well reflected in the fragmentation yields displayed in panel (c). In the case of the strongest static field, complete fragmentation is obtained after about 5000 fs, whereas for the weakest field only about 10 % of the molecules dissociate. A comparison with the bond-length expectation values contained in panel (b) shows, that in this case, it needs two and a half vibrational periods until parts of the wave packet have acquired enough energy to escape into the exit channel. The figure demonstrates

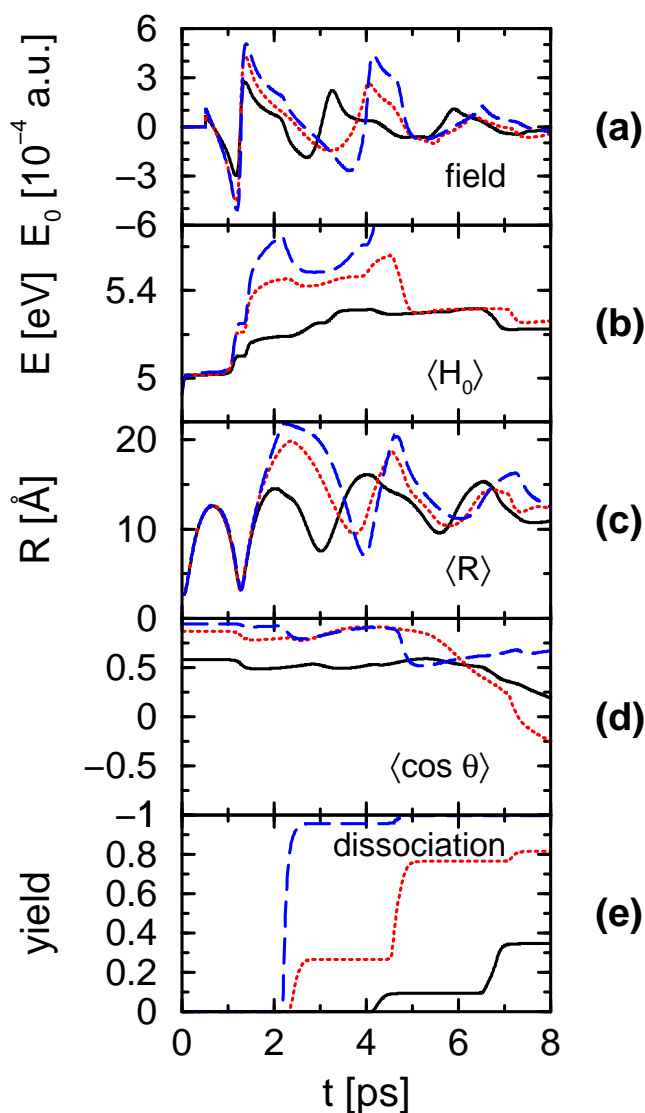


Figure 7.13: Local control including rotational motion and an additional static electric field  $E_s$ . The control field is constructed from the expectation value of  $P \cos \theta$ . Curves for field strengths of  $E_s = 10^5$  V/m (short dashed line),  $10^6$  V/m (long dashed line), and  $10^7$  V/m (solid line) are shown. The same quantities as in Figs. 7.10, 7.11 are contained in the different panels.

that the application of a reasonable strong static electric field results in an excellent control yield. In particular, with increasing field strength, where the orientation of the molecules along the direction of the applied field is enforced, one recovers the rotationless case discussed above. This can be illustrated with the help of the wave functions obtained for the different values of the static field strength. Figure 7.14

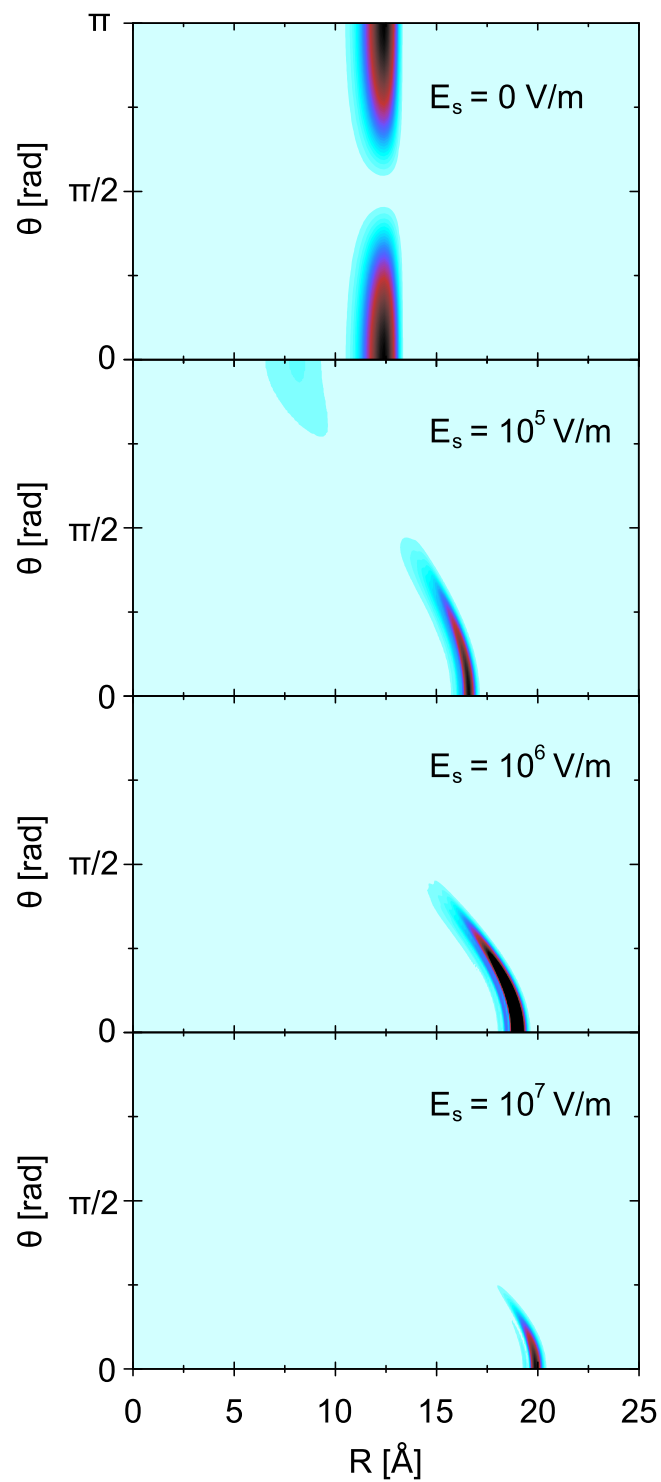


Figure 7.14: Modulus of the rotational-vibrational wave functions at a time of 2000 fs. The functions are shown for various static field strengths, as indicated. The field-free case is included for comparison.

collects the modulus squared of functions at a fixed time of 2000 fs. This is shortly before the first fragmentation products are built in the case of  $E_s = 10^6$  V/m and  $E_s = 10^7$  V/m (see Fig. 7.13). As can be taken from the figure, with increasing field strength, the density is localized at larger distances. This reflects the fact that a strong static field excites more free rotor states leading to a larger magnitude of the expectation value appearing in Eq. (7.40), i.e. to a stronger control field accelerating outgoing wave packets. Furthermore, the static field induces a localization around a value of  $\theta=0$  so that an increase of field strength results in an effective orientation of excited-state NaI molecules. This also means that fragments are built almost exclusively along the direction of the applied static field.

It is noted that it is possible to switch off the static field after the pump-pulse excitation. Concerning the control yield, one obtains the same numerical results as for a permanently present static field. This is due to the time-scale of rotation for free NaI, which is much longer than the times the control fields regarded here are active so that the pre-orientation still persists.

The algorithm of local control is applied to the excited-state photo-fragmentation of the NaI molecule. If the molecular axis is fixed in space, control fields can be constructed which are determined by the dynamical properties of the system and, in more detail, oscillate in phase with the mean momentum of the vibrational motion. In this way, it can be achieved that a 100 % dissociation takes place of the molecules excited by the pump pulse. Employing the same field construction in the case of a molecule which is not restricted to a fixed orientation is not successful without further modifications of the construction scheme. If the field is taken to be proportional to the radial momentum, molecules can, dependent on their orientation, absorb energy from the field but also can lose internal energy resulting in a decreased fragmentation yield. It is shown that, because the energy rate for the radial degree of freedom contains an expectation value of the product of the radial momentum times a  $\cos\theta$  function, a necessary condition to deposit energy in the system is to prepare a rotational wave packet consisting of several free rotor states. This can effectively be achieved by applying a static electric field. The huge dipole moment of NaI results in a large interaction energy, which is able to orient the molecule along the field direction. The application of an additional control field then results in highly efficient fragmentation, which is comparable to the



rotationless case, where the molecular axis is fixed to point along the direction of the control field polarization vector.

### 7.3 Molecular polarizability and orientation

In the last section, it was shown, that an orientation of a molecular sample is desirable to exert effective control with coherent laser light. Therefore, the control of orientation is now chosen as target. Moreover, the molecular polarizability is considered, because there, the electric field enters quadratically into the interaction, see below.

Once again, sodium iodide is chosen as the model system. The rotational degree of freedom is of main interest, so that the Hamiltonian reads

$$H_n = -\frac{1}{2m} \frac{\partial^2}{\partial R^2} + \frac{\hat{J}^2}{2mR^2} + V_n(R) + W(t). \quad (7.42)$$

Here, the laser interaction  $W(t)$  is regarded more precisely as in the previous sections and is taken as

$$W(t) = -\vec{\mu}_{total} \vec{E}(t) \quad (7.43)$$

The total molecular dipole moment  $\mu_{total}$  can be expanded as

$$\vec{\mu}_{total} = \mu + \frac{1}{2!} \alpha \vec{E} + \frac{1}{3!} \beta \vec{E}^2 + \dots, \quad (7.44)$$

where  $\mu$  is the permanent dipole moment,  $\alpha$  is the polarizability tensor and  $\beta$  is the first hyperpolarizability tensor. This series is truncated after the second term. From the latter only the components parallel ( $\alpha_{zz} = \alpha_{\parallel}$ ) and perpendicular ( $\alpha_{xx} = \alpha_{\perp}$ ) to the molecular axis are considered (a similarity transformation to obtain a diagonal matrix from its coordinate representation in  $x, y, z$  is not carried out, as the elements  $\alpha_{xz}, \dots$  are negligibly small). As a consequence, the interaction can be rewritten as [142]

$$W(t) = -\mu E(t) \cos \theta - \frac{1}{2} E^2(t) [\alpha_{\parallel} \cos^2 \theta + \alpha_{\perp} \sin^2 \theta]. \quad (7.45)$$

As the electric field enters quadratically in the second term, different behavior is expected for weak (predominance of the first term) and strong (predominance of the second term) field strengths.

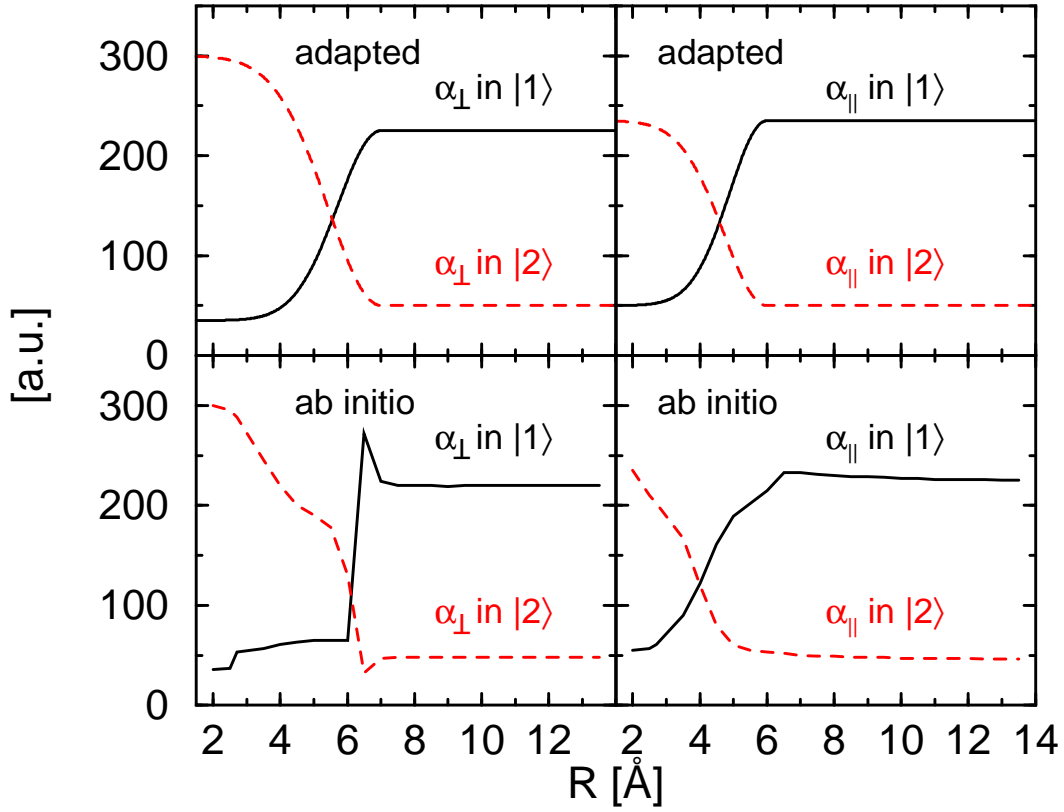


Figure 7.15: Polarizabilities parallel ( $\alpha_{\parallel}$ ) and perpendicular ( $\alpha_{\perp}$ ) to the molecular axis of the adiabatic ground state  $|1\rangle$  and the first excited state  $|2\rangle$  of NaI. In the lower panels, values from *ab initio* calculations are depicted. These results are fitted according to Eq. 7.46 to yield the curves in the upper panels.

The polarizabilities parallel ( $\alpha_{\parallel}$ ) and perpendicular ( $\alpha_{\perp}$ ) to the molecular axis for the adiabatic ground state and the first excited state were obtained from *ab initio* calculations with the RASSCF method [143]. The resulting curves in dependence

Table 7.1: Parameters for the adapted polarizability curves of NaI.

	$\alpha_{\parallel}$ in $ 1\rangle$	$\alpha_{\parallel}$ in $ 2\rangle$	$\alpha_{\perp}$ in $ 1\rangle$	$\alpha_{\perp}$ in $ 2\rangle$
$R_1$ [ $\text{\AA}$ ]	6.0	6.0	7.0	7.0
$\beta_1$ [ $\text{\AA}^{-2}$ ]	0.4	0.3	0.3	0.2
$c_1$ [a.u.]	185.0	-185.0	190.0	-250.0
$c_2$ [a.u.]	50.0	235.0	35.0	300.0
$c_3$ [a.u.]	235.0	50.0	225.0	50.0

of the interatomic distance  $R$  are depicted in Fig. 7.15. They were adapted to analytic forms according to

$$\alpha(R) = \begin{cases} c_1 \cdot e^{-\beta_1(R-R_1)^2} + c_2 & 0 \leq R \leq R_1, \\ c_3 & R_1 < R < \infty. \end{cases} \quad (7.46)$$

The parameters are summarized in Tab. 7.1.

To prove that these curves are realistic, the polarizability in the limit of infinite  $R$  is compared to the experimental values for  $\text{Na} + \text{I}$  or  $\text{Na}^+ + \text{I}^-$ , respectively. For the polarizabilities of the separate atoms or ions, the difference between parallel and perpendicular orientation can be neglected (in fact, for the ions, there is none as they exhibit closed shells; the difference for e.g. I, which stems from the orientation of differently populated  $p$ -orbitals in the external field, is extremely small). The experimental values of the polarizability are  $24.11 \text{ \AA}^3$  for Na [144],  $4 \text{ \AA}^3$  for I [145],  $0.16 \text{ \AA}^3$  for  $\text{Na}^+$  and  $7.81 \text{ \AA}^3$  for  $\text{I}^-$  [146]. This corresponds to  $\sim 190$  a.u. for  $\text{Na} + \text{I}$ , which is matched by  $\alpha_{\parallel} = 235$  a.u. or  $\alpha_{\perp} = 225$  a.u. in the adiabatic ground state  $|1\rangle$ , respectively. For  $\text{Na}^+ + \text{I}^-$ , the polarizabilities sum up to  $\sim 54$  a.u., which is matched by  $\alpha_{\parallel,\perp} = 50$  a.u. in adiabatic state  $|2\rangle$ , see Fig. 7.15.

The target is to achieve orientation. Therefore, the control field is chosen as

$$E(t) = \lambda \Im \left\langle \Psi(t) \left| \mu \left( \cos \theta + \sin \theta \frac{\partial}{\partial \theta} \right) \right| \Psi(t) \right\rangle, \quad (7.47)$$

compare Sec. 5.5. As a  $\sin \theta$  enters in the calculation, the propagation as described in Sec. 3.5 is not applicable. Here, only the part with  $T(J)$  is evaluated in terms of spherical harmonics. The other steps of the propagation are conducted with the reduced wave function  $\Psi(R, \theta, t)$  (compare Sec. 3.5) or its Fourier transform, where the angle  $\theta$  is explicitly treated. As in every time step now a projection of the wave function on the spherical harmonics is necessary and the wave function has to be reassembled afterwards, this propagation scheme is very slow compared to the representation in spherical harmonics only.

In addition to orientation, it is intended to examine the influence of the polarizability. Consequently, calculations with and without the interaction due to the polarizability are performed. The dynamics in the first excited adiabatic state is

investigated, where the non-adiabatic coupling around  $7 \text{ \AA}$  is neglected. The excitation is performed as described before within perturbation theory with a pulse of  $310 \text{ nm}$  and a full width at half maximum of  $50 \text{ fs}$ .

In Fig. 7.16, the results for the case without polarizability is shown, i.e. an interaction term of  $W(t) = -\mu E(t) \cos \theta$  is used. As can be seen from the figure, the field stays extremely small until  $\langle \cos \theta \rangle$  starts to deviate from zero. Only then, the

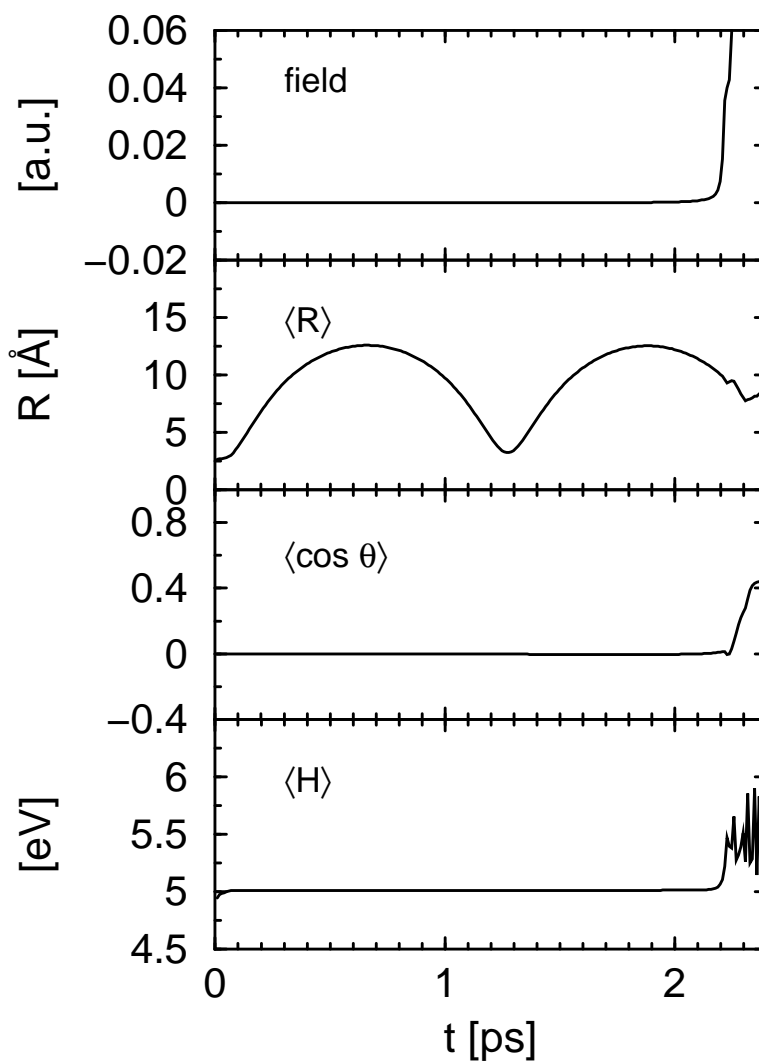


Figure 7.16: Interaction of the laser with the permanent dipole moment only (no polarizability). The different panels show the control field and the expectation values of the bondlength  $\langle R \rangle$ , of the measure for orientation  $\langle \cos \theta \rangle$  and of the system's energy  $\langle H \rangle$ , as indicated.

field starts to rise and in turn,  $\langle \cos \theta \rangle$  increases. This process goes in hand with a rapid population of ever higher  $J$ , which is depicted in Fig. 7.17. Almost instantly, as many  $J$  states as taken into account (here: 400) are occupied. Then, obviously, the expansion in  $J$  does not converge anymore giving rise to numerical errors. That the values afterwards are meaningless, becomes visible in the curves of  $\langle R \rangle$  and  $\langle H \rangle$  from Fig. 7.16: After  $t = 2.2$  ps, erratic oscillations can be observed.

As a conclusion, the local control algorithm finds the trivial solution to the problem of orientation, namely, a static field as strong as possible. When the interaction is chosen to include the polarizability, the same results are obtained, see Fig. 7.18. Once again, the field is almost zero until it increases strongly having the effect, that no converged results can be obtained.

If a higher field strength is selected, only a shift in time of the field's steep rise occurs. The stronger the field strength parameter  $\lambda$  is chosen, the earlier the field starts to deviate from zero significantly and hence, the calculation's breakdown happens earlier. No difference is found between the computations with or without polarizability.

To summarize, the local control algorithm is able to achieve the predefined target, but in this case, only the trivial solution emerges. The answer is a static

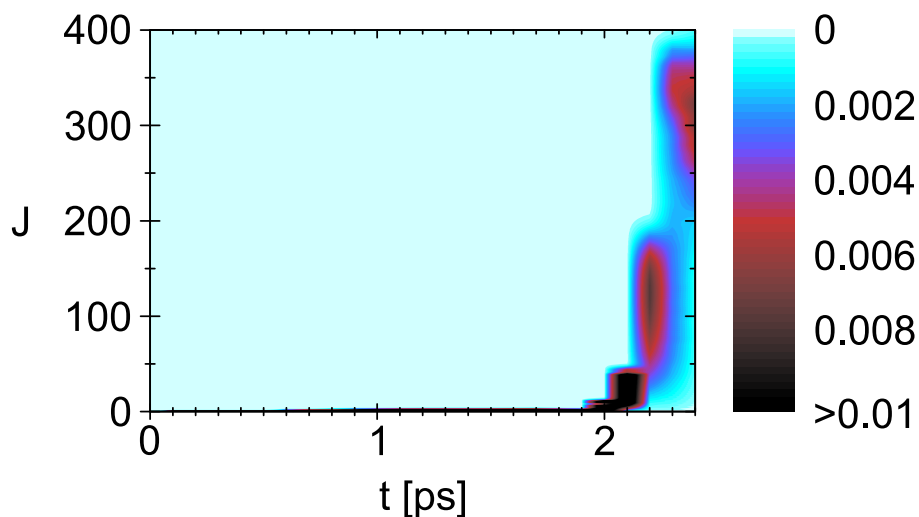


Figure 7.17: Population of the calculated  $J$  states in time. As soon as the control field becomes large (compare Fig. 7.16), all 400 considered  $J$  are almost instantly occupied.

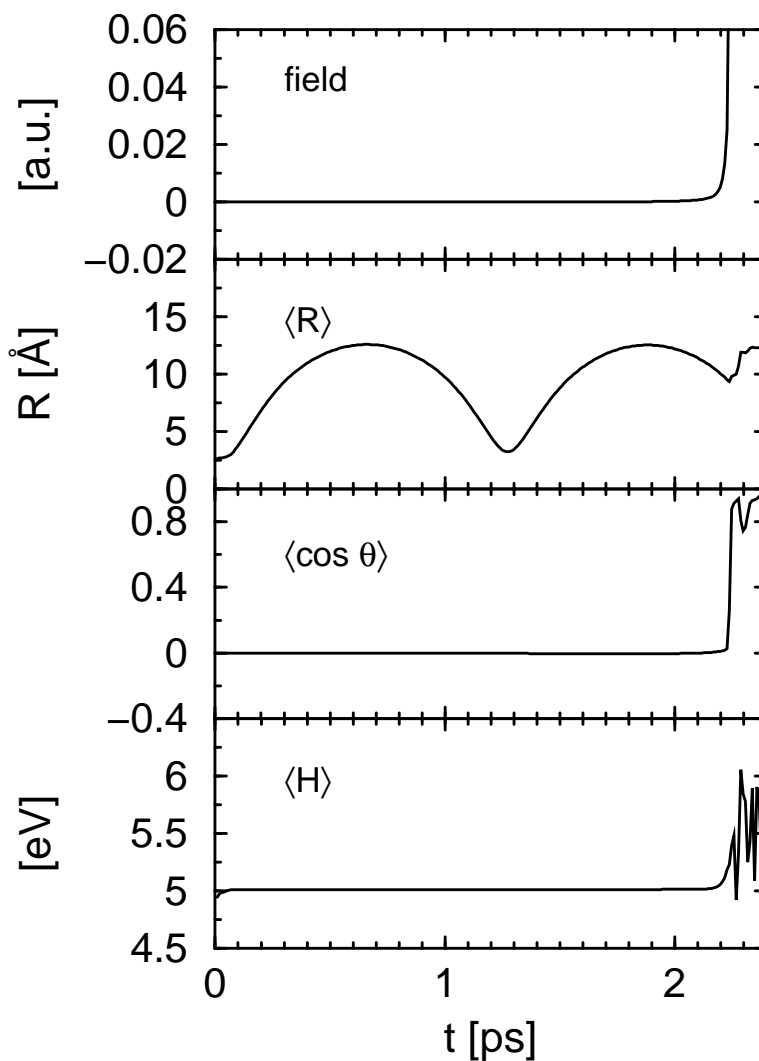


Figure 7.18: Same as Fig. 7.16, but now the interaction includes the polarizability.

electric field as strong as possible. In the simulation, the field increases steadily until all considered states with the rotational quantum number  $J$  are populated. Even 400  $J$ -states were not enough to succeed in a convergence of the calculation. The same results are obtained for computations, which either include or exclude an interaction with the laser due to the molecular polarizability. One can conclude, that the common ansatz to neglect the polarizability and higher terms of the dipole expansion is justified in this case.

## 8 Laser control of a molecular motor

The concept of a molecular motor has been discussed vividly in connection with the construction of nanoscale devices [147]. Recently, Tour and coworkers synthesized a model nanocar [148] and extended it to a motorized version [149]. Another example was studied theoretically by Fujimura and coworkers, who investigated the triggered molecular rotor motion in (R)-2-chloro-5-methylcyclopenta-2,4-dienecarbaldehyde [150–153]. They could show that it is possible, by shaping the perturbing electric field properly, to initiate a unidirectional angular motion of a CHO group. Below, the focus concentrates on the aspect that this can as well be achieved by locally adapted fields, which are interpretable on classical grounds. This then allows for an intuitive understanding of the control process and its outcome.

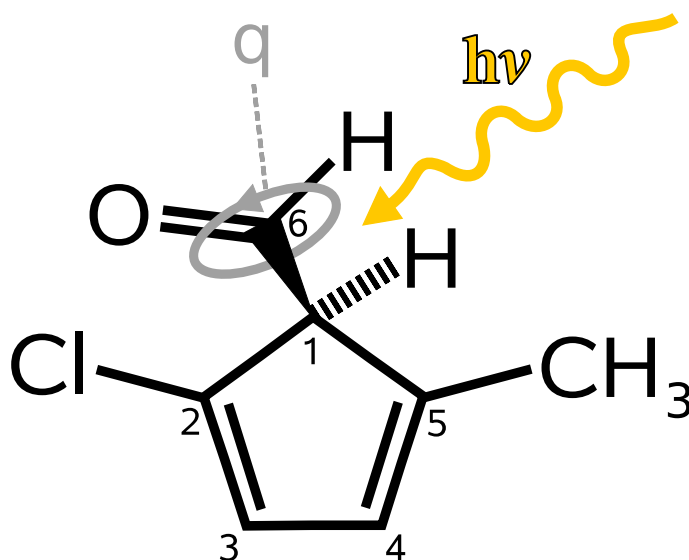


Figure 8.1: (R)-2-chloro-5-methylcyclopenta-2,4-dienecarbaldehyde serves as molecular motor, where the angular motion of the carboxy group is triggered with laser light.

## 8.1 Model and control scheme

Here, (R)-2-chloro-5-methylcyclopenta-2,4-dienecarbaldehyde is used as model system. The molecule is fixed in space and only the rotation around the C1-C6 bond is treated (see Fig. 8.1). The one-dimensional motion is thus taking place along an angular variable  $q$  with the potential curve  $V(q)$ . The latter is adopted from Ref. [150] as

$$V(q) = \sum_{n=1}^4 c_n e^{-\beta_n (q - q_n)^2} \quad (8.1)$$

where the function is only defined from  $-\pi$  to  $\pi$ . The numerical values of the corresponding parameters are listed in Tab. 8.1. The potential curve is depicted in Fig. 8.2, upper panel. Its form is rather complicated, exhibiting several local extrema.

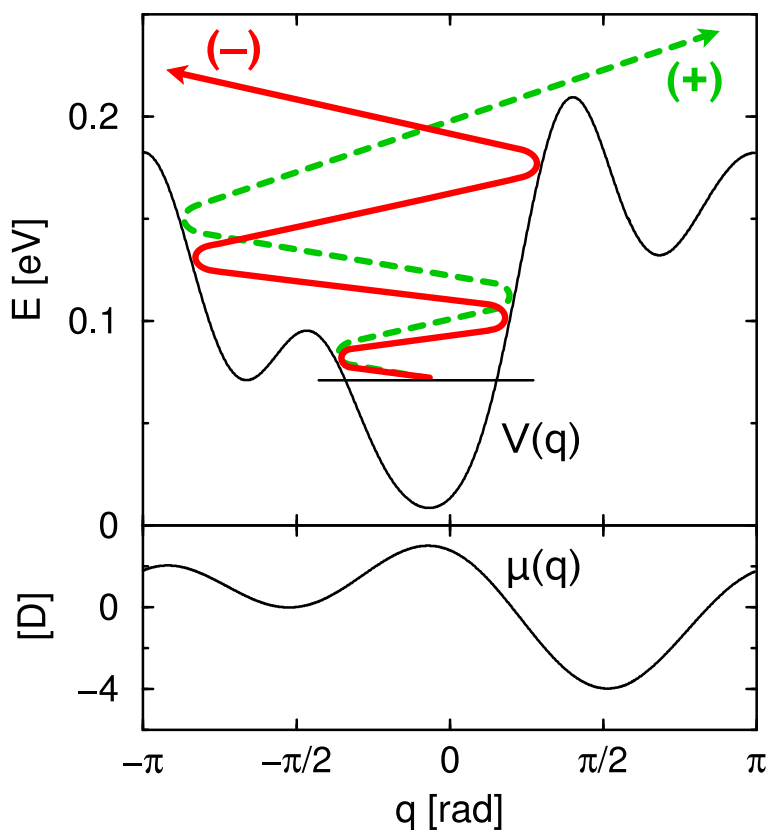


Figure 8.2: The potential energy curve  $V(q)$  for the rotation of the motor's CHO-group is displayed in the upper panel. Additionally, the initiation of a clockwise (+) or a counter-clockwise (-) motion via a heating field is sketched. In the lower panel, the dipole moment  $\mu(q)$  is shown.



Table 8.1: Parameters for the potential of the molecular motor.

	$n = 1$	$n = 2$	$n = 3$	$n = 4$
$c_n$ [eV]	0.1822	0.0930	0.1934	0.1822
$\beta_n$ [rad <sup>-2</sup> ]	$15 \pi$	$20 \pi$	$19 \pi$	$7 \pi$
$q_n$ [rad]	$-\pi$	$-0.45 \pi$	$0.4 \pi$	$\pi$

The dipole moment components depicted in Ref. [150] are approximated as

$$\mu_x(q) = c_x \cos(q + q_x) + b_x \quad (8.2)$$

$$\mu_y(q) = c_y \sin(q + q_y) + b_y \quad (8.3)$$

$$\mu_z(q) = c_z \cos(2q + q_z) + b_z, \quad (8.4)$$

where the respective parameters are collected in Tab. 8.2. The x- and y-components then yield the dipole moment  $\mu(q)$ , which enters in the interaction term with the external field (see below)

$$\mu(q) = -\cos(q) \mu_x(q) + \sin(q) \mu_y(q). \quad (8.5)$$

The resulting curve is shown in Fig. 8.2, lower panel.

Table 8.2: Parameters for the dipole moment components of the molecular motor.

	$x$		$y$		$z$
$c_x$ [D]	-2.3	$c_y$ [D]	-2.0	$c_z$ [D]	0.1
$q_x$ [rad]	0	$q_y$ [rad]	0	$q_z$ [rad]	$\pi$
$b_x$ [D]	-0.5	$b_y$ [D]	-2.0	$b_z$ [D]	-2.1

The Hamiltonian of the system consists of the potential energy  $V(q)$ , the interaction with the control field  $W(t) = -\mu E(t)$  and the rotational kinetic energy  $T(p)$ . The latter depends on the angular momentum  $p$ . The Hamiltonian reads (in atomic units):

$$\hat{H} = -\frac{1}{2I} \frac{d^2}{dq^2} + V(q) - \mu E(t), \quad (8.6)$$

where the moment of inertia  $I$  of 17.6 u is taken from Ref. [150].

Although only the rotation around a single bond is considered, this circular motion even at room temperature ( $T = 300$  K) is hindered (compare potential barriers of

$> 0.2$  eV and mean thermal energy at room temperature of  $kT \approx 0.026$  eV). The objective is now to deposit as much energy in the system as is necessary to initiate either a clockwise or a counter-clockwise rotation. Following classical considerations, the objective can be achieved as sketched in Fig. 8.2. Two trajectories (+) and (−) indicate two excitation pathways, which differ in their outcome. In one case (+), a heating occurs in such a way that the angular motion is positive, as soon as the continuum is reached. In contrast, for the second case (−), the motion has the opposite direction. Thinking in a classical way, both pathways are equally probable, if the phase of the trajectory relative to its energy is timed correctly.

It is noted, that another version of local control theory was used in Ref. [153] in connection with the driven motor motion, for a detailed analysis of this method see Ref. [154]. Here, we employ the simpler method as outlined in Sec. 5.1. Because the dipole moment  $\mu(q)$  is not a linear function of  $q$ , the commutator with the kinetic energy operator is evaluated in constructing the electric field, which is taken of the form (in atomic units)

$$E(t) = -\lambda \Im \langle \psi(t) | [\mu(q), T(p)] | \psi(t) \rangle. \quad (8.7)$$

Here,  $\lambda$  is a strength factor and  $\Im$  denotes the imaginary part. Because the expectation value appearing in the latter equation is purely imaginary, this choice ensures that the energy rate is positive at all times.

## 8.2 Ground state as initial state

In what follows, calculations are discussed which employ the ground-state wave function as initial state. In order to start the heating process, a short seed pulse is applied to the system, a procedure which is usually employed in local control theory [92].

Figure 8.3, upper panel, shows the quantum mechanical probability density for a field parameter of  $\lambda = 1.24 \cdot 10^{-5}$  a.u. It is seen, that it takes about 2 ps until a motion is induced. Then, the density exhibits regular oscillations visible in a modulation of its width. Shortly before 4 ps, the continuum is reached and parts of the wave function move towards smaller and also larger angles. In order to circumvent a further heating of the system, the control field is switched off after 4 ps. For

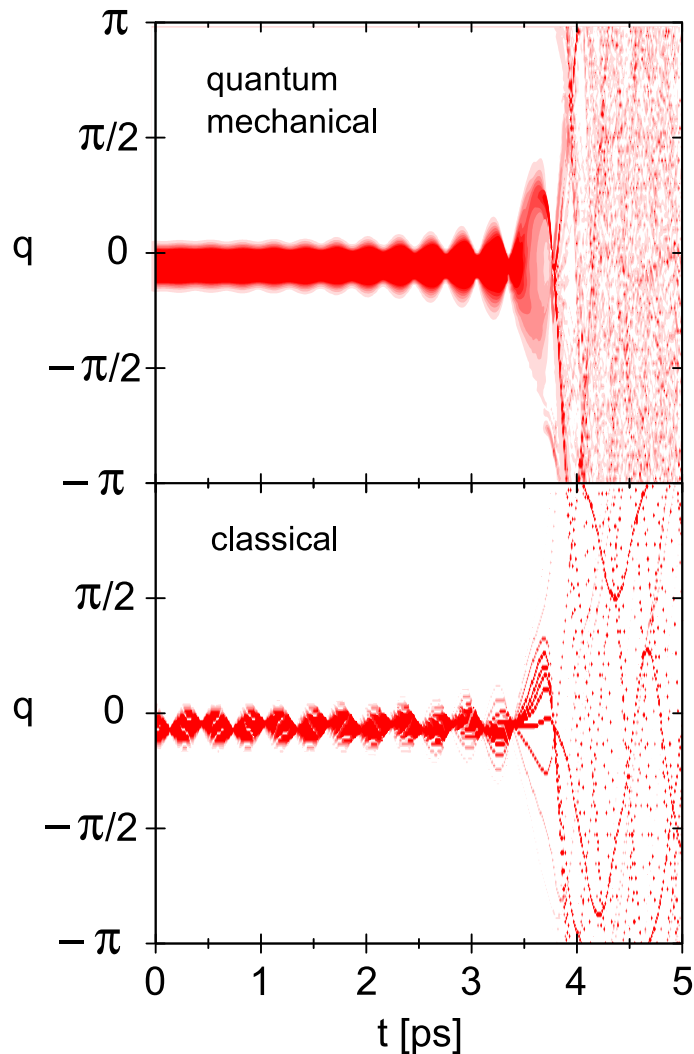


Figure 8.3: Heating of a rotor, where the initial state is the ground state of the unperturbed system. The quantum mechanical probability density (upper panel) is compared to an ensemble of trajectories (lower panel).

comparison, the lower panel of Fig. 8.3 contains the dynamics of an ensemble of 23 trajectories, where the classical dynamics is subject to the identical control field as constructed in the quantum mechanical calculation (upper panel of the figure). The initial positions and momenta are sampled from the quantum mechanical probability distributions after the seed pulse. It is obvious that quantum and classical densities exhibit the same basic features. This strengthens the point that local control is as close to intuition as possible. In particular, it is obvious that there are trajectories moving out of phase, i.e. against each other which leads to the bifurcation of the trajectory ensemble (and likewise, of the quantum wave packet).

From the densities alone, however, it is not possible to decide if the control field induces a net clockwise ((+) direction) or counter-clockwise ((-)-direction) motion. An analysis of the time-dependent wave function yields a ratio  $P_-/P_+ \approx 2.2$  for the integrated probability density moving in (-)- versus (+)-direction. This is not

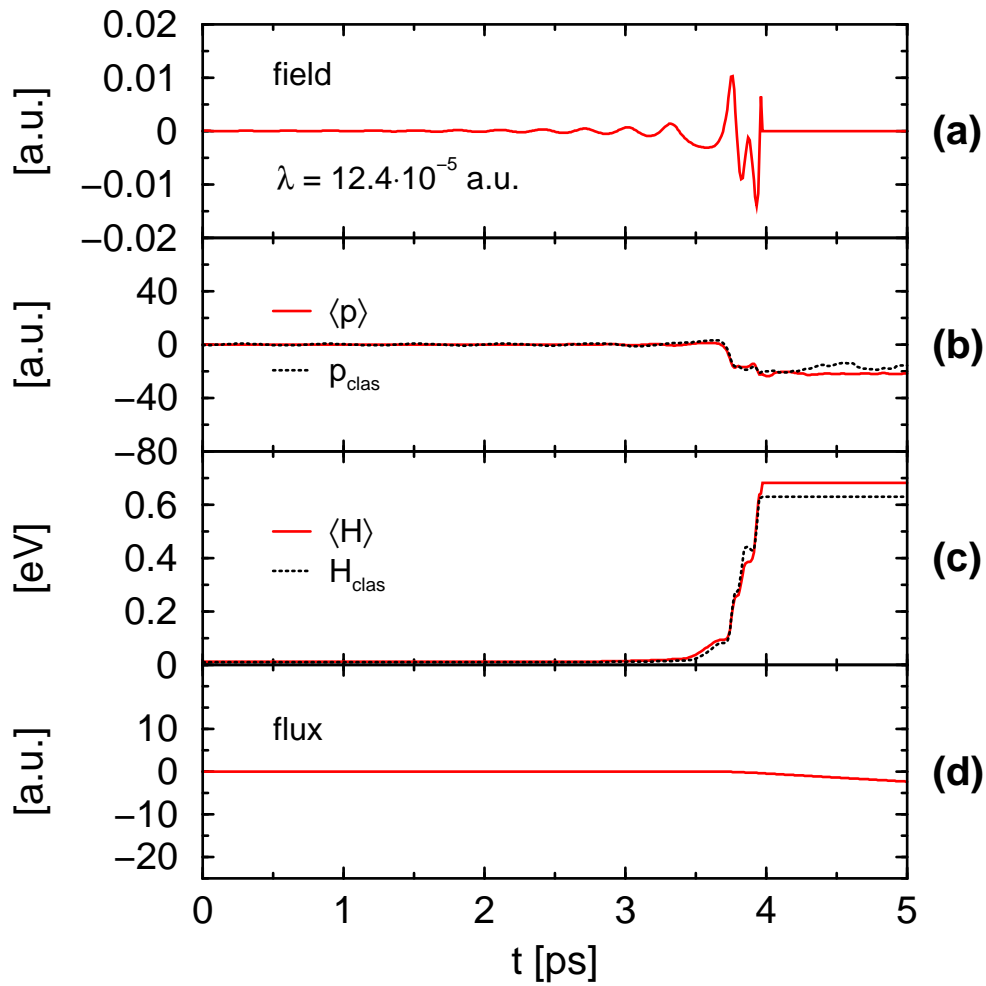


Figure 8.4: Heating of a rotor, where the initial state is the ground state of the unperturbed system. The control field is displayed in panel (a). A sign change in the dipole moment results in additional oscillations compared to the angular momentum expectation value (panel (b), contains also classical angular momentum). The latter would be proportional to the control field in case of a linear dipole moment. Panel (c) contains the energy expectation value calculated quantum mechanically and classically, as indicated. The time- and space integrated flux is shown in panel (d).

ideal and below the question is addressed how to improve the control yield. For now, it is demonstrated that indeed a net rotor motion in a preferential direction is triggered. Therefore, we calculate the time- and space integrated flux

$$F(t) = \frac{1}{2Ii} \int dq \int_0^t dt' \left\{ \psi^*(q, t') \frac{d}{dq} \psi(q, t') - \left( \frac{d}{dq} \psi^*(q, t') \right) \psi(q, t') \right\}. \quad (8.8)$$

This flux is shown in Fig. 8.4d. Its time behavior documents what has been stated above: as soon as the system is excited into the continuum, a negative integrated flux is obtained corresponding to the counter-clockwise rotor motion. The energy expectation value (solid/red line) of the system is displayed in panel (c) of Fig. 8.4. When its value exceeds the height of the left barrier ( $\sim 0.2$  eV), the flux starts to deviate from zero. The time dependence of the average energy documents the effective heating of the system. The same is obtained classically, which is documented in the figure by the dashed line curve. This line shows the average energy of the classical trajectories, which are promoted into the continuum.

The oscillatory behavior of the electric field (panel (a)) is directly connected to the wave packet motion, where the increasing period reflects the smaller energy separation of higher lying eigenstates of the system. It has to be kept in mind, that a sign change in the dipole moment (which occurs in the present case [150]) as well introduces a phase into the time-dependence of the field as can be readily taken from Eq. (8.7). These additional oscillations can be seen, when the field is compared to the angular momentum expectation value (panel (b) of Fig. 8.4), because  $\langle p \rangle$  would be directly proportional to the control field in case of a linear dipole moment, as was shown in Sec. 5.1. Panel (b) also contains the mean angular momentum from the classical trajectories. Here once again, the agreement between quantum mechanical and classical calculation is pronounced.

### 8.3 Arbitrary initial state

To increase the yield for an unidirectional motion, it seems reasonable to eliminate the bifurcation of the wave packet visible in Fig. 8.3. This can be realized, if the initial function is a localized wave packet being displaced from the global minimum of the potential. Here, a Gaussian of the form  $\Psi_i = N e^{-100(q-0.26)^2}$  was chosen, where  $N$  is a normalization constant. As a result, nearly 100% of the propability density move in the (+)-direction for  $\lambda = 4.2 \cdot 10^{-5}$  a.u. The same is achieved for

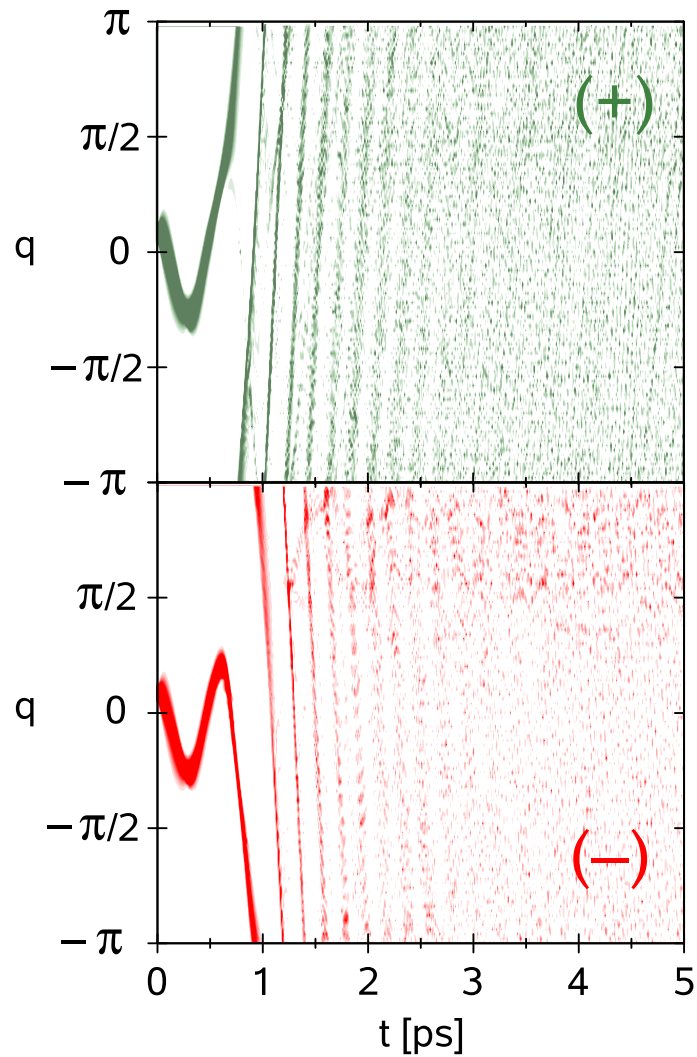


Figure 8.5: Controlled unidirectional motion for an arbitrarily chosen initial state. Almost 100% efficiency for either a clockwise (+) rotation (upper panel) or a counter-clockwise (-) motion (lower panel) is achieved.

the (-)-direction in case of  $\lambda = 3.5 \cdot 10^{-5}$  a.u., as can be taken from Fig. 8.5.

In Fig. 8.6, the corresponding fields (panel (a)), expectation values of the angular momentum (panel (b)) and the energy (panel (c)) and the time-integrated flux (panel (d)) are shown. The same conclusions as for Fig. 8.4 can be drawn. Here, the time-integrated flux takes higher values, also indicating a higher yield for the motion in the respective direction.

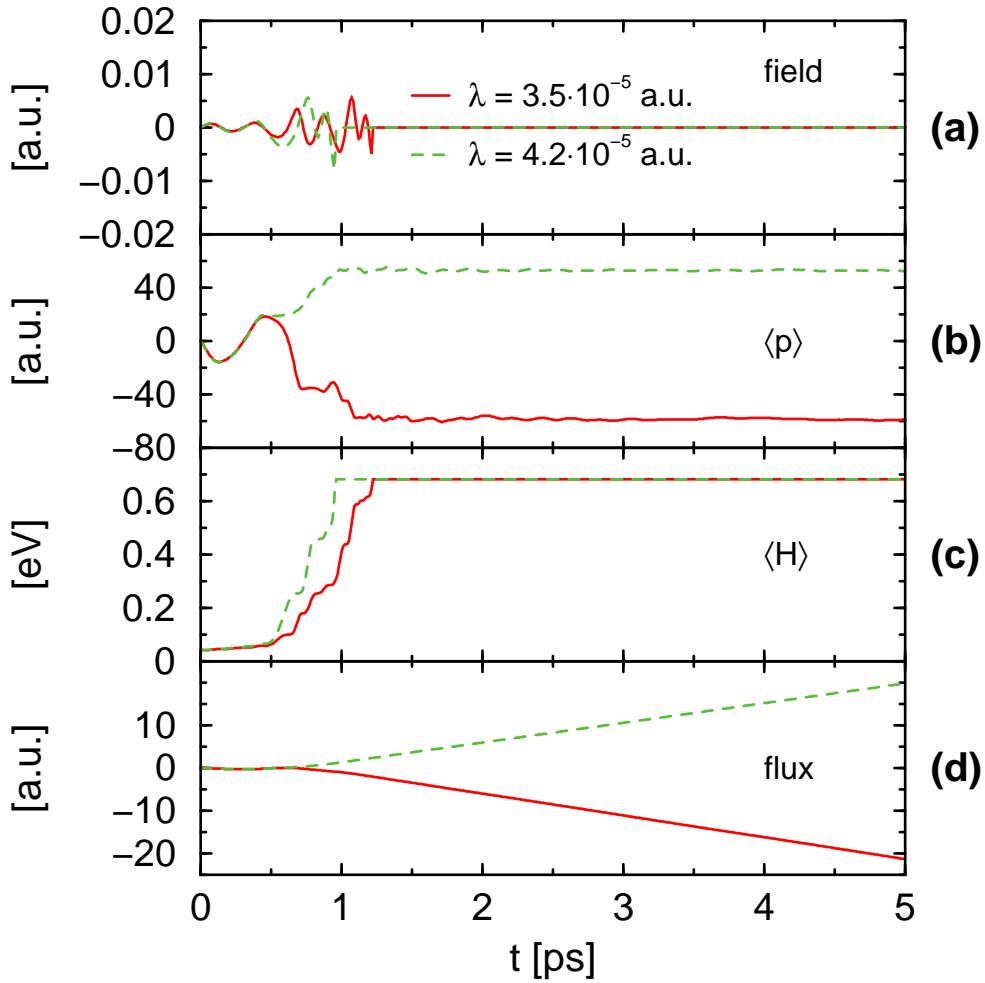


Figure 8.6: Controlled unidirectional rotation for an arbitrarily chosen initial state. The same quantum mechanical quantities as in Fig. 8.4 are shown for  $\lambda = 3.5 \cdot 10^{-5}$  a.u. and  $4.2 \cdot 10^{-5}$  a.u.

## 8.4 Dressed initial state in a static field

Of course, a displaced initial wave function can easily be achieved in a calculation. In order to mimic an experimental realization, where a displaced initial state is prepared, the following procedure is chosen. Suppose, the molecule is fixed in space and a static electric field (field-vector  $\vec{E}_s$ ) is applied anti-parallel to the direction of the dipole moment  $\vec{\mu}(q)$ . This then adds the term

$$H_s = -\vec{\mu}(q)\vec{E}_s = -\mu(q)E_s, \quad (8.9)$$

to the Hamiltonian of Eq. (8.6). Here,  $E_s$  is the field strength. As a consequence, the potential curve is tilted and the ground-state wave function in the field is dis-

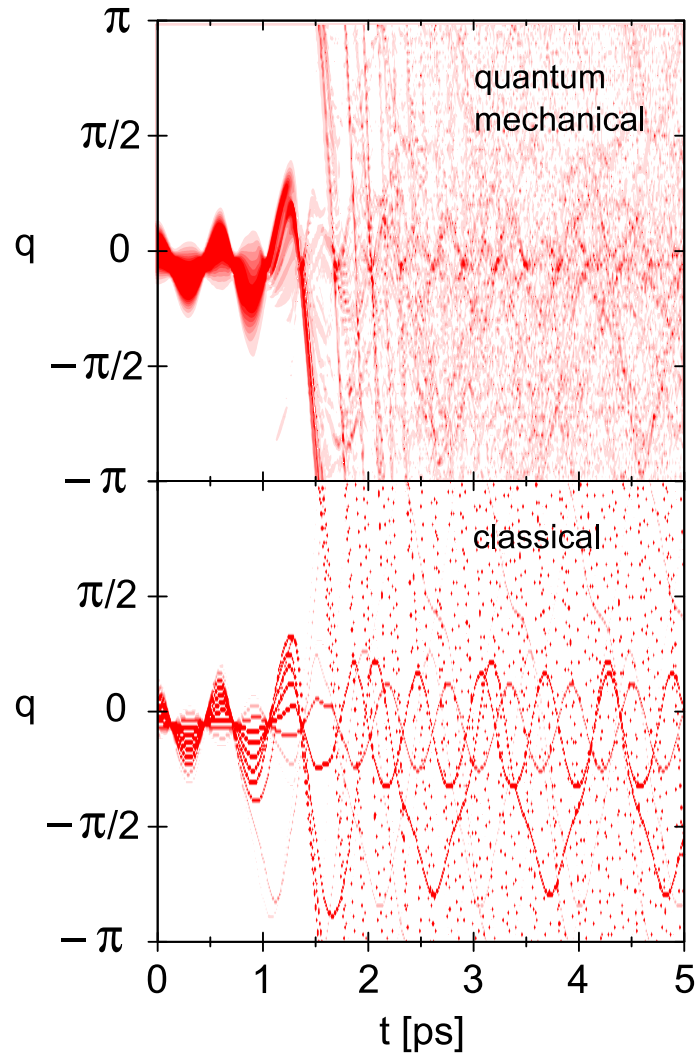


Figure 8.7: Controlled unidirectional motion in the counter-clockwise direction. The initial state is the ground state of the system in a static electric field. The quantum mechanical probability density (upper panel) is compared to an ensemble of trajectories (lower panel).

placed on the  $q$ -axis. This pendular state [134] is calculated for a field strength of  $E_s = 10^9$  V/m yielding a ground state of approximately Gaussian form with its maximum at  $q = 0.07$  rad. If the static field is turned off, the pendular motion starts and the control field can be determined without adding an additional seed pulse.

In Fig. 8.7 quantum mechanical (upper panel) and classical (lower panel) densities are compared for a field strength parameter of  $\lambda = 6.0 \cdot 10^{-5}$  a.u. Here, the



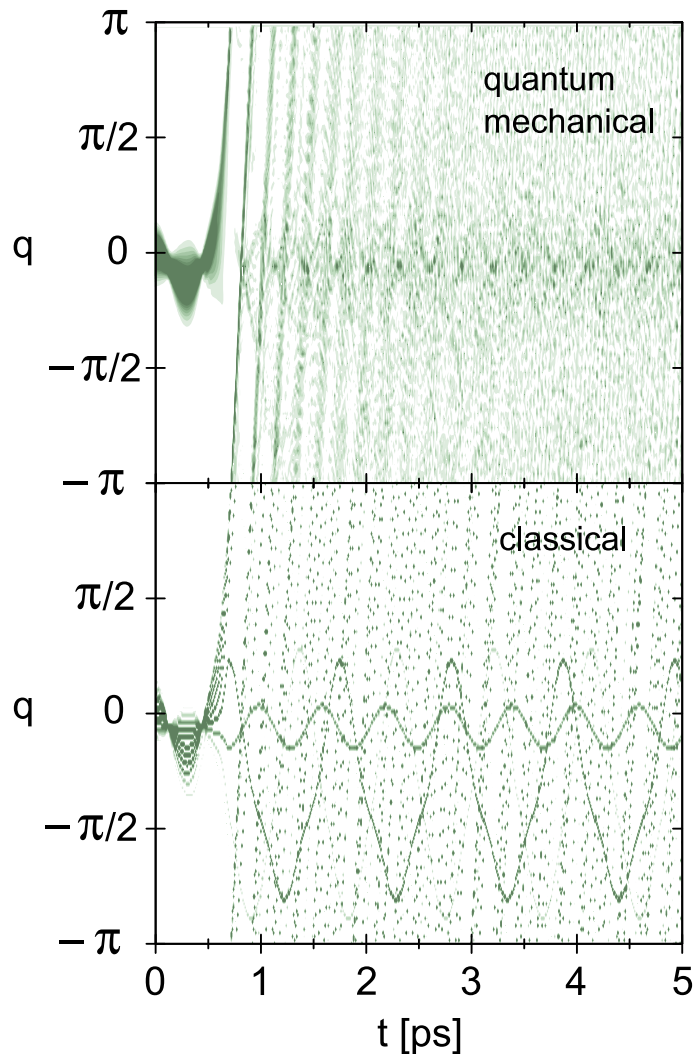


Figure 8.8: Controlled unidirectional motion in the clockwise direction. The initial state is the ground state of the system in a static electric field. The quantum mechanical probability density (upper panel) is compared to an ensemble of trajectories (lower panel).

density already reveals that a unidirectional motion in the  $(-)$ -direction is induced. This is due to the fact that the density now remains rather localized and does not exhibit a clear bifurcation. As a result, one finds that the ratio of molecules rotating in the counter-clockwise versus clockwise direction is  $\sim 83\%$ . Again, the classical density dynamics resembles very much the quantum motion. This even applies to those parts, which still move in the bound state part of the potential after the control field is turned off (after  $\sim 1.6$  ps), a fact which has been investigated theoretically in the connection with femtosecond pump-probe experiments [155].

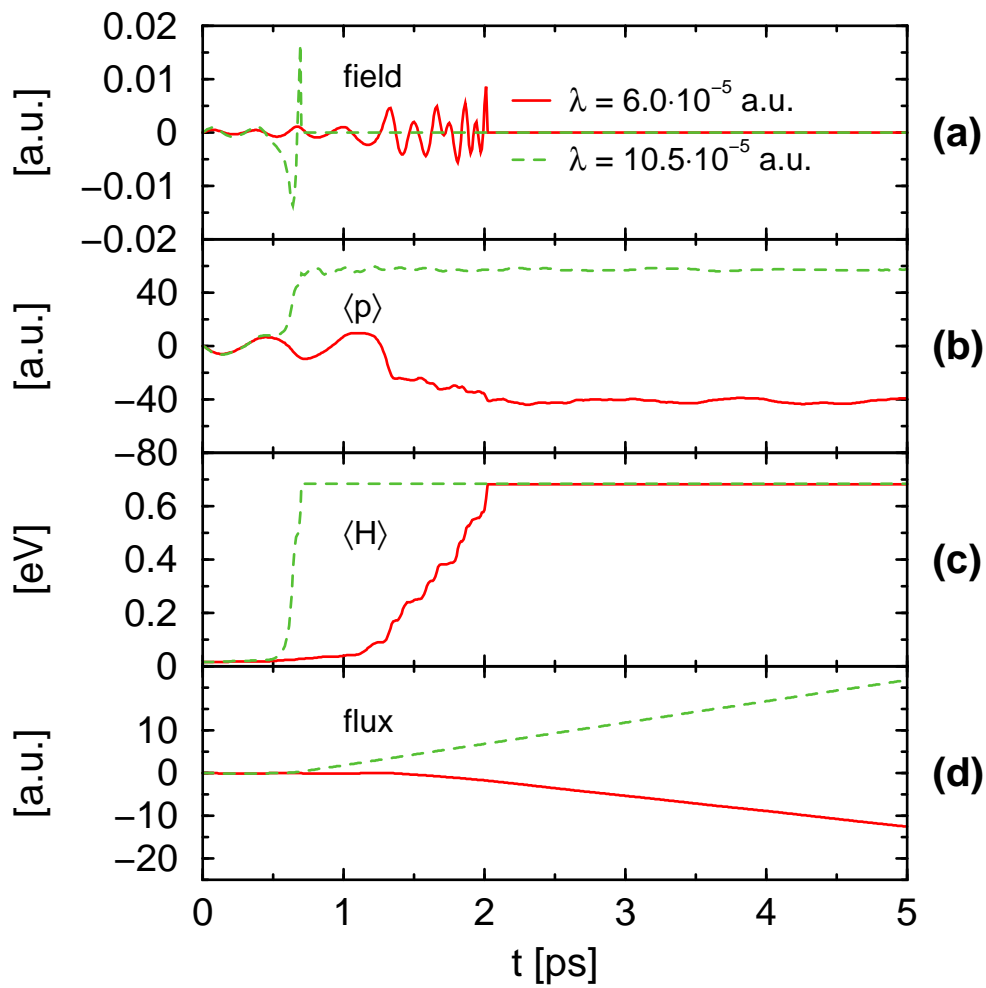


Figure 8.9: Control of directional motion for an initial state created by a static field. The control fields for the field strength parameters  $\lambda = 6.0 \cdot 10^{-5}$  a.u. and  $10.5 \cdot 10^{-5}$  a.u. are shown in panel (a). Panels (b) and (c) display the expectation values of the angular momentum and the energy, respectively. The time-integrated flux proves that an unidirectional motion is achieved (panel (d)).

Figure 8.8 illustrates the case, where the field is stronger ( $\lambda = 10.5 \cdot 10^{-5}$  a.u.). Because now the energy dissipation into the system is larger, the trajectories (and likewise, the quantum wave packet) move out into the continuum earlier. Here, the timing is such that the motion is triggered in the positive direction (with a yield of 86 %).

The control fields for the cases with the pendular state as initial function are dis-

played in Fig. 8.9 (a). The fields are switched off shortly after the energy expectation value (panel (c)) has become larger than the maximal potential barrier. Until then, a further heating is performed. The either clockwise ( $\lambda = 10.5 \cdot 10^{-5}$  a.u.) or counter-clockwise ( $\lambda = 6.0 \cdot 10^{-5}$  a.u.) rotation can already be extracted from the angular momentum expectation value in panel (b). The respective unidirectional motion can even better be inferred from the time-integrated flux in panel (d).

Starting from the ground state of the system, it is shown that an effective heating can be obtained which induces a free rotor motion. Although a net unidirectional motion is prepared, the yield is rather low. This is due to the presence of a bifurcation of the wave packet. The latter can be suppressed by starting from a localized initial state in the field-dressed potential, which is displaced from the equilibrium position of the unperturbed system. This situation can be achieved, if a static field is applied to the system prior to the control field. Thus, the control field acts on a non-bifurcating wave packet, which follows a mean classical path. Depending on the field strength of the driving field, the oscillation takes place such that either a motion into the counter-clockwise or clockwise direction is triggered upon reaching the continuum. Here, typical yields of more than 80 % are found. The latter result hints at the possibility to drive nanocars according to the sketch in Fig. 8.10.

Here, the control field induces a rotation of the motor group, which then pushes the whole nanocar in the desired direction on a surface. It may not be possible to propel the wheels directly, because they should be designed most symmetrically. On the other hand, the induction of a unidirectional motion by linearly polarized

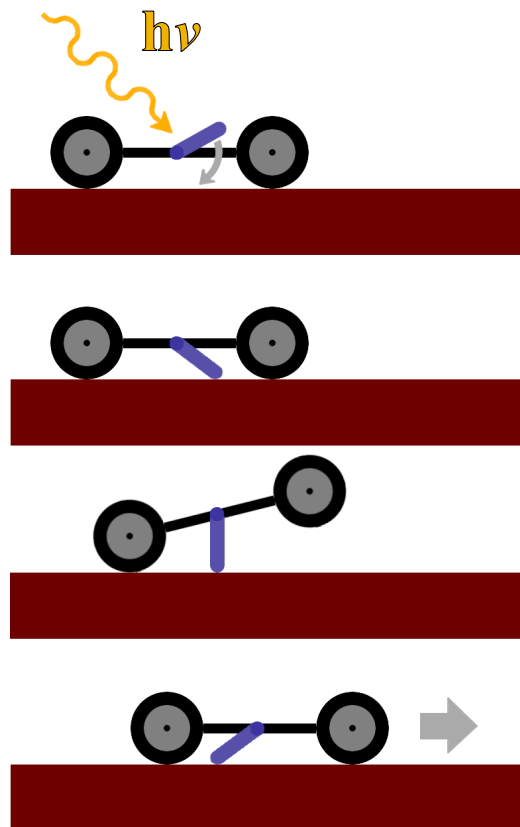


Figure 8.10: Driving a nanocar with an integrated molecular motor by shaped laser pulses.

light requires chiral molecules [150, 156, 157], because only the latter exhibit non-symmetrical potentials.

A comparison between classical and quantum densities shows that they exhibit the same characteristics. Because, within local control theory, the field is constructed from the dynamics (being either quantum mechanical or classical), properties of the fields directly relate to the underlying physics. There are two aspects which emerge from this fact. First, the particular form of a control field can be understood in terms of dynamics, and second, if the quantum motion can be represented reasonably well by an ensemble of trajectories, the control fields obtained from a classical calculation are very similar to the ones derived within a quantum approach. The latter fact should be very important concerning the simulation of control processes in complex systems.

# 9 Photoassociation

In photoassociation reactions, a molecule is formed from two colliding atoms, radicals or more generally, two particles, by the interaction with an electro-magnetic field. By this means, a transition from a free continuum state to a bound state is induced (free-bound transition) [158]. A large number of theoretical papers has been published regarding this issue, see e.g. Refs. [159–163]. In comparison to the reversed process of photodissociation (compare chapters 6, 7), photoassociation still imposes larger experimental problems. In order to form ground-state molecules, continuous-wave (cw) lasers are used (see e.g. Ref. [164]) to associate ultra-cold atoms in a magneto-optical trap (MOT) or a far off-resonance trap (FORT). With femto- or picosecond pulses, photoassociation has only been achieved in excited states [165, 166]. However, regarding the molecular groundstate, short pulses only seem to dissociate molecules already present in a MOT [167, 168].

Most of the above-mentioned work pursues the scheme to pump population from a continuum state into a bound level of an electronically excited state and afterwards dump it to a lower vibrational state in the electronic ground state (which is related to the fact that homonuclear molecules were considered, where no permanent dipole moment exists). Within this scheme, global control algorithms were employed to achieve the formation of ultracold molecules [169–171]. Here, another approach to ground-state photoassociation is investigated, where the molecule is formed directly via the interaction with a field in the electronic ground state and not involving further excited states [161, 172].

## 9.1 Model and control schemes

As in the previous chapters, local control theory is applied to determine the control fields. The questions to be asked are, how effective photoassociation is realized with fields derived from local control theory; which objectives can be formulated

to achieve an effective association yield, and how the control field can be interpreted.

In the effort to answer these questions, the starting point is a restricted model, where the rotational degree of freedom does not participate. The such derived control fields are then applied to the situation, where different rotational states are regarded as initial states, and rotational excitation is included.

Two atoms are regarded having the distance  $R$ . At first, the rotational degree of freedom is neglected, i.e. s-wave scattering is studied.

The association reactions of  $\text{H} + \text{F} \rightarrow \text{HF}$  and  $\text{H} + \text{I} \rightarrow \text{HI}$  are regarded. The potential curve  $V(R)$  and the dipole moment  $\mu(R)$  for HF are given as [173]

$$V(R) = D_0 (1 - e^{-\beta(R-R_e)})^2 \quad (9.1)$$

$$\mu(R) = aRe^{-bR^4}, \quad (9.2)$$

where  $D_0$  is the dissociation energy,  $R_e$  the equilibrium distance and  $\beta = \frac{\omega_e}{\sqrt{2D_0/m}}$  is the Morse parameter with the harmonic frequency  $\omega_e$  and the reduced mass  $m$ . These and the other constants can be found in Tab. 9.1.

For HI, the ground-state potential is also represented by a Morse function [172] The dipole moment function is taken from [174]

$$\mu(R) = \begin{cases} \sum_{n=3}^8 a_n R^n & 0 \leq R \leq R_1, \\ \sum_{n=0}^5 b_n R^n & R_1 < R \leq R_2, \\ c_1 R^\delta e^{-(\gamma_H + \gamma_I)R} + \frac{c_2}{R^4} & R_2 < R < \infty, \end{cases} \quad (9.3)$$

where  $\delta = \frac{2}{\gamma_H} + \frac{2}{\gamma_I} - \frac{2}{\gamma_H + \gamma_I} + 1$  and  $\frac{\gamma_H^2}{2}$  and  $\frac{\gamma_I^2}{2}$  are the ionization potentials of the corresponding atoms H and I. The parameters are listed in Tab. 9.1. Note, that in this work the values of  $R_1$  and  $R_2$  are adjusted to obtain functions as smooth as possible.

The dipole moment functions and the potential curves are depicted in Fig. 9.1, where also the eigenenergies of different vibrational states with quantum number  $v$  are indicated.

Table 9.1: Parameters for the HF and HI potentials and the respective dipole moments.

HF		HI			
$m$ [u.]	1.0447	$m$ [u.]	1.0079	$b_0$ [D]	2.26353
$R_e$ [Å]	0.9260	$R_e$ [Å]	1.60916	$b_1$ [DÅ <sup>-1</sup> ]	-4.55458
$D_0$ [a.u.]	0.2101	$D_0$ [eV]	3.054	$b_2$ [DÅ <sup>-2</sup> ]	4.26612
$\beta$ [a.u.]	1.22	$\omega_e$ [cm <sup>-1</sup> ]	2309.01	$b_3$ [DÅ <sup>-3</sup> ]	-1.85122
$a$ [a.u.]	0.4541	$a_3$ [DÅ <sup>-3</sup> ]	13.98892	$b_4$ [DÅ <sup>-4</sup> ]	0.36865
$b$ [a.u.]	0.0064	$a_4$ [DÅ <sup>-4</sup> ]	-35.77172	$b_5$ [DÅ <sup>-5</sup> ]	-0.02750
		$a_5$ [DÅ <sup>-5</sup> ]	37.84713	$c_1$ [DÅ <sup>-δ</sup> ]	41.91837
		$a_6$ [DÅ <sup>-6</sup> ]	-20.46105	$c_2$ [DÅ <sup>4</sup> ]	7.749
		$a_7$ [DÅ <sup>-7</sup> ]	5.62142	$R_1$ [Å]	1.71241
		$a_8$ [DÅ <sup>-8</sup> ]	-0.62615	$R_2$ [Å]	3.17551
		$\gamma_H$ [a.u.]	0.99970		
		$\gamma_I$ [a.u.]	0.87640		

The maximum quantum number  $v_{max}$  is given from the nearest integer below [175]

$$\frac{\sqrt{2D_0m}}{\hbar\beta} - 0.5 \quad (9.4)$$

and the total number of bound states is consequently  $v_{max} + 1$ . In the case of HF and HI, it is found that  $v_{max} = 22$  and  $v_{max} = 20$ , respectively.

The initial wave function, in each case, was implemented as a Gaussian of the form

$$\Psi_i = \sqrt[4]{\frac{2\beta}{\pi}} e^{-\beta_i(R-R_i)^2 - i\bar{p}R}, \quad (9.5)$$

centered at  $R_i = 15 \text{ \AA}$  with a full width at half maximum (FWHM) of  $5 \text{ \AA}$  ( $\beta_i = \frac{4\ln(2)}{FWHM^2}$ ). Here,  $\bar{p}$  is the mean momentum of the colliding particles so that the impact energy is  $E_p = \frac{\bar{p}^2}{2m}$ . Treating the initial wave packet as a Gaussian is justified for higher temperatures [163]. Note however, that a stationary continuum state has to be used for the association of ultra-cold atoms in the near-threshold regime, because the de Broglie wavelength becomes large compared to the interatomic separation and indeed, experiments with continuous-wave lasers identify several nodes of the stationary wave function as minima in the photoassociation signal [162].

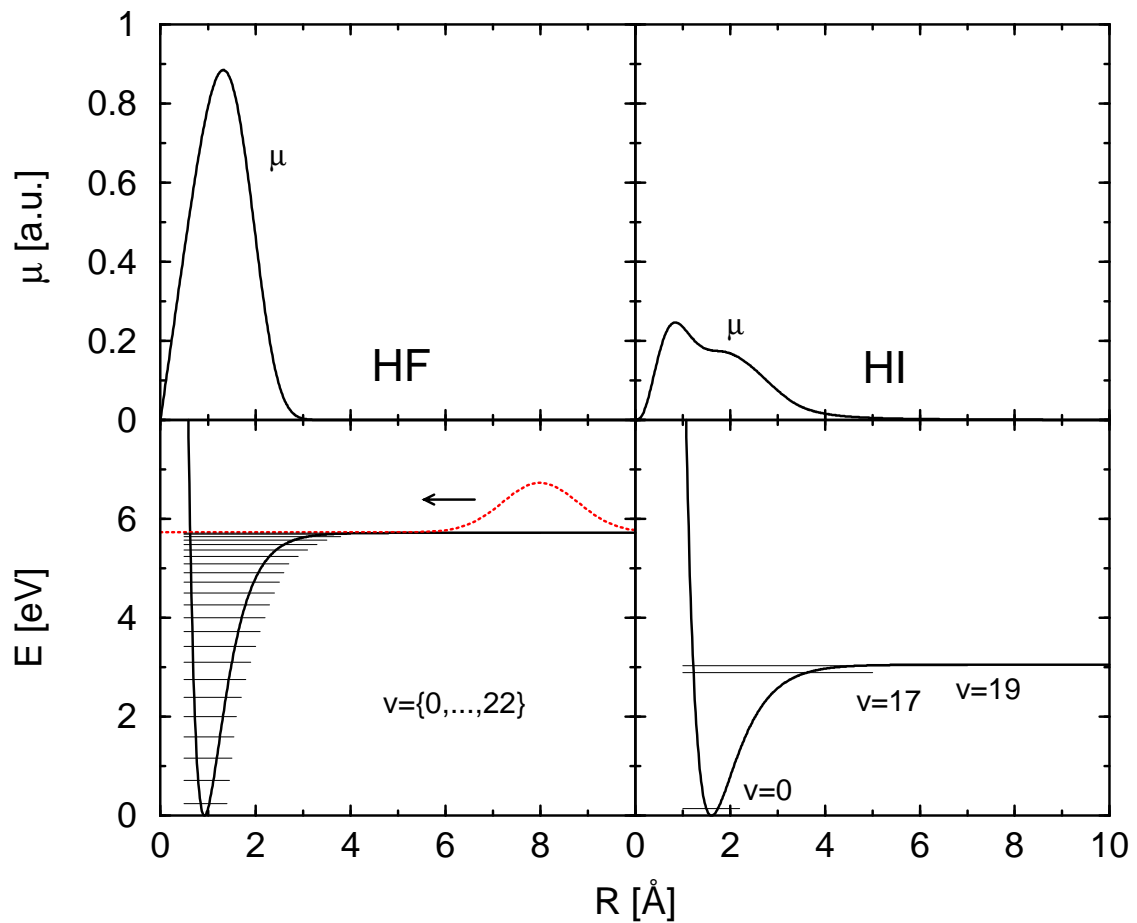


Figure 9.1: Potential energy curves  $V(R)$  and dipole moments  $\mu(R)$  for HF (left panels) and HI (right panels).

The model systems employed in this chapter are constrained to the limitation, that no other electronic states than the electronic groundstate are considered. For a complete simulation, additional states, like they can be found e.g. in [176] (HF) or [177] (HI), will have to be implemented.

To achieve photoassociation, two approaches are pursued. First, it is required that the system's energy decreases as a function of time, and second, it is required that the population in a defined target eigenstate increases monotonically.

A sufficient condition to reduce the energy of the system upon the interaction with an external field is, that the expectation value of  $H_0$  decreases as a function of time or equivalently, that its time-derivative (the energy rate) is less than zero.



Consequently, the field is chosen as

$$E(t) = \lambda \frac{i}{2m} \left\langle \frac{d^2\mu}{dR^2} + 2\frac{d\mu}{dR} \frac{d}{dR} \right\rangle, \quad (9.6)$$

with  $\lambda$  being a negative number (compare Sec. 5.1, p. 48). This type of field is used, when the realistic dipole moments of the molecules to build enter into the calculation. But also the special case of a linear dipole moment is treated, where the simplified form of the field according to

$$E(t) = \lambda \langle p \rangle. \quad (9.7)$$

can be applied (compare Eq. (5.10), p. 49).

Another expression for the field is obtained, if the objective is to increase the population in a target eigenstate  $|\phi_T\rangle$  of  $H_0$ . Here, the control field, which steadily increases the target state population is

$$E(t) = \lambda \Im\{\langle \Psi(t)|\mu|\phi_T\rangle\langle \phi_T|\Psi(t)\rangle\}, \quad (9.8)$$

with  $\lambda$  chosen to be positive (compare Sec. 5.2, p. 49). From this expression it is obvious, that some overlap between the wave packet  $|\Psi(t)\rangle$  and the target state  $|\phi_T\rangle$  must exist at some point, because otherwise the field remains zero at all times. This problem is overcome by artificially populating the target state with some small fraction of the total population, see below. It is, however, important to note that this is only necessary to start the numerical algorithm and is not needed in an experimental realization, working with the pre-calculated control field.

## 9.2 Fixed orientation: s-wave scattering

First, the photoassociation of  $\text{H} + \text{F}$  is discussed, where the mean momentum  $\bar{p}$  of the initial wave packet is chosen to yield an average energy of 0.1 eV above the dissociation limit. To have a system which is easily understandable, the dipole moment is set linearly, such that the field is determined according to Eq. (9.7). In this way, the system can be seen as an out-of-phase-driven oscillator. The linear dipole function is derived from the increasing part of the dipole moment depicted in Fig. 9.1, upper left panel. To avoid numerical problems, the field is smoothly switched on by multiplying it with a Gaussian envelope function, rising until its

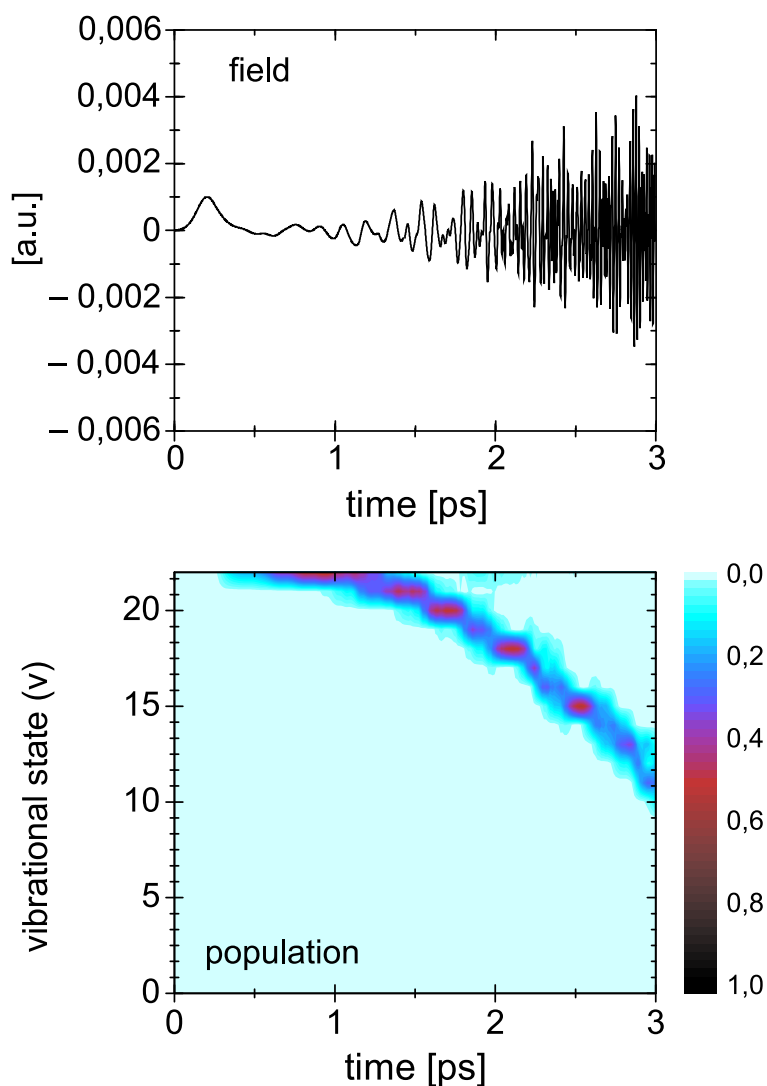


Figure 9.2: Photodissociation of HF assuming a linear dipole moment. The control field is shown in the upper panel. The time-dependent population in various eigenstates is shown as a contour plot in the lower panel.

maximum at 250 fs (FWHM of 177 fs) and then remaining at a value of one, see Fig. 9.2, upper panel. Here, a scaling parameter of  $\lambda = -1.2 \cdot 10^{-3}$  a.u. is employed. The lower panel displays the population  $P_v(t)$  in the various vibrational levels ( $v$ ). The contour plot documents that the association takes place via the highest vibrational levels. As time goes along, the population is consecutively transferred to ever lower-lying states. This mechanism is the opposite of the so-called 'ladder climbing' where, starting from the ground state, higher and higher states are excited [76, 121]. Here, the 'ladder descending' can be achieved, if the field carries an

up-chirp, corresponding to the increasing energy difference between the vibrational eigenstates for decreasing quantum number  $v$ . This up-chirp can be seen in the field (upper panel of Fig. 9.2) confirming that LCT delivers a field which can be interpreted in terms of properties of the perturbed system. For a discussion of the effects of a chirped field in ultracold collisions, see also Refs. [178, 179]. The yield of associated particles settles to about 60 % at a time of  $\sim 2.5$  ps, when the part of the wave packet built by continuum states has moved out of the potential well. Afterwards, the control field just 'cools' the system. In fact, at about 10 ps, the entire population is accumulated in the vibrational ground state (not shown).

Of course, the found association yield depends on the properties of the initial wave packet and in particular on the impact energy. It is found, that, if this energy is chosen too large, the efficiency of the process is low because the scattering proceeds to fast. On the other hand, for a much smaller energy, the wave packet moves slow and spreads, an effect being already present in the field-free case. Additionally, the interaction with the field enhances the spreading, and it is well known, that local control schemes works only for fairly localized wave packets [180–183].

It was shown, that the field obtained from LCT gives an excellent association yield if a linear dipole moment is assumed. Within a more realistic description, the dipole moment of HF is used in another calculation, so that the control field has to be determined according to Eq. (9.6). Also, a mean momentum  $\bar{p}$  corresponding to an impact energy of 0.01 eV above the dissociation limit is now chosen. This corresponds approximately to a relative velocity of 1400 m/s and a velocity distribution of 500 m/s, i.e. numbers which can be realized in molecular beam experiments [184]. It is noted that for an the impact energy used before (0.1 eV) the same trends as described below are found but the dynamics proceeds on a different timescale.

The field ( $\lambda = -1.4 \cdot 10^{-1}$  a.u.) and the populations of the vibrational eigenstates are shown in Fig. 9.3. As compared to the case discussed above (Fig. 9.2), the lower mean momentum has the effect that the region, where the vibrational eigenfunctions show a significant amplitude and association becomes possible, is reached at later times. Therefore, the populations of the eigenstates start to rise later. Moreover, the dipole moment now assumes only relatively small numbers at larger distances. As a consequence, the field strength has to be significantly higher to

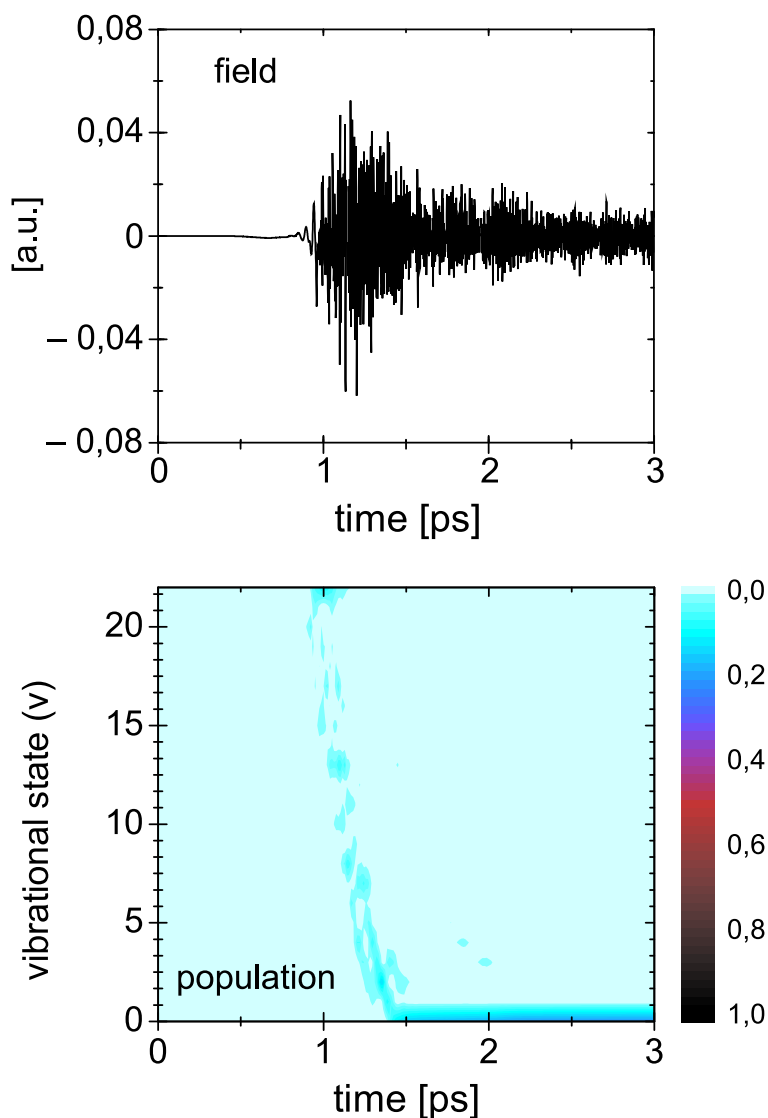


Figure 9.3: Same as in 9.2, but for a calculation incorporating the correct dipole moment of the HF molecule.

achieve association. It is seen, that cooling is now so effective that the vibrational ground state is reached at about 1.5 ps. However, the overall association yield of approximately 25 % is not as good as in the simplified system.

From the discussion above, it is clear that for the  $H + F$  scattering the deviation of the dipole moment from a linear form strongly influences the association yield. This effect is even more dramatic in the case of a  $H + I$  collision which possesses a smaller dipole moment. As before, the control field shows an up-chirp and the different vibrational states are populated consecutively, which underlines the

ladder-descending mechanism. Nevertheless, the total yield of associated particles settles at about 10 %, which is not satisfying.

Therefore, the strategy is adopted to increase the population in a defined vibrational eigenstate. Hence, the field is constructed according to Eq. (9.8). To start the algorithm, the target state is populated initially by choosing the initial wave function as a sum of the Gaussian (Eq. (9.5)) and the target eigenfunction with

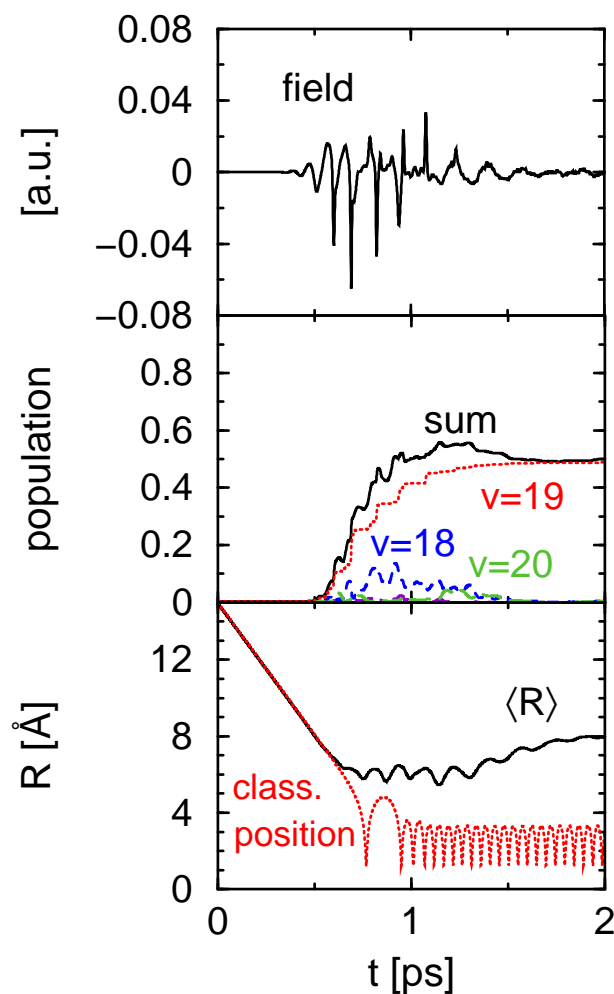


Figure 9.4: Association of HI, where the target is the vibrational eigenstate with quantum number  $v=19$ . The upper panel contains the field. The total population  $P(t)$  and the populations  $P_v(t)$  in various vibrational states ( $v$ ) are shown in the middle panel. The quantum mechanical coordinate expectation value  $\langle R \rangle_t$  is compared to a selected classical trajectory  $R(t)$  in the lower panel.

relative weights of 0.998 and 0.002, respectively. Again, it should be stressed, that this procedure is not necessary, when applying the control field in an experiment or another calculation.

First, the second-highest vibrational state  $v=19$  of HI is chosen as target, employing a value of  $\lambda = 9.0$  a.u. The results are depicted in Fig. 9.4. It is seen that population is selectively transferred into the target state. From the field oscillations (upper panel of Fig. 9.4), a mean frequency can be extracted. The latter matches the energy difference between the impact energy and the eigenenergy of the state with  $v=19$ . Thus, a clearly interpretable control field evolves from local control theory.

To document, that the results can also be understood in an even more intuitive way, classical calculations are performed. Here, a classical particle is subject to the control field from the quantum-mechanical simulation. The particle's position follows the trajectory  $R(t)$  depicted in the lower panel of Fig. 9.4 (dashed line). The expectation value of the inter-atomic distance  $\langle R \rangle_t$  obtained from the quantum calculation is plotted, for comparison. The deviation of the two curves stems from the fact, that the quantum mechanical wave packet is broadly distributed in  $R$ , while in the classical case, only a single trajectory is present. From the latter, it can be readily seen, that the control field is able to achieve association also in the classical regime. The field exerts a force on the particles, which compels them to perform a vibrational motion and takes energy away. The energy of the trapped trajectory is 0.102 eV and deviates not too much from the  $v=19$  eigenvalue of 0.111 eV. This is remarkable and underlines the close relation between wave-packet and classical dynamics [90, 183].

Although similar field strengths as in the previous case are applied here, the overall association yield is now much higher (almost 50 %). This proves, that different approaches are differently suited to achieve photoassociation in the case of local control.

Next, it was chosen to increase the occupation in the lower lying state with  $v=17$ . As can be seen from Fig. 9.5, the population in  $v=17$  steadily becomes larger, but the overall yield is not as good as in the  $v=19$  case. The field shows a higher frequency as in the latter case, corresponding to a higher energy difference between

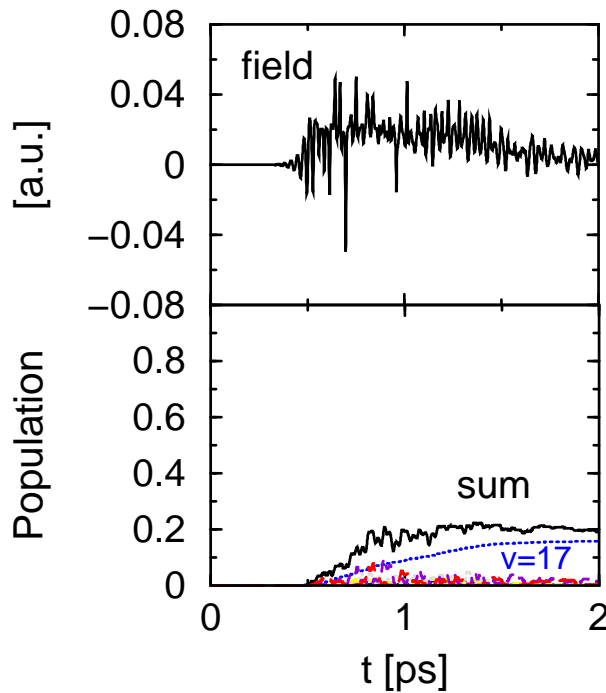


Figure 9.5: The control target is now to increase the population in  $v=17$ .

the continuum states and the bound state.

The trend of a decreasing overall association yield proceeds, if states with even lower quantum numbers are chosen. Defining the vibrational ground state as the target, association does not take place at all. This is documented in Fig. 9.6, which contains the same quantities as Fig. 9.4. Despite the more intense field ( $\lambda = 1.0 \cdot 10^6$  a.u.), only a negligible amount of population is transferred to the vibrational ground state. Nevertheless, a frequency analysis of the field shows, that the energy difference between the states and the ground state is matched. In an attempt to improve the association yield, the projector  $P_T = |\varphi_0\rangle\langle\varphi_0|$ , where  $|\varphi_0\rangle$  is the vibrational ground state of the unperturbed system, was replaced by the (time-dependent) projector containing the eigenstate in the external field, i.e. taking the Stark shift into account. This procedure, however, does not improve the results.

In the lower panel of Fig. 9.6, the quantum mechanical coordinate expectation value is compared to a classical trajectory which is run in the presence of the field (shown in the upper panel). It can be inferred from the figure, that the control field

does not promote association in the classical regime. Here, the classical oscillator is driven far off-resonant, so that its motion does not couple to the driving field. The respective quantum mechanical view is, that the Franck-Condon factors for a direct transition from the continuum states to the ground state are too small to achieve an association. Therefore, within a single electronic state, vibrational eigenstates of low quantum number  $v$  can only be reached by successive de-excitation via a ladder-descending mechanism.

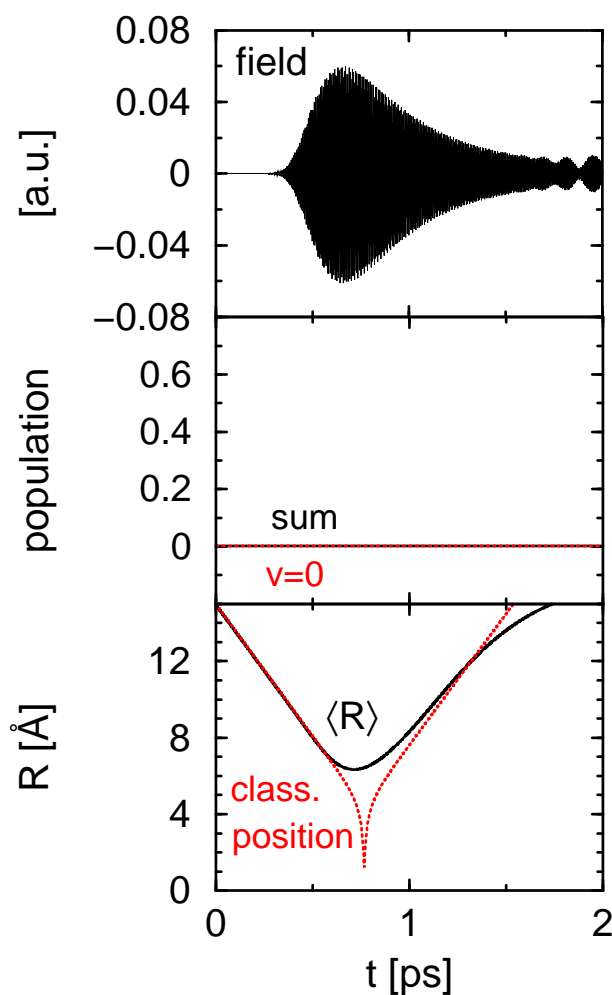


Figure 9.6: Photoassociation of HI. The same quantities as in Fig. 9.4 are shown for the case that the target is the vibrational ground state ( $v=0$ ).



### 9.3 The role of orientation

In an extended model, the rotational degree of freedom is included. The Hamiltonian and the employed propagation scheme are found in Sec. 3.5 (p. 36). It has been shown before, that a straightforward application of LCT to problems including rotation is difficult (see Sec. 7.2, p. 98). Therefore, all control fields discussed in the following part are constructed from the rotationless case, where the angular momentum operator is neglected (i.e.  $\vec{J} = 0$ ).

If the rotational degree of freedom is included, two questions have to be considered. The first is, how does the association yield change, if one starts from thermally populated different initial rotational states; and second, how does a possible rotational excitation from the control field influence the yield. Both questions are addressed in what follows.

The association of H + F is examined in the extended model system including rotations. Here, the field depicted in Fig. 9.3 is chosen to enter into the computations.

The association yield is computed as follows. The population  $P_{vJ}$  in an eigenstate  $\phi_{vJ}$  with vibrational quantum number  $v$  and rotational quantum number  $J$  is evaluated according to

$$P_{vJ} = \langle \phi_{vJ}(R) | \chi_J(R) \rangle, \quad (9.9)$$

where  $\chi_J(R)$  is the expansion coefficient of the reduced wavefunction, see Eq. (3.28). The total association yield  $P$  is then obtained by summation:

$$P = \sum_v \sum_J P_{vJ}. \quad (9.10)$$

In the numerical example, the initial  $J$  values are chosen as  $J_{Start} = \{0, \dots, 8\}$ . The laser field then couples the states with different quantum number  $J$ , so that rotational excitation becomes possible. However, in the present case,  $J_{Start}$  stays more or less solely occupied, as can be taken from Fig. 9.7. There, the population  $P_J = \langle \chi_J(R) | \chi_J(R) \rangle$  of the different rotational states is plotted at time  $t = 3.0$  ps for the initial wave packet starting in  $J = 0$  (black filled bars) and  $J = 6$  (dashed/red transparent bars). About 80 % of the molecules are still in the same rotational state as they started from. This statement holds at least for  $J_{Start}$  values  $< 8$  (not shown).

Here, the field from Fig. 9.3 is taken as control field in a slightly varied form. It is artificially set to zero after  $t = 2.5$  ps, when no significant effect is visible anymore for fixed orientation. This is also the case if rotations are included. After the interaction is set to zero, the different populations stay strictly constant, which is taken as a proof for numerical correctness (not shown). The latter may not be given, if the parts of the wave packet, which move out of the computed grid, are not removed smoothly enough. Then, reflections at the grid border would lead to interferences with the bound parts, giving rise to oscillations of the populations despite a zero field. Here, the cut-off function is defined in a half-gaussian shape, which decays from 1 to 0 over an spatial interval of  $24 \text{ \AA}$  starting at  $21 \text{ \AA}$ .

The association yield  $P$  at  $t = 3.0$  ps is displayed in Fig. 9.8 for different values of  $J_{Start}$ . As expected, the yield is less, if compared to the rotationless case (Fig. 9.3) and settles now at  $\sim 6\%$ . The energy expectation values for the different cases reveals, that here a cooling of the system is realized (not shown).

It is interesting, that in the present case,  $P$  is more or less the same for the different initial quantum numbers  $J_{Start}$ . Thus, an explicit thermal averaging is not necessary. As a conclusion, the fields derived for fixed orientation are still able to

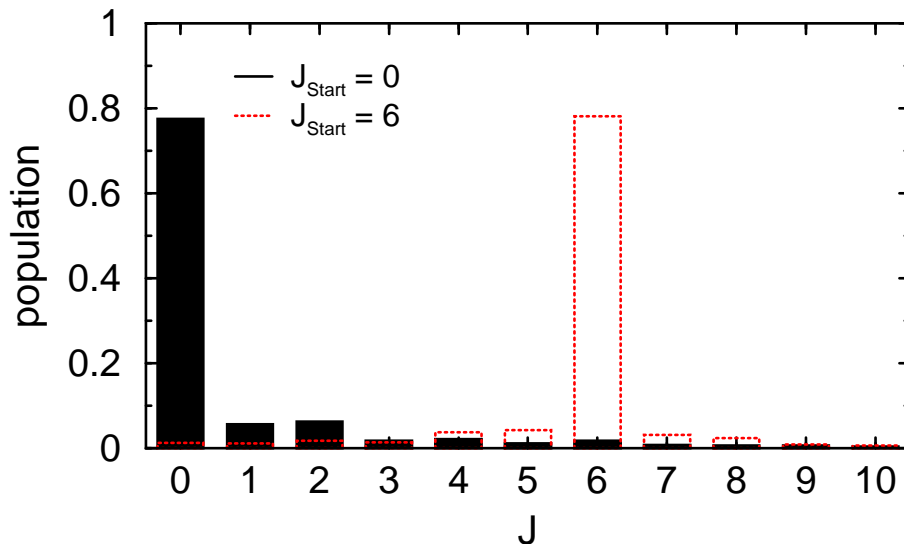


Figure 9.7: Distribution of the populations  $P_J$  in different rotational states at time  $t = 3.0$  ps for the initial wave packet starting in  $J = 0$  (black filled bars) and  $J = 6$  (dashed/red transparent bars).

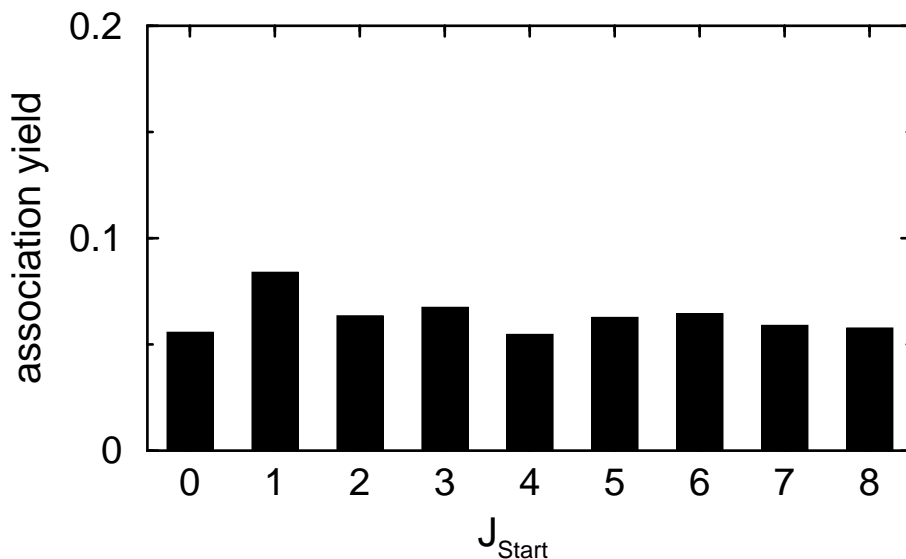


Figure 9.8: Association yield  $P$  for different  $J_{\text{Start}}$  at  $t = 3.0$  ps.

achieve photoassociation, even if the rotational degree is included. This proves, that the simplified analysis at fixed orientation is justified to gain insight into the mechanism of control fields.

To summarize this chapter, local control theory is applied to photoassociation reactions. The control fields are derived from two objectives. The requirement of a steadily decreasing system energy leads to an effective population of lower vibrational levels. The association yield strongly depends on the form of the dipole moment function which, for the numerical examples investigated, is rather localized and of small magnitude in the case of the HI molecule. During the interaction time, the population is transferred successively from higher to lower vibrational states. This 'ladder-descending' is reflected in the control field, which shows an up-chirp matching the increasing level spacing with decreasing vibrational quantum number.

If the objective is chosen to maximize the population in a selected vibrational level, it is found that high lying vibrational states can be accessed with an excellent yield whereas it is not possible to build photoassociated molecules in states with low vibrational quantum numbers. Here, the control fields carry the frequency corresponding to the energy difference between the impact energy and the eigenenergy of the target state.

Photoassociation is also achieved, if the rotational degree of freedom is included. Despite the decreased total yield, still a cooling is realized in the treated case. This justifies the simplified approach of fixed orientation, where the control mechanism is easily understood. It is even more intriguing that representative classical trajectories subject to the perturbation caused by the control field derived quantum mechanically, reflect the quantum results in a very clear way.

# 10 Molecular dump processes induced by chirped laser pulses

A vast amount of experiments and calculations have been carried out using tailored laser pulses. Mostly, a first pulse, inducing an electronic excitation, is shaped, while a second pulse, e.g. a dump pulse, which triggers a de-excitation, remains unchanged. Here, the reversed case is considered, where a pump pulse is followed by a shaped dump pulse. For an experimental realization, a probe pulse may be necessary to measure the outcome of the preceding processes such that a pump/shaped-dump/probe scheme evolves.

The study discloses information on potential energy surfaces and the wave-packet evolution in the excited-state of molecular systems. Several concepts have been developed to invert spectroscopic data to underlying potentials with unshaped pulses, e.g. high resolution pump-probe [185] or wave-packet interferometry [186–188]. Also schemes with a chirped excitation pulse have been analyzed regarding potential energy surfaces [189, 190].

In the common approach, a tailored electric field is applied to a quantum system in equilibrium to selectively excite it and steer it to a desired target state. However, the involved processes often crucially depend on properties of the potentials far away from the Franck-Condon region of the initial excitation. Hence, an analysis of selective de-excitation (dumping) with a shaped dump pulse, that can have a spectrum different from the pump pulse, is a promising approach, both to gain control over chemical reactions and to study the involved potentials. One of the main differences is, that the laser pulse now interacts with a moving wave packet instead of a stationary state. This is the reason, why the shape of the pulse may provide additional information not only on the underlying potentials, but also on the wave-packet evolution in the excited state. Unshaped dump pulses are fre-

quently applied [191–194], while a pump/shaped-dump/probe scheme has only been reported recently [17], demonstrating the versatility of shaped dump pulses.

Here, a theoretical analysis is performed, showing which shaped dump pulse efficiently transfers population back to the ground state after electronic excitation. Therefore, two general pulse forms are considered. First, the influence of a linear chirp is investigated. Second, a triangular phase is applied in frequency domain, yielding colored double pulses. Moreover, the concept of shaped-dump fitness landscapes is presented as a powerful tool to extract not only the shape of the underlying potentials, but also the velocity, dispersion and shape of the wave packet in the dumping region.

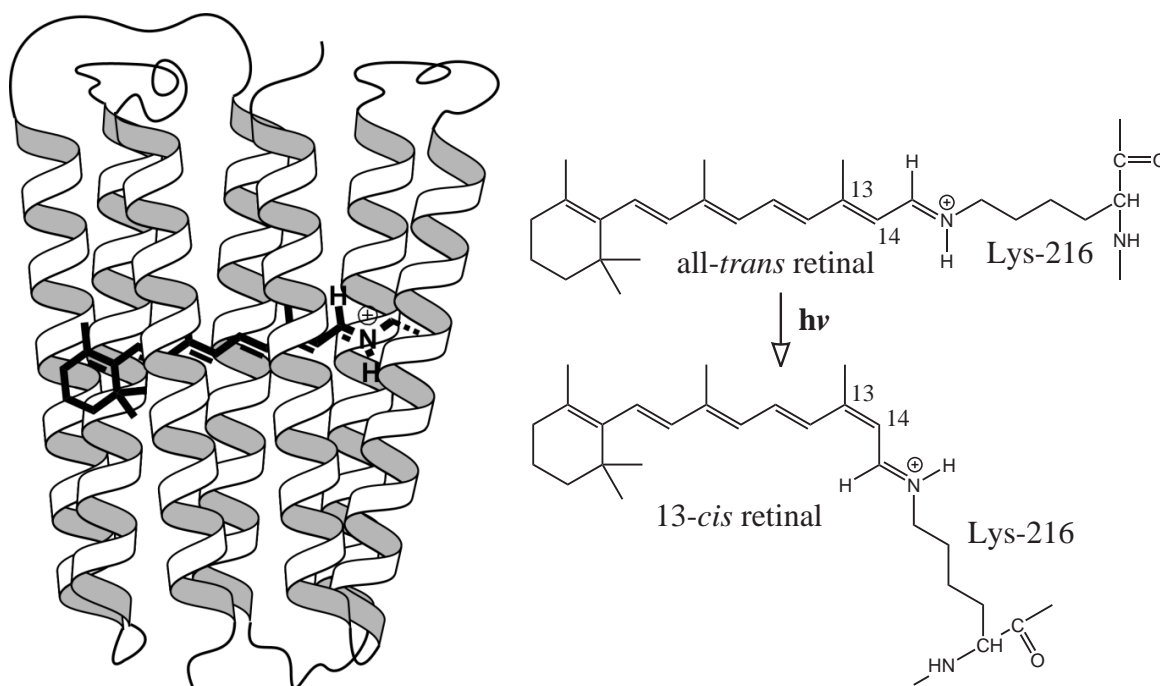


Figure 10.1: On the left-hand side, a ribbon model of bacteriorhodopsin is shown.

On the right-hand side, the photoisomerization reaction of the retinal chromophore is depicted.

The starting point for a model system is the retinal photoisomerization reaction in bacteriorhodopsin. Bacteriorhodopsin is a protein of 26 kDa (1 Dalton = 1 u), which can be found in the purple membrane of the archaebacterium *Halobacterium halobium*. Stimulated by visible light, the protein drives the synthesis of ATP (adenosine triphosphate) by translocating a proton from the cytoplasmic side of the membrane to the extracellular side. The light-absorbing chromophore is the

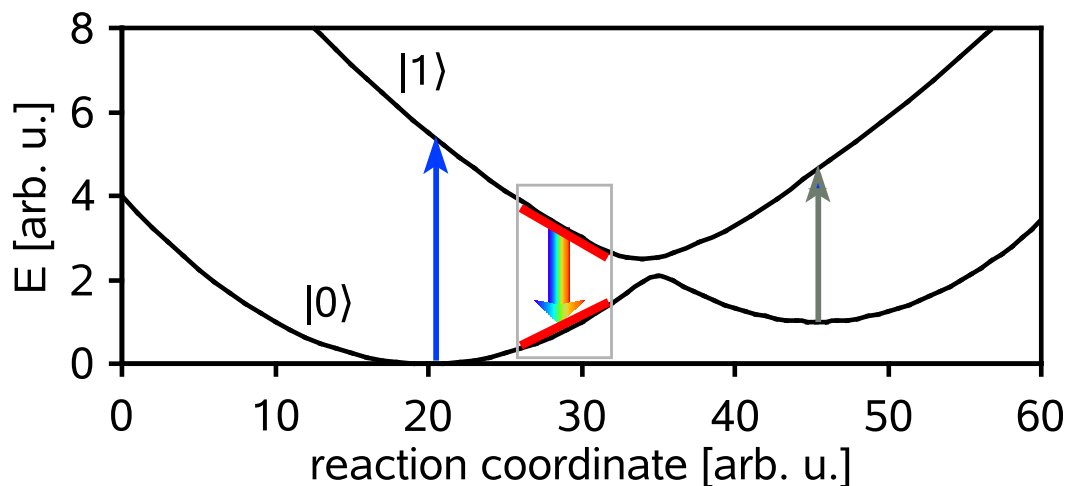


Figure 10.2: Simplified potential curves for the photoisomerization of retinal. Additionally, the transitions induced by a pump/shaped-dump/probe scheme are indicated by arrows. The calculations focus on the shaped dump pulse.

retinal molecule, which is covalently bound to the amino acid *Lys-216* of the protein (see Fig. 10.1). By photon absorption, the all-*trans* retinal is transformed to its 13-*cis* form. Afterwards, it spontaneously reverts to the all-*trans* isomer, and the photocycle is repeated [195].

As the retinal molecule, leave alone the bacteriorhodopsin complex, exhibits a very high number of degrees of freedom, an active mode analysis provides a simplified description of the favored reaction in one dimension [196]. A model scheme for the resulting potential curves of the rotation around the C13-C14 bond are depicted in Fig. 10.2. Details of the model used here are given in what follows.

## 10.1 Model

Only two electronic states ( $|0\rangle$ ,  $|1\rangle$ ) are considered. The parts of the potential curves, where resonant transitions can take place, are approximated by the linearized potentials  $V_0$  and  $V_1$  (gray box in Fig. 10.2). In this way, a system is introduced as simple as possible, which nevertheless includes all necessary features. The two states are then coupled by the interaction  $W_{nm}$  ( $nm = 01, 10$ ), where the transition dipole moment elements  $\mu_{nm}$  are set to 1 a.u., induced by (shaped) laser

pulses centered around 800 nm. Thus, the model Hamiltonian reads

$$H = |0\rangle(T + V_0)\langle 0| + |1\rangle(T + V_1)\langle 1| + |0\rangle W_{01}(t)\langle 1| + |1\rangle W_{10}(t)\langle 0|. \quad (10.1)$$

The pump process is simulated only indirectly by placing a Gaussian-shaped wave packet at time zero in the excited state, while the dump-pulse interaction is described exactly. The probe pulse is not necessary in the simulation, because the result of the dump process is already available. It is accessible by calculating the norm of the wave packet in the respective electronic state.

## 10.2 Linear chirp

At first, the influence of a linear chirp on the dump pulse is investigated. Here, the momentary frequency is varied linearly in time (see Sec. 2.3.1) and could be tuned to e.g. follow the diminishing potential energy gap indicated in Fig. 10.2. Nevertheless, the maximum intensity becomes smaller by introducing a chirp. Thus, the transform-limited pulse could be more efficient, although being resonant for a shorter time than the chirped pulse. These questions are addressed in the following.

Table 10.1: Parameters for the model potentials and the initial wave function (everything in a.u.).

$\Psi(t=0)$	$V_0$		$V_1$		
$\beta_i$	0.02	$m_0$	$1 \cdot 10^{-3}$	$m_1$	$-1 \cdot 10^{-3}$
$x_i$	66.14	$n_0$	$5.7 \cdot 10^{-3}$	$n_1$	$213.8 \cdot 10^{-3}$

Here, the potentials are set to (in a.u.)  $V_0 = m_0x + n_0$  and  $V_1 = m_1x + n_1$ . The system is assigned arbitrarily a reduced mass of 35500 a.u. and the initial wave packet is chosen as a Gaussian in the excited state of the form  $\Psi(x, t=0) = \sqrt{\frac{2\beta_i}{\pi}} e^{-\beta_i(x-x_i)^2}$ . The corresponding parameters can be found in Tab. 10.1. At the initial position  $x_i$ , the potential energy difference amounts to 600 nm. After 626.3 fs, the position of the wave packet (monitored by the expectation value of



the reaction coordinate) equals the value of  $x_d = 75.59$  a.u., where the potential energy difference (1.55 eV) is matched by the central frequency (800 nm) of the transform-limited dump pulse. The latter is constructed with a Gaussian envelope, where the full width at half maximum (FWHM) of the electric field is 10 fs (corresponding to an intensity FWHM of 7 fs). To compare the chirped pulses to the transform-limited one with the same pulse energy, the primary pulse is multiplied with  $e^{-i\frac{b_2}{2}(\omega-\omega_0)^2}$  in frequency domain (compare Eqns. (2.60) and (2.61), p. 15). Here,  $b_2$  is varied from  $-5000$  fs<sup>2</sup> to  $5000$  fs<sup>2</sup>.

The dump process is sketched in Fig. 10.3. At time  $t = 0$ , the wave packet starts to evolve down the gradient of the excited-state potential. After gaining some speed, it is dumped to the ground state, while the kinetic energy persists. For this reason, the wave packet moves a little bit uphill, before turning around and advancing down the slope of the ground-state potential. All these processes may influence the shape of the optimal dump pulse.

To investigate the effect of a linear change in the momentary laser frequency, chirp scans were computed at pulse energies corresponding to intensities of  $5 \cdot 10^9$  W/cm<sup>2</sup> to  $5 \cdot 10^{12}$  W/cm<sup>2</sup> for the transform-limited pulse. The population, remaining in the excited state after the dump process is finished, is plotted in Fig. 10.4.

For the smallest pulse energy, the curve exhibits a minimum at  $b_2 \approx -400$  fs<sup>2</sup>, i.e. a tailored field with this chirp parameter is the most efficient one. With higher pulse energy, a peak is arising around this value. For the highest energy, corresponding to an intensity of  $5 \cdot 10^{12}$  W/cm<sup>2</sup> for the transform-limited pulse, a second peak is visible around  $b_2 = 0$  fs<sup>2</sup>. From these curves, it is obvious, that shaped pulses are

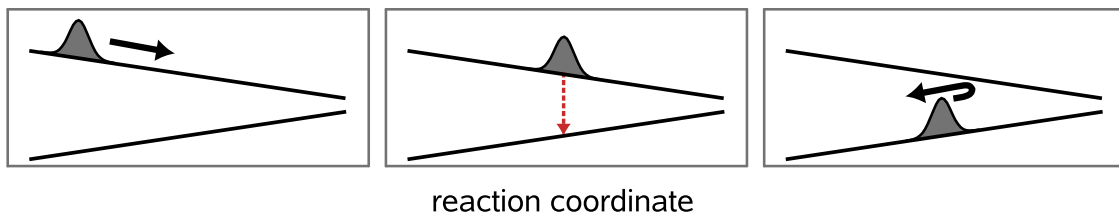


Figure 10.3: Scheme of the dump process. Kinetic energy gained in the excited state (left panel) is preserved during the dumping (middle panel). Therefore, the wave packet moves a little uphill in the groundstate, before turning around (right panel).

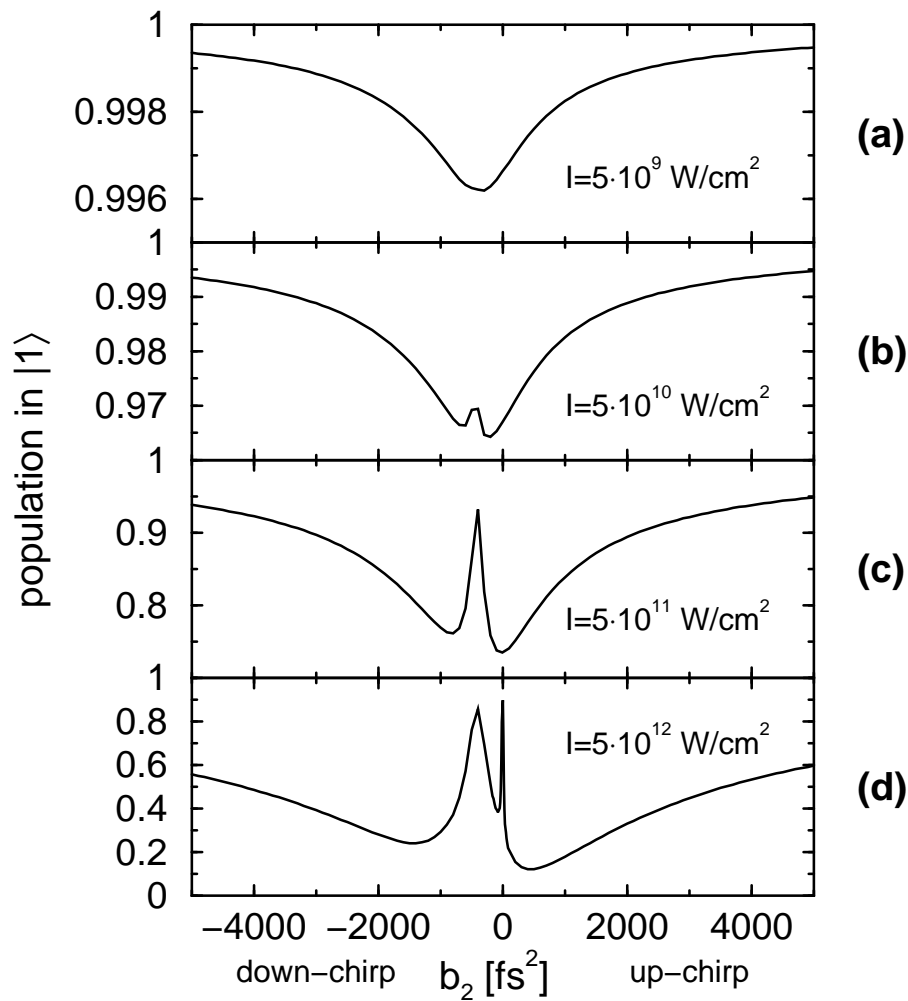


Figure 10.4: Linear chirp scan for different pulse energies. The different panels show the population, which remains in the excited state after the dump process, for various chirp parameters. The pulse energy corresponds to an intensity of  $5 \cdot 10^9 \text{ W/cm}^2$  to  $5 \cdot 10^{12} \text{ W/cm}^2$  for the transform-limited pulse, as indicated.

superior to transform-limited ones.

To investigate the origin of the peaks at higher intensities, the evolution of the population in time are regarded at distinct parameters  $b_2$ . The case, where the transform-limited pulse holds an intensity of  $5 \cdot 10^{12} \text{ W/cm}^2$ , is examined in Fig. 10.5. Here, the parameters belonging to the three minima and the two maxima from Fig. 10.4 (lowest panel) are chosen. In the upper panel of Fig. 10.5, the corresponding fields are plotted to visualize the variation of the pulse shape with

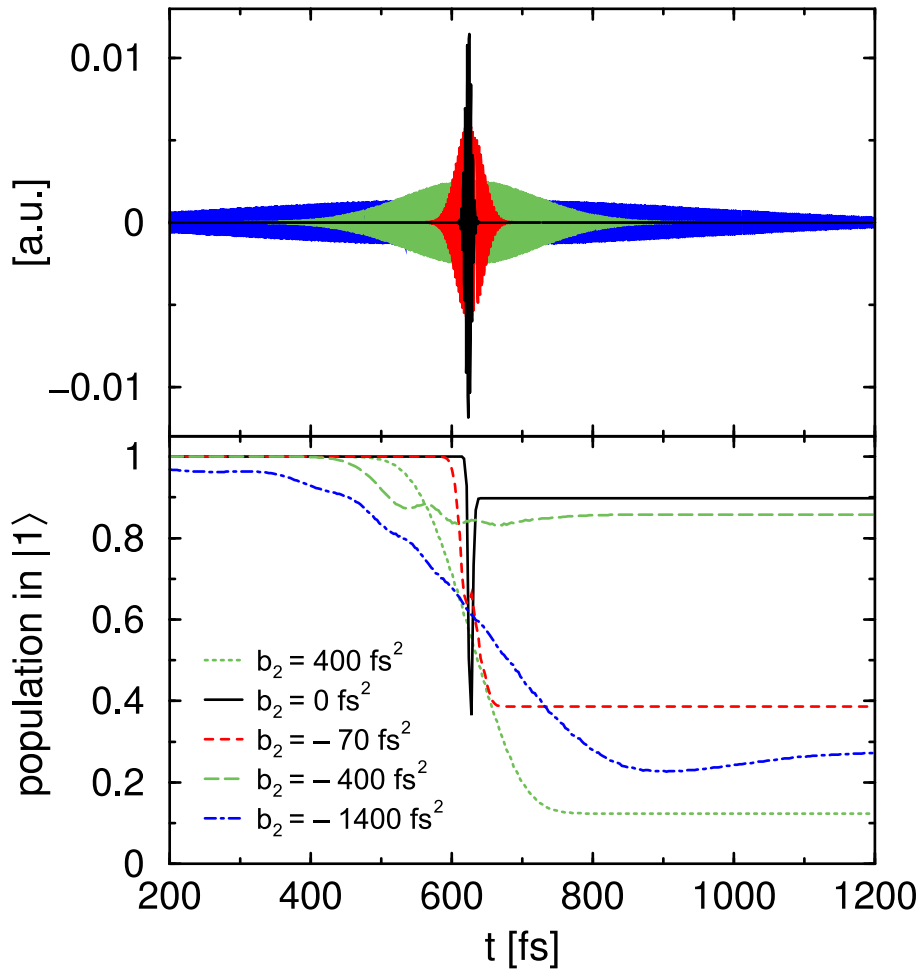


Figure 10.5: Temporal evolution of the population in the upper state for different chirp parameters (lower panel) and corresponding laser fields (upper panel). Here, the unchirped pulse exhibits a maximum intensity of  $5 \cdot 10^{12} \text{ W/cm}^2$ . The chirp parameters are chosen to show characteristic points from the chirp scan in Fig. 10.4.

changing chirp parameter. The lower panel contains the time-dependent population of the excited state for the above-mentioned chirp parameters. From the curve with  $b_2 = 0 \text{ fs}^2$ , it becomes clear, that Rabi oscillations take place. This explains the second peak in the chirp scan (Fig. 10.4). Also for  $b_2 = -400 \text{ fs}^2$ , Rabi-like oscillations are found. This parameter corresponds to the first peak, which is observed in the chirp scans of higher intensity. In contrast, no such oscillations are seen for  $b_2 = 400 \text{ fs}^2$ .

For a further analysis of the system's interplay with the laser field, the influence of

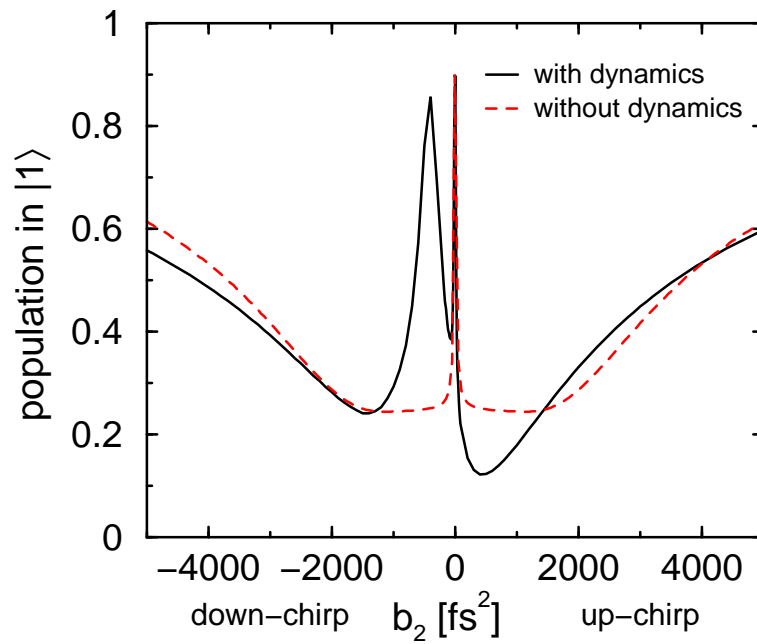


Figure 10.6: Comparison of calculations with and without including the kinetic propagation. The chirp scan is implemented for laser pulses of the same energy. The transform-limited pulse features an intensity of  $5 \cdot 10^{12} \text{ W/cm}^2$ .

the dynamics is explored. Here, a calculation including the full dynamics is compared to one, where the wave packet is centered in the dump region and the kinetic propagation is suppressed. The shape of the wave packet for the non-dynamical computation was taken from a calculation including the kinetic propagation but without a laser field at time  $t = 626.3 \text{ fs}$ , when the wave packet is centered in the dumping region. As can be seen from Fig. 10.6, the computation without dynamics yields a totally symmetric curve (dashed/red) in respect to the parameter  $b_2$ . The peak at  $b_2 = 0 \text{ fs}^2$ , which stems from Rabi oscillations due to the high intensity of the field, is still visible. On the other hand, the peak around  $b_2 = -400 \text{ fs}^2$  has vanished. Thus it can be concluded, that the occurrence of this maximum is a due to the molecular dynamics.

The peak around  $-400 \text{ fs}^2$  can be explained with the diminishing energy gap passed by the wave packet. Here, the momentary frequency exactly equals the potential difference over a large period of time. To prove this statement, it is proceeded as follows.

The chirp parameter, which should match the slope of the potential energy difference, is derived from a calculation, where no field is present. There, two points of the expectation value of the reaction coordinate are taken corresponding to different times:

1.  $x_1 = \langle x \rangle(t_1) = 75.423116$  a.u. with  $t_1 = 620.8$  fs
2.  $x_2 = \langle x \rangle(t_2) = 75.779264$  a.u. with  $t_2 = 633.6$  fs

The potential energy difference at these points is:

1.  $\Delta V(x_1) = 0.057276$  a.u.
2.  $\Delta V(x_2) = 0.056564$  a.u.

Thus, the momentary frequency  $\omega(t)$  has to change in time according to

$$\frac{d\omega}{dt} = \frac{\Delta V(x_2) - \Delta V(x_1)}{t_2 - t_1}. \quad (10.2)$$

As can be easily deduced from Eqns. (2.60), p. 15 (see expression for  $a_2$ ), and (2.65), p. 15, the time derivative of the frequency is connected to the chirp parameter  $b_2$  by [197]

$$\frac{d\omega}{dt} = \frac{b_2}{\frac{(4ln2)^2}{\varpi_I^4} + b_2^2}, \quad (10.3)$$

where  $\varpi_I = \frac{4ln2}{\tau_I}$  is the spectral width with  $\tau_I$  being the FWHM of the temporal intensity. From the above equation (10.3), it can be directly deduced that

$$b_2 = \frac{1}{2\frac{d\omega}{dt}} \pm \sqrt{\frac{1}{4\left(\frac{d\omega}{dt}\right)^2} - \frac{(4ln2)^2}{\Delta\omega^4}}. \quad (10.4)$$

By this formula, the chirp parameter, which is necessary to match the present energy gap at every moment in time, is calculated. Here,  $\frac{d\omega}{dt} = -1.345 \cdot 10^{-6}$  a.u. is given by Eq. (10.2),  $\Delta\tau = \frac{10 \text{ fs}}{\sqrt{2}} = 292.328$  a.u. and consequently,  $\Delta\omega = 0.0094845$  a.u. As a result, two values for  $b_2$  emerge:

$$b_2 = \begin{cases} -434.27 \text{ fs}^2 \\ -0.75 \text{ fs}^2 \end{cases}$$

The one around  $-400 \text{ fs}^2$  perfectly matches the peak already found in the above figures. The other value of  $-0.75 \text{ fs}^2$  seems not to cause a peak in the chirp scan. To understand this, the pulse duration has to be considered. The latter is evaluated according to [197]

$$\Delta t = \sqrt{\Delta\tau^2 + b_2^2 \Delta\omega^2}. \quad (10.5)$$

The corresponding curve for the used pulse is depicted in Fig. 10.7 (upper panel). Additionally, the slope of the momentary frequency as a function of the chirp parameter  $b_2$  is displayed. As already shown, a slope value can be produced by two different  $b_2$  values. Although the change of the momentary frequency in time is the same for the resulting pulses, they differ in their duration. Regarding the above found values of  $-434 \text{ fs}^2$  and  $-0.75 \text{ fs}^2$ , the difference in duration is substantial.

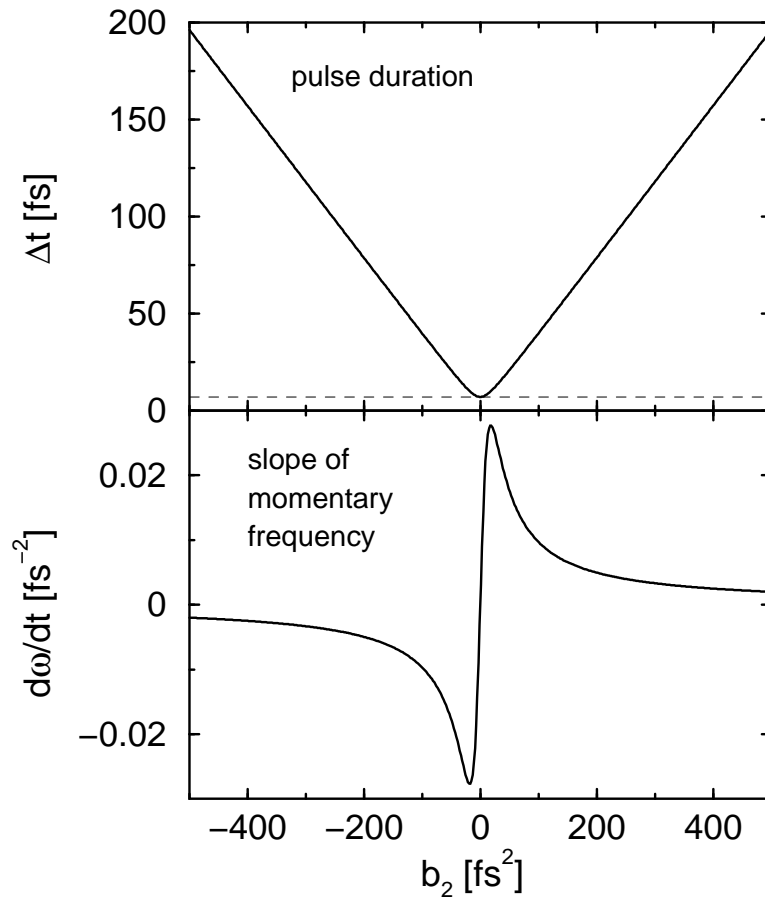


Figure 10.7: Upper panel: Pulse length  $\Delta t$  of a linearly chirped pulse in dependence on the second order spectral phase  $b_2$ . The horizontal dashed line indicates the shortest possible pulse duration  $\Delta\tau$ . Lower panel: Slope  $\frac{d\omega}{dt}$  of the momentary frequency  $\omega$  as a function of  $b_2$ .

The parameter of  $-0.75 \text{ fs}^2$  leads to a pulse, which is only slightly longer than and exhibits almost the same intensity as the transform-limited one. Here, the influence of the chirp can be neglected. In contrast, the pulse at  $b_2 = -434 \text{ fs}^2$  possesses much lower intensity and the time of interaction is substantially elongated. Thus, a tuning to match the diminishing energy gap, which is passed by the wave packet, is very important in this case.

Another effect, which also originates from the wave-packet motion, is the tilt of the residual curve in Fig. 10.6, if the peaks are disregarded. While the non-dynamical computation yields a symmetric curve, the full calculation shows, that a negative chirp parameter is superior to the positive one with the same absolute value.

This result is also found experimentally, as was shown by Vogt *et al.* [17]. There, the isomerization of retinal in bacteriorhodopsin is investigated. The all-*trans* isomer is excited with a 400 nm pump pulse. After propagation on the  $S_1$  potential energy surface, the created wave packet returns to the  $S_0$  state via a non-radiative transition. Without a dump pulse, the 13-*cis* isomer is produced with 65% efficiency.

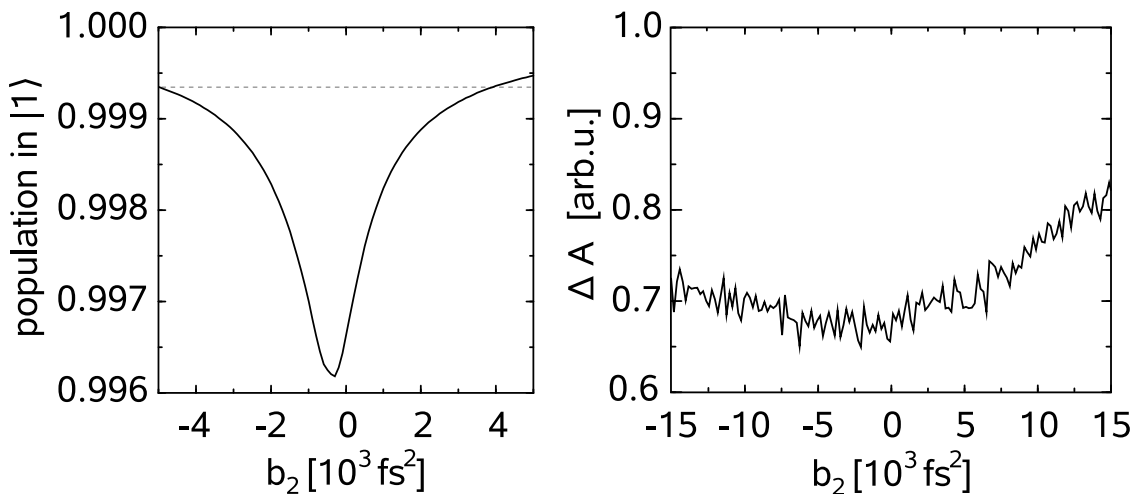


Figure 10.8: Right: Experimental absorption difference  $\Delta A$  as a function of the second-order spectral phase (i.e., linear chirp), with an additional linear phase offset (pump-probe delay) of 200 fs. The transient absorption signal (400 nm pump, 800 nm dump, 660 nm probe, 150 ps pump-probe delay) is proportional to the amount of produced 13-*cis* isomers of retinal in bacteriorhodopsin. Left: The calculated curve for low intensities (compare Fig. 10.4) shows the same qualities as the experimental one. Note the different scales.

This product is probed with a 660 nm pulse applied 150 ps after the pump pulse. If a (shaped) dump pulse is employed at a delay of 200 fs after the pump pulse (delay time of most efficient dumping), the absorption difference depicted in Fig. 10.8 is measured. As the dump pulse reduces the amount of produced 13-*cis* isomers, the minimum in the curve corresponds to the most efficient dump parameter. As the experimental study is conducted in solution, eventual peaks originating from processes like Rabi oscillations average out. Nevertheless, the better performance of negatively chirped pulses is clearly visible from the tilt in the curve. For comparison, the calculated curve for a pulse energy corresponding to an intensity of  $5 \cdot 10^9$  W/cm<sup>2</sup> for the transform-limited pulse is depicted on the left-hand side of Fig. 10.8.

To conclude, it was shown, that not the transform-limited pulse is best at transferring population back to the ground state after an excitation. Regarding linearly chirped pulses, the wave-packet dynamics is crucial to understand the shape of the optimal pulse. It was found, that the momentary frequency of the most effective pulse is tuned to match the diminishing energy gap, which is passed by the wave packet. Here, Rabi-like oscillations occur already at rather low intensities. In general, a negatively chirped field (down-chirp) is superior to a positively chirped one with the same absolute value of  $b_2$  for the regarded system. The latter finding was also verified experimentally [17].

### 10.3 Triangular phase

In this section, the pulse parameterization is restricted to triangular spectral phase patterns (Sec. 2.3.1). Starting from a transform-limited pulse, a linear spectral phase is applied to one part of the pulse spectrum. As a linear spectral phase shifts a pulse temporally, this spectral region is shifted e.g. forward in time. The same phase, but with opposite sign, is applied to the other part of the spectrum. Consequently, this spectral region is then shifted backward in time. The result is a double pulse, where one subpulse comprises only lower frequencies and the other subpulse consists of only higher frequencies. The resulting electric field is termed a “colored” double pulse.

In the example shown in Fig. 10.9, the application of a triangular phase to a transform-limited pulse is illustrated. If the slope of the triangular phase is small,



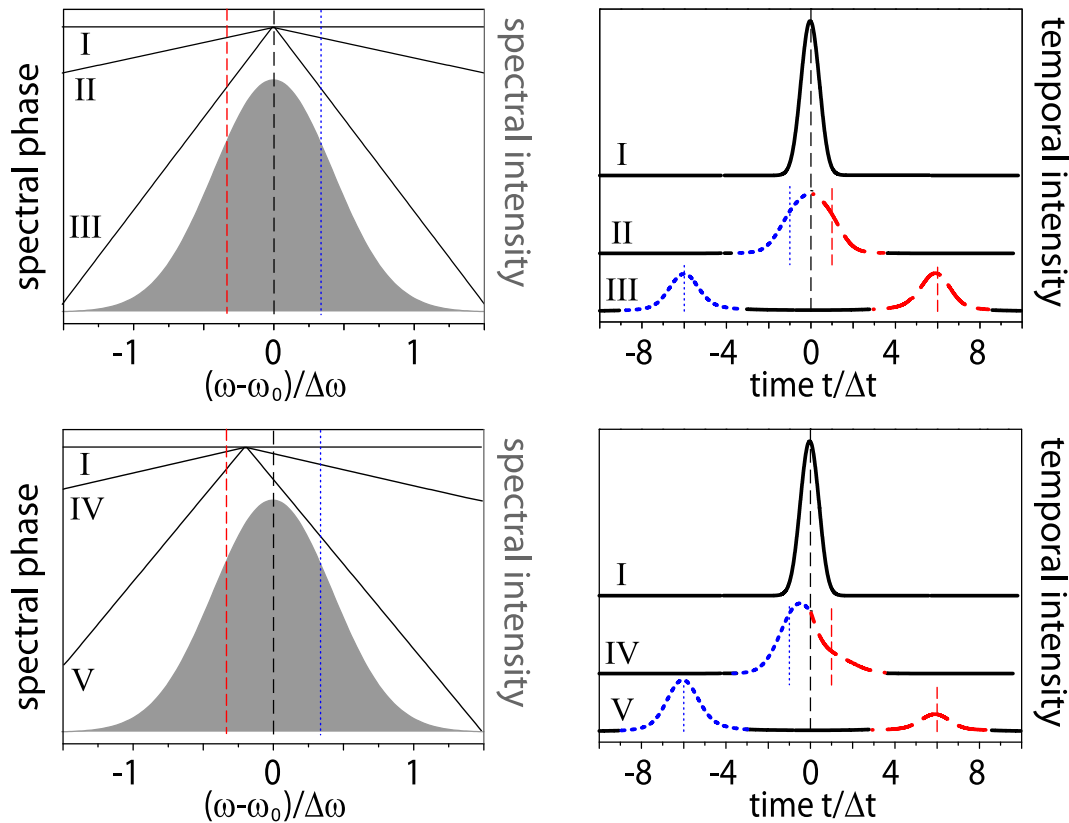


Figure 10.9: Creation of a double pulse by applying a triangular phase. Upper panels: To a transform-limited pulse (light gray), a triangular phase with different slopes is applied in frequency domain (left panel). Vertically indicated are the carrier frequencies of the different pulses (compare right panel, same color code). The subpulses of the resulting double pulse are more or less divided in time domain (right panel). Lower panels: Changing the break point (left panel) leads to different subpulse intensities in time domain (right panel).

the two subpulses are not yet divided. The pulse still has only one distinct maximum (see example II in Fig. 10.9), but is (approximately linearly) chirped. A steeper phase results in clearly divided subpulses with red-shifted or blue-shifted carrier frequency, respectively (example III). The latter is only a mean value, because a subpulse actually exhibits an intricate chirp, see below.

The frequency, where the sign of the linear spectral phase is flipped, is called the “spectral break point”. If it is centered at the carrier frequency of the transform limited pulse  $\omega_0$ , then two subpulses of equal intensity emerge. Otherwise, the relative peak heights vary as well as the spectral composition of the two subpulses

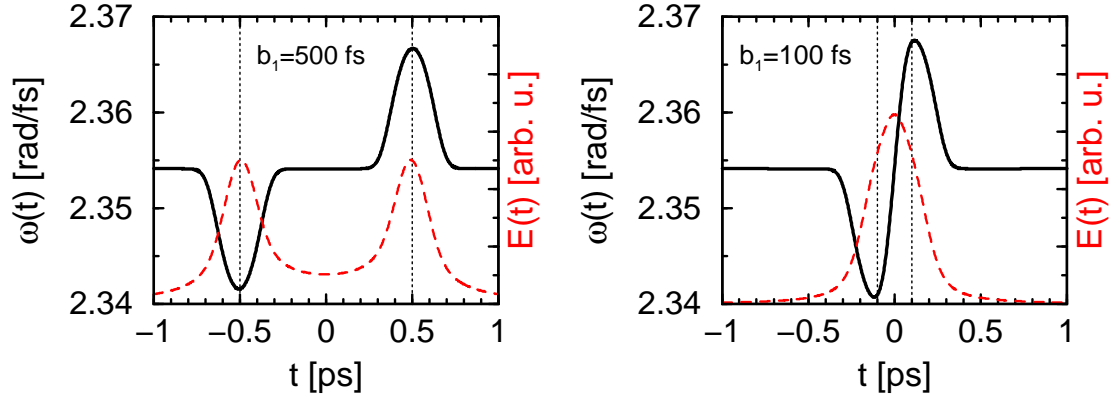


Figure 10.10: Momentary frequency  $\omega(t)$  (straight lines) of different colored double pulses. The corresponding field envelope (dashed/red lines) is overlaid to ease the interpretation. The phase slope is chosen as  $b_1 = 500$  fs (left panel) and  $b_1 = 100$  fs (right panel). This results in a subpulse separation of  $\Delta t = 1000$  fs and  $\Delta t = 200$  fs, respectively, which is indicated by vertical lines.

[198, 199]. Here, pulses with a smooth shoulder (see example IV in Fig. 10.9) or two subpulses of different intensity can be obtained (example V).

To illustrate the behaviour of the chirp for colored double pulses, the momentary frequency  $\omega(t)$  is plotted in Fig. 10.10 for two examples. The momentary frequency can be calculated according to

$$\omega(t) = \frac{d}{dt} \arccos \left( \frac{\Re[E(t)]}{|E(t)|} \right), \quad (10.6)$$

where  $\Re[E(t)]$  denotes the real part of the complex-defined field. In Fig. 10.10, the phase slope  $b_1$  is chosen as 100 fs or 500 fs, respectively, and the corresponding field envelope is overlaid (dashed/red line).

To investigate the effect of different pulse parameters and to visualize the outcome simultaneously in a clear way, so-called fitness landscapes [200, 201] are employed. In this way, only a small set of variables is used, compared to e.g. feedback algorithms (see Sec. 4.5). Nevertheless, it is expected to gain additional insight into the complex control mechanism of large systems by scanning only a small number of parameters, but now thoroughly and extensively.

The potentials of the model system are defined as before, but with slightly changed

parameters (see Tab. 10.2). In this way, longer pulses can be treated, which resemble the ones used in the corresponding experiment (performed by P. Nuernberger, G. Vogt, T. Brixner), see below. Here, not only a single wave packet is examined but also a double wave packet. The latter is created either by placing the Gaussian (parameters like before, but renormalized to 0.5) into the excited state at  $t = 0$  fs and add another such function at  $t = 1000$  fs, or as the sum of two such functions but now centered at different positions  $x = 62.36$  and  $x = 69.92$ . The difference between the two kinds of double wave packet is, that for the first one, the velocity of the two peaks differ at a given time but is equal when passing the same region of the potential, while for the second kind, the case is inversed.

Table 10.2: Parameters for the model potentials and the initial wave function (everything in a.u.).

$\Psi(t = 0)$		$V_0$		$V_1$	
$\beta_i$	0.02	$m_0$	$1 \cdot 10^{-4}$	$m_1$	$-1 \cdot 10^{-4}$
$x_i$	66.14	$n_0$	$737 \cdot 10^{-4}$	$n_1$	$1458 \cdot 10^{-4}$

After the initial excitation step at time  $t = 0$ , the wave packet will accelerate and evolve down the the potential  $V_1$ . At a later time, the energy gap between the potentials at the position of the wave packet will match the frequencies of the dump pulse. If this time coincides with the arrival time of the dump pulse, efficient transfer back to the lower potential  $V_0$  is possible. Here, the duration of the transform-limited pulse is chosen to be shorter than the time interval during which dumping is possible at all. The FWHM of the electric field is set to 150 fs (corresponding to an intensity FWHM of 106 fs).

For a single wave packet, either the transform-limited pulse or more likely, a pulse with a slight, negative triangular phase should be most efficient (the latter compares to a linearly chirped pulse, see Sec. 10.2). In the first case, the intensity is maximal, while in the second case, the frequency follows the diminishing energy gap between the two potential curves, which is passed by the wave packet.

To find out, which of the mentioned pulse forms is better and whether the intuitive, simplified picture is correct at all, numerically exact calculations (no perturbation

theory) were performed. For the first fitness landscapes, both the phase slope  $b_1$  of the triangular spectral phase, and the delay time  $t_{PD}$  between the pump pulse (not simulated) and the temporal center of the double pulse is varied. The phase slope  $b_1$  takes effect on the respective carrier frequencies of the subpulses and on the subpulse separation  $\Delta\tau$ . Thus, for a given  $t_{PD}$ , the two subpulses are symmetrically shifted apart in time with increasing  $b_1$ .

The amount of remaining excited-state population after interaction of a single wave packet with the dump pulse is determined for each pulse shape, resulting in the fitness landscape shown in Fig. 10.11. On the right, different sketches illustrate five relevant points of the landscape. It is clearly visible, that the fitness landscape is not symmetric around  $b_1 = 0$ , but the minimum is shifted to values  $b_1 < 0$ . For large subpulse separations, the single wave packet is only influenced by either of the two subpulses, leading to less efficient dumping (expressed in the X-shaped structure of Fig. 10.11a), or by neither of them, thus no dumping occurs (light

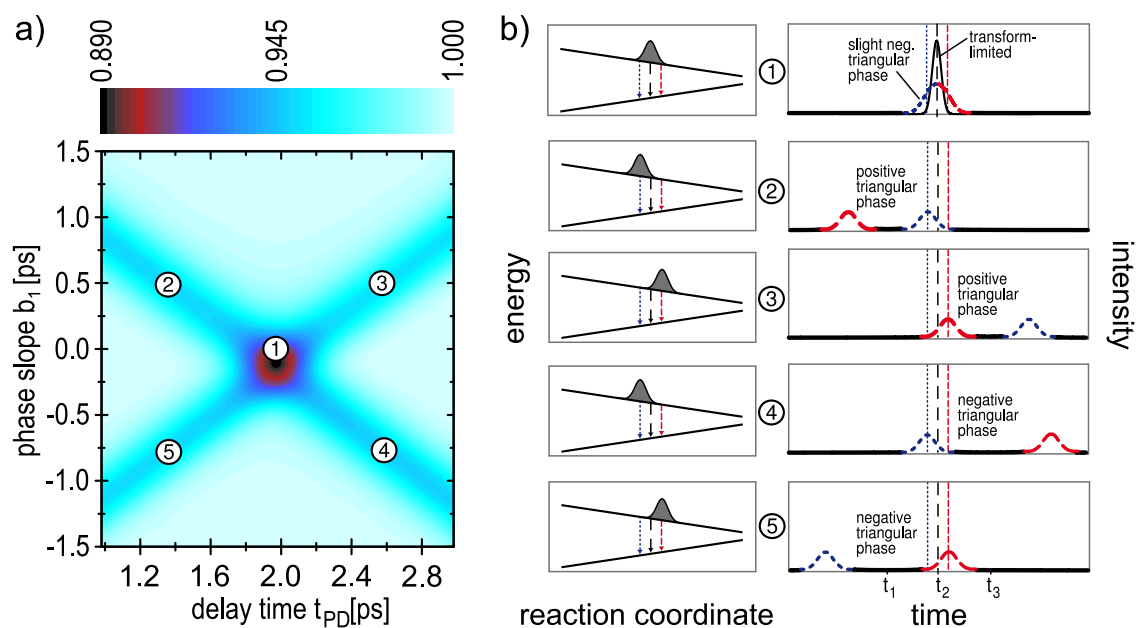


Figure 10.11: (a) Fitness landscape for a single wave packet. The excited-state population after the interaction with the dump pulse is shown. The two varied parameters are the delay time  $t_{PD}$  (abscissa) and the spectral phase slope  $b_1$  (ordinate). (b) The sketches indicate the connection between wave packet position and different double pulses (corresponding numbers at the sketches and in the landscape).

regions in Fig. 10.11a). The position of the minimum confirms that a dump pulse with a triangular spectral phase is superior to a transform-limited dump pulse. One can conclude that conventional pump–dump experiments could be performed more efficiently, if an appropriately shaped dump pulse was employed.

Instead of a single wave packet, a double wave packet can be formed, if different reaction paths towards the dumping region are present (e.g. if the wave packet has been split after the excitation by passing a barrier). The same mechanism as for a single wave packet accounts for dumping each part of the double wave packet, separately. Additionally, if the temporal separation of the two subpulses is high enough, for a single wave packet, only one of the pulses will have any effect. But in the case of a double wave packet, there is also in this case the possibility, that both subpulses are dumping parts of the wave packet. Here, the first subpulse might dump from the first part of the wave packet, and the second subpulse from the second part of the wave packet, respectively. Because the subpulses differ in their spectral composition, it then also makes a difference whether the high or the low frequency subpulse comes first.

The fitness landscape shown in Fig. 10.12 is obtained, if a double wave packet is employed, where the two parts have the same velocity in the dumping region. The landscape now exhibits four distinct minima. Thus, at first sight, it is possible to deduce whether the wave packet is split into several parts or not. One can conclude, that shaped-dump fitness landscapes allow an identification of the wave-packet shape.

The four minima of Fig. 10.12a are discussed in more detail in the following. Minima ① and ② relate to a situation where dumping occurs either from the first part or the second part of the wave packet by a shaped pulse of higher intensity. This situation is illustrated in Fig. 10.12b. There, the double wave packet together with the potentials (left side) and the electric fields performing the dumping process (right side) are shown. Either solely the first or the second part of the WP is dumped, and analogously to a single wave packet, a pulse with a slight triangular phase dumps more efficiently than a transform-limited pulse.

In contrast, minima ③ and ④ are due to dumping with the red-shifted subpulse

from the first part of the wave packet and with the blue-shifted subpulse from the second part of the wave packet (minimum ③) or vice versa (minimum ④). From the corresponding sketches, it also becomes clear, why the whole double X-shaped structure of the landscape is shifted to values of  $b_1 < 0$ . The reason is, that the red-shifted subpulse is in resonance at a later time (here:  $t_3$  or  $t_6$ ) than the blue-shifted subpulse (at  $t_1$  or  $t_4$ ) regarding one wave-packet part. As a consequence, the subpulse separation is smaller ( $\Delta\tau = t_4 - t_3$ ) for the pulse belonging to minimum ③ (positive spectral phase) than for the one ( $\Delta\tau = t_6 - t_1$ ) belonging to minimum ④ (negative spectral phase). Nevertheless, the corresponding delay times are the same. In other words, the subpulses will efficiently dump from different points on the potentials. Thus, the differences in the  $b_1$  values for optimal dumping reflect the shrinking energy gap between the potentials. To conclude, shaped-dump fitness landscapes allow a deduction of the shape of the potential in a region far away from the Franck-Condon region of the initial excitation.

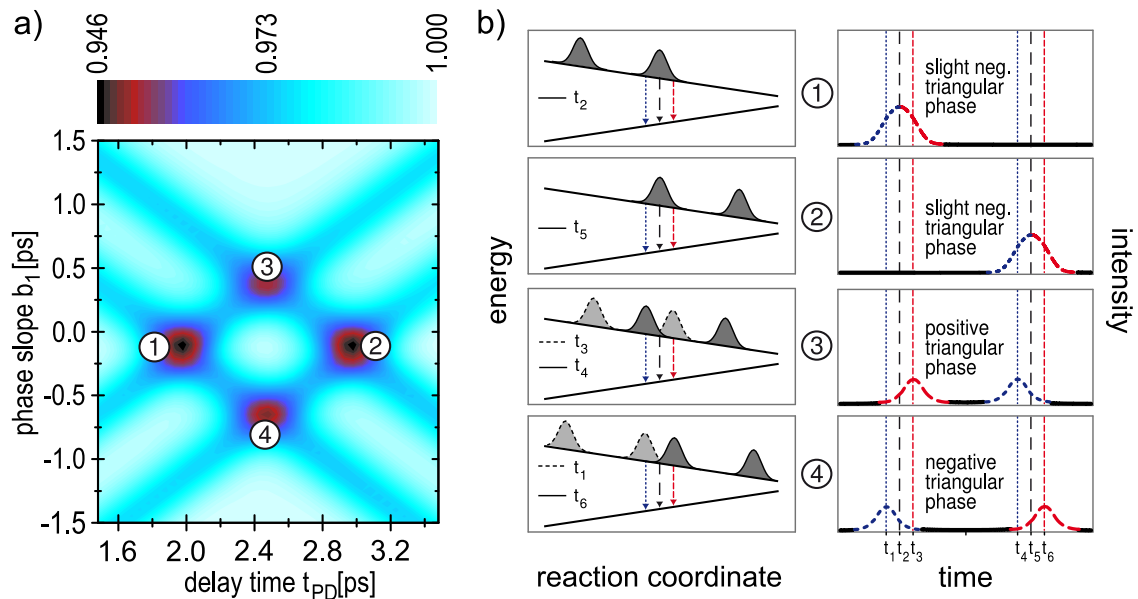


Figure 10.12: (a) Fitness landscape for a double wave packet, whose parts exhibit the same velocity in the dumping region. The excited-state population after the interaction with the dump pulse is depicted for different delay times  $t_{PD}$  and the spectral phase slopes  $b_1$ . The four emerging minima can be explained according to the sketches in (b). Left: position of the WP at times  $t_1$  to  $t_6$  when efficient dumping occurs. Right: Pulse shapes for efficient dumping from either one part of the wave packet only or from both parts.

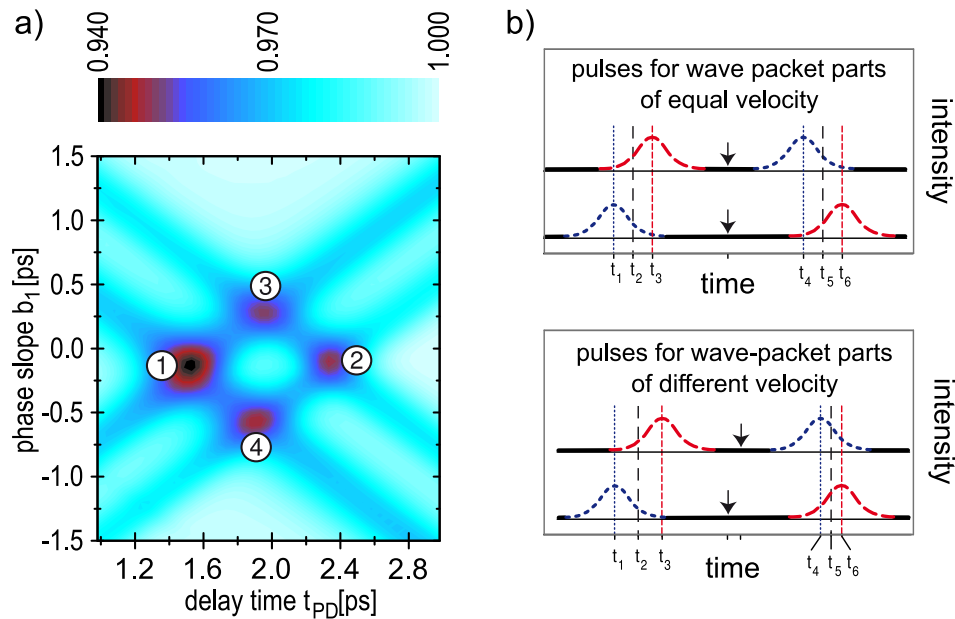


Figure 10.13: (a) Fitness landscape for a double wave packet of the type, where the second part exhibits a higher velocity in the dumping region than the first one. (b) Illustration of the different effects of the two types of double wave packet (compare Fig. 10.12). When the parts of the double wave packet are of the same velocity (upper panel) the temporal centers (indicated by arrows) of the two double pulses coincide, while they differ if the velocities are different (lower panel).

Minima ① and ② are more pronounced than minimum ③ and ④. The conclusion is drawn, that a single shaped pulse dumping only from one part of the wave packet is more effective than a double pulse dumping from both parts, which is not clear in advance.

Next, the second type of double wave packet is employed, where the velocity of the parts differs in the dumping region. Such a double wave packet could be created e.g. by exciting with two pump pulses of different colors at the same time. Here, the fitness landscape depicted in Fig. 10.13 evolves. Compared to the landscape of Fig. 10.12, a similar double-X structure is found, but the symmetry of the latter is lost. Now, minimum ① can be clearly identified as global. The reason for minimum ② (where only from the second part of the double wave packet is dumped) being less pronounced than minimum ① is wave-packet spreading. As the second part of the double wave packet starts at the same time than the first one but enters

the dumping region at a later time, it is more dispersed, which results in a decreased dumping efficiency. Once again, the phase slopes  $b_1^{(1)}$  and  $b_1^{(2)}$  corresponding to minima ① and ② have small negative values (i.e. the associated electric fields can be regarded as single pulses with a chirped character), which are not identical, but  $|b_1^{(1)}| < |b_1^{(2)}|$ .

Minima ③ and ④ now occur at different delay times, in contrast to Fig. 10.12, where the delay times were the same. To illustrate the cause of this difference, the corresponding intensity profiles are sketched in Fig. 10.13b. For equal velocity of the wave-packet parts (upper panel), the temporal centers of the two dump fields coincide as indicated by arrows, i.e.  $t_{PD}^{(3)} = t_{PD}^{(4)}$ . If the second part of the wave packet is faster than the first part in the dumping region (lower panel), then the associated time interval between dumping with different frequencies is actually shorter for the second subpulse ( $t_4$  to  $t_6$ ) than for the first one (with  $t_1$  to  $t_3$ ). As a consequence, the temporal centers  $t_{PD}^{(3)}$  and  $t_{PD}^{(4)}$  do not coincide anymore (the observation that  $|b_1^{(1)}| < |b_1^{(2)}|$  can be explained accordingly). This observation leads

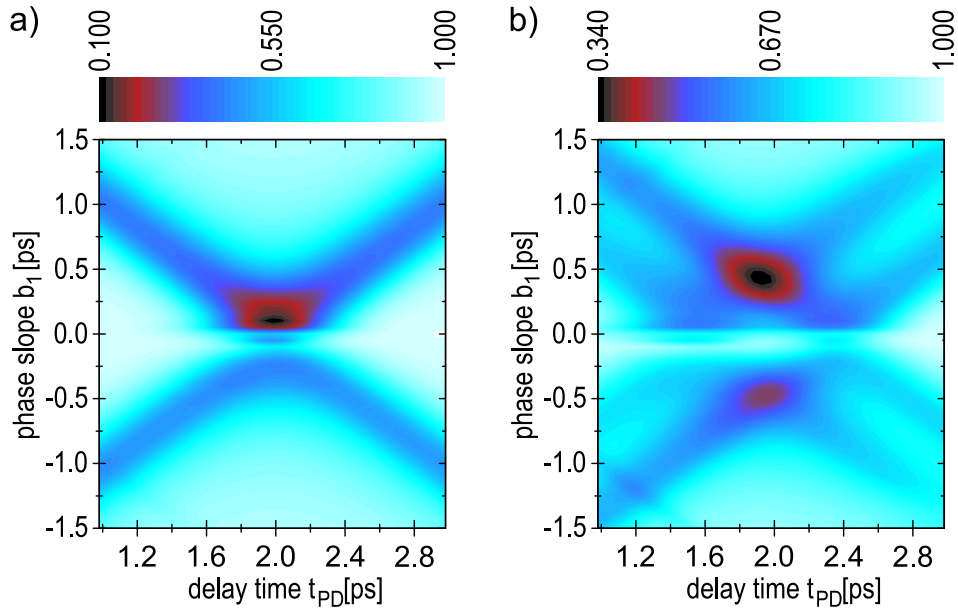


Figure 10.14: Fitness landscapes for higher pulse energies, corresponding to an intensity of  $5 \cdot 10^{10}$  W/cm<sup>2</sup> for the transform-limited pulse. Similar results as before emerge as well for a single wave packet (a) as for a double wave packet (b). Effects from Rabi oscillations at low phase slope values are the only visible difference.



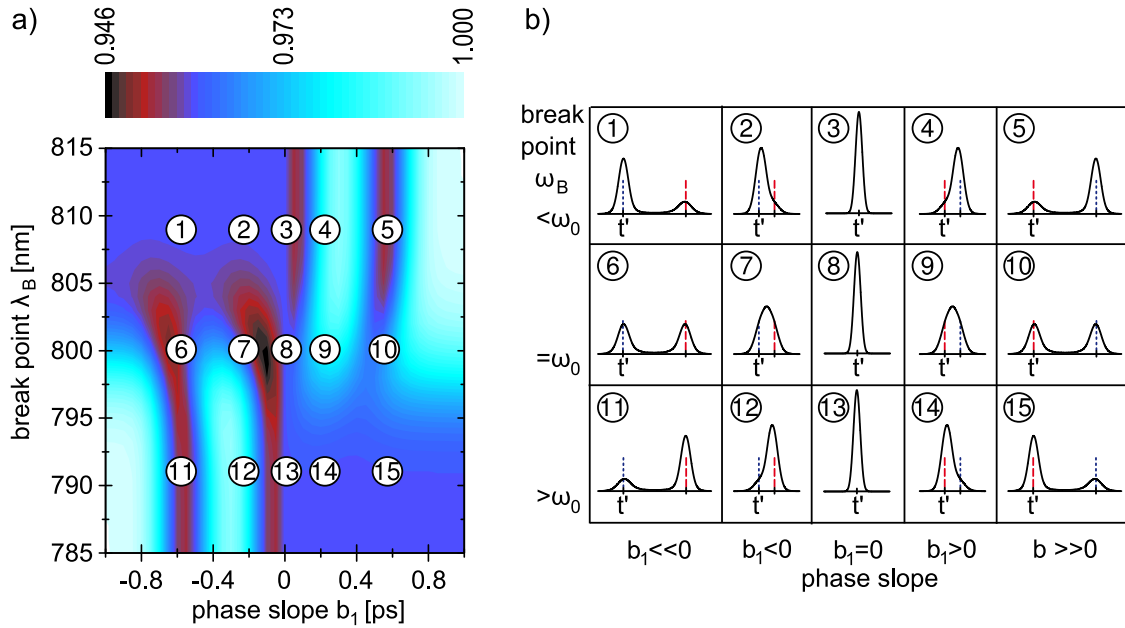


Figure 10.15: Fitness landscape, where the two varied parameters are the spectral breakpoint (ordinate) and the spectral phase slope (abscissa). Here, a double wave packet is investigated. Its parts hold the same velocity in the dumping region. The sketches in the right display exemplary intensity profiles for different regions of the fitness landscape (corresponding numbers). Blue-dotted/red-dashed lines indicate the subpulse comprising higher/lower frequency components, respectively. A change of  $\omega_B$  leads to a variation of the relative peak heights and the spectral composition of the subpulses.

to the inference, that shaped-dump fitness landscapes allow qualitative deductions of the wave-packet velocity (positive/negative) and its dispersion (large/none).

Additional calculations with higher field strengths show similar results, qualitatively, except for visible effects from Rabi oscillations at low phase slope values, where high intensities are present. The shaped-dump landscapes for a single wave packet and a double wave packet are displayed in Fig. 10.14. Here, the transform-limited pulse exhibits a maximum intensity of  $5 \cdot 10^{10} \text{ W/cm}^2$ .

As the next step, the parametrization of the shaped-dump fitness landscapes is changed. Combining the conclusions from fitness landscapes under different parametrizations can provide additional insight into the characteristics of the system. To demonstrate this, we vary the phase slope  $b_1$  again, but additionally the spectral

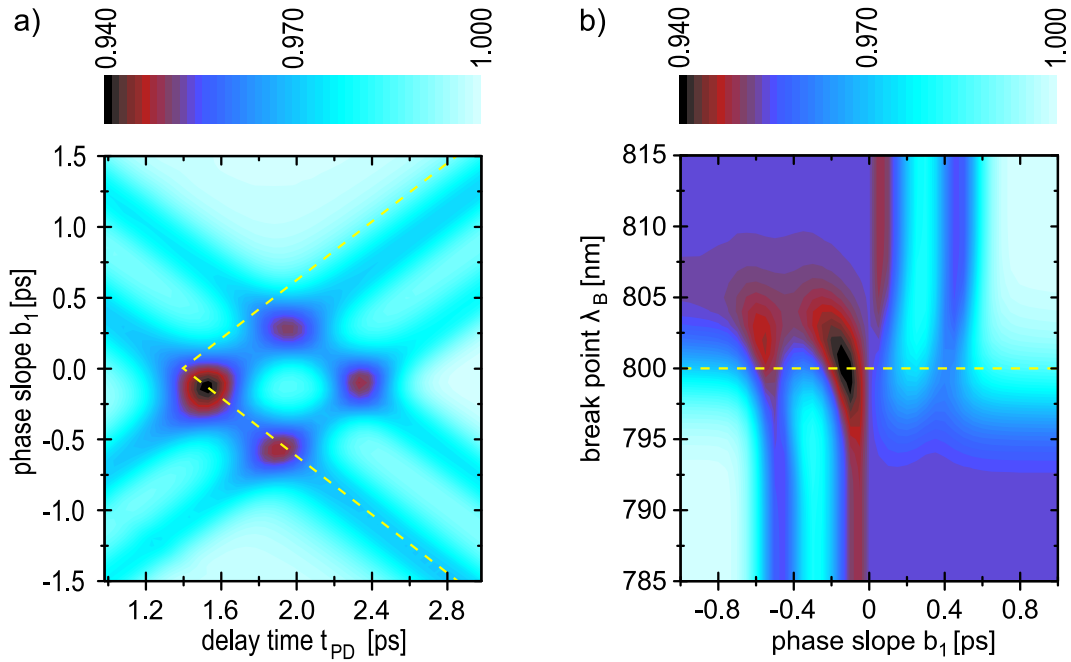


Figure 10.16: Comparison of fitness landscapes under different parameterization for a double wave packet with parts of different velocity in the dumping region. The dashed, yellow lines indicate a set of parameters leading to the same pulses in both landscapes. (a) Delay time vs. phase slope is plotted. (b) The varied parameters are phase slope and spectral break point.

break point  $\omega_B$  (or the corresponding wave length  $\lambda_B$ ). Results from the landscapes discussed so far enter as follows: The time  $t_{PD}$  for most efficient dumping is taken from the corresponding landscapes. This time now determines a new delay time  $t'$ , where the first of the two subpulses is fixed. As a result, the old delay time (between the pump and the double pulse center)  $t_{PD}$  is changed with varying  $b_1$  according to  $t_{PD} = t' + |b_1|$ .

In Fig. 10.15, the fitness landscape under the new parameterization is plotted for the double wave packet with parts of equal velocity. On the right-hand side of the figure, a sketch illustrates which dump pulses are employed and how they correspond to the data points in the fitness landscape. Also in this parameterization, it can be directly deduced whether a double wave packet is present or not, because for the double wave packet, two furrows appear (at nos. ⑤ and ⑩), which are not present in the single wave-packet landscape (compare Fig. 10.17).

The double wave packet, where the two parts exhibit different velocities in the dumping region, leads to the fitness landscapes displayed in Fig. 10.16. Here, both parameterizations are shown for comparison. The dashed, yellow line indicates, where the same parameters occur in both landscapes. This helps to visualize the connection between both parameterizations. Moreover, it is shown, that the global minimum from the landscape on the left (delay time vs. phase slope) is included in the landscape on the right (phase slope vs. break point). In the latter landscape, a dark region of most efficient dumping appears around this point. A thorough analysis of this region shows, that the best spectral break point is found around 800 nm. A shift occurs if  $t'$  is not exactly centered at the optimal delay time. Note, that the optimal value for  $t'$  is only matched by subtracting the value of  $b_1$  from the delay time, where the minimum appears. Only in this way, the point on the yellow line of Fig. 10.16a is retrieved, where the break occurs. This point is necessary to include the global minimum from Fig. 10.16a in the landscape of Fig. 10.16b. Nevertheless, even more efficient dump pulses could be found in general, by changing

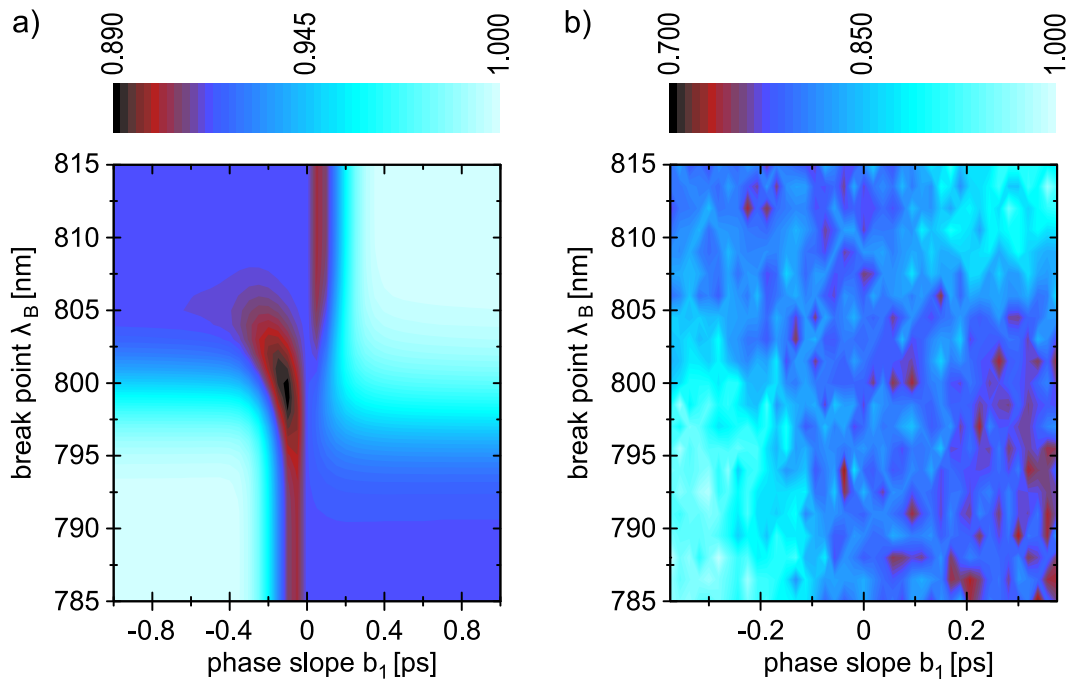


Figure 10.17: Fitness landscapes derived from a simulation (a) and recorded experimentally (b). A single wave packet is treated in the calculation. The experiment investigates the retinal photoisomerization in bacteriorhodopsin. For further experimental details and additional information see Ref. [17].

the parameterization.

The same conclusions can be drawn from the landscape obtained for a single wave packet (see Fig. 10.17a). Once again, the optimal pulse features a phase slope of  $b_1 < 0$ . As already mentioned, the furrows, which appear in the double wave-packet landscapes, have vanished, because they correspond to effective dumping with both subpulses of the double pulse at a large subpulse separation.

A first experimental fitness landscape under the same parameterization is shown in Fig. 10.17b for the retinal photoisomerization in bacteriorhodopsin. Although the noise level is too high to draw the conclusions derivable from the simulations in Figs. 10.15, 10.16 or 10.17a, the resemblance confirms that shaped-dump fitness landscapes can be recorded, even of complex biomolecular systems. Thus, the measurement encourages, that the method will prove to be a powerful tool in future experiments.

The simulations clearly indicate, that shaped-dump fitness landscapes give a good understanding of the excited-state evolution. Again, one could choose another parameterization in which the newly found most efficient dump pulse is included and record a fitness landscape in order to see, if even a more efficient pulse is found. This procedure can also be regarded as a systematic approach to iteratively improve the pulse shape, thus one mimicks the way of a learning algorithm towards the optimal solution, but with a lot of additional information facilitating an interpretation. Furthermore, with fitness landscapes employing colored double pulses information about the wave-packet evolution can be deduced. Not only a direct observation whether the wave packet is subdivided or not is possible, but also the shrinking energy gap and the speed and dispersion of the wave packet in the dumping region can be determined by analysis of the fitness landscape. Moreover, it was proven, that appropriately shaped pulses are able to dump more efficiently than transform-limited pulses. The possibility to systematically adapt the dump pulse to optimally dump the wave packet allows to explore dynamics not accessible in a similar way with other spectroscopic methods.

# 11 Summary

In this work, the laser control of molecules was investigated theoretically. In doing so, emphasis was laid on entering vectorial properties and in particular the orientation in the laboratory frame. Therefore, the rotational degree of freedom had to be included in the quantum mechanical description. The coupled vibrational and rotational dynamics was examined, which is usually not done in coherent control theory. Local control theory was applied, where the field is determined from the dynamics of a system, which reacts with an instantaneous response to the perturbation and, in turn, determines the field again. Thus, the field is entangled with the quantum mechanical motion and the presented examples document, that this leads to an intuitive interpretation of the fields in terms of the underlying molecular dynamics. The limiting case of a classical treatment was shown to give similar results and hence, eases to understand the complicated structure of the control fields. In a different approach, the phase- and amplitude shaping of laser fields was systematically studied in the context of controlling population transfer in molecules.

In a first example, electric fields were derived, which efficiently serve the objective to pump energy into a system (heating) or take energy away (cooling). It was demonstrated, that the determined fields are able to induce an effective control and for the heating case, are able to fragment sodium iodide in the excited electronic state. Regarding the cooling fields, a relaxation of the vibrational motion is achieved. The resulting IR pulses can be interpreted to be consistent with a ladder-climbing mechanism, where the vibrational levels with different energetic separation represent the rungs of a ladder. In the classical view, this mechanism corresponds to an in-phase-driven oscillator for the heating process and an out-of-phase-driven oscillator for the cooling case.

If a predissociation channel is included in the model system, the decay rates for the predissociation process are modified to a great extent by the constructed IR

pulses. In discussing the decay mechanisms of NaI interacting with control fields, the internal energy as well as the Stark shifts of the coupled potentials had to be taken into account. On one hand, the energy transfer influences the average relative velocity of the nuclei, and on the other hand, the external field modifies the potential curves in the crossing region. The interplay of both effects determines the time-dependence of the product yields. In the cooling case, the predissociative excited state can be stabilized, whereas in the heating case, excited-state dissociation can be triggered. Thus, it follows that the ratio between excited-state dissociation and predissociation – and hence, the ratio of different reaction products – can be controlled.

The model for investigating excited-state fragmentation was further extended. Contrary to the former studies, the treatment included the complete field-coupling and also non-adiabatic coupling between the two electronic states. Two field components were constructed within local control theory. Whereas the first component was used to transfer population to the excited state, the second field was chosen to induce energy deposition in the excited state, what finally should lead to dissociation. The sequential and the simultaneous application of such fields produces similar product yields. This is due to the frequency mismatch of the two components: the first field consists of a pulse train, where the sub-pulses are characterized by the electronic transition frequency. On the other hand, the second field oscillates with the mean excited-state vibrational frequency which is much smaller.

A further extension of the NaI model system included the rotational degree of freedom. Here, the wave-packet dynamics not in a control field but in static electric fields was investigated at first. Due to the strong permanent dipole moment of the molecule in its electronic ground state, an orientation is induced. Upon femtosecond excitation, a wave-packet motion is initiated in the predissociative excited electronic state. The bonding character in the latter changes from covalent to ionic, if the wave packet reaches larger ( $<7 \text{ \AA}$ ) interatomic distances. The change between these two bonding situations induced by the quasi-bound vibrational motion is important for the interaction with the static external field. If the wave packet is localized in the covalent region of the potential, where the dipole moment is negligible, the external field is not experienced, whereas in the ionic branch the interaction is large. This leads to an enhanced orientation of the molecule along

---

the axis of the applied field, which is influenced by the vibrational motion. A rotational dynamics can be observed with a period, which becomes shorter as the field strength increases.

Polarization sensitive pump-probe experiments were simulated, where a time-delayed probe pulse initiates a transition to a higher electronic state. The fluorescence yield from the latter is then detected as a function of the time delay. With probe-pulse polarization vectors chosen to be either parallel or perpendicular to the static field direction, different signals are obtained. The ratio of the latter directly monitors the rotational motion of the molecule, which thus allows for an experimental real-time observation of field induced orientational dynamics.

In the same way as the static fields, also fields from local control theory were applied to the extended model including rotations. Once again, excited-state photofragmentation of the NaI molecule was chosen as target. As shown before, a 100 % dissociation of the excited molecules can be achieved for fixed orientation, where the field oscillates in phase with the mean momentum of the vibrational motion. Employing the same field construction in the case of a molecule, which is not restricted to a fixed orientation, is not successful without further modifications of the construction scheme. If the field is taken to be proportional to the radial momentum, molecules can, depending on their orientation, absorb energy from the field but can also lose internal energy, resulting in a decreased fragmentation yield. It was shown that, because the energy rate for the radial degree of freedom contains an expectation value of the product of the radial momentum and a  $\cos \theta$  function, a necessary condition to deposit energy in the system is to prepare a rotational wave packet consisting of several free rotor states. This can effectively be achieved by applying a static electric field. The huge dipole moment of NaI results in a large interaction energy, which is able to orient the molecule along the field direction. The application of an additional control field then results in highly efficient fragmentation, which is comparable to the rotationless case, where the molecular axis is fixed to point along the direction of the control-field polarization vector.

Efforts were made to create orientation by a control field. In this case, the control algorithm yields a field, which becomes stronger until the numerical breakdown of the simulation. The algorithm thus finds the trivial solution to the problem, a static field with the highest possible strength. Also, effects on the matter-field

interaction, which stem from the molecular polarizability, were investigated in this connection. For the regarded field strengths, no difference was seen for the case with dipole moment and polarizability (second order coupling) compared to the interaction including a linear coupling to the field.

Another application of local control theory to rotational motion involved a simplified model of a molecular motor. There, the target was to induce either a clockwise or a counter-clockwise rotation of a functional group around a bond axis. Starting from the ground state of the system, it was shown that an effective heating, which induces a free rotor motion, can be obtained. Although a net unidirectional motion is then prepared, the yield is rather low. This is due to the presence of a bifurcation of the wave packet. The latter can be suppressed, if a static field is applied to the system prior to the control field. As a result, the initial state in the field-dressed potential is displaced from the equilibrium position of the unperturbed system. The control field then acts on a non-bifurcating wave packet, which follows a mean classical path. Depending on the field strength of the driving field, the oscillation takes place such that a motion into the desired direction is triggered upon reaching the continuum, where a free rotation takes place.

Within this work, photoassociation was treated for the first time employing local control theory. Two objectives were defined to derive suitable control fields. First, a continuous decrease in energy was aimed at and second, a selective population of a single vibrational eigenstate. For the energy decrease, up-chirped fields were found. Such a laser interaction transfers population successively from higher to lower vibrational states, where the up-chirp matches the increasing level spacing with decreasing vibrational quantum number. This 'ladder-descending' mechanism constitutes the counterpart to 'ladder climbing', which was found for the fragmentation process. Although an effective cooling is achieved in this way, the total association yields are improved, if the population in a selected vibrational state of high quantum number is maximized. The respective control fields carry the frequency corresponding to the energy difference between the impact energy and the eigenenergy of the target state. For low lying vibrational states, however, an access by a direct transition is not possible. This effect can be explained within the frame of classical calculations and also with vanishing Franck-Condon factors for the free-to-bound transitions in the quantum-mechanical regime. When the



---

rotational degree of freedom is included, photoassociation is still achieved with the cooling field derived from the rotationless case. Thus, the simplified approach of fixed orientation is justified, where the control mechanisms are easily understood.

For a systematic analysis of control field properties, an approach different from local control was chosen. Usually a first pulse is shaped in coherent control setups, while following pulses are not adapted. Here, the reversed case was examined. After an electronic excitation (pumping) with an unshaped pulse, the effectivity of a selective de-excitation (dumping) was investigated with tailored pulses. Within the applied method, only one or two chirp parameters are scanned systematically, while the other pulse parameters remain unchanged. Two pulse forms were employed, where one showed a linear chirp and the other was a colored double pulse. These tailored dump pulses were adopted to contain the same pulse energy for a straightforward comparison. It was found, that the dynamical features and the system's properties are reflected in the most effective pulse shape. For the treated example, it was shown, that the transform-limited pulse is not the most effective one.

In case of the linear chirp, a down-chirp is most efficient for population transfer. Already at rather low intensity, Rabi-like oscillations of the population in the involved states can be observed, if the momentary frequency of the pulse matches the potential energy difference passed by a moving wave packet. This effect vanishes, if the dynamics of the system is suppressed by keeping the wave packet fixed in the dumping region. As a conclusion, the best dump pulse is a shaped one due to the dynamical features of the system.

For the analysis of the colored double pulses, shaped-dump fitness landscapes were employed. The latter allow for an identification of the wave-packet shape and also a deduction of the shape of the potentials in a region far away from the Franck-Condon region of the initial excitation. Moreover, the wave packet velocity and its dispersion can be deduced qualitatively. By combining fitness landscapes under different parameterizations, a systematic scheme was presented to steadily improve the shape of a pulse and in this way, explore the dynamics not accessible in a similar way with other spectroscopic methods.

Altogether, it was shown, that coherent control is a most promising and fascinating technique, which already helps to unravel the yet unknown properties of the

most different systems and achieve most difficult objectives. Nevertheless, only a tiny part of what can be imagined is realized today. In this sense, the task remains:

*“To boldly go, where no one has gone before.”*

# 12 Zusammenfassung

Das Ziel dieser Arbeit war die theoretische Analyse der Laserkontrolle von Molekülen. Ein Schwerpunkt lag dabei auf vektoriellen Eigenschaften und im Besonderen auf der Orientierung eines Moleküls im Laboratorium. Hierfür wurde der Rotationsfreiheitsgrad in die quantenmechanische Beschreibung einbezogen. Die Kopplung zwischen Vibrations- und Rotationsdynamik wurde explizit berücksichtigt, während dieser Vorgang normalerweise bei theoretischen Untersuchungen zur kohärenten Kontrolle vernachlässigt wird. Als Kontrollschema wurde die lokale Kontrolltheorie (LCT) verwendet, in der das Feld aus der Dynamik eines Systems bestimmt wird, welche sofort auf diese äußere Störung antwortet und damit wiederum das Feld bestimmt. Somit ist das Feld mit der quantenmechanischen Bewegung verknüpft. Die vorgestellten Beispiele dokumentieren, dass dies zu einer intuitiven Interpretation der Felder bzgl. der zu Grunde liegenden molekularen Dynamik führt. In der vereinfachten, klassischen Darstellung der Probleme findet man vergleichbare Resultate. Die klassische Sichtweise ermöglicht ein anschauliches Verständnis der komplizierten Strukturen der Kontrollfelder.

Zusätzlich wurde mit einem anderen Ansatz die Phasen- und Amplitudenformung von Laserfeldern systematisch untersucht, wobei der Populationstransfer in Molekülen kontrolliert werden sollte.

In einem ersten Beispiel wurden elektrische Felder mit Hilfe von LCT bestimmt, welche entweder die effiziente Zufuhr von Energie in ein System (Erhitzen) oder Entnahme von Energie aus einem System (Abkühlen) zum Ziel hatten. Es wurde gezeigt, dass diese Felder sehr effektiv Kontrolle ausüben können und im Falle des Erhitzens in der Lage sind, Natriumiodid im elektronisch angeregten Zustand zu fragmentieren. Für den Fall des Abkühlens wird hingegen Schwingungsrelaxation erreicht. Die resultierenden IR-Pulse können durch den sog. "ladder-climbing"-Mechanismus (Leiter-Klettern) erklärt werden, in dem die Vibrationsniveaus mit unterschiedlichem Energieabstand die Leitersprossen darstellen. In der klassischen

Sichtweise entspricht dieser Mechanismus einem in Phase getriebenen Oszillator im Falle des Erhitzens und eines gegenphasig getriebenen Oszillators im Falle des Abkühlens.

Wenn ein Prädissoziationskanal in das Modellsystem einbezogen wird, wirken sich die IR-Pulse in großem Maß auf die Zerfallsraten des Prädissoziationsprozesses aus. Für die Diskussion des Zerfallsmechanismus müssen dann sowohl die innere Energie als auch der Stark-Effekt für die gekoppelten Potenziale berücksichtigt werden. Einerseits beeinflusst der Energietransfer die mittlere Relativgeschwindigkeit der Kerne, andererseits verändert das externe Feld die Potentialkurven in der Kreuzungsregion. Das Zusammenspiel beider Effekte bestimmt das zeitliche Verhalten der Produktausbeuten. Im Fall des Abkühlens kann der prädissoziative Zustand stabilisiert werden, während im Fall des Erhitzens Dissoziation im angeregten Zustand erzielt wird. Daraus folgt, dass das Verhältnis von Prädissoziation und Dissoziation im angeregten Zustand – und somit das Verhältnis unterschiedlicher Reaktionsprodukte – kontrolliert werden kann.

Das zuvor beschriebene Modell zur Untersuchung von Fragmentation im angeregten Zustand wurde weiter ausgebaut. Im Gegensatz zu vorherigen Studien schloss die Betrachtung nun sowohl die komplette Feldkopplung als auch die nicht-adiabatische Kopplung zwischen den beiden elektronischen Zuständen ein. Zwei Feldkomponenten wurden mit lokaler Kontrolltheorie konstruiert. Während die erste Komponente benutzt wurde, um Population in den angeregten Zustand zu transferieren, induzierte das zweite Feld eine Energieaufnahme im angeregten Zustand, was schließlich zur Dissoziation führte. Die aufeinanderfolgende und die simultane Anwendung solcher Felder erzielt ähnliche Produktausbeuten. Dies kann mit dem Frequenzunterschied der beiden Felder erklärt werden: Die eine Komponente beinhaltet einen Pulszug, in welchem die Subpulse durch die elektronische Übergangsfrequenz charakterisiert werden, während die andere Komponente mit der mittleren Vibrationsfrequenz des angeregten Zustandes oszilliert, welche bedeutend kleiner ist.

Eine zusätzliche Erweiterung des NaI-Modells stellt die Berücksichtigung des Rotationsfreiheitsgrades dar. Hier wurde zuerst die Wellenpaket-Dynamik in statischen Feldern untersucht. Aufgrund des starken Dipolmoments des Moleküls im Grundzustand induziert die entsprechende Wechselwirkung eine Orientierung im Raum.

Durch eine Anregung mit einem ultrakurzen Puls wird eine Wellenpaketbewegung im prädissoziativen elektronisch angeregten Zustand initiiert. Der Bindungscharakter im letzteren ändert sich von kovalent zu ionisch, wenn das Wellenpaket größere ( $<7 \text{ \AA}$ ) interatomare Abstände erreicht. Der Wechsel zwischen diesen beiden Bindungssituationen, induziert durch quasi-gebundene Vibrationsbewegung, ist wichtig für die Wechselwirkung mit dem statischen externen Feld. Wenn das Wellenpaket in der kovalenten Region, wo das Dipolmoment vernachlässigt werden kann, lokalisiert ist, hat das Feld keine Auswirkungen, während die Wechselwirkung im ionischen Bereich groß ist. Dies führt zu einer verbesserten Orientierung des Moleküls entlang der Achse des äußeren Feldes. Die resultierende Rotationsdynamik weist eine Periode auf, welche mit stärkerem Feld immer kürzer wird.

Polarisations-sensitive Pump-Probe-Experimente wurden simuliert, in denen ein zeitverzögerter Probe-Pulse einen Übergang in einen höher angeregten elektronischen Zustand initiiert. Die nachfolgende Fluoreszenz wird dann als Funktion der Verzögerungszeit gemessen. Wählt man den Polarisationsvektor des Probe-Pulses einmal parallel zu Richtung des statischen Feldes und einmal senkrecht dazu, so führt dies zu unterschiedlichen Signalen. Das Verhältnis der letzteren zeigt direkt die Rotationsbewegung des Moleküls, so dass auf diese Weise die feld-induzierte Orientierungsdynamik experimentell in Echtzeit beobachtet werden kann.

Ebenso wie die statischen Felder wurden auch Felder aus der lokalen Kontrolltheorie auf das um die Rotation erweiterte Modellsystem angewendet. Wiederum wurde Photofragmentation im angeregten Zustand des NaI-Moleküls als Ziel gewählt. Wie schon zuvor gezeigt, kann eine 100 %ige Dissoziation der angeregten Moleküle für unveränderliche Orientierung erreicht werden, wobei das Feld in Phase mit dem mittleren Impuls der Vibrationsbewegung oszilliert. Die Anwendung desselben Algorithmus zur Feldbestimmung für ein Molekül, dessen Rotation nicht festgesetzt wird, ist ohne zusätzliche Modifikationen am Konstruktionsschema nicht erfolgreich. Wenn das Feld proportional zum (radialen) Impuls gewählt wird, können Moleküle, abhängig von ihrer Orientierung, Energie aus dem Feld absorbieren aber auch interne Energie an selbiges verlieren, was in einer verminderten Fragmentationsausbeute resultiert. Es wurde gezeigt, dass die Energierate des radialen Freiheitsgrades einen Erwartungswert des Produkts von Impuls und einer  $\cos\theta$ -Funktion enthält. Daher ist die Erzeugung eines Rotations-Wellenpakets aus mehreren freien Rotorzuständen notwendige Voraussetzung, um Energie in das System zu transferieren. Solch

ein Rotations-Wellenpaket kann, wie aus den vorherigen Untersuchungen bekannt, durch das Anlegen eines statischen elektrischen Feldes erhalten werden. Die zusätzliche Anwendung eines Kontrollfeldes hat dann eine hocheffiziente Fragmentation zur Folge, mit vergleichbaren Ausbeuten wie beim rotationsfreien Fall, in welchem die Molekülachse unveränderlich in Richtung des Kontrollfeld-Polarisationsvektors zeigt.

Des Weiteren wurde versucht, Orientierung durch ein Kontrollfeld zu erzielen. In diesem Fall findet der Kontrollalgorithmus ein Feld, das immer stärker wird, bis die Simulation schließlich numerisch zusammenbricht. Der Algorithmus findet somit die triviale Lösung des Problems in Form eines statischen elektrischen Feldes maximaler Stärke. Im Zusammenhang mit dieser Problemstellung wurden auch Effekte der Feld-Materie-Wechselwirkung, die sich aus der molekularen Polarisierbarkeit ergeben, untersucht. Für die betrachteten Feldstärken konnte kein Unterschied für den Fall mit Dipolmoment und Polarisierbarkeit (Kopplung zweiter Ordnung) verglichen zu dem Fall, in welchem nur eine lineare Kopplung in die Wechselwirkung einging.

Eine andere Anwendung der lokalen Kontrolltheorie auf Rotationsbewegungen behandelte das vereinfachte Model eines molekularen Motors. Dort war das Ziel, die Rotation einer funktionellen Gruppe um eine Bindungsachse entweder im Uhrzeigersinn oder entgegen dem Uhrzeigersinn zu induzieren. Ausgehend vom Grundzustand des Systems wurde gezeigt, dass durch effektives Erhitzen eine freie Rotorbewegung erreicht wird. Obwohl netto eine Rotation in eine Vorzugsrichtung erzeugt wird, ist die Aubeute relativ niedrig. Dies kann mit einer Zweiteilung des Wellenpaketes erklärt werden. Die Bifurkation kann durch die Anwendung eines statischen Feldes, welche dem Kontrollfeld vorausgeht, unterdrückt werden. Infolgedessen wird der Anfangszustand im feldverschobenen Potenzial gegenüber der Gleichgewichtsposition des ungestörten Systems verlagert. Das Kontrollfeld wirkt dann auf ein nicht-zweigeteiltes Wellenpaket, das einem klassischen Pfad folgt. Abhängig von der Feldstärke des treibenden Feldes wird dann die Oszillation so angeregt, dass die Rotation in die gewünschte Richtung beim Erreichen des Kontinuums, wo eine freie Drehung möglich ist, stattfindet.

In dieser Arbeit wurde Photoassoziation das erste Mal im Rahmen der lokalen

Kontrolltheorie untersucht. Zwei Ziele wurden definiert, um passende Kontrollfelder herzuleiten. Im ersten Fall sollte eine kontinuierliche Abnahme der inneren Energie erzielt werden und im zweiten Fall eine selektive Bevölkung eines einzelnen Schwingungseigenzustandes. Für die Energieabnahme wurden Felder mit einem Up-Chirp gefunden. Durch die Wechselwirkung mit solch einem Laserfeld wird Besetzung sukzessiv von höheren zu niedrigeren Schwingungszuständen transferiert, wobei der Up-Chirp die Momentanfrequenz an die größerwerdenden Abstände zwischen den Energieniveaus mit kleinerwerdender Schwingungsquantenzahl anpasst. Dieses "Leiter-Hinabsteigen" stellt das Gegenstück zum "Leiter-Hinaufklettern" dar, welches für den Fragmentationsprozess beobachtet wurde. Obwohl auf diese Weise ein effektives Abkühlen möglich ist, wird die totale Assoziationsausbeute verbessert, wenn die Population in einem ausgewählten Vibrationsniveau hoher Quantenzahl maximiert wird. Die zugehörigen Kontrollfelder weisen die Frequenz auf, die der Energiedifferenz zwischen der Einschussenergie und der Eigenenergie des Zielzustands entspricht. Ein direkter Übergang in Vibrationszustände mit kleiner Quantenzahl ist jedoch nicht möglich. Dieses Ergebnis kann mit klassischen Rechnungen und im quantenmechanischen Regime mit verschwindenden Franck-Condon-Faktoren für die Übergänge von Kontinuumszuständen in die gebundenen Zustände erklärt werden. Wenn der Rotationsfreiheitsgrad berücksichtigt wird, findet unter Verwendung des Feldes aus dem rotationsfreien Fall immer noch Photoassoziation statt. Daher ist der vereinfachte Ansatz fester Orientierung gerechtfertigt, in dem die Kontrollmechanismen einfach zu verstehen sind.

Zur systematischen Analyse von Kontrollfelleigenschaften wurde ein anderer Ansatz als die lokale Kontrolltheorie verwendet. In üblichen Kontrollexperimenten wird ein erster Puls geformt, während nachfolgende Pulse nicht verändert werden. Hier wurde der umgekehrte Fall betrachtet. Nach einer elektronischen Anregung (pumping) mit einem ungeformten Puls wurde die Effektivität einer selektiven Abregung (dumping) mit modellierten Pulsen untersucht. In der verwendeten Methode werden nur ein bzw. zwei Chirpparameter systematisch verändert, während die anderen Pulsparameter konstant gehalten werden. Zwei Pulsformen wurden benutzt, zum einen ein Feld mit einem linearen Chirp und zum anderen ein farbiger Doppelpuls. Man konnte feststellen, dass sich die dynamischen Merkmale und die Eigenschaften des Systems in der Form des effektivsten Pulses widerspiegeln. Als wichtiges Resultat ergab sich, dass für das verwendete Beispiel nicht der transform-limitierte

Puls am effektivsten ist.

Im Fall des linearen Chirps bietet ein Down-Chirp die größte Effizienz für einen Populationstransfer. Schon bei verhältnismäßig kleinen Intensitäten können Rabi-ähnliche Oszillationen der Populationen in den beteiligten Zuständen beobachtet werden, wenn die Momentanfrequenz des Pulses der Potentialenergiedifferenz gleicht, welche vom sich bewegenden Wellenpaket passiert wird. Dieser Effekt verschwindet, wenn die Dynamik des Systems unterdrückt wird, indem man das Wellenpaket in der Dumping-Region festhält. Als Schlussfolgerung lässt sich festhalten, dass der beste Dump-Puls ein geformter Puls ist, wobei der Grund hierfür die aus der Dynamik stammenden Merkmale des Systems sind.

Um die farbigen Doppelpulse zu analysieren, wurden Fitness-Landschaften verwendet. Letztere erlauben die Identifikation von Wellenpaketsformen, sowie Rückschlüsse auf die Gestalt der Potentialkurven in einer Region, die weit entfernt von der Franck-Condon-Region der ursprünglichen Anregung liegen kann. Außerdem können die Geschwindigkeit des Wellenpakets und dessen räumliche Aufweitung qualitativ abgeleitet werden. Mit der Kombination von Fitness-Landschaften unter verschiedenen Parametrisierungen wurde ein systematisches Schema vorgestellt, um die Form eines Pulses stetig zu verbessern und währenddessen die Dynamik auf eine Weise zu erkunden, die mit anderen spektroskopischen Methoden nicht zugänglich ist.

Abschließend lässt sich sagen, dass kohärente Kontrolle eine vielversprechende und faszinierende Methode ist, die jetzt schon hilft die bislang unbekanntenen Eigenschaften der verschiedensten Systeme offenzulegen und die schwierigsten Ziele zu erreichen. Dennoch ist heute erst ein winziger Teil dessen, was in unserer Vorstellungskraft liegt, realisiert. In diesem Sinne bleibt als Aufgabe:

*In Bereiche vorzudringen, "die nie ein Mensch zuvor gesehen hat."*



# A Appendix

## A.1 Change between adiabatic and diabatic picture

Every real symmetric matrix  $\mathbf{A}$  can be diagonalized to  $\mathbf{D}$  via a similarity transformation with the orthogonal matrix  $\mathbf{C}$  [202]:

$$\mathbf{D} = \mathbf{C}^T \mathbf{A} \mathbf{C}. \quad (\text{A.1})$$

Here, the diagonal elements of  $\mathbf{D}$  are the eigenvalues of  $\mathbf{A}$  and the columns in  $\mathbf{C}$  are the corresponding eigenvectors. For a two-dimensional matrix,  $\mathbf{C}$  is a rotation matrix:

$$\mathbf{C} = \begin{pmatrix} \cos \gamma & -\sin \gamma \\ \sin \gamma & \cos \gamma \end{pmatrix}. \quad (\text{A.2})$$

Application to the NaI potentials (see section 2.5) yields

$$\begin{pmatrix} \cos \gamma & \sin \gamma \\ -\sin \gamma & \cos \gamma \end{pmatrix} \begin{pmatrix} V_1^d & V_{12}^d \\ V_{12}^d & V_2^d \end{pmatrix} \begin{pmatrix} \cos \gamma & -\sin \gamma \\ \sin \gamma & \cos \gamma \end{pmatrix} = \begin{pmatrix} V_1^a & 0 \\ 0 & V_2^a \end{pmatrix}. \quad (\text{A.3})$$

In this case  $\gamma$  can be evaluated by multiplying with  $\mathbf{C}$  from the left ( $\mathbf{C} \mathbf{C}^T = \mathbb{1}$ )

$$\begin{pmatrix} V_1^d & V_{12}^d \\ V_{12}^d & V_2^d \end{pmatrix} \begin{pmatrix} \cos \gamma & -\sin \gamma \\ \sin \gamma & \cos \gamma \end{pmatrix} = \begin{pmatrix} \cos \gamma & -\sin \gamma \\ \sin \gamma & \cos \gamma \end{pmatrix} \begin{pmatrix} V_1^a & 0 \\ 0 & V_2^a \end{pmatrix}. \quad (\text{A.4})$$

This results in linear equations, which can be solved to yield the rotation angle  $\gamma$ . By eliminating the unknown  $V_1^a$  and  $V_2^a$ , using  $\sin 2\gamma = 2 \sin \gamma \cos \gamma$ ,  $\cos 2\gamma = \cos^2 \gamma - \sin^2 \gamma$  and  $\cot \gamma = \frac{1}{\tan \gamma}$ , finally the following expression is obtained:

$$\gamma = \frac{1}{2} \arctan \left( \frac{2 V_{12}^d}{V_1^d - V_2^d} \right). \quad (\text{A.5})$$

Since  $V_1^a$  and  $V_2^a$  are the eigenvalues of the matrix  $\mathbf{A}$ , they can also be evaluated analytically [202]

$$\begin{vmatrix} V_1^d - \lambda & V_{12} \\ V_{12} & V_2^d - \lambda \end{vmatrix} = 0, \quad (\text{A.6})$$

where  $\lambda_1 = V_2^a$  and  $\lambda_2 = V_1^a$ .

$$\Rightarrow \lambda_{1,2} = \frac{V_1^d + V_2^d}{2} \pm \sqrt{\frac{(V_1^d - V_2^d)^2}{4} + V_{12}^2}. \quad (\text{A.7})$$

Consequently, the following expressions are derived

$$V_2^a = \frac{V_1^d + V_2^d}{2} + \sqrt{\frac{(V_1^d - V_2^d)^2}{4} + V_{12}^2} \quad (\text{A.8})$$

$$V_1^a = \frac{V_1^d + V_2^d}{2} - \sqrt{\frac{(V_1^d - V_2^d)^2}{4} + V_{12}^2}. \quad (\text{A.9})$$

To change from the adiabatic to the diabatic picture, a rather crude way is taken. Here, the adiabatic potentials are transformed manually via fitted straight lines to the diagonal elements in the diabatic representation. The coupling element  $V_{12}^d$  is then evaluated as

$$V_{12}^d = \sqrt{\left(V_1^a - \frac{V_1^d + V_2^d}{2}\right)^2 - \frac{(V_1^d - V_2^d)^2}{4}}. \quad (\text{A.10})$$

# Bibliography

- [1] S. A. Rice, M. Zhao, *Optical Control of Molecular Dynamics*, Wiley, New York (2000). 1
- [2] M. Shapiro, P. Brumer, *Principles of Quantum Control of Molecular Processes*, Wiley, New York (2003). 1, 44
- [3] D. Tannor, *Introduction to Quantum Mechanics: A Time-Dependent Perspective*, University Science Books, Sausalito (2006). 1
- [4] P. Brumer, M. Shapiro, *Laser control of molecular processes*, *Ann. Rev. Phys. Chem.* **43**, 257–282 (1992). 1, 39
- [5] R. J. Gordon, S. A. Rice, *Active Control of the dynamics of atoms and molecules*, *Ann. Rev. Phys. Chem.* **48**, 601–641 (1997). 1
- [6] S. A. Rice, *Perspectives on the control of quantum many-body dynamics: Applications to chemical reactions*, *Adv. Chem. Phys.* **101**, 213–283 (1997). 1
- [7] D. J. Tannor, R. Kosloff, A. Bartana, *Laser cooling of internal degrees of freedom of molecules by dynamically trapped states*, *Faraday Discuss.* **113**, 365 – 383 (1999). 1, 46, 61
- [8] T. Brixner, N. H. Damrauer, G. Gerber, *Femtosecond quantum control*, *Adv. At. Molec. Opt. Phys.* **46**, 1–54 (2001). 1
- [9] N. Vitanov, T. Halfmann, B. W. Shore, K. Bergmann, *Laser-induced population transfer by adiabatic passage techniques*, *Ann. Rev. Phys. Chem.* **52**, 763–809 (2001). 1
- [10] M. Shapiro, P. Brumer, *Coherent control of molecular dynamics*, *Rep. Prog. Phys.* **66**, 859–942 (2003). 1

- [11] P. Nuernberger, G. Vogt, T. Brixner, G. Gerber, *Femtosecond quantum control of molecular dynamics in the condensed phase*, Phys. Chem. Chem. Phys. **9**, 2470–2497 (2007). 1
- [12] M. Dantus, A. H. Zewail (Eds.), *Special issue on Femtochemistry*, Chem. Rev. **104**, 1717–2124 (2004). 2
- [13] I. Grenthe (Ed.), *Nobel Lectures, Chemistry 1996-2000*, World Scientific Publishing Co., Singapore (2003). 2
- [14] A. M. Weiner, *Femtosecond pulse shaping using spatial light modulators*, Rev. Sci. Instrum. **71**, 1929–1960 (2000). 2
- [15] *Picosecond Phenomena, Ultrafast Phenomena, Springer Series in Chemical Physics I-XII*, volume 4, 14, 23, 38, 46, 48, 53, 55, 60, 62, 63, 66, Springer, Heidelberg. 2
- [16] P. Král, M. Shapiro, *Complete adiabatic passage to arbitrarily sculpted superposition states*, Phys. Rev. A **65**, 043413/1–7 (2002). 4
- [17] G. Vogt, P. Nuernberger, T. Brixner, G. Gerber, *Femtosecond pump–shaped–dump quantum control of retinal isomerization in bacteriorhodopsin*, Chem. Phys. Lett. **433**, 211–215 (2006). 4, 148, 157, 158, 169
- [18] I. Newton, *Philosophiae naturalis principia mathematica*, Havard Univ. Press, Cambridge (1726). 5
- [19] J. L. Lagrange, *Mécanique analytique*, Mallet-Bachelier, Paris (1853). 5
- [20] W. Greiner, *Classical Mechanics*, Springer, Heidelberg (2003). 5
- [21] J. V. José, E. J. Saletan, *Classical Dynamics*, Cambridge University Press, Cambridge (1998). 5
- [22] R. Abraham, J. Marsden, *Foundations of Mechanics*, Benjamin/Cummings, Reading/Mass. (1878). 6
- [23] E. J. Heller, *Wigner phase space method: Analysis for semiclassical applications*, J. Chem. Phys. **65**, 1289–1298 (1976). 7
- [24] L. de Broglie, *Recherches sur la théorie de quanta*, Masson, Paris, Rééd. du texte de 1924 (1963). 7

- 
- [25] M. Jammer, *The Conceptual Development of Quantum Mechanics (The History of Modern Physics 1800-1950, Volume 12)*, Tomash Publishers, Los Angeles, second edition (1989). 7
- [26] E. Schrödinger, *Quantisierung als Eigenwertproblem*, Ann. Phys. **384**, 361–376 (1926). 8
- [27] J. S. Briggs, J. M. Rost, *Time dependence in quantum mechanics*, Euro. Phys. J. D **10**, 311–318 (2000). 8
- [28] J. S. Briggs, J. M. Rost, *On the derivation of the time-dependent equation of Schrödinger*, Foundation of Physics **31**, 693–712 (2001). 8
- [29] M. S. Child, *Semiclassical Mechanics with Molecular Applications*, Oxford University Press, Oxford (1991). 8
- [30] C. Cohen-Tannoudji, B. Diu, R. Laloë, *Quantum Mechanics, Vol. I*, Wiley, New York (1977). 10
- [31] J. C. Maxwell, *A Dynamical Theory of the Electromagnetic Field*, Phil. Trans. R. Soc. **155**, 459 – 512 (1865). 11
- [32] J. D. Jackson, *Classical Electrodynamics*, Wiley, New York, third edition (1998). 11
- [33] P. Meystre, M. S. III, *Elements of quantum optics*, Springer, Berlin (1991). 11, 12
- [34] M. O. Scully, M. S. Zubairy, *Quantum Optics*, Cambridge University Press, Cambridge (1997). 12, 24
- [35] L. S. Schulman, *Techniques and Applications of Path Integration*, Wiley, New York (1996). 14
- [36] H. J. Loesch, A. Remscheid, *Brute force in molecular reaction dynamics: A novel technique for measuring steric effects*, J. Chem. Phys. **93**, 4779 – 4790 (1990). 19
- [37] B. Friedrich, D. R. Herschbach, *On the possibility of orienting rotationally cooled polar molecules in an electric field*, Z. Phys. D - Atoms, Molecules and Clusters **18**, 153 – 161 (1991). 19

- [38] B. Friedrich, D. R. Herschbach, *Spatial orientation of molecules in strong electric fields and evidence for pendular states*, *Nature* **353**, 412 – 414 (1991). 19
- [39] C. Meier, V. Engel, *in: Femtosecond Chemistry - Volume 1*, VCH, Weinheim (1995). 19
- [40] G. C. Schatz, M. A. Ratner, *Quantum Mechanics in Chemistry*, Dover publications, Mineola (2002). 19
- [41] G. Baym, *Lectures on quantum mechanics*, Benjamin/Cummings, Menlo Park, CA (1973). 20
- [42] R. Loudon, *The Quantum Theory of Light*, Oxford University Press, Oxford, second edition (1983). 23
- [43] C. C. Gerry, P. L. Knight, *Introductory Quantum Optics*, Cambridge University Press, Cambridge (2005). 24
- [44] W. Domcke, G. Stock, *Theory of ultrafast non-adiabatic excited-state processes and their spectroscopic detection in real time*, *Adv. Chem. Phys.* **100**, 1–169 (1997). 29
- [45] L. D. Landau, *Theory of energy transfer*, *Phys. Z. Sowjetunion* **1**, 89 (1932). 29
- [46] L. D. Landau, *Theory of energy transfer. II*, *Phys. Z. Sowjetunion* **2**, 46 (1932). 29
- [47] C. Zener, *Non-adiabatic crossing of energy levels*, *Proc. Roy. Soc. Lond. A* **137**, 696–701 (1932). 29
- [48] R. D. Levine, *Molecular Reaction Dynamics*, Cambridge University Press, Cambridge (2005). 29
- [49] M. P. Allen, D. J. Tildesley, *Computer Simulation of Liquids*, Oxford University Press, Oxford (1987). 31
- [50] C. Leforestier, R. H. Bisseling, C. Cerjan, M. D. Feit, R. Friesner, A. Gulberg, A. Hammerich, G. Jolicard, W. Karrlein, H. D. Meyer, N. Lipkin, O. Roncero, R. Kosloff, *A comparison of different propagation schemes for*

- the time dependent Schrödinger equation*, J. Comput. Phys. **94**, 59–80 (1991). 32
- [51] R. Kosloff, *Time-dependent quantum-mechanical methods for molecular dynamics*, J. Phys. Chem. **92**, 2087–2100 (1988). 32
- [52] R. Kosloff, *Propagation methods for quantum molecular dynamics*, Ann. Rev. Phys. Chem. **45**, 145–178 (1994). 32
- [53] M. D. Feit, J. A. Fleck Jr., A. Steiger, *Solution of the Schrödinger Equation by a Spectral Method*, J. Comput. Phys. **47**, 412–433 (1982). 33, 83
- [54] M. D. Feit, J. A. Fleck Jr., *Solution of the Schrödinger equation by a spectral method II: Vibrational energy levels of triatomic molecules*, J. Chem. Phys. **78**, 301–308 (1982). 33
- [55] J. A. Fleck Jr., J. A. Morris, M. D. Feit, *Time-Dependent Propagation of High Energy Laser Beams through the Atmosphere*, Appl. Phys. **10**, 129–160 (1976). 33, 83
- [56] M. Frigo, S. G. Johnson, *The Design and Implementation of FFTW3*, Proceedings of the IEEE **93**, 216–231 (2005), special issue on "Program Generation, Optimization, and Platform Adaptation". 34
- [57] R. Kosloff, H. Tal-Ezer, *A direct relaxation method for calculating eigenfunctions and eigenvalues of the Schrödinger equation on a grid*, Chem. Phys. Lett. **127**, 223–230 (1986). 34
- [58] H. Stapelfeldt, T. Seideman, *Colloquium: Aligning molecules with strong laser pulses*, Rev. Mod. Phys. **75**, 543–557 (2003). 36, 81
- [59] M. Machholm, N. E. Henriksen, *Two-pulse laser control for selective photofragment orientation*, J. Chem. Phys. **111**, 3051–3057 (1999). 36, 63, 81
- [60] J. Broeckhove, B. Feyen, L. Lathouwers, F. Arickx, P. V. Leuven, *Quantum time evolution of vibrational states in curve-crossing problems*, Chem. Phys. Lett. **174**, 504–510 (1990). 38
- [61] C. Lanczos, *Applied analysis*, Dover publications, New York (1988). 38

- [62] T. Pang, *An Introduction to Computational Physics*, Cambridge University Press, Cambridge (1997). 38
- [63] G. M. Huang, T. J. Tarn, J. W. Clark, *On the controllability of quantum-mechanical systems*, J. Math. Phys. **24**, 2608–2618 (1983). 39
- [64] P. Brumer, M. Shapiro, *Control of unimolecular reactions using coherent light*, Chem. Phys. Lett. **126**, 541–546 (1986). 39
- [65] M. Shapiro, J. W. Hepburn, P. Brumer, *Simplified laser control of unimolecular reactions: simultaneous  $(\omega_1, \omega_3)$  excitation*, Chem. Phys. Lett. **149**, 451–454 (1988). 40
- [66] C. Chen, Y. Yin, D. S. Elliott, *Interference between optical transitions*, Phys. Rev. Lett. **64**, 507–510 (1990). 40
- [67] L. C. Zhu, V. D. Kleiman, X. N. Li, S. P. Lu, K. Trentelman, R. J. Gordon, *Coherent laser control of the product distribution obtained in the photoexcitation of HI*, Science **270**, 77–80 (1995). 40
- [68] U. Gaubatz, P. Rudecki, M. Becker, S. Schiemann, M. Kulz, K. Bergmann, *Population switching between vibrational levels in molecular beams*, Chem. Phys. Lett. **149**, 463–468 (1988). 40
- [69] K. Bergmann, H. Theuer, B. W. Shore, *Coherent population transfer among quantum states of atoms and molecules*, Rev. Mod. Phys. **70**, 1003–1025 (1998). 40
- [70] D. J. Tannor, S. A. Rice, *Control of selectivity of chemical reaction via control of wave packet evolution*, J. Chem. Phys. **83**, 5013–5018 (1985). 41, 44
- [71] D. J. Tannor, R. Kosloff, S. A. Rice, *Coherent pulse sequence induced control of selectivity of reactions: Exact quantum mechanical calculations*, J. Chem. Phys. **85**, 5805–5820 (1986). 41
- [72] T. Baumert, M. Grosser, R. Thalweiser, G. Gerber, *Femtosecond time-resolved molecular multiphoton ionization: The Na<sub>2</sub> system*, Phys. Rev. Lett. **67**, 3753–3756 (1991). 42
- [73] E. D. Potter, J. L. Herek, S. Pedersen, Q. Liu, A. H. Zewail, *Femtosecond laser control of a chemical reaction*, Nature **355**, 66–68 (1992). 42



- [74] T. Lohmüller, M. Erdmann, V. Engel, *Chirped pulse ionization: bondlength dynamics and interference effects*, Chem. Phys. Lett. **373**, 319–327 (2003). 42
- [75] C. J. Bardeen, Q. Wang, C. V. Shank, *Selective Excitation of Vibrational Wave Packet Motion Using Chirped Pulses*, Phys. Rev. Lett. **75**, 3410–3413 (1995). 42
- [76] S. Chelkowski, A. D. Bandrauk, P. B. Corkum, *Efficient molecular dissociation by a chirped ultrashort laser pulse*, Phys. Rev. Lett. **65**, 2355–2358 (1990). 42, 56, 60, 136
- [77] B. Broers, H. B. van Linden van den Heuvell, L. D. Noordam, *Efficient population transfer in a three-level ladder system by frequency-swept ultrashort laser pulses*, Phys. Rev. Lett. **69**, 2062–2065 (1992). 42, 60
- [78] Z. Michalewicz, *Genetic Algorithms + Data Structures = Evolution Programs*, Springer, Berlin (1999). 42
- [79] W. S. Warren, H. Rabitz, M. Dahleh, *Coherent Control of Quantum Dynamics: The Dream is alive*, Science **259**, 1581–15694 (1993). 43
- [80] T. Brixner, T. Pfeifer, G. Gerber, M. Wollenhaupt, T. Baumert, *in: Femtosecond Laser Spectroscopy*, Springer, Berlin (2005). 43
- [81] T. C. Weinacht, P. H. Bucksbaum, *Using feedback for coherent control of quantum systems*, J. Opt. B: Quantum Semiclass. Opt. **4**, R35–R52 (2003). 43
- [82] R. S. Judson, H. Rabitz, *Teaching lasers to control molecules*, Phys. Rev. Lett. **68**, 1500–1503 (1992). 43
- [83] R. Kosloff, S. A. Rice, P. Gaspard, S. Tersigni, D. J. Tannor, *Wavepacket dancing: Achieving chemical selectivity by shaping light pulses*, Chem. Phys. **139**, 201–220 (1989). 44, 45
- [84] A. P. Peirce, M. A. Dahleh, H. Rabitz, *Optimal control of quantum-mechanical systems: Existence, numerical approximation, and applications*, Phys. Rev. A **37**, 4950–4964 (1988). 44

- [85] S. Shi, A. Woody, H. Rabitz, *Optimal control of selective vibrational excitation in harmonic linear chain molecules*, J. Chem. Phys. **88**, 6870–6883 (1988). 44
- [86] S. Shi, H. Rabitz, *Selective excitation in harmonic molecular systems by optimally designed fields*, Chem. Phys. **139**, 185–199 (1989). 44
- [87] J. E. Combariza, B. Just, J. Manz, G. K. Paramonov, *Isomerizations controlled by ultrashort infrared laser pulses: Model simulations for the inversion of ligands (H) in the double-well potential of an organometallic compound,  $[(C_5H_5)(CO)_2FePH_2]$* , J. Phys. Chem. **95**, 10351–10359 (1991). 44
- [88] R. Kosloff, A. D. Hammerich, D. J. Tannor, *Excitation without demolition: Radiative excitation of ground-surface vibration by impulsive stimulated Raman scattering with damage control*, Phys. Rev. Lett. **69**, 2172–2175 (1992). 46
- [89] P. Gross, H. Singh, H. Rabitz, K. Mease, G. M. Huang, *Inverse quantum-mechanical control: A means for design and a test of intuition*, Phys. Rev. A **47**, 4593–4604 (1993). 46
- [90] Y. Chen, P. Gross, V. Ramakrishna, H. Rabitz, K. Mease, H. Singh, *Control of classical regime molecular objectives – applications of tracking and variations on the theme*, Automatica **33**, 1617–1633 (1997). 46, 140
- [91] W. Zhu, H. Rabitz, *Quantum control design via adaptive tracking*, J. Chem. Phys. **119**, 3619–3625 (2003). 46
- [92] V. Malinovsky, D. J. Tannor, *Simple and robust extension of the stimulated Raman adiabatic passage technique to N-level systems*, Phys. Rev. A **56**, 4929–4937 (1997). 46, 120
- [93] A. Bartana, R. Kosloff, D. J. Tannor, *Laser cooling of molecular internal degrees of freedom by a series of shaped pulse*, J. Chem. Phys. **99**, 196–210 (1993). 46, 56
- [94] H. Tang, R. Kosloff, S. A. Rice, *A generalized approach to the control of the evolution of a molecular system*, J. Chem. Phys. **104**, 5457–5471 (1996). 46

- [95] S. E. Sklarz, D. J. Tannor, *Local control theory for unitary transformations: Application to quantum computing without leakage*, Quantum Physics (de.arxiv.org) **quant-ph**, 0404081 (2004). 46
- [96] S. E. Sklarz, D. J. Tannor, *Quantum computation via local control theory: direct sum vs. direct product Hilbert spaces*, Chem. Phys. **322**, 87–97 (2006). 46
- [97] C. Meier, M.-C. Heitz, *Laser control of vibrational excitation in carboxyhemoglobin: A quantum wave packet study*, J. Chem. Phys. **123**, 044504/1–11 (2005). 46
- [98] M. Sugawara, Y. Fujimura, *Control of quantum dynamics by a locally optimized laser. Application to ring puckering isomerization*, J. Chem. Phys. **100**, 5646–5655 (1994). 46
- [99] M. Sugawara, Y. Fujimura, *Control of quantum dynamics by a locally optimized laser. II. Application to a system with dissipation*, J. Chem. Phys. **101**, 6586–6592 (1994). 46
- [100] S. Gräfe, P. Marquetand, N. E. Henriksen, K. B. Møller, V. Engel, *Quantum control fields from instantaneous dynamics*, Chem. Phys. Lett. **398**, 180–185 (2004). 46
- [101] S. Gräfe, C. Meier, V. Engel, *Instantaneous dynamics and quantum control fields: Principle and numerical applications*, J. Chem. Phys. **122**, 184103/1–8 (2005). 46, 75
- [102] P. Marquetand, V. Engel, *Predissociation and dissociation dynamics in quantum control fields*, Chem. Phys. Lett. **407**, 471–476 (2005). 46
- [103] S. Gräfe, M. Erdmann, V. Engel, *Population transfer in the multi-photon excitation of molecules*, Phys. Rev. A **72**, 013404/1–7 (2005). 46, 98
- [104] P. Marquetand, C. Meier, V. Engel, *Local control of molecular fragmentation: The role of orientation*, J. Chem. Phys. **123**, 204320/1–7 (2005). 46
- [105] P. Marquetand, S. Gräfe, D. Scheidel, V. Engel, *Local control of the quantum dynamics in multiple potential wells*, J. Chem. Phys. **124**, 054325/1–7 (2006). 46

- [106] P. Marquetand, V. Engel, *Complete local control of molecular excited states photodissociation*, Chem. Phys. Lett. **426**, 263–267 (2006). 46
- [107] S. Gräfe, V. Engel, *Local control theory applied to coupled electronic and nuclear motion*, Chem. Phys. **329**, 118–125 (2006). 46
- [108] J. J. Sakurai, *Modern Quantum Mechanics*, Benjamin Cummings Publishing, Menlo Park (1985). 48
- [109] L. Solymar, *Lectures on Fourier Series*, Oxford University Press, Oxford (1988). 51
- [110] T. S. Rose, M. J. Rosker, A. H. Zewail, *Femtosecond real-time observation of wave packet oscillations (resonance) in dissociation reactions*, J. Chem. Phys. **88**, 6672–6673 (1988). 53, 96
- [111] T. S. Rose, M. J. Rosker, A. H. Zewail, *Femtosecond real-time probing of reactions. IV. The reactions of alkali halides*, J. Chem. Phys. **91**, 7415–7436 (1989). 53, 96
- [112] J. L. Herek, A. Materny, A. H. Zewail, *Femtosecond control of an elementary unimolecular reaction from the transition-state region*, Chem. Phys. Lett. **228**, 15–25 (1994). 53, 63
- [113] T. Taneichi, T. Kobayashi, Y. Ohtsuki, Y. Fujimura, *Control of non-adiabatic photodissociation of sodium iodide using ultrashort pump and control pulses*, Chem. Phys. Lett. **231**, 50–54 (1994). 53, 63
- [114] C. J. Bardeen, J. Che, K. R. Wilson, V. V. Yakovlevi, P. Cong, B. Kohler, J. L. Krause, M. Messina, *Quantum control of NaI photodissociation reaction product states by ultrafast tailored light pulses*, J. Phys. Chem. A **101**, 3815–3822 (1997). 53
- [115] E. Charron, A. Giusti-Suzor, *Femtosecond dynamics of NaI ionization and dissociative ionization*, J. Chem. Phys. **108**, 3922–3931 (1998). 53, 63
- [116] M. Grønager, N. E. Henriksen, *Real-time control of electronic motion: Application to NaI*, J. Chem. Phys. **109**, 4335–4341 (1998). 53, 63

- [117] B. H. Hosseini, H. R. Sadeghpour, N. Balakrishnan, *Control of polarized iodine branching ratio in NaI photodissociation*, Phys. Rev. A **71**, 023402 (2005). 53
- [118] V. Engel, H. Metiu, *A Quantum Mechanical Study of Predissociating NaI Excited by a Femtosecond Laser Pulse*, J. Chem. Phys. **90**, 6116–6128 (1989). 53, 90
- [119] V. Engel, H. Metiu, *Two-photon excitation of NaI with femtosecond laser pulses*, J. Chem. Phys. **91**, 1596–1602 (1989). 53
- [120] G. H. Peslherbe, R. Bianco, J. T. Hynes, B. M. Ladanyi, *On the photodissociation of alkali/metal halides in solution*, J. Chem. Soc., Faraday Trans. **93**, 977–988 (1997). 54, 72
- [121] T. Witte, T. Hornung, L. Windhorn, D. Proch, R. de Vivie-Riedle, M. Motzkus, K. L. Kompa, *Controlling molecular ground-state dissociation by optimizing vibrational ladder climbing*, J. Chem. Phys. **118**, 2021–2024 (2003). 56, 60, 136
- [122] A. Bartana, R. Kosloff, D. J. Tannor, *Laser cooling of molecular internal degrees of freedom. II*, J. Chem. Phys. **106**, 1435–1448 (1997). 56
- [123] R. Kosloff, D. Kosloff, *Absorbing boundaries for wave propagation problems*, J. Comput. Phys. **63**, 363–376 (1986). 58, 76, 84
- [124] D. Neuhauser, M. Baer, *The Time Dependent Schrödinger Equation: Application of Absorbing Boundary Conditions*, J. Chem. Phys. **90**, 4351–4355 (1989). 58, 76, 84, 102
- [125] U. V. Riss, H.-D. Meyer, *Investigation on the reflection and transmission properties of complex absorbing potentials*, J. Chem. Phys. **105**, 1409–1419 (1996). 58, 76, 84, 102
- [126] B. Poirier, T. Carrington, *Semiclassically optimized complex absorbing potentials of polynomial form. I. Pure imaginary case*, J. Chem. Phys. **118**, 17–28 (2003). 58, 76, 84, 102

- [127] B. Poirier, T. Carrington, *Semiclassically optimized complex absorbing potentials of polynomial form. II. Complex case*, J. Chem. Phys. **119**, 77–89 (2003). 58, 76, 84
- [128] R. W. Heather, *An asymptotic wavefunction splitting procedure for propagating spatially extended wavefunctions: application to intense field photodissociation of  $H_2^+$* , Comput. Phys. Commun. **63**, 446–459 (1991). 65
- [129] V. S. Malinovsky, C. Meier, D. J. Tannor, *Optical paralysis in electronically congested systems: application to large-amplitude vibrational motion of ground state  $Na_2$* , Chem. Phys. **221**, 67–76 (1997). 74
- [130] M. Machholm, N. E. Henriksen, *Field-free orientation of molecules*, Phys. Rev. Lett. **87**, 193001 (2001). 81
- [131] A. Matos-Abiague, J. Berakdar, *Controlling the orientation of polar molecules by half-cycle pulses*, Chem. Phys. Lett. **382**, 475–480 (2003). 81
- [132] A. Matos-Abiague, J. Berakdar, *Sustainable orientation of polar molecules induced by half-cycle pulses*, Phys. Rev. A **68**, 063411 (2003). 81
- [133] P. Marquetand, A. Materny, N. E. Henriksen, V. Engel, *Molecular orientation via a dynamically induced pulse-train: Wave packet dynamics of NaI in a static electric field*, J. Chem. Phys. **120**, 5871–5874 (2004). 82
- [134] J. M. Rost, J. C. Griffin, B. Friedrich, D. R. Herschbach, *Pendular States and Spectra of Oriented Molecules*, Phys. Rev. Lett. **68**, 1299–1302 (1992). 89, 91, 92, 107, 126
- [135] A. Materny, *private communication*. 95
- [136] J. R. Hiskes, *Dissociation of Molecular Ions by Electric and Magnetic Fields*, Phys. Rep. **122**, 1207–1217 (1961). 95
- [137] D. Kröner, L. Gonzalez, *Optical enantioselection in a random ensemble of unidirectionally oriented chiral olefins*, Chem. Phys. **298**, 55–63 (2004). 98
- [138] G. Turinici, H. Rabitz, *Optimally controlling the internal dynamics of a randomly oriented ensemble of molecules*, Phys. Rev. A **70**, 063412 (2004). 98

- [139] A. Pelzer, S. Ramakrishna, T. Seideman, *Optimal control of molecular alignment in dissipative media*, J. Chem. Phys. **126**, 034503 (2007). 98
- [140] T. Hornung, R. de Vivie-Riedle, *Molecular population control including rotation*, Europhys. Lett. **64**, 703–708 (2003). 98
- [141] R. Schinke, *Photodissociation Dynamics*, Cambridge University Press, Cambridge (1993). 100
- [142] C. M. Dion, A. Keller, O. Atabek, A. D. Bandrauk, *Laser-induced alignment dynamics of HCN: Roles of the permanent dipole moment and polarizability*, Phys. Rev. A **59**, 1382–1391 (1999). 111
- [143] R. Fink, *private communication*. 112
- [144] C. R. Ekstrom, J. Schmiedmayer, M. S. Chapman, T. D. Hammond, D. E. Pritchard, *Measurement of the electric polarizability of sodium with an atom interferometer*, Phys. Rev. A **51**, 3883–3888 (1995). 113
- [145] V. S. Zuev, V. A. Katulin, V. Y. Nosach, O. Y. Nosach, *xxx*, Sov. Phys. JETP **35**, 870–x (1972). 113
- [146] H. Coker, *Empirical free-ion polarizabilities of the alkali metal, alkaline earth metal, and halide ions*, J. Phys. Chem. **80**, 2078–2084 (1976). 113
- [147] V. Balzani, M. Venturi, A. Credi, *Molecular Devices and Machines*, Wiley-VCH, Weinheim (2003). 117
- [148] Y. Shirai, A. J. Osgood, Y. Zao, K. F. Kelly, J. M. Tour, *Directional Control in Thermally Driven Single-Molecule Nanocars*, Nano Lett. **5**, 2330–2334 (2005). 117
- [149] J.-F. Morin, Y. Shirai, J. M. Tour, *En Route to a Motorized Nanocar*, Org. Lett. **8**, 1713–1716 (2006). 117
- [150] K. Hoki, M. Yamaki, S. Koseki, Y. Fujimura, *Molecular motors driven by laser pulses: role of molecular chirality and photon helicity*, J. Chem. Phys. **118**, 497–504 (2003). 117, 118, 119, 123, 130

- [151] K. Hoki, M. Yamaki, S. Koseki, Y. Fujimura, *Mechanism of unidirectional motions of chiral molecular motors driven by linearly polarized pulses*, J. Chem. Phys. **119**, 12393–12398 (2003). 117
- [152] K. Hoki, M. Yamaki, Y. Fujimura, *Chiral Molecular Motors Driven by a Nonhelical Laser Pulse*, Angew. Chem., Int. Ed. Engl. **42**, 2976 – 2978 (2003). 117
- [153] M. Yamaki, K. Hoki, Y. Ohtsuki, H. Kono, Y. Fujimura, *Quantum control of a chiral molecular motor driven by laser pulses*, J. Am. Chem. Soc. **127**, 7300–7301 (2005). 117, 120
- [154] Y. Ohtsuki, H. Kono, Y. Fujimura, *Quantum control of nuclear wave packets by locally designed optimal pulses*, J. Chem. Phys. **109**, 9318–9331 (1998). 120
- [155] V. A. Ermoshin, V. Engel, C. Meier, *Oscillatory pump-probe signals from delocalized wave packets*, J. Chem. Phys. **113**, 5770–5775 (2000). 127
- [156] N. Koumura, R. W. J. Zijlstra, R. A. van Delden, N. Harada, B. L. Feringa, *Light-driven monodirectional molecular rotor*, Nature **401**, 152–155 (1999). 130
- [157] K. Hoki, M. Sato, M. Yamaki, R. Sahnoun, L. Gonzalez, S. Koseki, Y. Fujimura, *Chiral Molecular Motors Ignited by Femtosecond Pump-Dump Laser Pulses*, J. Phys. Chem. B **108**, 4916–4921 (2004). 130
- [158] P. D. Lett, P. S. Julienne, W. D. Phillips, *Photoassociative spectroscopy of laser-cooled atoms*, Ann. Rev. Phys. Chem. **46**, 423–452 (1995). 131
- [159] H. R. Thorsheim, J. Weiner, P. S. Julienne, *Laser-Induced Photoassociation of Ultracold Sodium Atoms*, Phys. Rev. Lett. **58**, 2420–2423 (1987). 131
- [160] M. Machholm, A. Giusti-Suzor, F. H. Mies, *Photoassociation of atoms in ultracold collisions probed by wave-packet dynamics*, Phys. Rev. A **50**, 5025–5036 (1994). 131
- [161] M. V. Korolkov, J. Manz, G. K. Paramonov, B. Schmidt, *Vibrationally state-selective photoassociation by infrared sub-picosecond laser pulses: model simulations for  $O + H \rightarrow OH(v)$* , Chem. Phys. Lett. **260**, 604–610 (1996). 131



- [162] E. Luc-Koenig, R. Kosloff, F. Masnou-Seeuws, M. Vatasescu, *Photoassociation of cold atoms with chirped laser pulses: Time-dependent calculations and analysis of the adiabatic transfer within a two-state model*, Phys. Rev. A **70**, 033414/1–19 (2004). 131, 133
- [163] C. P. Koch, R. Kosloff, E. Luc-Koenig, F. Masnou-Seeuws, A. Crubellier, *Photoassociation with chirped laser pulses: calculation of the absolute number of molecules per pulse*, J. Phys. B: At. Mol. Phys. **39**, S1017–S1041 (2006). 131, 133
- [164] A. Fioretti, D. Comparat, A. Crubellier, O. Dulieu, F. Masnou-Seeuws, P. Pillet, *Formation of Cold Cs<sub>2</sub> Molecules through Photoassociation*, Phys. Rev. Lett. **80**, 4402–4405 (1998). 131
- [165] U. Marvet, M. Dantus, *Femtosecond photoassociation spectroscopy: coherent bond formation*, Chem. Phys. Lett. **245**, 393–399 (1995). 131
- [166] F. Fatemi, K. M. Jones, H. Wang, I. Walmsley, P. D. Lett, *Dynamics of photoinduced collisions of cold atoms probed with picosecond laser pulses*, Phys. Rev. A **64**, 033421/1–7 (2001). 131
- [167] B. L. Brown, A. J. Dicks, I. A. Walmsley, *Coherent Control of Ultracold Molecule Dynamics in a Magneto-Optical Trap by Use of Chirped Femtosecond Laser Pulses*, Phys. Rev. Lett. **96**, 173002/1–4 (2006). 131
- [168] W. Salzmann, U. Poschinger, R. Wester, M. Weidemüller, A. Merli, S. M. Weber, F. Sauer, M. Plewicky, F. Weise, A. M. Esparza, L. Wöste, A. Lindinger, *Coherent control with shaped femtosecond laser pulses applied to ultracold molecules*, Phys. Rev. A **73**, 023414/1–5 (2006). 131
- [169] C. P. Koch, J. P. Palao, R. Kosloff, F. Masnou-Seeuws, *Stabilization of ultracold molecules using optimal control theory*, Phys. Rev. A **70**, 013402/1–14 (2004). 131
- [170] U. Poschinger, W. Salzmann, R. Wester, M. Weidemüller, C. P. Koch, R. Kosloff, *Theoretical model for ultracold molecule formation via adaptive feedback control*, J. Phys. B: At. Mol. Phys. **39**, S1001–S1015 (2006). 131

- [171] B. Schafer-Bung, R. Mitric, V. Bonacic-Koutecky, *Photostabilization of the ultracold Rb-2 molecule by optimal control*, J. Phys. B: At. Mol. Phys. **39**, S1043–S1053 (2006). 131
- [172] Y. Niu, S. Wang, S. Cong, *Vibrational state-selectivity of product HI in photoassociation reaction  $I + H \rightarrow HI$* , Chem. Phys. Lett. **428**, 7–12 (2006). 131, 132
- [173] A. Guldberg, G. D. Billing, *Laser-induced dissociation of hydrogen fluoride*, Chem. Phys. Lett. **186**, 229–237 (1991). 132
- [174] M. A. Buldakov, V. N. Cherepanov, *The semiempirical dipole moment functions of the molecules HX ( $X = F, Cl, Br, I, O$ ), CO and NO*, J. Phys. B: At. Mol. Phys. **37**, 3973–3986 (2004). 132
- [175] J. Manz, G. K. Paramonov, *Laser control scheme for state-selective ultrafast vibrational excitation of the HOD molecule*, J. Phys. Chem. **97**, 12625–12633 (1993). 133
- [176] C. F. Bender, E. R. Davidson, *Theoretical Study of Several Electronic States of the Hydrogen Fluoride Molecule*, J. Chem. Phys. **49**, 4989–4995 (1968). 134
- [177] I. Levy, M. Shapiro, *Theory of electronic branching in the photodissociation of HI and DI*, J. Chem. Phys. **89**, 2900–2908 (1988). 134
- [178] M. J. Wright, S. D. Gensemer, J. Vala, R. Kosloff, P. L. Gould, *Control of Ultracold Collisions with Frequency-Chirped Light*, Phys. Rev. Lett. **95**, 063001/1–4 (2005). 137
- [179] M. J. Wright, J. A. Pechkis, J. L. Carini, S. Kallush, R. Kosloff, P. L. Gould, *Coherent control of ultracold collisions with chirped light: Direction matters*, Phys. Rev. A **75**, 051401/1–4 (2007). 137
- [180] C. D. Schwieters, H. Rabitz, *Optimal control of nonlinear classical systems with application to unimolecular dissociation reactions and chaotic potentials*, Phys. Rev. A **44**, 5224–5238 (1991). 137

- [181] C. D. Schwieters, H. Rabitz, *Optimal control of classical systems with explicit quantum-classical-difference reduction*, Phys. Rev. A **48**, 2549–2557 (1993). 137
- [182] Y. Zhao, O. Kühn, *Competitive local laser control of photodissociation reaction  $HCo(CO)_4$ :  $HCo((CO)_3+CO$  in electronic ground state*, J. Phys. Chem. A **104**, 4882–4888 (2000). 137
- [183] S. Gräfe, P. M. V. Engel, *Classical aspects emerging from local control of energy and particle transfer in molecules*, J. Photochem. Photobiol. A: Chem. **180**, 271–276 (2006). 137, 140
- [184] T. D. Gaily, S. D. Rosner, R. A. Holt, *New laser-induced fluorescence method for molecular beam velocity analysis*, Rev. Sci. Instrum. **47**, 143–145 (1976). 137
- [185] M. Gruebele, G. Roberts, M. Dantus, R. M. Bowman, A. H. Zewail, *Femtosecond temporal spectroscopy and direct inversion to the potential: Application to iodine*, Chem. Phys. Lett. **166**, 459–469 (1990). 147
- [186] V. Engel, H. Metiu, *2-Photon Wave-Packet Interferometry*, J. Chem. Phys. **100**, 5448–5458 (1994). 147
- [187] N. F. Scherer, R. J. Carlson, A. Matro, M. Du, A. J. Ruggiero, V. Romero-Rochin, J. A. Cina, G. R. Fleming, S. A. Rice, *Fluorescence-detected wave packet interferometry: Time resolved molecular spectroscopy with sequences of femtosecond phase-locked pulses*, J. Chem. Phys. **95**, 1487–1511 (1991). 147
- [188] T. S. Humble, J. A. Cina, *Molecular State Reconstruction by Nonlinear Wave Packet Interferometry*, Phys. Rev. Lett. **93**, 060402/1–4 (2004). 147
- [189] A. Assion, T. Baumert, J. Helbing, V. Seyfried, G. Gerber, *Coherent control by a single phase shaped femtosecond laser pulse*, Chem. Phys. Lett. **259**, 488–494 (1996). 147
- [190] C. J. Bardeen, J. Cao, F. L. H. Brown, K. R. Wilson, *Using time-dependent rate equations to describe chirped pulse excitation in condensed phases*, Chem. Phys. Lett. **302**, 405–410 (1999). 147

- [191] F. Gai, J. C. McDonald, P. A. Anfinrud, *xxx*, *J. Am. Chem. Soc.* **119**, 6201 (1997). 148
- [192] S. Ruhman, B. Hou, N. Friedman, M. Ottolenghi, M. Sheves, *xxx*, *J. Am. Chem. Soc.* **124**, 8854 (2002). 148
- [193] D. S. Larsen, I. H. M. van Stokkum, M. Vengris, M. A. van der Horst, F. L. de Weerd, K. J. Hellingwerf, R. van Grondelle, *Incoherent Manipulation of the Photoactive Yellow Protein Photocycle with Dispersed Pump-Dump-Probe Spectroscopy*, *Biophys. J.* **87**, 1858–1872 (2004). 148
- [194] W. Wohlleben, T. Buckup, J. L. Herek, M. Motzkus, *Coherent Control for Spectroscopy and Manipulation of Biological Dynamics*, *ChemPhysChem* **6**, 850–857 (2005). 148
- [195] F. Gai, K. C. Hasson, J. C. McDonald, P. A. Anfinrud, *Chemical Dynamics in Proteins: The Photoisomerization of Retinal in Bacteriorhodopsin*, *Science* **279**, 1886–1891 (1998). 149
- [196] Y. Ohtsuki, K. Ohara, M. Abe, K. Nakagami, Y. Fujimura, *New quantum control pathway for a coupled-potential system*, *Chem. Phys. Lett.* **369**, 525–533 (2003). 149
- [197] P. N. *et al.*, *Linearly chirped versus colored double femtosecond laser pulses: differences and analogies*, to be submitted (2007). 155, 156
- [198] G. Vogt, P. Nuernberger, R. Selle, F. Dimler, T. Brixner, G. Gerber, *Analysis of femtosecond quantum control mechanisms with colored double pulses*, *Phys. Rev. A* **74**, 033413 (2006). 160
- [199] M. Renard, R. Chaux, B. Lavorel, O. Faucher, *Pulse trains produced by phase-modulation of ultrashort optical pulses: tailoring and characterization*, *Opt. Express* **12**, 473–482 (2004). 160
- [200] H. Rabitz, M. Hsieh, C. Rosenthal, *Quantum Optimally Controlled Transition Landscapes*, *Science* **303**, 1998–2001 (2004). 160
- [201] H. A. Rabitz, M. Hsieh, C. Rosenthal, *Optimal control landscapes for quantum observables*, *J. Chem. Phys.* **124**, 204107/1–6 (2006). 160

- 
- [202] I. N. Bronstein, K. A. Semendjaev, G. Musiol, H. Mühlig, *Taschenbuch der Mathematik*, Verlag Harri Deutsch, Frankfurt/Main (2001). 183, 184



# List of publications

1. M. Erdmann, P. Marquetand, V. Engel  
*Combined electronic and nuclear dynamics in a simple model system*  
J. Chem. Phys. **119**, 672 - 679 (2003).
2. S. Gräfe, P. Marquetand, V. Engel, N. E. Henriksen, K. B. Møller  
*Quantum control fields from instantaneous dynamics*  
Chem. Phys. Lett. **398**, 180 - 185 (2004).
3. P. Marquetand, A. Materny, N. E. Henriksen, V. Engel  
*Molecular orientation via a dynamically induced pulse-train: Wave packet dynamics of NaI in a static electric field*  
J. Chem. Phys. **120**, 5871 - 5874 (2004).
4. P. Marquetand, V. Engel  
*Femtosecond pulse induced predissociation dynamics in static electric fields*  
Phys. Chem. Chem. Phys. **7**, 469 - 474 (2005).
5. P. Marquetand, V. Engel  
*Predissociation and dissociation dynamics in quantum control fields*  
Chem. Phys. Lett. **407**, 471 - 476 (2005).
6. P. Marquetand, C. Meier, V. Engel  
*Local control of molecular fragmentation: The role of orientation*  
J. Chem. Phys. **123**, 204320/1 - 7 (2005).

7. P. Marquetand, S. Gräfe, D. Scheidel, V. Engel  
*Local control of the quantum dynamics in multiple potential wells*  
J. Chem. Phys. **124**, 054325/1 - 7 (2006).
  
8. S. Gräfe, P. Marquetand, V. Engel  
*Classical aspects emerging from local control of energy and particle transfer in molecules*  
J. Photochem. Photobiol. A: Chem. **180**, 271 - 276 (2006).  
Special Issue: "Coherent Control of Photochemical and Photobiological Processes"
  
9. P. Marquetand, V. Engel  
*Complete local control of molecular excited states photodissociation*  
Chem. Phys. Lett. **426**, 263 - 267 (2006).
  
10. J. Seibt, P. Marquetand, V. Engel, F. Würthner, Z.Chen, V. Dehm  
*On the geometry dependence of molecular dimer spectra with an application to aggregates of perylene bisimide*  
Chem. Phys. **328**, 354 - 362 (2006).
  
11. P. Marquetand, S. Gräfe, V. Engel, C. Meier  
*Instantaneous dynamics and quantum control: principles and applications*  
in: Coherent Control of Molecules, B. Lasorne and G. A. Worth (Eds.), CCP6, Daresbury, 2006.
  
12. S. Koller, J. Seibt, P. Marquetand, V. Engel  
*Application of a reflection principle to spectroscopic transitions in molecular dimers*  
Chem. Phys. Lett. **433**, 199 - 203 (2006).



- 
13. Z. Chen, V. Stepanenko, V. Dehm, P. Prins, L. Siebbeles, J. Seibt, P. Marquetand, V. Engel, F. Würthner  
*Photoluminescence and conductivity of self-assembled  $\pi$ - $\pi$  stacks of perylene bisimide dyes*  
Chem. Eur. J. **13**, 436 - 449 (2007).
  
  14. P. Marquetand, V. Engel  
*Local control theory applied to molecular photoassociation*  
J. Chem. Phys. **127**, 084115/1 - 6 (2007).
  
  15. P. Marquetand, P. Nuernberger, G. Vogt, T. Brixner, V. Engel  
*Properties of wave packets deduced from quantum control fitness landscapes*  
Europhys. Lett. **accepted**, (2007).
  
  16. P. Marquetand, V. Engel  
*Analysis of photoassociation laser fields derived from local control theory*  
J. Phys. B **submitted**, (2007).
  
  17. P. Marquetand, P. Nuernberger, G. Vogt, T. Brixner, V. Engel  
*Molecular dump processes induced by chirped laser pulses*  
**in preparation**, (2007).



# Danksagung

Allen Menschen, die mich auf dem Weg während meiner Doktorarbeit begleitet haben, danke ich an dieser Stelle. An erster Stelle steht hierbei mein Betreuer Prof. Dr. Volker Engel, ohne den diese Arbeit nicht möglich gewesen wäre. Er war immer offen für Fragen aller Art und sorgte stets für das Wohl seiner Gruppe. Dabei ließ er viele Freiheiten und blieb aufgeschlossen und locker im Umgang mit allerlei Spaß und Zwischenmenschlichem. Besonders danke ich ihm auch dafür, dass er mir Forschungsaufenthalte im Ausland und den Besuch zahlreicher Fachtagungen ermöglichte.

Mein Dank gilt ebenfalls den Mitgliedern des Arbeitskreises: Anfangen möchte ich bei Dr. Marco Erdmann, der mich schon als F-Praktikant betreute und bei dem ich auch heute noch bei allen Computer-technischen Fragen Rat finde. Mit Steffi Gräfe wurde es nie langweilig, nicht zuletzt durch die verschiedensten Gespräche, ob fachlich oder privat. Auch wenn Theo Lohmüller uns besuchte, war es immer lustig. Daniel Scheidel lockerte mit seiner eigenen Art der Variablenbenennung den Alltag auf. Joachim Seibt war als Physiker für unser Arbeitsgebiet bestens gerüstet und die Zusammenarbeit daher einfach und angenehm. Anu Schaumlöffel zeigte schon in den ersten Wochen ihrer Diplomarbeit, dass sie mit Herz bei der Sache ist. Und dann gab es da noch die F-Praktikanten, nicht nur meine, sondern alle, die sich hier für die Theorie interessierten: Silvia Baumann, Ciprian Padurariu, Andre Berkefeld, Stephan Koller, Eva-Maria Tanzer, Sebastian Östreicher und Maximilian Aulbach. Mit ihnen konnte ich die Arbeit von verschiedenen Seiten betrachten.

Des weiteren danke ich meinen Kooperationspartnern. Besonders mit Patrick Nürnberger bereitete mir die Zusammenarbeit viel Freude. Die Fouriertransformationen mit ihm und Susanne Fechner in der Cafeteria werde ich so schnell nicht vergessen. Auch die Diskussionen mit Dr. Gerhard Vogt waren sehr anregend. Prof. Dr. Tobias Brixner schätze ich sehr wegen seiner exzellenten Ideen bzgl. der kohärenten

Kontrolle aber auch wegen Ratschlägen zu anderen Themen. Prof. Dr. Gustav Gerber danke ich für die Möglichkeit an den ersten beiden Workshops zur Ultrakurzzeitphysik und Quantenkontrolle teilzunehmen. Seine fachliche Kompetenz kann ich nicht genug würdigen. Seinem ganzen Arbeitskreis bin ich sehr verbunden, weil ich dort viel Neues lernte und das gemeinsame Ski- und Snowboardfahren viel Spaß machte. Mein Dank gilt ebenfalls Prof. Dr. Reinhold Fink, der sich immer viel Zeit für meine Probleme mit der Polarisierbarkeit nahm. Prof. Dr. Christoph Meier danke ich nicht nur für eine tolle Zeit in Toulouse, sondern auch für sein Vertrauen, als ich kurzfristig seinen Vortrag in Birmingham übernehmen durfte. Für den netten Empfang in Kalifornien bedanke ich mich bei Prof. Dr. Horia Metiu, die Zeit dort war einfach zu kurz. Außerdem danke ich Prof. Dr. Arnulf Materny für seinen Rat bei den Untersuchungen zu den statischen Feldern. Ihn und Prof. Dr. Ulrich Kleinekathöfer in Bremen zu besuchen war sehr interessant.

Schließlich haben alle Mitarbeiter aus dem zweiten Stockwerk des Instituts für Physikalische Chemie zu einer tollen Arbeitsatmosphäre beigetragen: Stefan Dümmler, Christoph Groß, Juliane Köhler, Ulrich Lorenz, Dr. Raman Maksimenka, Markus Margraf, Bastian Noller, Dr. Wolfgang Roth, Michael Schneider, Christof Schon, Dr. Thomas Schüßler und Dr. Matthias Zierhut. Die Zeit mit ihnen möchte ich nicht missen. Hierbei danke ich Stefan Dümmler besonders für das Korrekturlesen dieser Arbeit. Nicht zu vergessen sind auch Prof. Dr. Otto Dopfer, der mir u.a. die Welt von Mac und Apple eröffnet hat, und Prof. Dr. Ingo Fischer, dessen gute Laune immer ansteckend war. Dr. Roland Colditz danke ich für seine lustigen Anekdoten und witzige Stunden im Praktikum. Und dann gab es da noch die Sekretärinnen, die den Betrieb am Laufen hielten: Elvira König, Andrée Meyer und Gudrun Mühlrath.

Besonders herzlich bedanke ich mich bei meiner Freundin Kerstin Nicklaus. Sie war immer für mich da und stand mir mit Rat und Tat zur Seite. Für ihre Liebe und ihren Beistand bin ich ihr sehr dankbar.

Meine Eltern glaubten stets an mich und meine Arbeit, wofür ich ihnen innig danke. Ohne ihre Unterstützung wäre mein Studium wohl kaum möglich gewesen. Auch meinen Geschwistern Ann-Sophie, Christoph und Justus danke ich für so manche schöne Stunde und für ihr Interesse an meiner Forschung.





# Erklärung

Hiermit erkläre ich an Eides statt, dass ich die Dissertation

## **Vectorial properties and laser control of molecular dynamics**

selbständig angefertigt und keine anderen als die von mir angegebenen Quellen und Hilfsmittel benutzt habe.

Ich erkläre weiterhin, dass diese Dissertation weder in gleicher oder anderer Form bereits in einem anderen Prüfungsverfahren vorgelegen hat.

Ich habe früher außer den mit dem Zulassungsgesuch urkundlich vorgelegten Graden keine weiteren akademischen Grade erworben oder zu erwerben versucht.

Würzburg, den 10.07.2007

Philipp Marquetand







Philipp Marquetand

---

Diplom-Chemiker

Tel.: +49 931 - 45 26 937

+49 170 - 488 68 53

Email: pmarquetand@web.de



# Curriculum Vitae

## Persönliche Daten

---

Nachname: Marquetand  
Vorname: Philipp  
Adresse: Moritzgasse 3  
97070 Würzburg  
Geburtsdatum/-ort: 10. Oktober 1978, Heidelberg  
Nationalität: deutsch  
Familienstand: ledig

## Schulbildung

---

1985 - 1989 Nibelungen-Grundschule Heppenheim  
1989 - 1992 Starkenburg-Gymnasium Heppenheim  
1992 - 1998 Gymnasium Michelstadt  
06/1998 Allgemeine Hochschulreife (Note: 1,5)

## Studium

---

1999 - 2001 Grundstudium der Chemie an der Universität Heidelberg  
2001 - 2004 Hauptstudium der Chemie an der Universität Würzburg  
08/2003 - 02/2004 Diplomarbeit bei Prof. Dr. V. Engel  
Titel: Vibrations-Rotationsdynamik in statischen Feldern  
02/2004 Diplom in Chemie (Note: sehr gut)  
03/2004 - 10/2007 Dissertation bei Prof. Dr. V. Engel

## Tätigkeiten

---

Sommersemester 2001	Betreuung einer Übungsgruppe für Mathematik für Chemiker
Sommersemester 2002	Betreuung des chemischen Praktikums für Mediziner
seit 10/2003	Administrator des CIP-Pools Chemie
seit 04/2004	Betreuung des physikalisch-chemischen Praktikums für Chemiker
seit 04/2004	Betreuung einer Übungsgruppe für Quantenchemie für Chemiker

## Sonstige Qualifikationen

---

Sprachen:	Deutsch (Muttersprache) Englisch (fließend) Französisch (fortgeschritten) Spanisch (Grundkenntnisse)
EDV-Kenntnisse:	Programmieren in Fortran, HTML Kenntnisse in C++, Perl Administration von High Performance Clustern und Netzwerken Unix, Linux, Windows MS Office, TeX
Wehrdienst:	09/1998 - 06/1999 Transportbataillon 370, Diez/Lahn
Internat. Erfahrungen:	10/2004 - 11/2004 Université-Paul-Sabatier, Toulouse, France 11/2005 - 12/2005 University of California at Santa Barbara, USA
Fortbildungen:	Geprüfter Projektmanager Wirtschaftschemie GDCh (Abschluss 03/2006) BWL für Chemiker (02/2005)
Ehrenamtl. Tätigkeiten:	Aktives Mitglied der Fachschaft Chemie (2002 - 2004) Mitglied im Bundesvorstand des JungChemikerForums (JCF; junge Organisation innerhalb der Gesellschaft Deutscher Chemiker) Sprecher des JungChemikerForums Würzburg Betreuer von Kinder- und Jugendfreizeiten
Sonstiges:	Teilnahme an der 55. Nobelpreisträgertagung 2005 Posterpreis der QQQ des IOP
Hobbys:	Kampfsport, Gesellschaftstanz, Fußball, Reiten